Origami Structures Based on Rigidly Foldable Tessellation Patterns



David Xing

Keble College

A dissertation submitted for the degree of Doctor of Philosophy in the

Department of Engineering Science at the University of Oxford

Michaelmas Term, 2022

To My Family

Abstract

Origami Structures Based on Rigidly Foldable Tessellation Patterns

David Xing, Keble College, Oxford

A dissertation submitted for the degree of Doctor of Philosophy at the University of Oxford

---

This dissertation details the geometry and kinematics of novel origami tessellation structures designed to possess desirable properties found in commonly studied classical origami tessellations. Research on these novel origami models consists of geometric and kinematic analysis of their crease patterns and partially folded states. Each proposed origami tessellation is flat-foldable and rigidly foldable. Multiple sheets of origami tessellations assemble to form stacked origami structures that are also rigidly foldable. The research conducted in this dissertation produced the following main achievements.

First, an investigation into the geometry and kinematics of 4C origami tessellations reveals many different stacked origami structures. The degree-4 single-vertex origami model, 4C, is the simplest unit in any 4C origami tessellation. A composite model called the Double 4C demonstrates the mechanisms that emerge when stacking two flat-foldable 4Cs. A thick-panel version of the Double 4C shows it can accommodate panel thickness. The matrix method determines the kinematics of 4C origami tessellations, which reveals some to be flat-foldable and rigidly foldable. Geometric proofs show that certain 4C origami tessellations are crease-stackable, in which sheets of the origami tessellation can stack along designated sets of creases to form stacked origami structures. Crease stacking, panel stacking, and weaving are three methods to stack 4C origami tessellations, and each method yields a distinct stacked origami structure.

Second, the origami claw tessellation, OCT, presents a novel flat-foldable, rigidly foldable, and crease-stackable origami tessellation. By combining 4Cs with 6Cs, called claw units, the OCT possesses multiple DOFs. The matrix method determines the kinematics of the 4Cs and claw units. Geometric proofs show the OCT is crease-stackable by examining the geometry of the 4Cs and claw units. The numerical method computes the exact number of DOFs in the OCT. Stacking sheets of the OCT results in a stacked structure with only one DOF. Families of OCTs are defined as sets of OCTs such that any two in the same family are crease-stackable with each other, resulting in self-locking stacked OCTs.

Third, the modular origami horn chain, MOHC, and the modular origami claw chain, MOCC, are proposed. Both are flat-foldable, rigidly foldable, and crease-stackable. These origami tessellations match the shape of a non-intersecting planar curve in a specified partially folded state. A proposed algorithm converts a planar curve into a piecewise-linear curve, which is converted into the crease pattern of a MOHC/MOCC. Stacking these origami tessellations results in the stacked MOHC/MOCC. The concept of families of MOHCs and MOCCs is used to assemble self-locking stacked origami chains.

For each of these proposed origami tessellations, physical models are constructed to demonstrate their kinematic properties. CAD software is used to assemble stacked origami structures. The research in this dissertation has the potential to unfold a new generation of origami tessellations and their stacked structures across engineering fields.

Keywords: Origami Tessellations, Flat-foldable Origami, Rigid Origami, Kinematics, Mechanical Linkage.

Acknowledgements

I want to thank my family, friends, and colleagues for all their help and inspiration throughout my academic endeavor. I could not have completed this journey without them.

I gratefully acknowledge my academic supervisor, Dr. Zhong You, for being patient and resourceful in guiding me during my time in Oxford University. When I had questions, he provided me with the answers and resources I needed. He would keep my colleagues and me up to date on the latest origami research. I feel I have become a more confident and punctual researcher thanks to him. This experience will surely guide me in the next chapter of my life.

My time in the University of Oxford would not be what it was without my friends and colleagues in the Department of Engineering Science and Keble College. It has been an unforgettable experience getting to know them and learning about their own areas of interest. Spending time with such brilliant and gregarious researchers has made my experience in Oxford a delight.

To my family, you have always encouraged me to pursue my passions. I was always told to find something I was passionate about and become the best version of myself in that discipline. My parents nurtured a sense of curiosity in me ever since I was young, and this is exactly how I have gotten the inspiration to research origami. I look forward to seeing how my future unfolds.

Contents

ABSTRACT……..……..II

ACKNOWLEDGEMENT……..…….…..…….…..……..IV

CONTENTS……...V

LIST OF FIGURES…….IX

LIST OF TABLES……XVI

NOMENCLATURE……XVII

CHAPTER 1 INTRODUCTION..…….1

1.1 Origami Tessellations in Engineering...…….1

1.2 Scope and Aim..……5

1.3 Outline of Dissertation…….7

CHAPTER 2 LITERATURE REVIEW……10

2.1 Origami Tessellations……10

2.1.1 Crease Patterns of Origami Tessellations…….10

2.1.2 Origami Tessellation Properties……12

2.1.3 Thick-Panel Origami……..15

2.2 Origami Tessellations as Mechanical Linkages……..17

2.2.1 Mechanical Linkages……..17

2.2.2 Matrix Method for Origami Tessellations……22

2.2.3 Matrix Method for Thick-Panel Origami…….26

2.2.4 Numerical Method for Calculating DOFs……30

2.3 Classical Origami Tessellations……33

2.3.1 Classical Miura-ori Pattern……...33

2.3.2 4C Origami Tessellations……...35

2.3.3 Origami Tessellations with Higher-Degree Vertices……...38

2.4 Stacking Origami Tessellations……42

2.4.1 Stacked Miura-ori Pattern…….42

2.4.2 Self-Locking Stacked Miura-ori Pattern……..44

2.4.3 Miura-ori Tubes……..45

2.5 Rigidly Foldable Origami Horns……..47

2.6 Summary…….49

CHAPTER 3 STACKING 4Cs AND 4C TESSELLATIONS…….....51

3.1 Introduction……51

3.2 Origami 4C and Double 4C……...52

3.2.1 Flat-Foldable Origami 4C……..52

3.2.2 Double 4C……56

3.2.3 Coplanarity Property of Flat-Foldable 4C……...61

3.3 Thick-Panel 4C and Double 4C……63

3.3.1 Thick-Panel Flat-Foldable 4C……63

3.3.2 Thick-Panel Double 4C……..68

3.4 Crease-Stackable 4C Origami Tessellation…….74

3.4.1 Crease-Stackable Classical Miura-ori Pattern…….74

3.4.2 Crease-Stackable Generalized Miura-ori Pattern……...79

3.5 Stacking Miura-ori Patterns…….85

3.5.1 Crease Stacking Miura-ori Patterns ……85

3.5.2 Panel Stacking Miura-ori Tubes……...87

3.5.3 Weaving Miura-ori Tubes……..90

3.6 Conclusion…….92

CHAPTER 4 ORIGAMI CLAW TESSELLATION (OCT)……...95

4.1 Introduction……95

4.2 Origami Claw Tessellation (OCT)……96

4.3 Computing DOFs of OCT……...107

4.4 Stacked OCT……114

4.5 Self-Locking Stacked OCT…….122

4.6 Conclusion……132

CHAPTER 5 MODULAR ORIGAMI HORN/CLAW CHAIN (MOHC/MOCC)..135

5.1 Introduction……..135

5.2 Origami Horn and Claw Units……...136

5.3 MOHC and MOCC Construction Algorithm……...148

5.4 Stacked MOHC and MOCC……...155

5.5 Self-Locking Stacked MOHC and MOCC ……...160

5.6 Conclusion……165

CHAPTER 6 CONCLUSION……...168

6.1 Main Achievements……..168

6.2 Future Works……...171

APPENDICES……174

Appendix A: Generalized Kinematics of 4C……...174

Appendix B: Generalized Kinematics of Thick-Panel 4C……..180

Appendix C: Generalized Kinematics of 6C……...185

Appendix D: Numerical Method for OCT……...190

REFERENCES……...193

List of Figures

Chapter 1

Figure 1.1: Origami tessellation example (Callens and Zadpoor, 2017)…….2
Figure 1.2: Stacking origami tessellations example (Filipov et al., 2015)……..4

Chapter 2

Figure 2.1: Crease pattern examples: (a) mountain, (b) valley, and (c) paper crane (Hull, 2013)……11
Figure 2.2: Miura-ori crease patterns: (a) classical Miura-ori and (b) generalized Miura-ori (Hu et al., 2019)…….12
Figure 2.3: Flat-foldability and rigid foldability of Miura-ori (Tachi, 2009)……....13
Figure 2.4: Flat-foldable and rigidly foldable Miura-ori derivative with one DOF (Gattas et al. 2013)…….15
Figure 2.5: Methods to accommodate thickness: (a) hinge shift, (b) volume trimming, (c) offset panel, and (d) offset crease (Ku and Demaine, 2016)……16
Figure 2.6: Origami of thick panels: (a) flat-foldable 4C and (b) square twist (Chen et al., 2015a)……17
Figure 2.7: Planar linkages: (a) scissor mechanism (Li et al., 2017) and (b) parallelogram linkage (Yu et al., 2009)……18
Figure 2.8: Spatial 4-bar linkages: (a) spherical 4-bar linkage (Pennestri et al., 2016) and (b) Bennett linkage (Lu et al., 2017)……...19
Figure 2.9: A flat-foldable 4C: (a) origami model and (b) its equivalent spherical 4-bar linkage (Barreto et al., 2020)……21
Figure 2.10: Spherical 4-bar linkage used to model a 4C (Chen et al., 2017)……...23
Figure 2.11: Origami model composed of 4Cs: (a) crease pattern and (b) each of the four vertices as spherical 4-bar linkages (Peng et al., 2018)…….26
Figure 2.12: A schematic diagram of a spatial 4-bar linkage……27
Figure 2.13: Classical Miura-ori pattern: (a) crease pattern, (b) partially folded state, and (c) mostly folded state (Evans et al., 2015)……...34

Figure 2.14: Miura-ori origami tessellation with unit shaded: (a) flat unfolded state,
(b) partially folded state, and (c) flat folded state (Gattas et al., 2013)…….34
Figure 2.15: Generalized symmetric Miura-ori pattern: (a) crease pattern,
(b) partially folded state, and (c) mostly folded state (Evans et al., 2015)……36
Figure 2.16: Barreto's Mars pattern: (a) crease pattern, (b) partially folded state, and
(c) mostly folded state (Evans et al., 2015)……...37
Figure 2.17: Huffman grid: (a) crease pattern, (b) partially folded state, and
(c) mostly folded state before collision (Evans et al., 2015)…….38
Figure 2.18: Yoshimura pattern: (a) crease pattern, (b) partially folded state, and
(c) mostly folded state before collision (Evans et al., 2015)…….39
Figure 2.19: Ron Resch triangle tessellation: (a) crease pattern,
(b) partially folded state, and (c) fully folded non-flat state (Callens and Zadpoor)…….40
Figure 2.20: Square waterbomb tessellation: (a) crease pattern,
(b) partially folded state, and (c) fully folded non-flat state (Callens and Zadpoor)…….41
Figure 2.21: Stacking Miura-ori sheets: (a) individual layers and
(b) stacked Miura-ori pattern (Ma et al., 2018)…….42
Figure 2.22: A 4-layer stacked Miura-ori pattern (Ma et al., 2018)……..43
Figure 2.23: Self-locking stacked Miura-ori pattern (Schenk and Guest, 2013a)…….45
Figure 2.24: Miura-ori tube: (a) assembly from two Miura-ori strips,
(b) origami tube, and (c) parallel alignment (Tachi, 2019)……46
Figure 2.25: Assembly of a rigidly foldable origami horn: (a) top and bottom crease
patterns and (b) rigidly foldable origami horn (Tachi, 2016)……47
Figure 2.26: Rigidly foldable origami horn in action: (a) folding until self-collision and
(b) reinforcing generalized Miura-ori pattern (Tachi, 2016)…….48

Chapter 3

Figure 3.1: 4Cs obtained from 4C origami tessellations: (a) Miura-ori pattern and
(b) generalized Miura-ori pattern……...53
Figure 3.2: Flat-foldable 4C: (a) flat unfolded state and (b) partially folded state……54
Figure 3.3: Folding sequence of the flat-foldable 4C……56
Figure 3.4: Double 4C in a partially folded state……...57

Figure 3.5: Folding sequence of the Double 4C……59
Figure 3.6: Schematic diagrams of Double 4C: (a) Preserving the panel shapes and
(b) simplifying the connections diagram……...60
Figure 3.7: Geometric proof of the coplanarity property for a flat-foldable 4C:
(a) sector angles labeled and (b) dihedral angles labeled……..61
Figure 3.8: Panels in the thick-panel flat-foldable 4C……...64
Figure 3.9: Thick-panel flat-foldable 4C in a partially folded state……..65
Figure 3.10: Folding sequence of the thick-panel flat-foldable 4C……...67
Figure 3.11: Thick-panel Double 4C in a partially folded state……69
Figure 3.12: Folding sequence of the thick-panel Double 4C……...70
Figure 3.13: Schematic diagrams of thick-panel Double 4C:
(a) preserving the panel shapes and (b) simplifying the connections diagram……..72
Figure 3.14: Two Miura-ori units: (a) type-M and (b) type-V……..75
Figure 3.15: Two 3 × 3 classical Miura-ori patterns generated from (a) type-M units and
(b) type-V units……..75
Figure 3.16: Two Miura-ori units in partially folded states: (a) type-M and (b) type-V...76
Figure 3.17: Miura-ori tube unit: (a) stacking a type-M on a type-V unit and
(b) a physical model……...78
Figure 3.18: Stacking sheets of the 3 × 3 classical Miura-ori pattern:
(a) type-M and type-V sheets, (b) 2-layer structure, and (c) 4-layer structure……..79
Figure 3.19: Two generalized Miura-ori units: (a) type-M and (b) type-V……..80
Figure 3.20: Two 3 × 3 generalized Miura-ori crease patterns generated from
(a) type-M units and (b) type-V units……81
Figure 3.21: Two generalized Miura-ori units in partially folded states: (a) type-M and
(b) type-V……...82
Figure 3.22: Generalized Miura-ori tube unit: (a) stacking a type-M on a type-V unit and
(b) a physical model……...85
Figure 3.23: Stacking pairs of type-M and type-V 3 × 3 Miura-ori sheets along their
creases: (a) one pair and (b) three pairs……86
Figure 3.24: A 2-layer stacked Miura-ori pattern: (a) partially folded state and
(b) mostly folded state……...87

Figure 3.25: Construction of Miura-ori tube: (a) type-M and type-V 1 × 3 Miura-ori sheets and (b) 1 × 3 Miura-ori tube……88
Figure 3.26: Arranging Miura-ori tubes in two layers in perpendicular directions: (a) three green tubes and (b) three red tubes……..88
Figure 3.27: Stacking Miura-ori tubes along their panels: (a) two Miura-ori tube layers and (b) stacked egg box pattern……..89
Figure 3.28: Construction of Miura-ori tube: (a) type-M and type-V 1 × 2 Miura-ori sheets and (b) 1 × 2 Miura-ori tube……90
Figure 3.29: Weaving Miura-ori tubes: (a) three green tubes, (b) three red tubes, and (c) the 3 × 3 woven Miura-ori pattern……91
Figure 3.30: Physical model of a 3 × 3 woven Miura-ori pattern in partially folded states……...92

Chapter 4

Figure 4.1: Claw unit with $\alpha = \pi / 6$ and $\beta = \pi / 3$……..97
Figure 4.2: Four types of claw units: (a) type-M1, (b) type-M2, (c) type-V1, and (d) type-V2…….98
Figure 4.3: A 4 × 4 OCT……99
Figure 4.4: A 2 × 2 OCT rigidly folding……..100
Figure 4.5: The OCT's 4C in a partially folded state……..101
Figure 4.6: Dihedral angle relations in the OCT's 4C with $\alpha = \pi / 6$ and $\beta = \pi / 3$…….101
Figure 4.7: Claw unit in a partially folded state……...103
Figure 4.8: Dihedral angle relations in the claw unit with $\alpha = \pi / 6$ and $\beta = \pi / 3$……...104
Figure 4.9: Numbering of creases and vertices in the 2 × 2 OCT……...108
Figure 4.10: Five DOFs of the 2 × 2 OCT with highlighted lines indicating fixed creases: (a) planar folding, (b) upper-right half folding, (c) lower-left half folding, (d) upper-right corner folding, and (e) lower-left corner folding……113
Figure 4.11: Creases in the 3 × 3 OCT that fold according to the five DOFs…….114
Figure 4.12: Claw units in partially folded states: (a) type-M1 and (b) type-V1……115
Figure 4.13: Stacked claw unit in a partially folded state……..……..116

Figure 4.14: Schematic diagrams of the stacked claw unit:
(a) preserving the panel shapes and (b) simplifying the connections diagram……117
Figure 4.15: Stacking claw units: (a) type-M1 on type-V1 and
(b) type-V1 on type-M1……...120
Figure 4.16: Two 4 × 4 OCTs: (a) type-M and (b) type-V ……120
Figure 4.17: Stacking sheets of the 4 × 4 OCT: (a) type-M, (b) type-V, and
(c) 2-layer stacked 4 × 4 OCT……121
Figure 4.18: Stacking 2 × 2 OCTs: (a) two 2 × 2 OCTs, (b) 2-layer stacked 2 × 2 OCT,
(c) two 2-layer stacked 2 × 2 OCTs, and (d) 4-layer stacked 2 × 2 OCT……122
Figure 4.19: 2-layer stacked 2 × 2 OCT……..122
Figure 4.20: Planar projection of one claw unit on another: (a) claw units and
(b) their respective planar zigzags……...123
Figure 4.21: Claw units in the same family: (a) $(\alpha_1, \beta_1) = (\pi / 6, \pi / 3)$ and
(b) $(\alpha_2, \beta_2) = (\tan^{-1}(1 / 3), \pi / 4)$……...125
Figure 4.22: Folding sequence of the claw unit with $(\alpha_1, \beta_1) = (\pi / 6, \pi / 3)$:
(a) $\phi_1 = 1.9106$, (b) $\phi_1 = 1.2310$, and (c) $\phi_1 = 0.9154$……..127
Figure 4.23: Folding sequence of the claw unit with $(\alpha_2, \beta_2) = (\tan^{-1}(1 / 3), \pi / 4)$:
(a) $\phi_1' = \pi$, (b) $\phi_1' = \pi / 2$, and (c) $\phi_1' = 1.1437$……127
Figure 4.24: Folding sequence of the self-locking stacked claw unit:
(a) $(\phi_1, \phi_1') = (1.9106, \pi)$, (b) $(\phi_1, \phi_1') = (1.2310, \pi / 2)$, and
(c) $(\phi_1, \phi_1') = (0.9154, 1.1437)$……128
Figure 4.25: Dihedral angle relations in the self-locking stacked claw unit……129
Figure 4.26: 2 × 2 OCTs in the same family: (a) $(\alpha_1, \beta_1) = (\pi / 6, \pi / 3)$ and
(b) $(\alpha_2, \beta_2) = (\tan^{-1}(1 / 3), \pi / 4)$……...130
Figure 4.27: Folding sequence of the 2 × 2 OCT with $(\alpha_1, \beta_1) = (\pi / 6, \pi / 3)$:
(a) $\phi_1 = 1.9106$, (b) $\phi_1 = 1.2310$, and (c) $\phi_1 = 0.9154$……..130
Figure 4.28: Folding sequence of the 2 × 2 OCT with $(\alpha_2, \beta_2) = (\tan^{-1}(1 / 3), \pi / 4)$:
(a) $\phi_1' = \pi$, (b) $\phi_1' = \pi / 2$, and (c) $\phi_1' = 1.1437$……131
Figure 4.29: Folding sequence of the self-locking stacked 2 × 2 OCT:
(a) $(\phi_1, \phi_1') = (1.9106, \pi)$, (b) $(\phi_1, \phi_1') = (1.2310, \pi / 2)$, and
(c) $(\phi_1, \phi_1') = (0.9154, 1.1437)$……132

Figure 4.30: Self-locking 4-layer stacked 2 × 2 OCT……..132

Chapter 5

Figure 5.1: Horn unit: (a) crease pattern and (b) truncated horn unit……..137
Figure 5.2: Claw unit (a) crease pattern and (b) truncated claw unit……...139
Figure 5.3: Truncated horn unit: (a) flat unfolded state and (b) partially folded state…141
Figure 5.4: Truncated claw unit: (a) flat unfolded state and (b) partially folded state…143
Figure 5.5: Stacked units: (a) stacked horn unit, (b) truncated stacked horn unit,
(c) stacked claw unit, and (d) truncated stacked claw unit……..144
Figure 5.6: Connections diagrams: (a) the stacked horn unit and
(b) stacked claw unit……145
Figure 5.7: Units in the same family:
(a) two horn units, (b) projecting one horn unit on the other,
(c) two claw units, and (d) projecting one claw unit on the other……...147
Figure 5.8: Origami tessellations matching the shape of a curve:
(a) MOHC and (b) MOCC……...148
Figure 5.9: Converting a planar curve to a piecewise-linear approximation: (a) target
curve, (b) marking next vertex, (c) continuing to mark vertices, and
(d) connecting the vertices and marking the midpoints of the segments…….149
Figure 5.10: Constructing templates for horn units and claw units: (a) Miura-ori pattern,
(b) rotating panels, and (c) templates for the horn units and claw units……..150
Figure 5.11: Concatenating horn units and claw units:
(a) horn units form (b) a MOHC and (c) claw units form (d) a MOCC……..151
Figure 5.12: Origami chains in partially folded states: (a) MOHC, (b) MOCC, and
(c) a chain combining horn units and claw units…….152
Figure 5.13: Deployment of a MOHC and its piecewise-linear curves……...154
Figure 5.14: Stacking two origami chains: (a) stacking MOHCs and
(b) stacking MOCCs……156
Figure 5.15: A stacked MOHC: (a) fully unfolded state, (b) partially folded state, and
(c) fully folded state…….156
Figure 5.16: Dihedral angle relations in the MOHC with $\alpha = \pi / 6$ and $\beta = \pi / 3$……157

Figure 5.17: A 2-layer stacked MOCC: (a) fully unfolded state,
(b) partially folded state, and (c) fully folded state……..158
Figure 5.18: Dihedral angle relations in the MOCC with $\alpha = \pi / 6$ and $\beta = \pi / 3$……158
Figure 5.19: A 4-layer stacked MOCC……159
Figure 5.20: Connections diagrams: (a) stacked MOHC and
(b) 2-layer stacked MOCC……...159
Figure 5.21: Deployment of a stacked MOHC……160
Figure 5.22: A self-locking stacked MOHC: (a) fully folded state,
(b) partially folded state, and (c) self-locking state…….161
Figure 5.23: A self-locking 2-layer stacked MOCC:
(a) fully folded state, (b) partially folded state, and (c) self-locking state……...162
Figure 5.24: A self-locking 4-layer stacked MOCC:
(a) fully folded state, (b) partially folded state, and (c) self-locking state……...162
Figure 5.25: MOHCs in the same family:
(a) $\alpha_1 = \pi / 12$, $\beta_1 = 5\pi / 12$ and (a) $\alpha_2 = 0.1948$, $\beta_2 = 7\pi / 18$……..163
Figure 5.26: Deployment of a MOHC:
(a) $\phi_{1g} = \phi_{1max}$, (b) $\phi_{1g} = 3\pi / 4$, and (c) $\phi_{1g} = \pi / 2$……...163
Figure 5.27: Deployment of a MOHC:
(a) $\phi_{1p} = \pi$, (b) $\phi_{1p} = 2.5044$, and (c) $\phi_{1p} = 1.6274$……...164
Figure 5.28: Deployment of a self-locking stacked MOHC: (a) $\phi_{1g} = \phi_{1max}$, $\phi_{1p} = \pi$,
(b) $\phi_{1g} = 3\pi / 4$, $\phi_{1p} = 2.5044$, and (c) $\phi_{1g} = \pi / 2$, $\phi_{1p} = 1.6274$……...164
Figure 5.29: Dihedral angle relations in the self-locking stacked MOHC……..165

Appendices

Figure A.1: Flat-foldable 4C in a partially folded state……...174
Figure B.1: Spatial 4-bar linkage with shifting coordinate systems……180
Figure C.1: Flat-foldable 6C in a partially folded state……...185
Figure D.1: Numbering of creases and vertices in the 2 × 2 OCT……..190
Figure D.2: The null space of J_{comb} of the 2 × 2 OCT with $\alpha = \pi / 6$ and $\beta = \pi / 3$……..192

List of Tables

Chapter 3

Table 3.1: Mechanisms in the Double 4C and Thick-Panel Double 4C……73

Chapter 4

Table 4.1: Number of DOFs in the $M \times N$ OCT……..112

Table 4.2: Mechanisms in the stacked claw unit…….119

Nomenclature

Chapter 2

n	Degree of vertex
v	Number of vertices
c	Number of creases
$\alpha_{i(i+1)}$	Sector angle between creases i and $(i+1)$
$d_{i(i+1)}$	Distance between axis of hinge i and axis of hinge $(i+1)$
ϕ_i	Dihedral angle at crease i
θ_i	Fold angle at crease i
θ	Vector of fold angles
$\Delta\theta$	Vector of changes in fold angles
$Q(\alpha_{i(i+1)}, \theta_i)$	Transformation matrix from crease i to crease $(i+1)$
$Q(\alpha_{i(i+1)}, \theta_i)^{-1}$	Transformation matrix from crease $(i+1)$ to crease i
$Q'(\alpha_{i(i+1)}, \theta_i)$	Derivative of $Q(\alpha_{i(i+1)}, \theta_i)$ with respect to θ_i
$Q(\alpha_{i(i+1)}, \theta_i, d_{i(i+1)})$	Transformation matrix from hinge i to hinge $(i+1)$
$Q(\alpha_{i(i+1)}, \theta_i, d_{i(i+1)})^{-1}$	Transformation matrix from hinge $(i+1)$ to hinge i
$R_x(\alpha_{i(i+1)})$	Rotation matrix about x-axis
$R_z(\theta_i)$	Rotation matrix about z-axis
$T_x(d_{i(i+1)})$	Translation matrix along x-axis
M_i	Product of transformation matrices
$0_{i\times j}$	$i \times j$ zero matrix
$I_{n\times n}$	$n \times n$ identity matrix

J	Jacobian matrix
J_{comb}	Combined Jacobian matrix

Chapter 3

n	Degree of vertex
$\alpha_{i(i+1)}$	Sector angle between creases i and $(i + 1)$
$d_{i(i+1)}$	Distance between axis of hinge i and axis of hinge $(i + 1)$
a, a_1, a_2, b, b_1, b_2	Miura-ori crease lengths
h, h_1, h_2	Miura-ori unit height
ϕ_i	Dihedral angle at crease i
θ_i	Fold angle at crease i
L, M, N	Dimensions of Miura-ori pattern
$Q(\alpha_{i(i+1)}, \theta_i)$	Transformation matrix from crease i to crease $(i + 1)$
$Q(\alpha_{i(i+1)}, \theta_i)^{-1}$	Transformation matrix from crease $(i + 1)$ to crease i
$Q(\alpha_{i(i+1)}, \theta_i, d_{i(i+1)})$	Transformation matrix from hinge i to hinge $(i + 1)$
$Q(\alpha_{i(i+1)}, \theta_i, d_{i(i+1)})^{-1}$	Transformation matrix from hinge $(i + 1)$ to hinge i
$I_{n\times n}$	$n \times n$ identity matrix

Chapter 4

n	Degree of vertex
v	Number of vertices
c	Number of creases
α, β, γ	Angles of claw unit

$\alpha_{i(i+1)}$	Sector angle between creases i and $(i + 1)$
a_1, a_2, a_3, a_4	Claw unit side lengths
ϕ_i	Dihedral angle at crease i
θ_i	Fold angle at crease i
θ	Vector of fold angles
$\Delta\theta$	Vector of changes in fold angles
L, M, N	Dimensions of Miura-ori pattern
$Q(\alpha_{i(i+1)}, \theta_i)$	Transformation matrix from crease i to crease $(i + 1)$
$Q(\alpha_{i(i+1)}, \theta_i)^{-1}$	Transformation matrix from crease $(i + 1)$ to crease i
$Q'(\alpha_{i(i+1)}, \theta_i)$	Derivative of $Q(\alpha_{i(i+1)}, \theta_i)$ with respect to θ_i
M_i	Product of transformation matrices
$0_{i\times j}$	$i \times j$ zero matrix
$I_{n\times n}$	$n \times n$ identity matrix
J	Jacobian matrix
J_{comb}	Combined Jacobian matrix

Chapter 5

α, β	Horn unit/claw unit angles
$\alpha_{i(i+1)}$	Sector angle between creases i and $(i + 1)$
γ	Angle of bend in planar curve at a knuckle vertex
a, b, c	Horn/claw unit side lengths
ϕ_i	Dihedral angle at crease i
h	Horn/claw unit height

1

Introduction

1.1 Origami Tessellations in Engineering

Origami is a traditional art form that transforms a flat sheet of paper into a 3D model through folding, a form of isometric transforming, without stretching, gluing, or tearing the material (Chen et al., 2019; Tachi, 2010b). The advantage of using origami in many engineering fields is the potential to transform the geometry of sheet-like material by folding. The folding found in origami models mirrors the movements found in mechanical linkages, so origami models are also deployable structures. Origami-based designs have provided novel solutions to existing engineering problems across disciplines, including bioengineering, architectural engineering, aerospace engineering, and robotics (Meloni et al., 2021). Several advantages found in origami include deployability, scalability, and ease of manufacture (Chen et al., 2015a). The subset of origami that makes efficient use of these properties is origami tessellations.

Origami tessellations are foldable paper models that utilize repeated patterns in the geometry of their crease patterns (Zhang and Chen, 2019). An origami tessellation, such as the one shown in Figure 1.1, starts from a flat sheet and folds according to its crease pattern to transform its geometry into a 3D folded state. Simply repeating the pattern found in the crease pattern grows the origami tessellation to its desired size and level of intricacy. The folding motion of the origami model changes its dimensions and shape, which can be determined geometrically. The origami tessellation's partially folded configuration continuously transforms as the model folds.

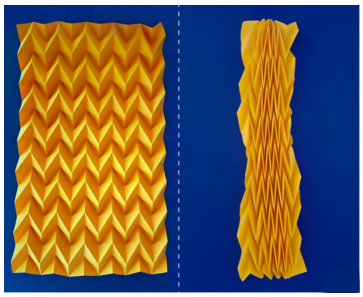


Figure 1.1: Origami tessellation example (Callens and Zadpoor, 2017)

Research in the past decade has revealed many engineering applications of origami tessellations (Meloni et al., 2021). These include deployable solar panels, tunable metamaterials, and origami-inspired robots (Evans et al. 2015). One objective origami researchers have is to discover new origami tessellations with important geometric and kinematic properties, which include flat-foldability and rigid foldability. These properties simplify the calculations that determine kinematic behavior of origami tessellations and their respective engineering structures. A common technique to find new designs is to use a classical origami tessellation and modify its crease pattern. These modifications would ideally preserve specific geometric and kinematic characteristics in the origami tessellation while optimizing the structure to perform certain functions.

One classical origami tessellation is the Miura-ori pattern (Barreto et al., 2020). Its crease pattern is a lattice of repeated units, each consisting of four parallelogram facets sharing a common vertex (Schenk and Guest, 2013). The simplicity in the geometry of the Miura-ori crease pattern makes it one of the most studied origami tessellations in engineering (Sareh and Guest, 2015). Flat-foldability allows the Miura-ori pattern to fold into a flat stack of sheets, and rigid foldability allows it to fold without bending or stretching the panels. The Miura-ori pattern also has only one degree of

freedom, DOF, of mobility (Gattas et al., 2013). The Miura-ori pattern also possesses the ability to stack with multiple copies of the origami tessellation. While origami engineers have thoroughly studied many techniques to modify and configure the Miura-ori pattern, these efforts are limited by its intrinsic geometry. Even so, research on the Miura-ori pattern and its variations reveals how generalizable and applicable the origami tessellation can be (Sareh and Guest, 2015).

Origami tessellations are limited to a single sheet, but copies of origami tessellations can form stacked origami structures, such as the one shown in Figure 1.2, composed of repeated unit cells in a 3D lattice (Ma et al., 2017). Stacking sheets not only adds height to the structure but also forms new geometries that cannot be constructed from a single sheet. Not all flat-foldable and rigidly foldable origami tessellations can form stacked structures that preserve these properties. An interesting origami research objective is to determine the geometric criteria these origami tessellations must satisfy to form stacked structures. Tachi and Miura have shown that layering and attaching folded sheets creates a rigidly flexible cellular mechanism, which is a stacked origami mechanism that remains rigidly foldable regardless of the number of sheets stacked in the structure (Lang, 2018). The overall dimensions of the rigidly foldable structure change in different proportions as the mechanism is actuated (Lang 2018). The stacked Miura-ori pattern is one of the most common stacked origami structures, but additional origami tessellations can be used to assemble similar stacked structures (Lang, 2018). Depending on the arrangement of the Miura-ori units in each individual sheet, the stacked Miura-ori pattern takes on many forms, including Miura-ori tubes and folded metamaterials (Schenk and Guest, 2013).

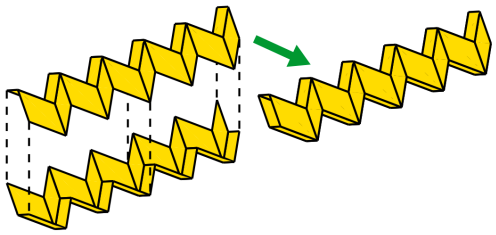


Figure 1.2: Stacking origami tessellations example (Filipov et al., 2015)

Various other origami tessellations possess their own unique set of characteristics (Meloni et al., 2021). Some examples are the Yoshimura pattern, Ron Resch triangle tessellation, and square waterbomb tessellation (Callens and Zadpoor, 2017). Each of these rigidly foldable origami tessellations possesses multiple DOFs. The limitation of these origami tessellations is that they lack some of the properties found in the Miura-ori pattern. Mainly, these origami tessellations cannot stack to form stacked origami structures that remain rigidly foldable (Callens and Zadpoor, 2017). This raises the question of whether there exist other origami tessellations that can stack in a similar manner to that of the Miura-ori pattern.

In addition to forming stacked origami structures from flat sheets, origami tessellations can fold to match the shapes of arbitrary non-intersecting curves. Instead of tessellating the entire plane, these origami tessellations fold into partially folded states that match the shapes of curves. Tachi designed a rigidly foldable origami horn that deploys into the shape of a 3D curve (Tachi, 2016). He also developed an algorithm that transforms a given 3D curve into horn-shaped origami sheets that form a stacked structure called the origami horn. When deployed into a partially folded state, the rigidly foldable origami horn matches the shape of the 3D curve. While they are useful for engineering applications, these origami horns come with their own limitations. Not every

curve can be transformed into an origami horn, and the origami horn may collide with itself as it deploys.

Origami tessellations have inspired many engineering applications, but most research on them is limited to conventional origami designs. These origami tessellations have been known for a long time, so discovering new origami tessellations would reveal exciting new research directions. The limitations to the current study of origami tessellations offer many opportunities for research discoveries. This dissertation will address the research problems outlined above by presenting novel origami tessellations and stacking them to form their stacked structures.

1.2 Scope and Aim

The origami tessellations of interest in this dissertation are limited to those that are developable, meaning they can be constructed from a flat planar sheet (Yellowhorse et al., 2018). While most traditional origami models are folded into a fixed form that is not later unfolded, the origami tessellations in this dissertation are those that can fold and unfold freely. In other words, all origami tessellations in this dissertation are shape-changing structures (Chen et al., 2015a). The design of these origami tessellations involves geometric and kinematic analysis of their crease patterns and folding processes. Physical origami models and computer simulations are used to validate and demonstrate the geometric and kinematic properties of the proposed origami tessellations.

The first aim is to determine the geometry of flat-foldable and rigidly foldable origami tessellations that are crease-stackable with each other. Crease-stackability is a property describing rigidly foldable origami models that can stack along designated sets

of creases to form rigidly foldable stacked origami structures. Kinematic analysis of single-vertex models determines the geometric requirements for them to stack and remain rigidly foldable. These single-vertex models are the basic units for origami tessellations. Proving the basic units are crease-stackable helps show the origami tessellations are also crease-stackable. Examining the linkages found in the stacked origami models reveals their DOFs. Also, the origami models made from zero-thickness sheets can be converted to thick-panel versions, transforming their constituent linkages.

The second aim is to design a novel flat-foldable, rigidly foldable, and crease-stackable origami tessellation that is not a derivative of the Miura-ori pattern, which consists entirely of degree-4 vertices. The proposed origami tessellation combines degree-4 vertices with degree-6 vertices to increase the number of DOFs. Kinematic analysis of this origami tessellation proves it is flat-foldable and rigidly foldable and computes its DOFs. Geometric proofs show this origami tessellation is also crease-stackable. Examining the linkages found in the origami tessellation's stacked structure shows it is flat-foldable and rigidly foldable with one DOF. Additional geometric proofs show which origami tessellations are crease-stackable with each other.

The third aim is to design chain-like origami tessellations that match the shape of a planar curve when they are in partially folded states. The proposed algorithm shows how to convert a given planar curve into two types of flat-foldable, rigidly foldable, and crease-stackable origami tessellations that match the shape of the curve in partially folded states. This algorithm creates the crease patterns of the origami tessellations, and geometric proofs show they are crease-stackable. Stacking distinct origami tessellations that are crease-stackable with each other results in stacked origami structures with self-

locking states. When fully deployed, these self-locking stacked origami structures match the shape of the planar curve.

1.3 Outline of Dissertation

This dissertation consists of a literature review, three research chapters on original designs of origami tessellations and their stacked structures, and a conclusion.

Chapter 2 is a literature review discussing research on origami concepts and past origami tessellations. Relevant origami concepts include mechanical linkages, mathematics of origami crease patterns, thick-panel origami, and stacked origami structures. This chapter details the mathematical techniques used to analyze the origami models described in later chapters. These techniques include the matrix method and the numerical method. This chapter also discusses the geometric and kinematic properties of various known origami tessellations. The most researched origami tessellation is the Miura-ori pattern, and many designs of origami tessellations take inspiration from this origami tessellation. Physical models accompany the discussion of these origami tessellations.

Chapter 3 examines the geometry and kinematics of origami tessellations consisting of 4Cs, which are degree-4 vertices. These origami tessellations are derivatives of the Miura-ori pattern, and the 4C serves as the basic origami unit of these origami tessellations. The matrix method helps derive equations describing the kinematics of 4C origami tessellations. The Double 4C, a new stacked structure introduced in this dissertation, is a composite stacked origami model constructed from two identical flat-foldable 4Cs. Examination of the Double 4C reveals it to be a rigidly foldable mechanism

with only one DOF. The Double 4C is later converted to its thick-panel version, which is also a rigidly foldable mechanism with only one DOF. Original geometric proofs show that certain 4C origami tessellations are crease-stackable. Sheets of certain 4C origami tessellations can be attached along their creases to form stacked origami structures. Three methods to stack 4C origami tessellations are proposed: crease stacking, panel stacking, and weaving. Each method produces a unique stacked origami structure. One new stacked origami structure introduced is the woven Miura-ori pattern, which is formed by weaving Miura-ori tubes.

Chapter 4 presents a novel origami tessellation that is flat-foldable, rigidly foldable, and crease-stackable while also possessing multiple DOFs. This new pattern is called the origami claw tessellation, OCT, which consists of 4Cs and 6Cs. The OCT is also the first known crease-stackable origami tessellation that is not a derivative of a Miura-ori pattern. The 6Cs of the OCT are called claw units, which each have three DOFs. The dimensions of the OCT depend on the number of claw units in the origami tessellation. The matrix method proves the OCT is rigidly foldable while the numerical method shows that the number of DOFs in the OCT depends on the dimensions of the OCT. A geometric proof shows that the claw unit is crease-stackable, and two claw units stack to make a stacked claw unit, which has only one DOF. By extension, the OCT is crease-stackable, and stacking identical sheets of the OCT results in the stacked OCT. The stacked OCT is a flat-foldable and rigidly foldable structure with only one DOF. Furthermore, a family of claw units is defined as a set of claw units in which any two are crease-stackable with each other. Two claw units in the same family stack to form the

self-locking claw unit. Similarly, two OCTs in the same family are crease-stackable with each other, and they stack to form the self-locking stacked OCT.

Chapter 5 presents a new algorithm showing how to construct two types of chain-like origami tessellations. Each one deploys into the shape of an arbitrary non-intersecting planar curve when the origami model is in a partially folded state. These models are the modular origami horn chain, MOHC, and the modular origami claw chain, MOCC, and they intend to improve upon the previous design of rigidly foldable origami horns. The MOHC and MOCC are composed of horn units and claw units, respectively. These units are proven to be flat-foldable, rigidly foldable, and crease-stackable origami models. The construction algorithm shows how an arbitrary non-intersecting planar curve is transformed into a MOHC and a MOCC. This algorithm concatenates horn units in a MOHC and claw units in a MOCC. Stacking identical sheets of the MOHC results in the stacked MOHC while stacking identical sheets of the MOCC results in the stacked MOCC. Both stacked structures deploy to match the shape of the planar curve. Moreover, self-locking stacked MOHCs and self-locking stacked MOCCs are constructed such that their self-locking states match the shape of the planar curve.

Chapter 6 is a conclusion that summarizes the main achievements of the research and provides a discussion on future works.

2

Literature Review

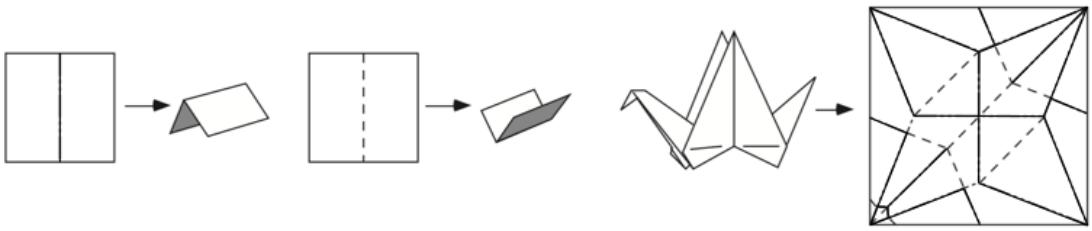
2.1 Origami Tessellations

2.1.1 Crease Patterns of Origami Tessellations

An origami tessellation starts from a flat sheet of paper, a developable surface with zero Gaussian curvature, and folds along a set of crease lines to form a 3D model (Callens and Zadpoor, 2017; Ma et al., 2018). This set of creases forms a crease pattern, which is a planar embedding on the flat sheet displaying all creases as line segments (Hull, 2013). The crease pattern uniquely defines the origami tessellation and resembles a planar graph. Creases are the edges, and endpoints of the creases are the vertices. The vertex's degree is the number of creases incident to it. The crease pattern also divides the sheet into planar sections called panels. Since the panels form a covering of the entire sheet without gaps or overlaps, the panels form a tessellation of the sheet. Origami tessellations commonly utilize repeated patterns in their crease patterns (Zhang and Chen, 2019; Davis et al., 2013).

Creases serve as rotational joints about which the panels are allowed to rotate. Creases are either mountains or valleys, which make the sheet appear convex or concave, respectively (Hull, 2013). Mountains and valleys, which will be displayed hereafter as solid and dashed lines, respectively, are the two possible parities of a crease. Figure 2.1(a) and (b) are examples of mountain and valley folds, respectively. In Figure 2.1(c), the flapping bird's crease pattern assigns each crease as mountain or valley and divides the square sheet into panels (Chen et al., 2015a). The boundary edges of the sheet are

labeled mountains or valleys, which is useful when the crease pattern follows an ongoing pattern. This concept of expanding the crease pattern by continuing the pattern is pertinent to origami tessellations with a periodic pattern.

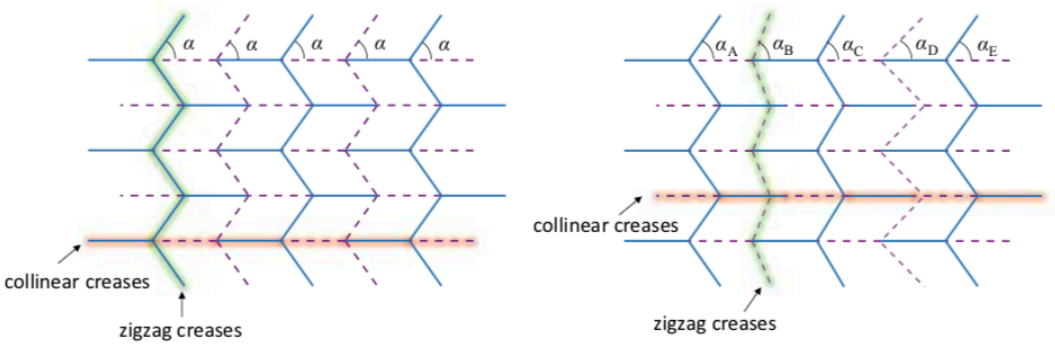


(a) (b) (c)

Figure 2.1: Crease pattern examples:

(a) mountain, (b) valley, and (c) paper crane (Hull, 2013)

One of the most well-known origami tessellations is the Miura-ori pattern. The Miura-ori crease pattern forms a tessellation of parallelograms on the sheet (Miura, 1985). Its crease pattern consists of parallel longitudinal lines of collinear creases along one direction and transverse lines of zigzag creases along the perpendicular direction, as shown in Figure 2.2(a) (Hu et al., 2019). The Miura-ori pattern is comprised entirely of degree-4 vertices, 4Cs. Kinematically, it folds flat in a single folding motion, giving it only one DOF (Xiang et al., 2021). Most efforts to research new origami tessellations involve discovering derivatives of pre-existing ones (Yellowhorse et al., 2018; Evans et al., 2015). By altering the geometry of the Miura-ori crease pattern, its derivative patterns are discovered. Figure 2.2(b) shows one such example. The simplicity of its geometry and kinematic properties makes the Miura-ori pattern a classical origami tessellation. Therefore, the modifications made to the classical Miura-ori pattern ought to preserve its geometric and kinematic properties.



(a) (b)

Figure 2.2: Miura-ori crease patterns:

(a) classical Miura-ori and (b) generalized Miura-ori (Hu et al., 2019)

2.1.2 Origami Tessellation Properties

Two important qualities in origami tessellations are flat foldability and rigid foldability, which can be determined from the geometry of the crease pattern (Gattas et al., 2013; Tachi, 2009; Schenk and Guest, 2011). An origami tessellation is flat-foldable if it can be folded along its crease pattern and pressed flat without creating additional creases. The Miura-ori pattern in Figure 2.3 shows the folding process from a flat unfolded state to a flat folded one (Tachi, 2009). An origami tessellation is rigidly foldable if all panels remain rigid and deformation only occurs at the crease lines during deployment (Evans et al., 2015; Lang, 2018). The Miura-ori pattern in Figure 2.3 demonstrates rigid foldability as well. Deployable structures inspired by rigidly foldable origami tessellations can be constructed from stiff sheet-like materials. These structures can be folded into a smaller compact shape to save space (Gattas et al., 2013; Schenk and Guest, 2013a). Examples of such structures include space solar arrays, accordion shelters, and surgical equipment (Hu et al., 2019; Liu et al., 2016; Xiang et al., 2021).

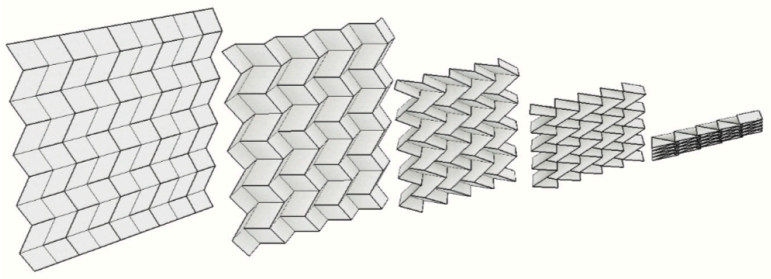


Figure 2.3: Flat foldability and rigid foldability of Miura-ori (Tachi, 2009)

A flat-foldable crease pattern must satisfy Maekawa's theorem and Kawasaki's theorem (Hull, 2013; 2015). Maekawa's theorem states that for any vertex on the crease pattern, the absolute difference between the number of mountain creases, M, and valley creases, V, incident to it is 2, so $|M - V| = 2$ (Hull, 2013; 2015). Therefore, the degree of any vertex in a flat-foldable crease pattern is even and greater than or equal to 4. Kawasaki's theorem states that for any vertex on the crease pattern, the sum of the even angles equals the sum of the odd angles, which equals π. Suppose $\alpha_{12}, \alpha_{23}, \ldots, \alpha_{n1}$ are the sector angles of a degree-n vertex in clockwise order, so $\alpha_{12} + \alpha_{34} + \ldots + \alpha_{(n-1)n} = \pi$, and $\alpha_{23} + \alpha_{45} + \ldots + \alpha_{n1} = \pi$ (Hull, 2013; 2015). Maekawa's theorem and Kawasaki's theorem are necessary conditions to satisfy local flat foldability, but they do not account for cases in which the model experiences self-collision while folding. Consequently, the criteria for global flat foldability are not fully understood as determining global flat foldability is an NP-complete problem (Akitaya et al., 2017). Origami researchers often turn to physical models to determine flat foldability. Flat-foldable origami structures have a large deployment ratio, which is advantageous for deployable structures that need to be transported in a smaller compact state (Hu et al., 2019).

Rigidly foldable origami tessellations can be folded without stretching or bending

its panels (Chen et al., 2015a; Tachi, 2011; Liu et al., 2016). Therefore, the partially folded state of a rigidly foldable origami tessellation depends on the extent to which each crease is folded. The dihedral angle of a crease is the angle between the crease's two incident panels. Each dihedral angle is between 0 and π, inclusive, and measures how closely the two adjacent panels are folded together (Evans and Lang, 2015; Hull and Tachi, 2018). Hence, the list of dihedral angles describing all creases in an origami tessellation defines its partially folded state. While deciding whether a general origami crease pattern is rigidly foldable is an NP-hard problem, origami tessellations with repetitive geometry simplify this problem (Akitaya et al., 2018). For any flat-foldable and rigidly foldable origami tessellation, all creases' dihedral angles range from 0 to π as the model deploys from its flat folded state to its flat unfolded state.

One method to determine whether a crease pattern is rigidly foldable is to derive the set of mathematical relations describing the creases' dihedral angles. These relations are a system of equations in which the sector angles of each vertex and parities of each crease are the input parameters and the dihedral angles are the variables (Evans and Lang, 2015; Hull and Tachi, 2018; Beggs, 1966). An origami tessellation is rigidly foldable if there is a system of equations with at least one DOF that describes the relations among all creases' dihedral angles. Here, the DOF of a system of equations is the number of dihedral angles that are necessary to uniquely determine the remaining ones. The matrix method with DH notation, introduced by Denavit and Hartenberg to standardize frames of reference for mechanical linkages, is used to derive this system of equations (Chen and You, 2015b). For origami tessellations, a finite set of single-vertex models is repeated over the entire sheet, simplifying the matrix method.

The DOF of the system of equations describing the dihedral angles also translates to the number of independent rigid folding modes in the origami tessellation. An origami tessellation with a small number of DOFs has more restricted movement (Tachi and Hull, 2017; Fang et al., 2016). Controlling this origami tessellation's folded configuration becomes rather simple. In general, the DOF of a single-vertex origami model equals the vertex's degree minus 3 (Chen et al., 2015a). For instance, a 4C has one DOF while a 6C has three DOFs. Origami tessellations comprised entirely of 4Cs have one DOF, but origami tessellation with both 4Cs and 6Cs may possess multiple DOFs (Chen et al., 2015a; 2019). Figure 2.4 illustrates an origami tessellation comprised entirely of 4Cs with only one DOF (Gattas et al. 2013).

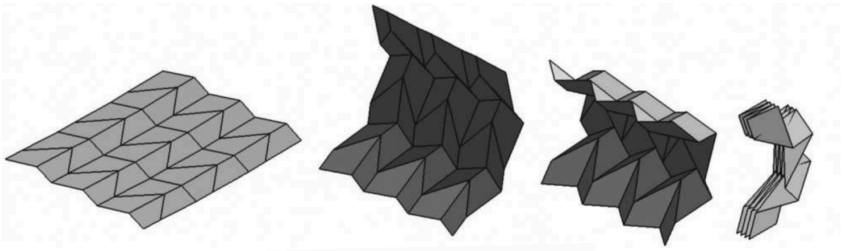


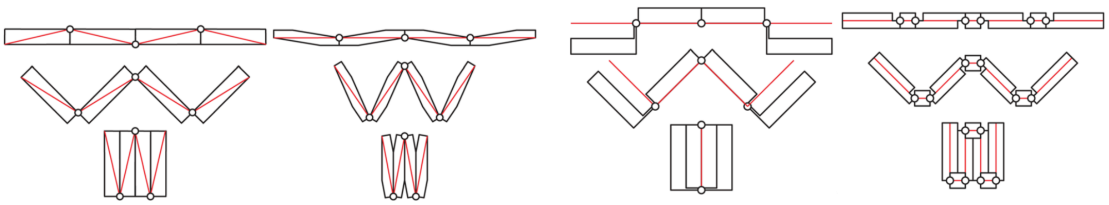
Figure 2.4: Flat-foldable and rigidly foldable Miura-ori derivative with one DOF (Gattas et al. 2013)

2.1.3 Thick-Panel Origami

Most research into origami tessellations assumes the sheet has zero-thickness, which is adequate for some applications, such as thin-walled energy absorption structures (Ma et al., 2018). However, for other applications, the thickness of the sheet must be considered (Chen et al., 2015a; Yellowhorse et al., 2018). These applications include kinetic architecture, deployable solar arrays, and robotics (Yellowhorse et al., 2018; Ku and Demaine, 2016). Thick-panel versions of rigidly foldable origami models replace the

zero-thickness sheet with material of nonzero thickness and replace creases in the sheet with revolute hinges (Chen et al., 2015a). Four methods to accommodate thickness are hinge shift, volume trimming, offset panel, and offset crease (Ku and Demaine, 2016). Each method modifies an origami crease pattern whose panels lie on a folding plane.

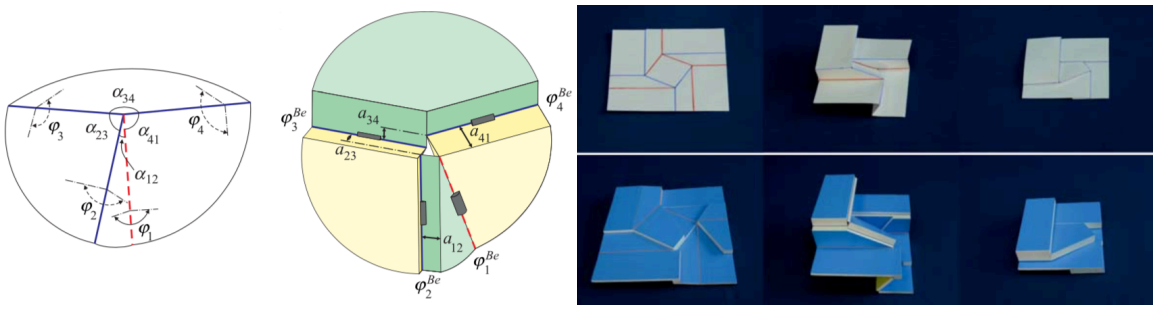
The hinge shift method in Figure 2.5(a) shifts the hinges out of the folding plane. While useful for origami models that fold along one dimension, this method does not translate well to crease patterns that have bi-directional folding (Ku and Demaine, 2016). Rigidly foldable origami tessellations may experience deformation in their panels when this method is used. The volume trimming method in Figure 2.5(b) keeps the hinges in place and tapers the panels near the hinges. This method preserves the kinematics of the origami model but limits its range of motion (Ku and Demaine, 2016). The offset panel method in Figure 2.5(c) also keeps the hinges in place but shifts the panels out of the folding plane. This method preserves the kinematics of the origami model and its full range of motion, but the structure is difficult to fabricate (Ku and Demaine, 2016). The offset crease method in Figure 2.5(d) replaces each crease with two hinges, each having half the range of motion of the crease. The crease pattern is modified, but the structure is easier to fabricate (Ku and Demaine, 2016).



(a) (b) (c) (d)

Figure 2.5: Methods to accommodate thickness: (a) hinge shift, (b) volume trimming, (c) offset panel, and (d) offset crease (Ku and Demaine, 2016)

Chen et al. proposed a method using spatial mechanisms as templates to construct thick-panel versions of origami models. This method preserves the kinematics and full range of motion of the origami model by shifting the hinges out of the folding plane and adjusting the thickness of the panels (Chen et al., 2015a; 2015b). Figure 2.6(a) illustrates the thick-panel analog of a flat-foldable 4C using this method. Figure 2.6(b) illustrates the thick-panel analog of a square twist comprised entirely of 4Cs (Chen et al., 2015a). These thick-panel structures preserve the kinematic motion of their origami counterparts. When applied to origami tessellations, this method converts them into their thick-panel counterparts.



(a) (b)

Figure 2.6: Origami of thick panels:

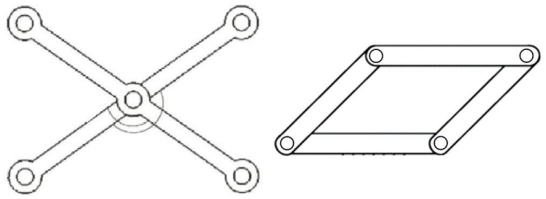
(a) flat-foldable 4C and (b) square twist (Chen et al., 2015a)

2.2 Origami Tessellations as Mechanical Linkages

2.2.1 Mechanical Linkages

Mechanical linkages are assemblies of rigid bodies connected by joints (Barreto et al., 2020). The mechanical linkages of interest here are those with revolute joints, or hinges. When all axes of rotation are normal to a common plane, the mechanical linkage is planar. Examples include the scissor mechanism in Figure 2.7(a) and the parallelogram

linkage in Figure 2.7(b). Both mechanisms have one DOF of mobility. A scissor mechanism consists of one or multiple pairs of rigid bodies each linked by a revolute joint (Li et al., 2017; Vlachaki and Liapi, 2021). A parallelogram linkage is a closed loop linkage in which opposite pairs of links are of identical lengths (Liu and Wang, 2003). There are two bifurcation states in which all four links are collinear, giving the parallelogram linkage two DOFs of mobility in these states. Outside of these states, the parallelogram linkage has only one DOF of mobility (Yu et al., 2009).

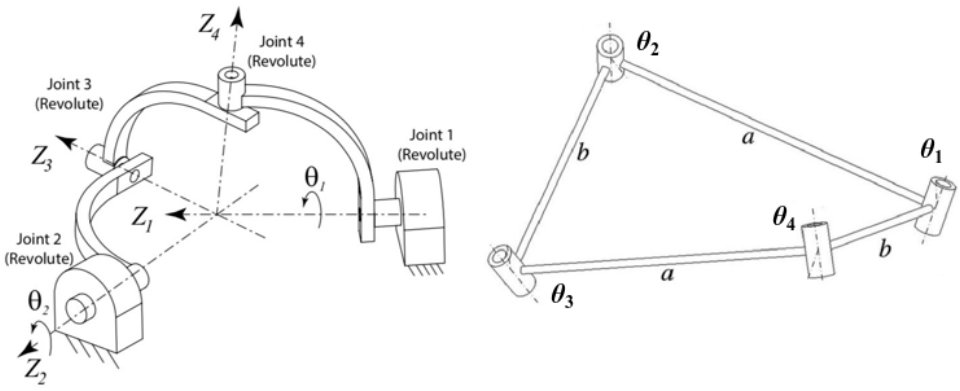


(a) (b)

Figure 2.7: Planar linkages:

(a) scissor mechanism (Li et al., 2017) and (b) parallelogram linkage (Yu et al., 2009)

Mechanical linkages in which the rigid bodies experience movement in three dimensions are spatial linkages. Examples include the spherical linkage in Figure 2.8(a) and the Bennett linkage in Figure 2.8(b). A spherical linkage consists of rigid links connected by revolute joints whose axes intersect a common point (Pennestri et al., 2016). The simplest closed loop spherical linkage is the spherical 4-bar linkage, which has one DOF of mobility (Barreto et al., 2021; Zhuang et al., 2015). A Bennett linkage is a 4-bar spatial linkage in which not all the revolute joints' axes intersect at one point (Zhang and Chen, 2018). When certain symmetry conditions are met, the Bennett linkage has one DOF of mobility (Beggs, 1966).



(a) (b)

Figure 2.8: Spatial 4-bar linkages: (a) spherical 4-bar linkage (Pennestri et al., 2016) and (b) Bennett linkage (Lu et al., 2017)

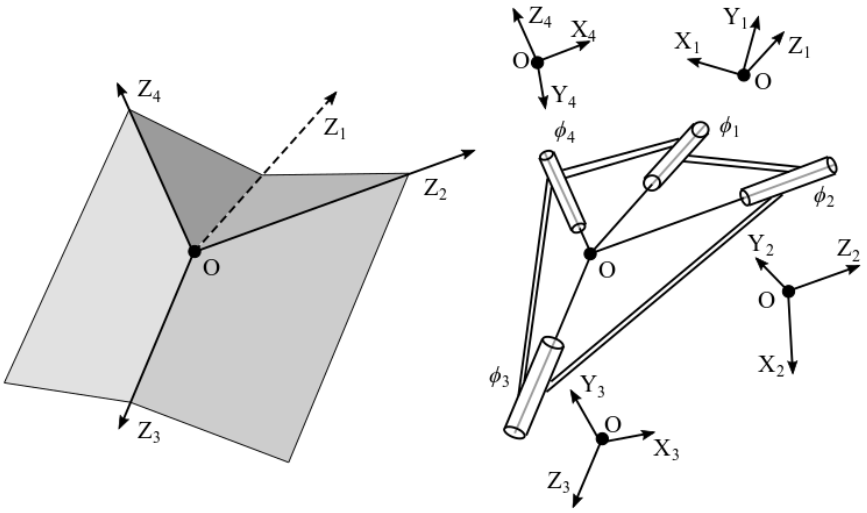
The Bennett linkage is an example of an overconstrained mechanism, which is a mechanism that has more DOFs than determined by the mobility formula (Beggs, 1966). This formula counts the number of parameters that define a mechanism's configuration. For origami tessellations, this calculated number of DOFs depends on the number of panels and creases, which impose constraints on the mechanism (Beggs, 1966). For an origami model, the rigid bodies and joints are the panels and creases, respectively. In general, overconstrained mechanisms have a positive number of DOFs because some of the constraints in the mechanism are redundant. For instance, while the degree-4 vertex is rigidly foldable, the Miura-ori tessellation quickly becomes overconstrained as the pattern grows. The Miura-ori pattern has one DOF because symmetries in the crease pattern make some of the constraints redundant (Tachi, 2009). The Kokotsaki quadrilateral mesh is a generalized overconstrained origami tessellation (Tachi, 2010a). Conversely, the square twist fold, in which all creases in the square have the same parity,

is not rigidly foldable (Evans and Lang, 2015). In fact, rigid foldability is uncommon among origami tessellations because special conditions need to be met to offset mechanical constraints. Flat-foldablity is a property that imposes symmetries in the crease pattern, so focusing on flat-foldable origami tessellations simplifies the search for rigidly foldable ones (Tachi, 2009).

Rigid origami patterns are designed for zero-thickness sheets, but these patterns cannot be directly applied to tangible sheet-like materials, which have nonzero thickness (Chen et al., 2015a). While perfectly rigidly foldable origami models are theoretical, it is still valuable to study them to design physical models that are close approximations. These physical origami models are folded from sheets with negligible thickness, and they serve as approximations of rigid origami patterns (Chen et al., 2015a). The panels of physical models will experience a negligible amount of deformation. Origami models constructed from thicker material will experience more noticeable deformation in the panels. Sheets with an appropriate amount of thickness will be used to construct rigidly foldable origami models. Therefore, rigidly foldable origami tessellations will refer to the zero-thickness design that is approximated with origami models folded from sheets of negligible thickness.

Every rigidly foldable origami model is a mechanical linkage in which the panels are rigid bodies and the creases between panels are revolute joints. As the origami model rigidly folds, it deploys according to its corresponding mechanical linkage (Barreto et al., 2020). For instance, a single-vertex origami model corresponds to a closed loop spherical linkage (Barreto et al., 2020; Peng et al., 2018). Figure 2.9 shows a flat-foldable 4C and its equivalent spherical 4-bar linkage (Barreto et al., 2020). The panels and creases in the

flat-foldable 4C are used to define transforming coordinate systems, which are later used for the matrix method. This method derives a system of equations for the vertex's dihedral angles. Origami tessellations are assemblies of vertices, and adjacent vertices have a common crease defined by a dihedral angle. Combining the dihedral angle equations for each vertex results in a system of equations describing all dihedral angles in the origami tessellation. To show the origami tessellation is rigidly foldable, this system of equations must have fewer independent constraints than it has dihedral angles.



(a) (b)

Figure 2.9: A flat-foldable 4C:

(a) origami model and (b) its equivalent spherical 4-bar linkage (Barreto et al., 2020)

Thick-panel origami models consist of panels with nonzero thickness. These thick-panel models are modeled as spatial linkages in which creases are replaced by hinges placed either at the top or bottom of the panels. Origami researchers have proposed methods to construct thick-panel versions of classical origami tessellations that have analogous kinematics (Yellowhorse and Howell, 2019). Zhang and Chen designed a

thick-panel version of the Miura-ori pattern based on mobile assemblies of Bennett linkages (Zhang and Chen, 2018). Kinematic analysis on spatial linkages is used to determine the kinematics of thick-panel versions of origami tessellations.

2.2.2 Matrix Method for Origami Tessellations

The kinematic analysis of origami tessellations and their equivalent mechanical linkages uses the matrix method with the Denavit-Hartenberg (DH) notation (Beggs, 1966; Saito et al., 2015). Every origami tessellation is composed of single-vertex origami models, each of which is a closed loop spherical linkage because all creases meet at a common vertex (Yu et al., 2009; Chen and You, 2005). The matrix method solves for the kinematics of any closed loop spherical n-bar linkage for any integer n greater than or equal to 4 (Chen et al., 2015b; Beggs, 1966). A rigidly foldable degree-n single-vertex origami model consists of n panels, each adjacent to two creases and a common vertex, connected in a loop. As the single-vertex model rigidly folds, these panels rotate in space with respect to the axes of their respective adjacent creases. The panel's sector angle is the angle between its two adjacent creases, and the crease's dihedral angle is the angle between its two adjacent panels.

The derivation of the matrix method with DH notation originates from the geometry of the n-crease single-vertex origami model in an arbitrary partially folded state (Chen et al., 2019). The n creases are numbered from 1 to n, and the panel adjacent to creases i and $(i + 1)$ is panel $i(i + 1)$. Every instance of $(n + 1)$ is replaced with 1. In any partially folded state, each sector angle $\alpha_{i(i+1)}$ is constant while each dihedral angle ϕ_i is a value between 0 and π. The sector angles describe the shape of the panels while the

dihedral angles describe the extent to which the creases are folded. Figure 2.10 illustrates an example of a spherical 4-bar linkage, which models a 4C (Chen et al., 2017).

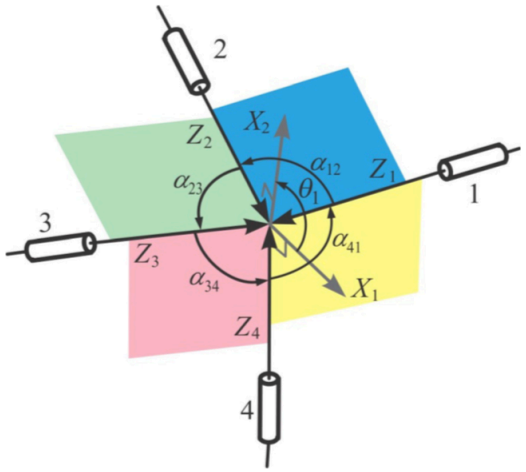


Figure 2.10: Spherical 4-bar linkage used to model a 4C (Chen et al., 2017)

Each crease in a single-vertex origami model defines a 3D coordinate system. In this coordinate system, the vertex is the origin, the *z*-axis is along the crease, the *x*-axis is normal to the adjacent panel in the clockwise direction, and the *y*-axis is the axis determined using the right-hand rule. A transformation matrix represents a conversion from one crease's coordinate system to that of a neighboring crease. Starting from one crease's coordinate system, applying these transformations from one crease to another around the vertex in a loop returns to the starting crease. Therefore, the product of these transformation matrices equals the identity matrix. Each vertex in the origami model imposes a system of equations describing the relations of the creases' dihedral angles. The system of equations obtained from all vertices strictly inside the crease pattern determines the origami model's rigid foldability (Peng et al., 2018).

The transformation matrix from the coordinate system on crease i to that on crease $(i + 1)$ is a product of a rotation matrix about crease i and a rotation matrix about

the normal to panel $i(i + 1)$. The fold angle, θ_i, is the supplement of the dihedral angle, ϕ_i, and the rotation angle about crease i is the fold angle, whose sign depends on its parity (Lang, 2018). If the crease is a mountain, then let $\theta_i = \phi_i - \pi$, and if the crease is a valley, then let $\theta_i = \pi - \phi_i$. Figure 2.10 shows a rotation of θ_1 about crease Z_1. The rotation angle about the normal to panel $i(i + 1)$ is the sector angle, $\alpha_{i(i+1)}$. The following is the transformation matrix,

$$Q\left(\alpha_{i(i+1)},\theta_i\right) = R_z\left(\theta_i\right) R_x\left(\alpha_{i(i+1)}\right), \tag{2.1}$$

in which the rotation matrix about the z-axis is

$$R_z\left(\theta_i\right) = \begin{pmatrix} \cos\theta_i & \sin\theta_i & 0 \\ -\sin\theta_i & \cos\theta_i & 0 \\ 0 & 0 & 1 \end{pmatrix}, \tag{2.2}$$

and the rotation matrix about the x-axis is

$$R_x\left(\alpha_{i(i+1)}\right) = \begin{pmatrix} 1 & 0 & 0 \\ 0 & \cos\alpha_{i(i+1)} & \sin\alpha_{i(i+1)} \\ 0 & -\sin\alpha_{i(i+1)} & \cos\alpha_{i(i+1)} \end{pmatrix}. \tag{2.3}$$

Equation (2.1) can be expressed as (2.4), which is the transformation matrix from the coordinate system on crease i to the coordinate system on crease $(i + 1)$ (Chen et al., 2015b),

$$Q\left(\alpha_{i(i+1)},\theta_i\right) = \begin{pmatrix} \cos\theta_i & \cos\alpha_{i(i+1)}\sin\theta_i & \sin\alpha_{i(i+1)}\sin\theta_i \\ -\sin\theta_i & \cos\alpha_{i(i+1)}\cos\theta_i & \sin\alpha_{i(i+1)}\cos\theta_i \\ 0 & -\sin\alpha_{i(i+1)} & \cos\alpha_{i(i+1)} \end{pmatrix}. \tag{2.4}$$

Taking the inverse of (2.4) gives (2.5), which is the transformation matrix from the coordinate system on crease (i + 1) to the coordinate system on crease i (Chen et al., 2015b),

$$Q\left(\alpha_{i(i+1)},\theta_i\right)^{-1}=\begin{pmatrix}\cos\theta_i & -\sin\theta_i & 0\\ \cos\alpha_{i(i+1)}\sin\theta_i & \cos\alpha_{i(i+1)}\cos\theta_i & -\sin\alpha_{i(i+1)}\\ \sin\alpha_{i(i+1)}\sin\theta_i & \sin\alpha_{i(i+1)}\cos\theta_i & \cos\alpha_{i(i+1)}\end{pmatrix}. \tag{2.5}$$

Looping around the single-vertex model returns to the starting coordinate system, so the following closure equation holds (Chen et al., 2015b),

$$\prod_{i=1}^{n} Q\left(\alpha_{i(i+1)},\theta_i\right)=I_{3\times3}. \tag{2.6}$$

Equation (2.6) states that the product of transformation matrices looping around the single-vertex model once is equal to the identity transformation. Here, $I_{3\times3}$ is a 3 × 3 identity matrix. Since n is even for a flat-foldable single-vertex model, equation (2.6) can be rearranged to form the following closure equation (Chen et al., 2015b)

$$\prod_{i=1}^{n/2} Q\left(\alpha_{i(i+1)},\theta_i\right)=\prod_{i=1}^{n/2} Q\left(\alpha_{(n-i+1)(n-i+2)},\theta_{(n-i+1)}\right)^{-1}. \tag{2.7}$$

Appendices A and C show the computed values of the left-hand side, LHS, and right-hand side, RHS, of (2.7) when n = 4 and n = 6, respectively. The DOF of this system of equations equals the DOF of the mechanical linkage, which also equals the DOF of the origami model (Chen et al., 2015a). Each vertex in a rigidly foldable origami tessellation yields a closure equation in the form of (2.7), which helps determine the kinematics of the entire model. Figure 2.11 illustrates a four-vertex crease pattern whose 4Cs are each modeled by spherical 4-bar linkages. The closure equations for these four 4Cs form a system of equations determining the DOFs of this origami model. Other

origami tessellations can be decomposed into 4Cs and 6Cs, and the DOFs of these origami tessellations are computed in a similar manner.

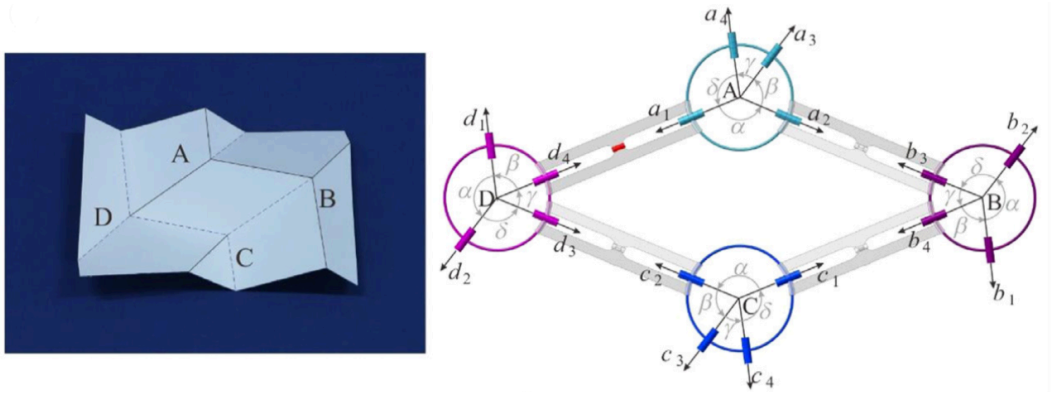


Figure 2.11: Origami model composed of 4Cs: (a) crease pattern and (b) each of the four vertices as spherical 4-bar linkages (Peng et al., 2018)

2.2.3 Matrix Method for Thick-Panel Origami

Chen et al. presented a method to construct thick-panel analogs of rigidly foldable origami models (Chen et al., 2015). This method adds thickness to the panels in the origami crease pattern and replaces creases with hinges either on the top or bottom surface of panels (Chen et al., 2015). These hinges behave like creases because they are rotational joints. Unlike the creases in zero-thickness origami, the hinges' axes in the thick-panel version of a single-vertex origami model no longer intersect at a common point. The distance between the axes of adjacent hinges is the thickness of the panel. Therefore, the thicknesses of the panels are additional parameters for the matrix method.

The matrix method for thick-panel models uses transformation matrices to represent shifting 3D coordinate systems (Chen et al., 2015a). In the thick-panel version of an degree-n single-vertex origami model, the n hinges are numbered from 1 to n, and the panel adjacent to hinges i and $(i + 1)$ is panel $i(i + 1)$. Again, every instance of $(n + 1)$

is replaced with 1. In any partially folded state, each sector angle, $\alpha_{i(i+1)}$, is constant while each dihedral angle, ϕ_i, is a value between 0 and π. The panel's sector angle is the angle between its two adjacent hinges, and the hinge's dihedral angle is the angle between its two adjacent panels. Figure 2.12 illustrates an example of a spatial linkage when $n = 4$, which models a thick-panel version of a flat-foldable 4C. To be mobile, this mechanical linkage needs to satisfy symmetry conditions corresponding to a Bennett linkage (Beggs, 1966; Chen et al., 2015a).

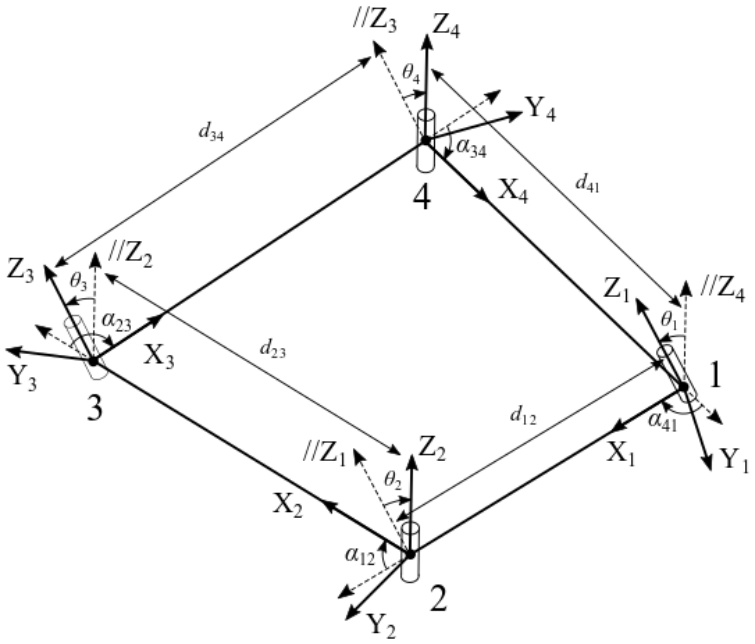


Figure 2.12: A schematic diagram of a spatial 4-bar linkage

The transformation matrix from the coordinate system on hinge i to the coordinate system on hinge $(i + 1)$, is a product of a rotation matrix about hinge i, a translation matrix along the x-axis, and a rotation matrix about the normal to panel $i(i + 1)$. The rotation angle about hinge i is the fold angle, θ_i, which depends on the parity of the corresponding crease in the origami crease pattern (Lang, 2018). If the crease is a

mountain, then let $\theta_i = \phi_i - \pi$, and if the crease is a valley, then let $\theta_i = \pi - \phi_i$. The distance between the axis of hinge i and the axis of hinge $(i + 1)$ is the translation distance, $d_{i(i+1)}$. The rotation angle about the normal to panel $i(i + 1)$ is the sector angle, $\alpha_{i(i+1)}$. For thick-panel origami, the matrix method uses 4 × 4 matrices (Beggs, 1966). These matrices are structured such that the upper-left 3 × 3 square matrix represents a rotational matrix while the 3 × 1 column vector in the upper-right represents a translational vector. The following is the transformation matrix,

$$Q\left(\alpha_{i(i+1)},\theta_i,d_{i(i+1)}\right)=R_z\left(\theta_i\right)T_x\left(d_{i(i+1)}\right)R_x\left(\alpha_{i(i+1)}\right), \tag{2.8}$$

in which the rotation matrix about the z-axis is

$$R_z\left(\theta_i\right)=\begin{pmatrix}\cos\theta_i & \sin\theta_i & 0 & 0\\ -\sin\theta_i & \cos\theta_i & 0 & 0\\ 0 & 0 & 1 & 0\\ 0 & 0 & 0 & 1\end{pmatrix}, \tag{2.9}$$

the translation matrix along the x-axis is

$$T_x\left(d_{i(i+1)}\right)=\begin{pmatrix}1 & 0 & 0 & d_{i(i+1)}\\ 0 & 1 & 0 & 0\\ 0 & 0 & 1 & 0\\ 0 & 0 & 0 & 1\end{pmatrix}, \tag{2.10}$$

and the rotation matrix about the x-axis is

$$R_x\left(\alpha_{i(i+1)}\right)=\begin{pmatrix}1 & 0 & 0 & 0\\ 0 & \cos\alpha_{i(i+1)} & \sin\alpha_{i(i+1)} & 0\\ 0 & -\sin\alpha_{i(i+1)} & \cos\alpha_{i(i+1)} & 0\\ 0 & 0 & 0 & 1\end{pmatrix}. \tag{2.11}$$

Equation (2.8) can be expressed as (2.12), which is the transformation matrix from the coordinate system on hinge i to the coordinate system on hinge $(i + 1)$ (Chen et al.,

2015b),

$$Q\left(\alpha_{i(i+1)},\theta_i,d_{i(i+1)}\right)=\begin{pmatrix}\cos\theta_i & \cos\alpha_{i(i+1)}\sin\theta_i & \sin\alpha_{i(i+1)}\sin\theta_i & d_{i(i+1)}\cos\theta_i\\ -\sin\theta_i & \cos\alpha_{i(i+1)}\cos\theta_i & \sin\alpha_{i(i+1)}\cos\theta_i & -d_{i(i+1)}\sin\theta_i\\ 0 & -\sin\alpha_{i(i+1)} & \cos\alpha_{i(i+1)} & 0\\ 0 & 0 & 0 & 1\end{pmatrix}. \quad (2.12)$$

Taking the inverse of (2.12) gives (2.13), which is the transformation matrix from the coordinate system on hinge (i + 1) to the coordinate system on hinge i (Chen et al., 2015b),

$$Q\left(\alpha_{i(i+1)},\theta_i,d_{i(i+1)}\right)^{-1}=\begin{pmatrix}\cos\theta_i & -\sin\theta_i & 0 & -d_{i(i+1)}\\ \cos\alpha_{i(i+1)}\sin\theta_i & \cos\alpha_{i(i+1)}\cos\theta_i & -\sin\alpha_{i(i+1)} & 0\\ \sin\alpha_{i(i+1)}\sin\theta_i & \sin\alpha_{i(i+1)}\cos\theta_i & \cos\alpha_{i(i+1)} & 0\\ 0 & 0 & 0 & 1\end{pmatrix}. \quad (2.13)$$

Looping around the thick-panel version of the single-vertex model returns to the starting coordinate system, so the following closure equation holds (Chen et al., 2015b),

$$\prod_{i=1}^{n} Q\left(\alpha_{i(i+1)},\theta_i,d_{i(i+1)}\right)=I_{4\times4}. \quad (2.14)$$

Equation (2.14) states that the product of transformation matrices looping around the thick-panel version of the single-vertex model once is equal to the identity transformation. Here, $I_{4\times4}$ is the 4 × 4 identity matrix. When n is even, equation (2.14) can be rearranged to form the following closure equation (Chen et al., 2015b),

$$\prod_{i=1}^{n/2} Q\left(\alpha_{i(i+1)},\theta_i,d_{i(i+1)}\right)=\prod_{i=1}^{n/2} Q\left(\alpha_{(n-i+1)(n-i+2)},\theta_{(n-i+1)},d_{(n-i+1)(n-i+2)}\right)^{-1}. \quad (2.15)$$

Appendix B shows the computed values of the LHS and RHS of (2.15) when n = 4.

2.2.4 Numerical Method for Calculating DOFs

While the matrix method calculates the exact relations among the dihedral angles in a rigidly foldable origami tessellation, there is a numerical method to model its motion (Gan and Pellegrino, 2006; Tachi, 2010a). This method is based on the analytical expressions for the relations of the fold angles derived from the matrix method. Given an initial configuration, the numerical method simulates the motion of the origami tessellation by carrying out an incremental solution to the loop closure equations (Gan and Pellegrino, 2006; Tachi, 2009). The numerical method also computes the DOFs of the origami tessellation (Gan and Pellegrino, 2006). Tomohiro Tachi implemented these methods in his rigid origami model simulator, which allows the user to understand how rigid origami models fold from their crease patterns (Tachi, 2009).

Consider a degree-n single-vertex origami model, whose creases are numbered from 1 to n, in a partially folded state. The initial partially folded state is denoted by $n \times 1$ vector, $\theta = (\theta_1, \theta_2, \ldots, \theta_n)^{\mathrm{T}}$. Given the sector angles, $\alpha_{12}, \alpha_{23}, \ldots, \alpha_{n1}$, in the vertex, the closure equation in (2.6) holds. Starting from the initial configuration, an incremental change in the fold angles, denoted by $n \times 1$ vector, $\Delta\theta = (\Delta\theta_1, \Delta\theta_2, \ldots, \Delta\theta_n)^{\mathrm{T}}$, is imposed. Once the incremental change is applied, the same loop closure equation, in which the transformation matrices in (2.4) are used, must be satisfied,

$$\prod_{i=1}^{n} Q\left(\alpha_{i(i+1)}, \theta_i + \Delta\theta_i\right) = I_{3\times 3}. \tag{2.16}$$

The LHS of (2.16) is a product of 3×3 matrices, and each of them can be simplified with first order approximations of trigonometric functions. Using the derivatives of each transformation matrix with respect to θ_i,

$$Q'\left(\alpha_{i(i+1)},\theta_i\right)=\begin{pmatrix} -\sin\theta_i & \cos\alpha_{i(i+1)}\cos\theta_i & \sin\alpha_{i(i+1)}\cos\theta_i \\ -\cos\theta_i & -\cos\alpha_{i(i+1)}\sin\theta_i & -\sin\alpha_{i(i+1)}\sin\theta_i \\ 0 & 0 & 0 \end{pmatrix}, \tag{2.17}$$

equation (2.16) can be simplified to

$$\prod_{i=1}^{n}\left(Q\left(\alpha_{i(i+1)},\theta_i\right)+Q'\left(\alpha_{i(i+1)},\theta_i\right)\Delta\theta_i\right)=I_{3\times3}. \tag{2.18}$$

Taking the first-order terms in (2.18) gives

$$\sum_{i=1}^{n}M_i\Delta\theta_i=0_{3\times3}, \tag{2.19}$$

in which $0_{3\times3}$ is the 3 × 3 zero matrix, and for $1\le i\le n$, matrix M_i can be expressed as

$$M_i=Q\left(\alpha_{12},\theta_1\right)...Q'\left(\alpha_{i(i+1)},\theta_i\right)...Q\left(\alpha_{n1},\theta_n\right). \tag{2.20}$$

Matrix M_i is the product of n transformation matrices in which the i^{th} matrix is replaced by its derivative with respect to θ_i. The entries in M_1, M_2, …, M_n can be rearranged to form matrix J, called the Jacobian matrix, which satisfies

$$J\Delta\theta=0_{9\times1}. \tag{2.21}$$

In equation (2.21), J is a 9 × n matrix, $\Delta\theta$ is an n × 1 vector, and $0_{9\times1}$ is the 9 × 1 zero vector. The nine entries in M_i are in the i^{th} column of J because it corresponds to the i^{th} crease angle. Since each rotation matrix is skew-symmetric, the Jacobian matrix has redudant constraints, which won't affect the analysis of DOFs (Tachi, 2009). Equation (2.21) is a homogeneous system of linear equations, and the number of linearly independent solutions to (2.21) equals the number of DOFs in the single-vertex origami model. In other words, the dimension of the null space of J equals the number of DOFs in the single-vertex origami model. The singular value decomposition, SVD, of J yields a

set of linearly independent vectors that span the null space of J. The number of independent vectors in the null space equals the number of singular values equal to zero. A potential source of error is that programs that perform SVD on a matrix consider nonzero singular values zero if they are smaller than a small positive threshold. The dimension of the null space depends on the reported number of singular values equal to zero, which may be subject to rounding errors. This source of error can be mitigated by scaling the matrix up by a constant or decreasing the threshold for values considered equal to zero.

The numerical method can be applied to multi-vertex origami tessellations. Suppose the origami tessellation consists of v vertices numbered from 1 to v and c creases numbered from 1 to c. An initial partially folded configuration of the origami tessellation is denoted by a $c \times 1$ vector of fold angles, $\theta = (\theta_1, \theta_2, \ldots, \theta_c)^T$. The numerical method computes the possible incremental changes in the fold angles, which is denoted by $c \times 1$ vector, $\Delta\theta = (\Delta\theta_1, \Delta\theta_2, \ldots, \Delta\theta_c)^T$. Each vertex has a corresponding Jacobian matrix computed with its sector angles and incident creases' fold angles as inputs. The entries in these Jacobian matrices $J_1, J_2, \ldots, J_v$ can be rearranged to form a combined Jacobian matrix, J_{comb}, which satisfies

$$J_{comb}\Delta\theta = 0_{9v\times 1}. \tag{2.22}$$

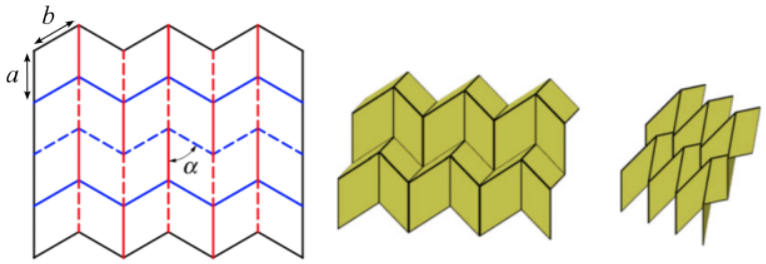
In equation (2.22), J_{comb} is a $(9v) \times c$ matrix, $\Delta\theta$ is a $c \times 1$ vector, and $0_{9v\times 1}$ is the $(9v) \times 1$ zero vector. Each 9×1 column in Jacobian matrix J_i for $1 \le i \le v$ corresponds to one of the c creases. Suppose the j^{th} column in J_i corresponds to crease k, for $1 \le k \le c$. The 9×1 j^{th} column in J_i is the 9×1 column vector in J_{comb} in rows $(9i - 8)$ through $(9i)$, inclusive, and column k. All remaining entries in J_{comb} not occupied by a column in one of the

vertices' Jacobian matrices are zeroes. Equation (2.22) is another homogeneous system of linear equations. Similar to the single-vertex case, the dimension of the null space of J_{comb} equals the DOF of the entire origami tessellation. To determine the DOF of an origami tessellation with increasing complexity, the numerical method simplifies the computation.

2.3 Classical Origami Tessellations

2.3.1 Classical Miura-ori pattern

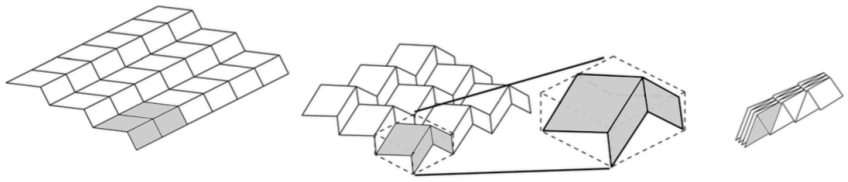
The classical Miura-ori pattern is a flat-foldable and rigidly foldable origami tessellation based on a simple fold geometry (Schenk and Guest 2013a). In 1972, astrophysicist Koryo Miura coined the term Miura-ori to describe the crease pattern that would become one of the most recognizable patterns in origami (Miura, 1985; Xiang et al., 2021). The classical Miura-ori crease pattern consists of identical symmetric 4Cs and subdivides the sheet into congruent parallelogram-shaped panels (Gattas et al., 2013). In the longitudinal direction, the creases lie on evenly spaced parallel lines, and in the transverse direction, the creases lie on evenly spaced zigzag lines. Figure 2.13 shows the classical Miura-ori crease pattern and partially folded states (Evans et al., 2015). Only two side lengths, a and b, and one angle, α, are necessary to determine the geometry of the crease pattern. The origami tessellation remains flat-foldable and rigidly foldable for any $\alpha < \pi / 2$.



(a) (b) (c)

Figure 2.13: Classical Miura-ori pattern: (a) crease pattern, (b) partially folded state, and (c) mostly folded state (Evans et al., 2015)

The simplest unit of the classical Miura-ori pattern is the four-panel unit, one of which is shaded in Figure 2.14 (Gattas et al., 2013). In any partially folded state, all units are identical, as shown in Figure 2.14(b). Given any two units in the classical Miura-ori pattern, their corresponding dihedral angles are equal. Additionally, the origami tessellation stays in a planar form, meaning the model deploys while a set of creases on each unit is restricted to a plane (Evans et al., 2015). The classical Miura-ori pattern produces a 1-DOF mechanism capable of rigidly folding from one flat unfolded state to a flat folded state (Tachi, 2010a). This classical origami tessellation enables compact packaging of the structure, and its synchronized folding motion makes the model easy to manipulate (Miura, 1985).



(a) (b) (c)

Figure 2.14: Classical Miura-ori pattern with unit shaded: (a) flat unfolded state, (b) partially folded state, and (c) flat folded state (Gattas et al., 2013)

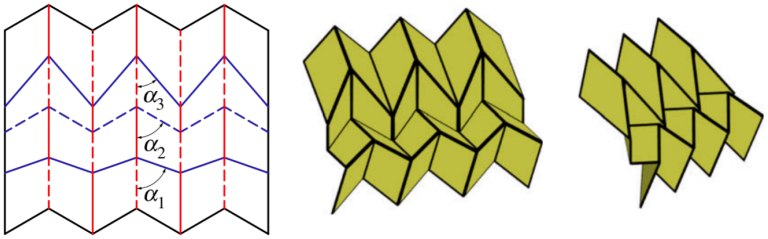
The classical Miura-ori pattern is also auxetic, meaning it has a negative Poisson's ratio (Fang et al., 2016; Schenk and Guest, 2013a). When compressed in one planar direction, the origami tessellation also shrinks in the orthogonal planar direction. By adjusting the geometry of its crease pattern, the classical Miura-ori pattern's kinematic properties, including the Poisson's ratio and deployment ratio, can be programmed (Schenk and Guest, 2013b; Fang and Xia, 2018). The classical Miura-ori pattern is found in folded cores for composite materials. The partially folded classical Miura-ori pattern produces a sandwich core, and the geometry of the crease pattern gives the material a high energy absorption capacity (Filipov et al., 2015).

2.3.2 4C Origami Tessellations

Given the versatility of the classical Miura-ori pattern, origami researchers have designed origami tessellations that are derivative of this pattern. When designing these origami tessellations, the connections between vertices are preserved (Eppstein, 2019). Starting from the classical Miura-ori crease pattern, no vertices or creases are added or removed, but the vertices and creases are shifted in the sheet. These modifications create new origami tessellations while preserving the topology of the original crease pattern. The crease patterns of the generalized symmetric Miura-ori pattern, Barreto's Mars pattern, and Huffman grid consist entirely of 4Cs and quadrilateral-shaped panels.

The generalized symmetric Miura-ori pattern is a flat-foldable and rigidly foldable origami tessellation that consists of multiple different symmetric 4Cs. Figure 2.15 shows its crease pattern and partially folded states (Evans et al., 2015). One way to construct this crease pattern is to displace the vertices and their incident creases on the classical

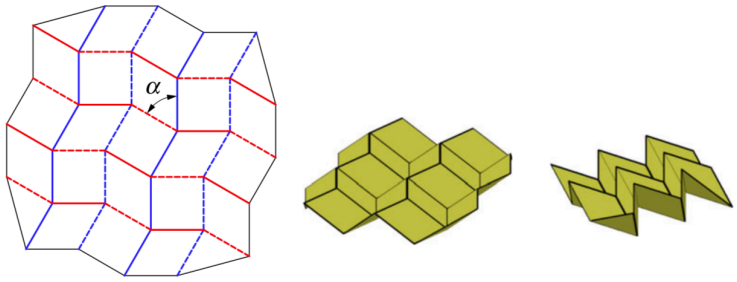
Miura-ori pattern while ensuring each 4C remains symmetric and flat-foldable (Sareh and Guest, 2015b). The longitudinal lines remain the same while the transverse zigzags are determined by acute angles, α_i (Evans et al., 2015). Unlike the classical Miura-ori pattern, the generalized symmetric Miura-ori pattern might experience self-collision as it deploys.



(a) (b) (c)

Figure 2.15: Generalized symmetric Miura-ori pattern: (a) crease pattern, (b) partially folded state, and (c) mostly folded state (Evans et al., 2015)

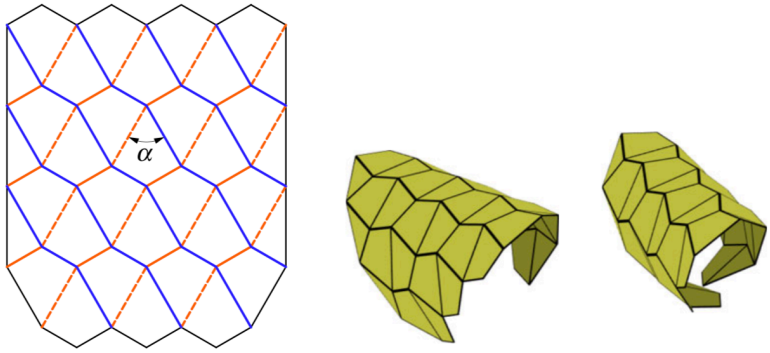
Another flat-foldable and rigidly foldable origami tessellation is the Barreto's Mars pattern (Evans et. al., 2015). Figure 2.16 shows its crease pattern and partially folded states (Evans et al., 2015). Its crease pattern consists of identical 4Cs and subdivides the sheet into congruent squares and congruent rhombi. The 4Cs are flat-foldable but not symmetric. Only one acute angle, α, is necessary to determine the geometry of the crease pattern, as shown in Figure 2.16(a) (Evans et. al., 2015). The Barreto's Mars pattern is considered a derivative of the Miura-ori pattern in which the longitudinal lines are evenly spaced zigzag lines (Evans et. al., 2015). The Barreto's Mars pattern also folds with a full range of motion and does not experience self-collision as it deploys (Paris et al., 2018).



(a) (b) (c)

Figure 2.16: Barreto's Mars pattern: (a) crease pattern, (b) partially folded state, and (c) mostly folded state (Evans et al., 2015)

The Huffman grid is another flat-foldable and rigidly foldable origami tessellation. Figure 2.17 shows its crease pattern and partially folded states (Evans et al., 2015). The crease pattern consists of identical 4Cs and subdivides the sheet into identical kites. For each kite, two of its angles are right angles (Evans et. al., 2015). Only one acute angle, α, is necessary to determine the geometry of the crease pattern, as shown in Figure 2.17(a). While the classical Miura-ori pattern and Barreto's Mars pattern each have an equal distribution of mountain and valley creases, the Huffman grid has an unequal distribution (Evans et al., 2015). As shown in Figure 2.17(a), mountain creases are more common than valley creases are. While the Huffman grid satisfies both necessary theorems for flat foldability, it experiences self-collision as it deploys (Paris et al., 2018). The crease pattern folds into a cylindrical form because of the uneven distribution of mountain and valley creases, as shown in Figure 2.17(c) (Evans et al., 2015).



(a) (b) (c)

Figure 2.17: Huffman grid: (a) crease pattern, (b) partially folded state, and (c) mostly folded state before collision (Evans et al., 2015)

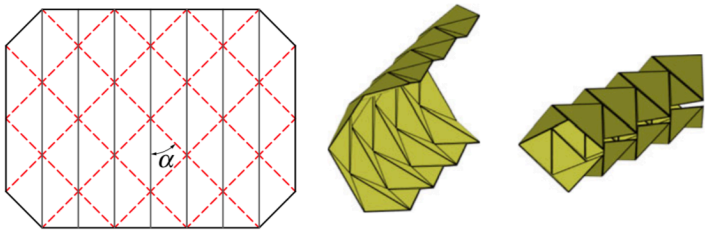
By adjusting the crease pattern of the classical Miura-ori pattern, a plethora of derivative origami tessellations arise. Some of these origami tessellations preserve the flat foldability and rigid foldability intrinsic to the classical Miura-ori pattern. Others encounter issues with self-collision while deploying. Nevertheless, they are all restricted to the general arrangement of vertices and creases found in the classical Miura-ori pattern. These origami tessellations only have one DOF. More origami tessellations are revealed by considering crease patterns with vertices whose degree is greater than four.

2.3.3 Origami Tessellations with Higher-Degree Vertices

All vertices in the previously discussed origami tessellations are 4Cs, and these origami tessellations are restricted to one DOF. This means they are restricted to one rigid folding mode. Origami tessellations with higher degree vertices have multiple DOFs. Some examples are the Yoshimura pattern, Ron Resch triangle tessellation, and square waterbomb tessellation (Tachi, 2010b). While finding origami tessellations with

more DOFs helps satisfy different design needs, examples of such origami tessellations come with their own geometric limitations as well.

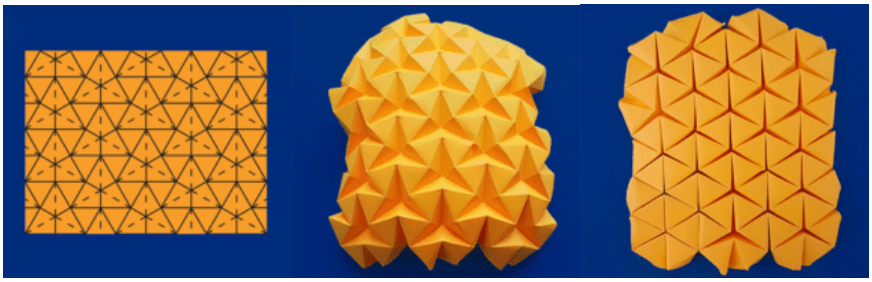
The Yoshimura pattern is a flat-foldable and rigidly foldable origami tessellation consisting entirely of 6Cs and triangular panels (Tachi, 2010b). Figure 2.18 shows the crease pattern of the Yoshimura pattern along with its partially folded states (Evans et al., 2015). Each 6C in the Yoshimura pattern has three DOFs, giving the entire origami tessellation multiple DOFs. Its crease pattern is an evenly spaced crisscross lattice of diagonal creases combined with parallel lines of creases in the longitudinal direction (Evans et. al., 2015). Only one acute angle, α, is necessary to determine the geometry of the crease pattern. The Yoshimura pattern also has an unequal distribution of mountain and valley creases (Evans et. al., 2015). As shown in Figure 2.18(a), valley creases are more common than mountain creases are. While the Yoshimura pattern satisfies both necessary theorems for flat foldability, it experiences self-collision as it deploys (Paris et al., 2018). The crease pattern folds into a cylindrical form because of the uneven distribution of mountain and valley creases, as shown in Figure 2.18(c) (Evans et al., 2015).



(a) (b) (c)

Figure 2.18: Yoshimura pattern: (a) crease pattern, (b) partially folded state, and (c) mostly folded state before collision (Evans et al., 2015)

Computer scientist Ron Resch designed an origami tessellation composed entirely of triangular panels (Yang et al., 2022). Figure 2.19 shows its crease pattern along with its partially folded states (Callens and Zadpoor, 2017). The Ron Resch triangle tessellation consists entirely of 6Cs (Callens and Zadpoor, 2017). These 6Cs come in two types, and neither are flat-foldable as they do not satisfy both necessary theorems for flat foldability. Even though this origami tessellation is rigidly foldable, it is not flat-foldable (Callens and Zadpoor, 2017). The furthest state it can deploy to is the state shown in Figure 2.19(c), which is not a flat state. Also, despite having multiple DOFs, the origami tessellation experiences self-collision as it deploys (Callens and Zadpoor, 2017).

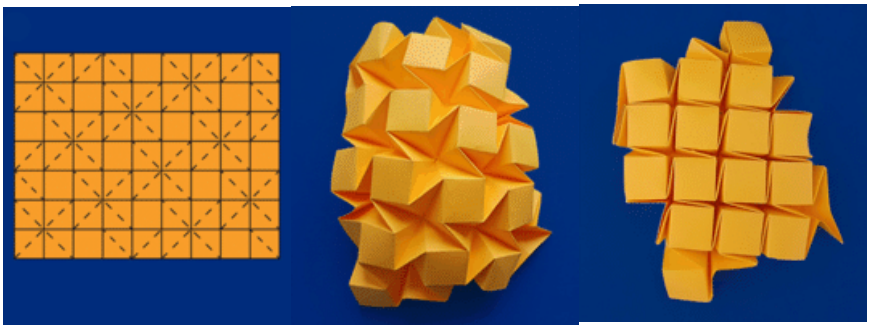


(a) (b) (c)

Figure 2.19: Ron Resch triangle tessellation: (a) crease pattern,
(b) partially folded state, and (c) fully folded non-flat state (Callens and Zadpoor, 2017)

The square waterbomb tessellation consists of degree-5 vertices, 5Cs, and degree-8 vertices, 8Cs, and has multiple DOFs (Chen et al., 2016). Figure 2.20 shows the crease pattern of the square waterbomb tessellation along with its partially folded states (Callens and Zadpoor, 2017). Even though this origami tessellation is rigidly foldable, it is not flat-foldable (Callens and Zadpoor, 2017). The furthest state it can deploy to is the state

shown in Figure 2.20(c), which is not a flat state. Also, despite having multiple DOFs, the origami tessellation experiences self-collision as it deploys (Callens and Zadpoor, 2017).



(a) (b) (c)

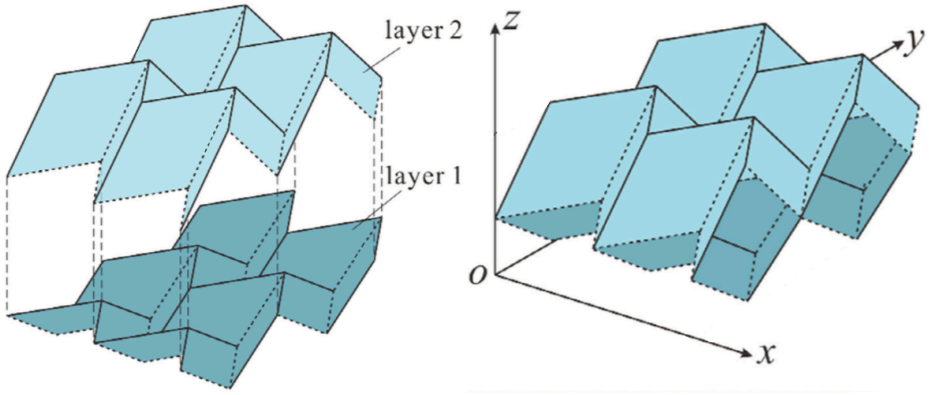
Figure 2.20: Square waterbomb tessellation: (a) crease pattern, (b) partially folded state, and (c) fully folded non-flat state (Callens and Zadpoor, 2017)

The provided examples of classical origami tessellations indicate that while the Miura-ori pattern and its derivatives possess desirable kinematic properties, the more intricate origami tessellations sacrifice some of these properties. As of now, there is a need for flat-foldable and rigidly foldable origami tessellations that have multiple DOFs while not experiencing self-collisions as they fold. Origami tessellations with only one DOF only fold along one path, so all creases fold simultaneously. Origami tessellations with multiple DOFs enable multiple deployment paths, so they require sequential folding (Callens and Zadpoor, 2017). At each folding step, some creases fold while the rest remain fixed (Callens and Zadpoor, 2017). These new origami tessellations would offer a new set of geometric and kinematic properties that is not restricted by the conventions of past origami tessellations.

2.4 Stacking Origami Tessellations

2.4.1 Stacked Miura-ori Pattern

Some origami tessellations possess a property allowing them to stack to form complex foldable structures that cannot be constructed from a single sheet. Crease-stackability is a property describing origami tessellations that can form rigidly foldable stacked structures (Schenk and Guest, 2013a). Sheets of origami tessellations stack by attaching them along a select set of creases (Schenk and Guest, 2013a). The Miura-ori pattern is crease-stackable because copies of the Miura-ori pattern can be stacked in this manner to form the stacked Miura-ori pattern (Filipov et al., 2015; Suto et al., 2018). Figure 2.21(a) demonstrates how two identical Miura-ori sheets with opposite crease parities are stacked by attaching their creases (Ma et al., 2018). The stacked Miura-ori pattern in Figure 2.21(b) is a flat-foldable and rigidly foldable structure with only one DOF (Ma et al., 2018). Each sheet in the stacked structure retains its own range of motion.



(a) (b)

Figure 2.21: Stacking Miura-ori sheets:

(a) individual layers and (b) stacked Miura-ori pattern (Ma et al., 2018)

When more layers are added, the stacked structure grows. Figure 2.22 shows a 4-layer stacked Miura-ori pattern in which adjacent layers have opposite crease parities (Ma et al., 2018). When stretched along its length, the stacked Miura-ori pattern in Figure 2.22 shrinks along its height and expands along its width. This stacked structure has a negative Poisson's ratio in one direction and a positive Poisson's ratio in the other direction (Lang, 2018). Schenk and Guest showed a different stacking configuration of the stacked Miura-ori pattern in which adjacent layers are different patterns but have matching crease parities (Schenk and Guest, 2013a). In this configuration, the stacked structure has an omni-directional negative Poisson's ratio (Schenk and Guest, 2013a).

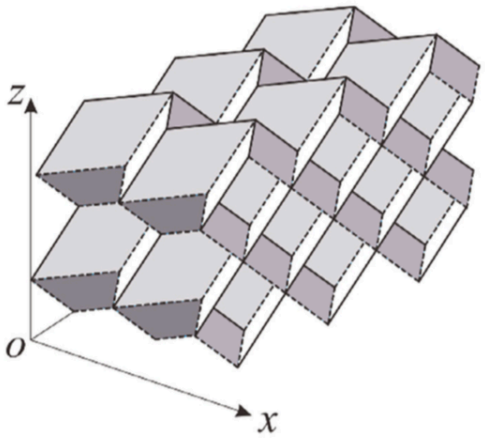


Figure 2.22: A 4-layer stacked Miura-ori pattern (Ma et al., 2018)

The stacked Miura-ori pattern adds height and complexity to the single-sheet origami tessellation (Schenk and Guest, 2013a). Stacked origami structures have inspired the construction of mechanical metamaterials. These are mechanisms that behave like bulk materials even though they exhibit mechanical properties different from those of the underlying material (Lang, 2018). In this case, the stacked Miura-ori pattern displays a negative Poisson's ratio (Ma et al., 2018). Examples of metamaterials inspired by the

stacked Miura-ori pattern include honeycomb tubes and sandwich panels (Cheung et al., 2014). So far, the Miura-ori pattern is the primary origami tessellation used when referring to stacking sheets to form stacked origami structures. Yet, this property of stacking copies of origami tessellations along their creases is not unique to the Miura-ori pattern. Stacking identical sheets of a derivative of the Miura-ori pattern along their creases also results in a stacked origami structure.

2.4.2 Self-Locking Stacked Miura-ori Pattern

While stacking identical sheets of the Miura-ori pattern forms a flat-foldable and rigidly foldable structure, stacking different sheets of the Miura-ori pattern along their creases forms a self-locking structure (Yuan et al., 2020). Figure 2.23 is an example of a self-locking stacked Miura-ori pattern consisting of two different types of Miura-ori sheets, A and B (Schenk and Guest, 2013a). The units found in layers A and B must share at least three geometric parameters for them to stack along their creases (Schenk and Guest, 2013a). This assembly is identical to the assembly shown in Figure 2.21. Starting from the flat folded state, the stacked structure rigidly folds until the type A sheets are fully unfolded, as shown in Figure 2.23. In this self-locking state, the type B sheets are in a partially folded state. This stacked structure can only deploy from its flat folded state to its self-locking state, which are the leftmost and rightmost states, respectively, in Figure 2.23 (Schenk and Guest, 2013a).

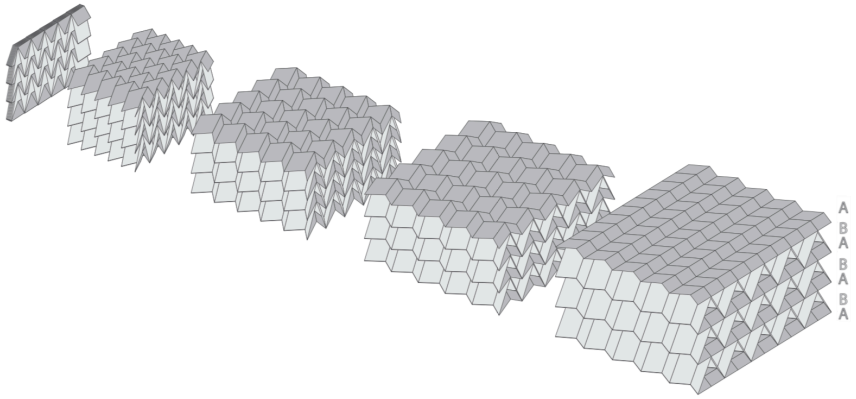


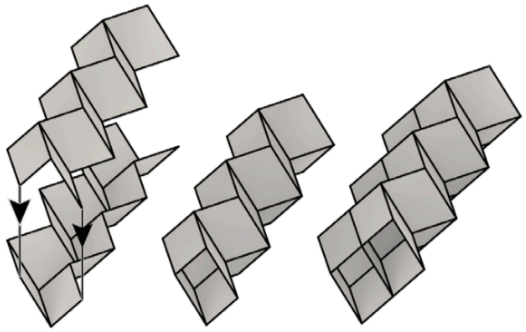
Figure 2.23: Self-locking stacked Miura-ori pattern (Schenk and Guest, 2013a)

Ma et al. demonstrated that stacking different sheets of the Miura-ori pattern forms a stacked cellular structure with graded stiffness when subjected to out-of-plane compression (Ma et al., 2018). Under compression, the stacked structure undergoes rigid folding and then structural crumpling, in which the panels deform (Ma et al., 2018). Self-locking occurs during the transfer between these two folding modes. Self-locking stacked Miura-ori patterns have been used in energy absorption structures and deployable structures (Ma et al., 2018). Similar constructions are possible with derivatives of the Miura-ori pattern, which allow for more geometric variation (Gattas et al., 2013).

2.4.3 Miura-ori Tubes

Rigidly foldable origami tubes are non-developable origami structures that have open ends (Chen et al., 2017). The Miura-ori tube is formed by stacking two identical zigzag Miura-ori sheets with opposite crease parities. Figure 2.24(a) shows the assembly of the Miura-ori tube by attaching the corresponding boundary edges on the sheets (Tachi, 2019). In Figure 2.24(b), the Miura-ori tube has a uniform parallelogram-shaped cross section (Tachi, 2019). The Miura-ori tubes are flat-foldable and rigidly foldable

because they are simple versions of the stacked Miura-ori pattern. They are also stronger than the individual sheets (Filipov et al., 2015). Miura-ori tubes can be stacked to form many different stacked structures (Filipov et al., 2015). Here, stacking two Miura-ori tubes can refer to attaching creases on separate tubes such that their respective vertices align. Alternatively, stacking two Miura-ori tubes can refer to attaching panels on separate tubes such that their respective creases align, as shown in Figure 2.24(c) (Liu et al., 2016).



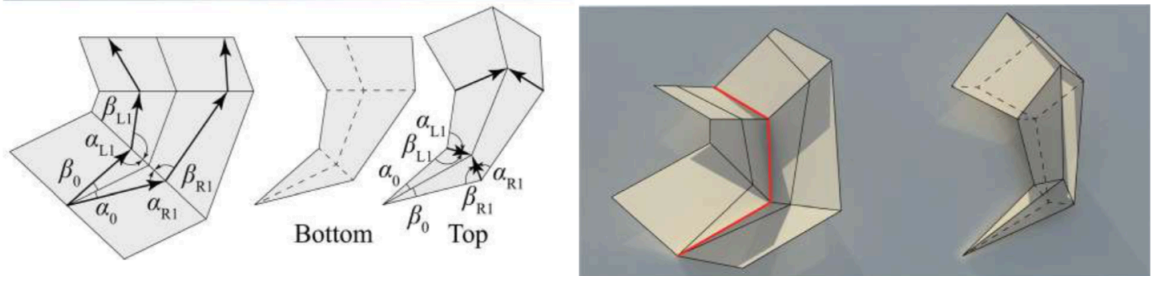
(a) (b) (c)

Figure 2.24: Miura-ori tube: (a) assembly from two Miura-ori strips, (b) origami tube, and (c) parallel alignment (Tachi, 2019)

Stacking copies of the Miura-ori pattern forms rigidly foldable structures, but other known origami tessellations can stack in a similar manner. These include the egg-box pattern, Barreto's Mars pattern, and square-twist pattern, which are derivatives of the Miura-ori pattern. Each of these crease patterns consists entirely of 4Cs. The question that arises is whether there exists a crease-stackable origami tessellation that contains vertices of higher degrees. Such an origami tessellation would give rise to a greater variety of stacked origami structures.

2.5 Rigidly Foldable Origami Horns

The previously mentioned origami tessellations are designed to tessellate the entire sheet. Another function origami tessellations serve is matching the shape of a curve. Tomohiro Tachi designed a method to transform any space curve into a flat-foldable and rigidly foldable origami horn with one DOF. The top and bottom sheets in Figure 2.25(a) are designed to stack along their boundary edges to form an origami horn that matches the shape of a given space curve (Tachi, 2016). When the origami horn is in a partially folded state, its shape is determined by the sequence of creases strictly inside the crease pattern. This sequence of creases forms a piecewise-linear path that approximates the shape of the space curve. Tachi proved geometrically that the union of two rigidly foldable origami structures is also rigidly foldable, making the origami horn flat-foldable and rigidly foldable (Tachi, 2016). The conical structure formed by attaching the two sheets along their boundary creases in Figure 2.25(b) gives the origami horn non-uniform width along its length (Tachi, 2016). The angle parameters of the origami horn can be adjusted so that the width is uniform, resulting in the Miura-ori tube described earlier (Cheung et al., 2014).

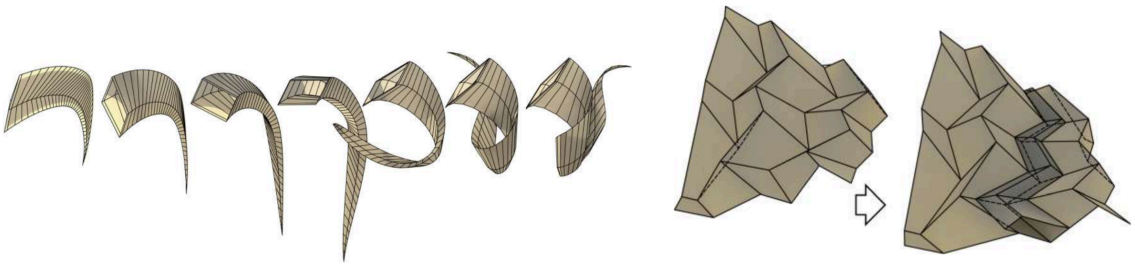


(a) (b)

Figure 2.25: Assembly of a rigidly foldable origami horn:

(a) top and bottom crease patterns and (b) rigidly foldable origami horn (Tachi, 2016)

The rigidly foldable origami horn generalizes the shape of past rigidly foldable tubular structures (Tachi, 2016). Unlike the Miura-ori tube, the origami horn is sealed at one end, which can allow pneumatic actuation from the other end. Tachi determined that the volume of the origami horn is proportional to the sine of one of its dihedral angles (Tachi, 2016). While the rigidly foldable origami horn is designed to unfold to match the shape of a space curve, there is no proposed method to self-lock the origami horn in a specific partially folded state. The origami horn may also collide with itself as it folds. Figure 2.26(a) shows the folding motion of an origami horn that collides with itself at a certain point (Tachi, 2016). One application of the rigidly foldable horn is structural reinforcement to crease lines in origami tessellations (Tachi, 2016). Figure 2.26(b) shows a generalized Miura-ori pattern with an origami horn designed to match the shape of the crease curve (Tachi, 2016). While Tachi's rigidly foldable origami horns come with their geometric limitations, they serve as useful structures in many engineering applications. These including deployable structures, self-configurable robots, and folding-based fabrication (Tachi, 2016).



(a) (b)

Figure 2.26: Rigidly foldable origami horn in action: (a) folding until self-collision and (b) reinforcing a generalized Miura-ori pattern (Tachi, 2016)

2.6 Summary

Research on origami tessellations and their stacked structures examines a multitude of crease patterns that improve upon classical designs. In particular, the Miura-ori tessellation inspired the designs of a variety of 4C origami tessellations. Stacking origami tessellations, either along their creases or their panels, forms rigidly foldable stacked structures that cannot be constructed from a single sheet. These stacked structures can be programmed to possess self-locking states. Also, the origami tubes constructed from the Miura-ori pattern can assemble to form deployable structures. To generalize the Miura-ori tube further, the rigidly foldable origami horn is designed to match the shape of a desired curve when deployed. All in all, origami tessellations have great potential for design applications in multiple engineering fields, but some areas of origami research still need development.

First, the Miura-ori pattern is crease-stackable with copies of itself, and the same property applies to some of its derivative patterns. The Miura-ori pattern has a planar folding mode, restricting a set of its creases to a plane as the model folds. Copies of the Miura-ori pattern can stack by attaching them along this set of creases. As it is a relatively new approach to assembling origami structures, stacking Miura-ori sheets is not a geometrically formalized procedure. Therefore, mathematically formalizing the stacking of Miura-ori patterns would reveal more stacked origami structures and provide a better understanding of how they fold.

Second, all known crease-stackable origami tessellations can be derived from the Miura-ori pattern. This invites the possibility of a crease-stackable origami tessellation that combines 4Cs with 6Cs. The concept of crease-stackability can be applied to a new

origami tessellation that is not a derivative of the Miura-ori pattern. Stacking copies of this origami tessellation would result in a new stacked origami structure unlike the stacked Miura-ori pattern.

Third, the current design of the rigidly foldable origami horn that matches the shape of a curve comes with its drawbacks. Before reaching the shape of the curve, self-collision may occur. Also, there is no proposed method to self-lock the origami horn in a specific partially folded state. It is worth exploring an improved design that can match the shape of a general curve without self-collision. Turning the origami horn into an origami tessellation would make the model modular and easier to modify. The concept of crease-stackability can be applied to this origami tessellation to create self-locking stacked structures.

The aim of this dissertation is to address all research problems listed above.

3

Stacking 4Cs and 4C Tessellations

3.1 Introduction

Origami tessellations that consist entirely of degree-4 vertices, 4Cs, are some of the most studied origami tessellations (Gattas et al., 2013). This chapter examines the geometry of flat-foldable 4C origami tessellations by considering the generalized flat-foldable 4C. Constructing composite structures from copies of flat-foldable 4Cs reveals interesting geometric and kinematic properties. The Double 4C is one such construction that demonstrates relations among the dihedral angles of any flat-foldable 4C. An important consequence is that pairs of panels in the Double 4C remain coplanar regardless of the folded configuration of the Double 4C. The coplanar panels, without crossing each other, behave like scissor mechanisms commonly used to create deployable structures (Li et al., 2017). In addition, there exists a thick-panel version of the Double 4C that preserves the kinematic motion of the origami model. An examination of the Double 4C and its thick-panel counterpart reveals their constituent mechanisms.

The classical Miura-ori pattern is the main 4C origami tessellation examined. Its derivative patterns reveal how the classical Miura-ori pattern can be generalized such that it remains flat-foldable, rigidly foldable, and crease-stackable. The geometry of the flat-foldable 4C makes the classical Miura-ori pattern and its derivative patterns crease-stackable, which allows sheets of these origami tessellations to stack. In this context, stacking sheets of the Miura-ori pattern refers to many methods, each resulting in a different stacked origami structure. Further inspection reveals the intricate lattice of

linkages found in the classical Miura-ori pattern, its derivative patterns, and its stacked structures (Xing and You, 2019).

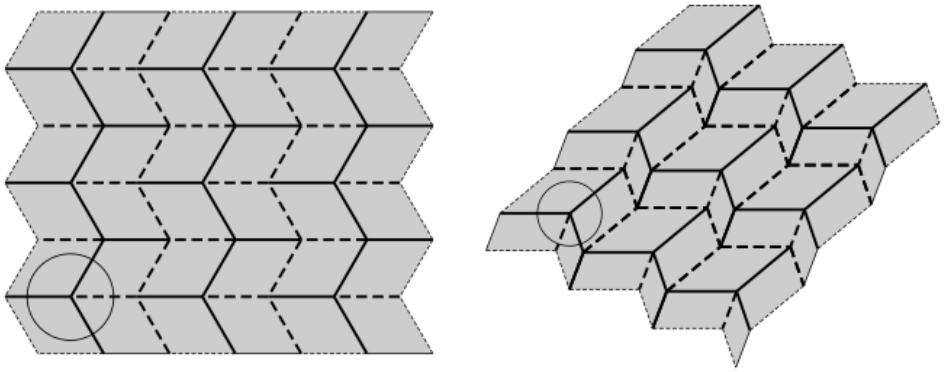
This chapter has the following layout. Section 3.2 examines the geometry and kinematics of the flat-foldable 4C. Kinematic analysis of the flat-foldable 4C shows that it possesses a geometric property in which a select set of vertices and creases remain coplanar regardless of the 4C's partially folded state. This property allows two copies of a flat-foldable 4C to stack and form the Double 4C, which is a flat-foldable and rigidly foldable structure. Section 3.3 presents thick-panel versions of the flat-foldable 4C and Double 4C. These thick-panel versions are designed to preserve the dihedral angle relations in the origami 4C. Section 3.4 generalizes the classical Miura-ori crease pattern so that it remains crease-stackable. The concept of crease-stackability is formally defined to describe the ability to form stacked structures from sheets of origami tessellations. Section 3.5 presents three methods to construct stacked origami structures from the classical Miura-ori pattern. Section 3.6 is a discussion of the origami models constructed.

3.2 Origami 4C and Double 4C

3.2.1 Flat-Foldable Origami 4C

Flat-foldable 4Cs possess special kinematic properties that allow them to form rigidly foldable stacked structures. Flat-foldability is a property that simplifies the analysis of the geometry of the 4Cs, revealing elegant equations describing their geometry. These equations will later be used to show flat-foldable 4Cs can stack with each other. A simplified version of the flat-foldable 4C is a circular sheet with the vertex as the center and the creases as four radii (Alperin and Orozco, 2018; Evans, et. al., 2015). Given a 4C

origami tessellation, a 4C can be obtained by drawing a circle centered at a vertex. Figure 3.1 shows how a 4C can be obtained from two different flat-foldable 4C origami tessellations. For the classical Miura-ori pattern in Figure 3.1(a), the 4C is symmetric, but for the generalized Miura-ori pattern in Figure 3.1(b), the 4C is not necessarily symmetric. The loop closure equations of the flat-foldable 4C can be derived using the matrix method with the Denavit-Hartenberg (DH) notation (Chen et al., 2015b).



(a) (b)

Figure 3.1: 4Cs obtained from 4C origami tessellations:

(a) Miura-ori pattern and (b) generalized Miura-ori pattern

The crease pattern of the flat-foldable 4C in Figure 3.2(a) consists of one vertex, O, and four creases of equal length. Its four panels, A, B, C, and D, are circular sectors with sector angles α_{12}, α_{23}, α_{34}, and α_{41}, respectively, which satisfy

$$\alpha_{12} + \alpha_{23} + \alpha_{34} + \alpha_{41} = 2\pi. \tag{3.1}$$

Maekawa's theorem states that for any flat-foldable vertex, the absolute difference between the number of mountain and valley creases incident to it is two (Hull, 2013; 2015). There are two cases, which are symmetric versions of each other. A type-M 4C has three mountain creases and one valley crease while a type-V 4C has three valley creases and one

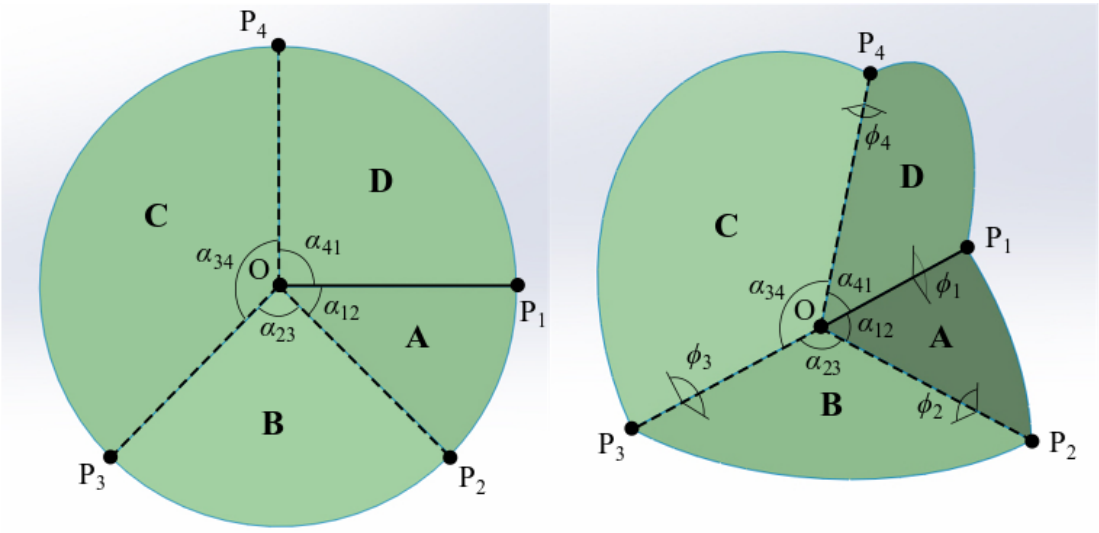
mountain crease. Figure 3.2(a) shows a type-V flat-foldable 4C in which the sole mountain crease is between panels A and D. Since the 4C cannot self-intersect, the following restrictions are imposed:

$$\alpha_{12} \le \alpha_{23},\ \alpha_{41} \le \alpha_{34}. \tag{3.2}$$

Kawasaki's theorem states that for any flat-foldable vertex, the sum of the even angles equals the sum of the odd angles (Hull, 2013; 2015), which gives

$$\alpha_{12} + \alpha_{34} = \alpha_{23} + \alpha_{41} = \pi. \tag{3.3}$$

When the flat-foldable 4C is in a partially folded state, each pair of adjacent panels forms a dihedral angle. For i = 1, 2, 3, and 4, let ϕ_i be the dihedral angle at crease OP_i, as shown in Figure 3.2(b).



(a) (b)

Figure 3.2: Flat-foldable 4C: (a) flat unfolded state and (b) partially folded state

The matrix method for spherical linkages derives the loop closure equations for the dihedral angles in a flat-foldable 4C. The matrix method first converts the dihedral angle

of each crease to its corresponding fold angle. The fold angle is the supplement of the dihedral angle, and its sign depends on the parity of the crease. Let $\theta_i = \phi_i - \pi$ if crease OP_i is a mountain crease, and $\theta_i = \pi - \phi_i$ if crease OP_i is a valley crease. The following are the fold angles: $\theta_1 = \phi_1 - \pi$, $\theta_2 = \pi - \phi_2$, $\theta_3 = \pi - \phi_3$, and $\theta_4 = \pi - \phi_4$. The transformation matrix from OP_i to $OP_{(i+1)}$ is a 3 × 3 matrix in which $\alpha_{i(i+1)}$ and θ_i are the inputs. Since the matrix method is used on a 4-bar linkage, when $i = 4$, every instance of $(i + 1)$ is replaced with 1. The following is the formula of the transformation matrix from OP_i to $OP_{(i+1)}$ (Chen et al., 2015b):

$$Q\left(\alpha_{i(i+1)},\theta_i\right)=\begin{pmatrix} \cos\theta_i & \cos\alpha_{i(i+1)}\sin\theta_i & \sin\alpha_{i(i+1)}\sin\theta_i \\ -\sin\theta_i & \cos\alpha_{i(i+1)}\cos\theta_i & \sin\alpha_{i(i+1)}\cos\theta_i \\ 0 & -\sin\alpha_{i(i+1)} & \cos\alpha_{i(i+1)} \end{pmatrix}. \tag{3.4}$$

Since the 4C is a closed loop linkage, the following closure equation holds (Chen et al., 2015b),

$$Q\left(\alpha_{12},\theta_1\right)Q\left(\alpha_{23},\theta_2\right)Q\left(\alpha_{34},\theta_3\right)Q\left(\alpha_{41},\theta_4\right)=I_{3\times3}. \tag{3.5}$$

Here, $I_{3\times3}$ is the 3 × 3 identity matrix. Rearranging (3.5) gives

$$Q\left(\alpha_{12},\theta_1\right)Q\left(\alpha_{23},\theta_2\right)=Q\left(\alpha_{41},\theta_4\right)^{-1}Q\left(\alpha_{34},\theta_3\right)^{-1}. \tag{3.6}$$

Appendix A lists all 9 entries on the LHS and RHS of (3.6). For any flat-foldable 4C, the loop closure equation in (3.6) is equivalent to the following system of equations:

$$\phi_1=\phi_3,\ \ \phi_2=\phi_4,\ \ \frac{\tan\frac{\phi_1}{2}}{\tan\frac{\phi_2}{2}}=\frac{\sin\left(\frac{\alpha_{23}+\alpha_{12}}{2}\right)}{\sin\left(\frac{\alpha_{23}-\alpha_{12}}{2}\right)}. \tag{3.7}$$

Appendix A shows the derivation of the system of equations in (3.7), a result previously obtained (Chen et al., 2015a; Evans and Lang, 2015). The four sector angles are known

values for the crease pattern, and the four dihedral angles are variables. Given input angle ϕ_1, the remaining dihedral angles are determined using the equations in (3.7), indicating the flat-foldable 4C is rigidly foldable with only one DOF. Figure 3.3 shows the flat-foldable 4C rigidly folding from its flat unfolded state to its flat folded state. The equations in (3.7) state that $\phi_1 = \phi_3$ and $\phi_2 = \phi_4$, which are useful relations for the assembly of the Double 4C constructed next.

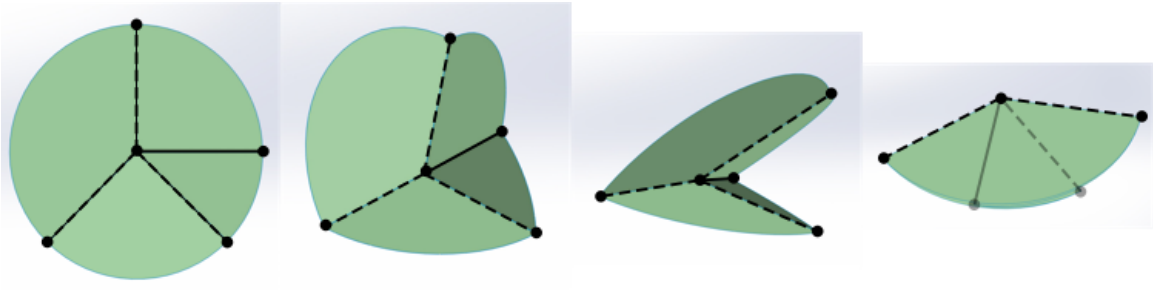


Figure 3.3: Folding sequence of the flat-foldable 4C

3.2.2 Double 4C

The geometry of the flat-foldable 4C reveals interesting relations among the four dihedral angles, which are described in (3.7). These relations hold regardless of the partially folded state of the flat-foldable 4C. The Double 4C is the origami structure constructed from two copies of the flat-foldable 4C. The construction of the Double 4C is a form of crease stacking. Geometrically speaking, crease stacking two origami models means attaching a set of creases on one model to a set of creases on the other such that corresponding end vertices match.

To construct the Double 4C, a copy of the original flat-foldable 4C is made. In the following example, all corresponding components on the copy are labeled with a prime after the name. Figure 3.4 shows the original 4C in green and the copy in yellow. To

combine these two 4Cs, creases OP_2 and OP_4 on the green 4C are attached to creases $O'P_4'$ and $O'P_2'$, respectively, on the yellow 4C so that the corresponding end vertices of these creases match. As a result, vertices O and O' are the same vertex, points P_2 and P_4' are the same point, and points P_4 and P_2' are the same point, as shown in Figure 3.4.

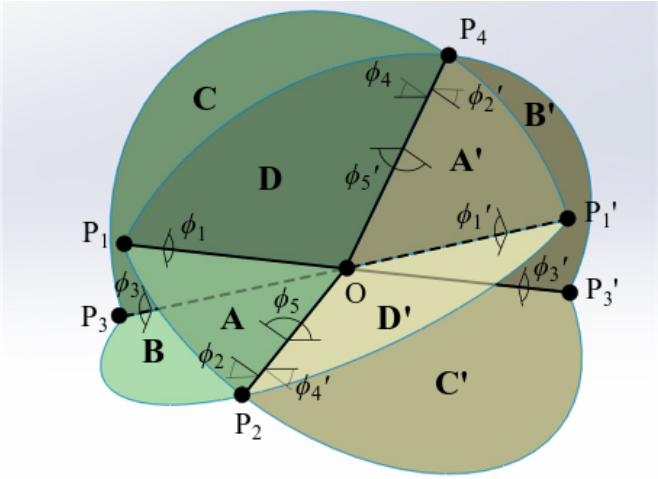


Figure 3.4: Double 4C in a partially folded state

Consider the Double 4C in the partially folded state shown in Figure 3.4, which has 10 dihedral angles labeled. For i = 1, 2, 3, and 4, let ϕ_i be the dihedral angle at OP_i in the green 4C, and ϕ_i' be the dihedral angle at $O'P_i'$ in the yellow 4C. Also, let ϕ_5 be the dihedral angle between panels A and D', and ϕ_5' be the dihedral angle between panels D and A'. The origami model composed of panels A, D, A', and D' connected in a loop is a bidirectionally flat-foldable and rigidly foldable 4C cone. The sector angles in the 4C cone are α_{12}, α_{41}, α_{12}, and α_{41}, and opposite panels are congruent. All creases in the 4C cone are valley creases, and the four dihedral angles are ϕ_1, ϕ_5, ϕ_1', and ϕ_5'. The following are the fold angles: $\theta_1 = \pi - \phi_1$, $\theta_5 = \pi - \phi_5$, $\theta_1' = \pi - \phi_1'$, and $\theta_5' = \pi - \phi_5'$. These angle values are substituted in closure equation (3.6) to obtain

$$Q(\alpha_{12},\theta_1)Q(\alpha_{41},\theta_5)=Q(\alpha_{41},\theta_5')^{-1}Q(\alpha_{12},\theta_1')^{-1}. \tag{3.8}$$

Closure equation (3.8) is equivalent to the following set of equations:

$$\phi_1=\phi_1',\ \phi_5=\phi_5',\ \tan\frac{\phi_1}{2}\tan\frac{\phi_5}{2}=\frac{\cos\left(\frac{\alpha_{41}-\alpha_{12}}{2}\right)}{\cos\left(\frac{\alpha_{41}+\alpha_{12}}{2}\right)}. \tag{3.9}$$

Appendix A shows a derivation of the system of equations in (3.9). Given input angle ϕ_1, the remaining three dihedral angles are determined using the equations in (3.9), indicating the 4C cone has only one DOF. Using the system of equations in (3.7) for both green and yellow 4Cs and the system of equations in (3.9) for the 4C cone, the following set of equations describes all 10 dihedral angles in the Double 4C:

$$\phi_1=\phi_3=\phi_1'=\phi_3',\ \phi_2=\phi_4=\pi-\phi_5=\phi_2'=\phi_4'=\pi-\phi_5',$$

$$\frac{\tan\frac{\phi_1}{2}}{\tan\frac{\phi_2}{2}}=\frac{\sin\left(\frac{\alpha_{23}+\alpha_{12}}{2}\right)}{\sin\left(\frac{\alpha_{23}-\alpha_{12}}{2}\right)}. \tag{3.10}$$

Given input angle ϕ_1, the remaining 9 angles are determined using the system of equations in (3.10). Each dihedral angle ranges from 0 to π, so the Double 4C is a flat-foldable and rigidly foldable structure with only one DOF.

Figure 3.5 shows the Double 4C rigidly folding from its flat unfolded state to its flat folded state. The system of equations in (3.10) states that $\phi_i = \phi_i'$ for i = 1, 2, 3, and 4. This implies that both green and yellow 4Cs are always in identical partially folded states. The system of equations in (3.10) also states that $\phi_2 = \pi - \phi_5 = \phi_4'$ and $\phi_4 = \pi - \phi_5' = \phi_2'$. This implies that the following pairs of panels are coplanar: A and C', B and D', C and A', and D and B'. Despite the fact they never cross each other, panels A, B, C', and D' behave

like a scissor mechanism, which is commonly formed by connecting two cross beams with a pivot (Li et al., 2017). Panels A', B', C, and D behave like a scissor mechanism as well. The system of equations in (3.10) describing the Double 4C can also be derived geometrically (Xing and You, 2019).

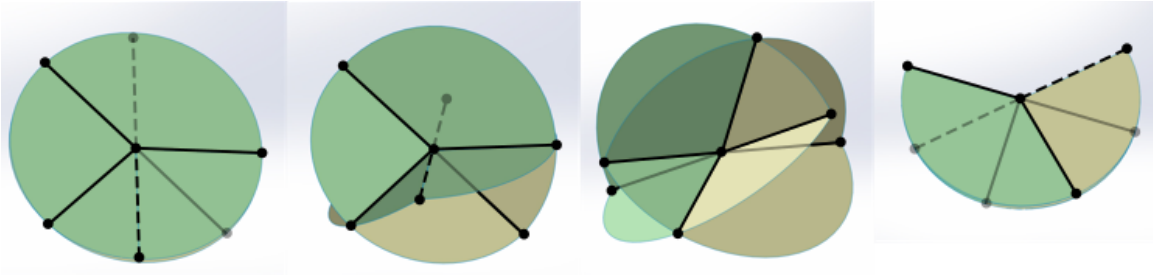
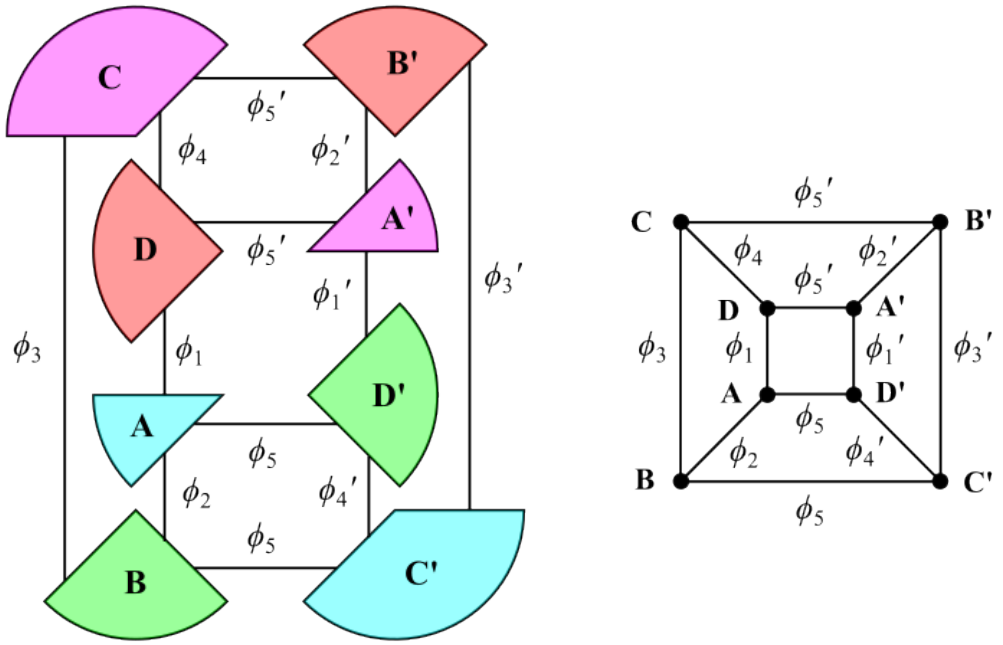


Figure 3.5: Folding sequence of the Double 4C

The schematic diagrams in Figure 3.6 serve as topological graphs of the Double 4C. These diagrams represent 3D origami structures as 2D diagrams that indicate connections between adjacent panels. These connections are independent of the values of the angle parameters. These diagrams also do not depend on the partially folded configuration of the origami structure. The advantage of schematic diagrams is that they show closed loop linkages as closed loops in the graphs. For more complex origami structures, these diagrams show the assemblies of linkages and help compute the DOFs of the origami structures.

The Double 4C is an assembly of six 4-bar linkages, each consisting of four panels connected in a loop. Figure 3.6(a) shows the schematic diagram of the Double 4C that preserves the shapes of the panels. A line between adjacent panels represents a crease. Panels A, B, C, and D and panels A', B', C', and D' each form a flat-foldable 4C, which is a spherical 4-bar linkage. Panels A, D, A', and D' and panels B, C, B', and C' each form a

4C cone, which is also a spherical 4-bar linkage. Panels A, B, C', and D' and panels A', B', C, and D each form a scissor mechanism, in which opposite panels are coplanar. The Double 4C has only one DOF, and each of these mechanisms also has only one DOF. Figure 3.6(b) shows a simplified schematic diagram in which panels are represented as dots, and a line between adjacent dots represents a crease. The connections diagram in Figure 3.6(b) is a planar graph of a cube. The six faces of the planar graph in Figure 3.6(b) represent the six 4-bar linkages in the Double 4C.



(a) (b)

Figure 3.6: Schematic diagrams of Double 4C:

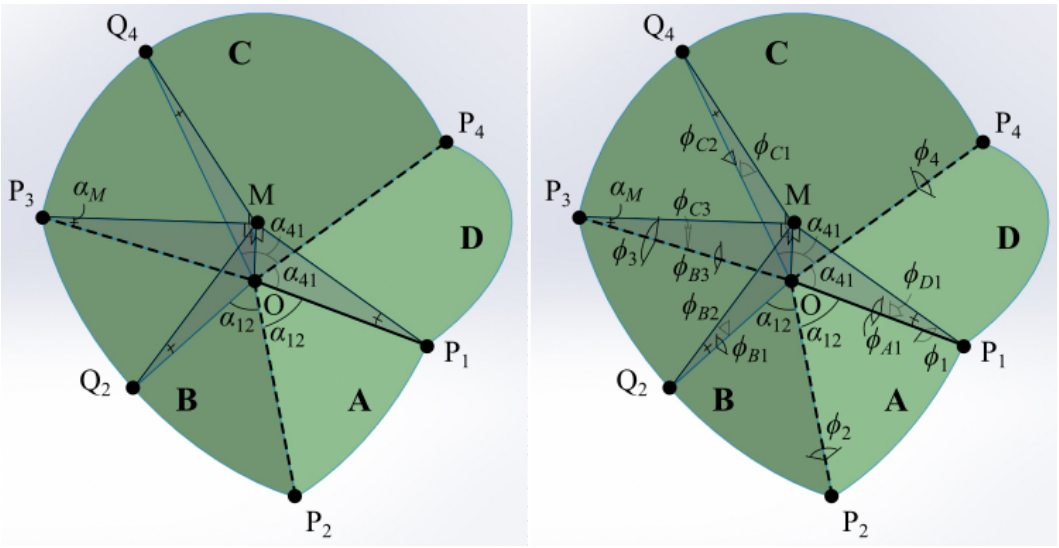
(a) Preserving the panel shapes and (b) simplifying the connections diagram

The construction of the Double 4C is the simplest example of stacking origami models by attaching them along their creases. The stacked structure obtained reveals an assembly of 4-bar linkages. In later sections, the Double 4C appears in structures assembled

from 4C origami tessellations. The derived system of equations in (3.10) describing the Double 4C helps determine the kinematics of these stacked structures.

3.2.3 Coplanarity Property of Flat-Foldable 4C

A geometric proof reveals an interesting property for any flat-foldable 4C called the coplanarity property. Figure 3.7 demonstrates this property using the flat-foldable 4C from Figure 3.2. The center vertex of the 4C is O, and the four creases are OP_1, OP_2, OP_3, and OP_4. Let point Q_2 be on the arc of panel B such that the angle between OQ_2 and OP_2 is α_{12}. Let point Q_4 be on the arc of panel C such that the angle between OQ_4 and OP_4 is α_{41}. The coplanarity property for the flat-foldable 4C states that points P_1, Q_2, P_3, and Q_4 always remain coplanar as the 4C rigidly folds. Furthermore, there always exists a circle, whose center is M, containing points P_1, Q_2, P_3, and Q_4, and this circle lies in a plane perpendicular to line OM. The following is the proof of this property.



(a) (b)

Figure 3.7: Geometric proof of the coplanarity property for a flat-foldable 4C:

(a) sector angles labeled and (b) dihedral angles labeled

Consider the 4C in a partially folded state, as shown in Figure 3.7. For i = 1, 2, 3, and 4, let ϕ_i be the dihedral angle at crease OP_i, as shown in Figure 3.7. Let point M be the circumcenter of triangle $P_1Q_2Q_4$, so line segments P_1M, Q_2M, and Q_4M are the same length. Since points P_1, Q_2, Q_4, and M are coplanar, and OP_1, OQ_2, and OQ_4 are the same length. It follows that P_1OM, Q_2OM, and Q_4OM are congruent right triangles with right angles on point M. Therefore, line OM is perpendicular to the plane containing points P_1, Q_2, and Q_4. Showing that point P_3 lies on the circumscribed circle of triangle $P_1Q_2Q_4$ proves the flat-foldable 4C possesses the coplanarity property.

Some additional angles need to be defined. Let ϕ_{A1} be the dihedral angle between triangle P_1OM and panel A, and ϕ_{D1} be the dihedral angle between triangle P_1OM and panel D. Triangle Q_2OM and panel B form two dihedral angles. Let ϕ_{B1} be the dihedral angle between triangles Q_2OM and Q_2OP_2, and ϕ_{B2} be the dihedral angle between triangles Q_2OM and Q_2OP_3. Triangle Q_4OM and panel C form two dihedral angles. Let ϕ_{C1} be the dihedral angle between triangles Q_4OM and Q_4OP_4, and ϕ_{C2} be the dihedral angle between triangles Q_4OM and Q_4OP_3. Finally, let ϕ_{B3} be the dihedral angle between triangle P_3OM and panel B, and ϕ_{C3} be the dihedral angle between triangle P_3OM and panel C. The following angle relations hold: $\phi_1 = 2\pi - (\phi_{A1} + \phi_{D1})$, $\phi_{B1} = \pi - \phi_{B2}$, $\phi_{C1} = \pi - \phi_{C2}$, and $\phi_3 = \phi_{B3} + \phi_{C3}$.

Since triangles P_1OM and Q_2OM are congruent, and triangles P_1OP_2 and Q_2OP_2 are congruent, it follows that $\phi_{A1} = \phi_{B1}$. Similarly, since triangles P_1OM and Q_4OM are congruent, and triangles P_1OP_4 and Q_4OP_4 are congruent, it follows that $\phi_{D1} = \phi_{C1}$. Since the 4C is flat-foldable, equation (3.3) implies that $(\alpha_{23} - \alpha_{12}) = (\alpha_{34} - \alpha_{41})$. The angle between OQ_2 and OP_3 is $(\alpha_{23} - \alpha_{12})$, and the angle between OQ_4 and OP_3 is $(\alpha_{34} - \alpha_{41})$, so these two angles are equal. Since OQ_2, OP_3, and OQ_4 are of equal length, triangles P_3OQ_2

and P_3OQ_4 are congruent. Since triangles Q_2OM and Q_4OM are congruent, it follows that $\phi_{B3} = \phi_{C3}$. The equations in (3.7) state that $\phi_1 = \phi_3$, so the following set of equations holds:

$$\phi_{A1} = \phi_{B1} = \phi_{C1} = \phi_{D1} = \pi - \frac{\phi_1}{2},\ \phi_{B2} = \phi_{B3} = \phi_{C2} = \phi_{C3} = \frac{\phi_1}{2}. \tag{3.11}$$

Since OQ_2 and OP_3 are of equal length and $\phi_{B2} = \phi_{B3}$, it follows that Q_2OM and P_3OM are congruent right triangles. Therefore, point P_3 lies on the circumscribed circle of triangle $P_1Q_2Q_4$, which means points P_1, Q_2, P_3, and Q_4 always lie on a circle in a plane perpendicular to line OM, in which point M is the center of the circle.

This geometric proof shows that the flat-foldable 4C contains points that are always coplanar regardless of the 4C's partially folded state. The coplanarity property of the flat-foldable 4C implies that the shape of the sheet can be cut such that sets of boundary edges remain coplanar. The construction of the Double 4C and the coplanarity property illustrate the stacking capabilities of the flat-foldable 4C. Later geometric proofs will show that certain flat-foldable 4C origami tessellations are crease-stackable.

3.3 Thick-Panel 4C and Double 4C

3.3.1 Thick-Panel Flat-Foldable 4C

While the sheets used to construct origami models have negligible thickness, it is possible to construct thick-panel versions of origami models. The flat-foldable 4C in Figure 3.2 has a thick-panel analog that accommodates the thickness of the panels. Chen et al. designed a thick-panel counterpart to the flat-foldable 4C that preserves the kinematics and range of folding motion (Chen et al., 2015a). Some of the panels do not have uniform thickness, but their shapes prevent self-collision as the model deploys. These panels are connected in a loop by four revolute joints to form the thick-panel flat-foldable 4C. A

modified version of the matrix method is used to derive the relations of the dihedral angles in the thick-panel flat-foldable 4C.

Panels A, B, C, and D in the flat-foldable 4C in Figure 3.2 are given the appropriate thickness to form the panels shown in Figure 3.8. The sector angles of panels A, B, C, and D are α_{12}, α_{23}, α_{34}, and α_{41}, respectively, which satisfy equation (3.3). Four additional lengths, d_{12}, d_{23}, d_{34}, and d_{41}, determine the thicknesses of these panels. Panel A is a right circular sector prism with sector angle α_{12} and height d_{12}. Panel B merges two right circular sector prisms: one with sector angle α_{12} and height d_{23} and another with sector angle $(\alpha_{23} - \alpha_{12})$ and height d_{23}. Panel C merges two right circular sector prisms: one with sector angle α_{41} and height d_{34} and another with sector angle $(\alpha_{34} - \alpha_{41})$ and height d_{34}. Panel D is a right circular sector prism with sector angle α_{41} and height d_{41}. The sector angles and panel heights are the known values for the geometry of the panels.

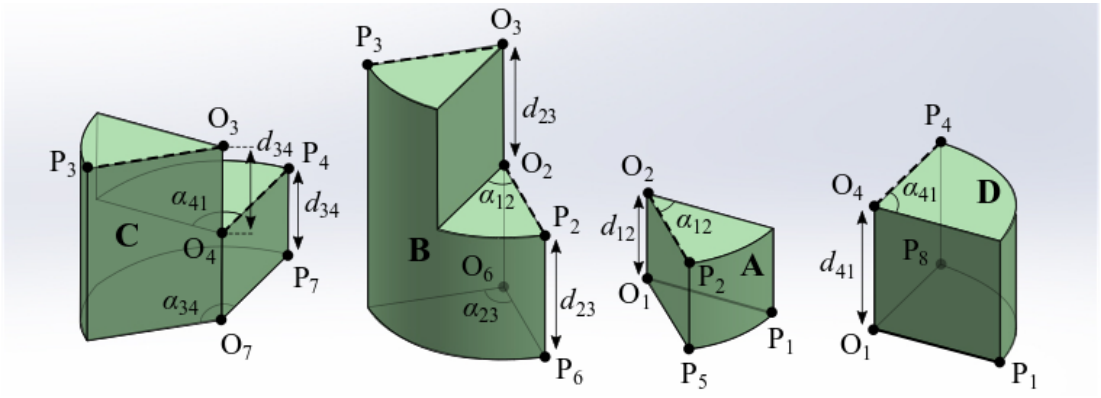


Figure 3.8: Panels in the thick-panel flat-foldable 4C

To assemble the thick-panel flat-foldable 4C, the panels in Figure 3.8 are connected in a loop by four revolute joints, as shown in Figure 3.9. For $i = 1, 2, 3$, and 4, let ϕ_i be the dihedral angle at revolute joint O_iP_i. The parity of the revolute joint is the same as the parity of the corresponding crease in the origami model. A mountain crease in the origami model

corresponds to a revolute joint connecting the bottom faces of adjacent panels, and the angle between those two faces is the dihedral angle. A valley crease in the origami model corresponds to a revolute joint connecting the top faces of adjacent panels, and the angle between those two faces is the dihedral angle. For the thick-panel flat-foldable 4C in Figure 3.9, O_1P_1 is a mountain revolute joint, and O_2P_2, O_3P_3, and O_4P_4 are valley revolute joints. The axes of these revolute joints do not meet at a common vertex, so the thick-panel flat-foldable 4C is a spatial linkage.

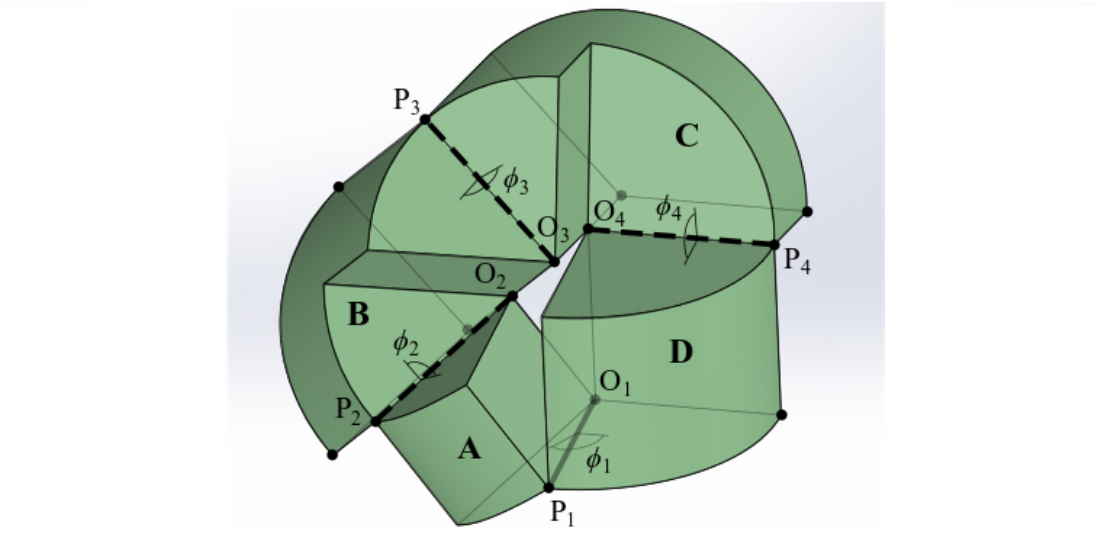


Figure 3.9: Thick-panel flat-foldable 4C in a partially folded state

The matrix method for spatial linkages derives the loop closure equations for the dihedral angles in the thick-panel flat-foldable 4C. The matrix method first converts the dihedral angle of each revolute joint to its corresponding fold angle. The fold angle is the supplement of the dihedral angle, and the sign of the fold angle depends on the parity of the revolute joint. Let $\theta_i = \phi_i - \pi$ if O_iP_i is a mountain, and $\theta_i = \pi - \phi_i$ if O_iP_i is a valley. The following are the fold angles: $\theta_1 = \phi_1 - \pi$, $\theta_2 = \pi - \phi_2$, $\theta_3 = \pi - \phi_3$, and $\theta_4 = \pi - \phi_4$. The transformation matrix from O_iP_i to $O_{(i+1)}P_{(i+1)}$ is a 4×4 matrix in which $\alpha_{i(i+1)}$, θ_i, and $d_{i(i+1)}$

are the inputs. Since the matrix method is used on a 4-bar linkage, when $i = 4$, every instance of $(i + 1)$ is replaced with 1. The transformation matrices are structured such that the upper-left 3 × 3 square matrix represents a rotational matrix while the 3 × 1 column vector in the upper-right represents a translational vector, which translates the origin. The following is the formula of the transformation matrix from O_iP_i to $O_{(i+1)}P_{(i+1)}$ (Chen et al., 2015b):

$$Q\left(\alpha_{i(i+1)},\theta_i,d_{i(i+1)}\right)=\begin{pmatrix} \cos\theta_i & \cos\alpha_{i(i+1)}\sin\theta_i & \sin\alpha_{i(i+1)}\sin\theta_i & d_{i(i+1)}\cos\theta_i \\ -\sin\theta_i & \cos\alpha_{i(i+1)}\cos\theta_i & \sin\alpha_{i(i+1)}\cos\theta_i & -d_{i(i+1)}\sin\theta_i \\ 0 & -\sin\alpha_{i(i+1)} & \cos\alpha_{i(i+1)} & 0 \\ 0 & 0 & 0 & 1 \end{pmatrix}. \quad (3.12)$$

Since the thick-panel flat-foldable 4C is a closed loop linkage, the following closure equation holds (Chen et al., 2015b):

$$Q\left(\alpha_{12},\theta_1,d_{12}\right)Q\left(\alpha_{23},\theta_2,d_{23}\right)Q\left(\alpha_{34},\theta_3,d_{34}\right)Q\left(\alpha_{41},\theta_4,d_{41}\right)=I_{4\times4}. \quad (3.13)$$

Here, $I_{4\times4}$ is the 4 × 4 identity matrix. Rearranging (3.13) gives

$$Q\left(\alpha_{12},\theta_1,d_{12}\right)Q\left(\alpha_{23},\theta_2,d_{23}\right)=Q\left(\alpha_{41},\theta_4,d_{41}\right)^{-1}Q\left(\alpha_{34},\theta_3,d_{34}\right)^{-1}. \quad (3.14)$$

Appendix B lists all 16 entries on the LHS and RHS of (3.14), from which the following equations that make the thick-panel flat-foldable 4C rigidly foldable are derived:

$$\frac{d_{12}}{\sin\alpha_{12}}=\frac{d_{23}}{\sin\alpha_{23}}=-\frac{d_{34}}{\sin\alpha_{34}}=-\frac{d_{41}}{\sin\alpha_{41}}. \quad (3.15)$$

The relations in (3.3) simplify the equations in (3.15) to

$$d_{12}=-d_{34},\ d_{23}=-d_{41},\ \frac{d_{12}}{\sin\alpha_{12}}=\frac{d_{23}}{\sin\alpha_{23}}. \quad (3.16)$$

A positive value of $d_{i(i+1)}$ means O_iP_i is below $O_{(i+1)}P_{(i+1)}$, and a negative value of $d_{i(i+1)}$

means O_iP_i is above $O_{(i+1)}P_{(i+1)}$. In either case, the absolute value of $d_{i(i+1)}$ equals the panel height. Suppose the thick-panel flat-foldable 4C satisfies the equation in (3.16). The loop closure equation in (3.14) is equivalent to the following system of equations:

$$\phi_1 = \phi_3, \;\; \phi_2 = \phi_4, \;\; \frac{\tan\frac{\phi_1}{2}}{\tan\frac{\phi_2}{2}} = \frac{\sin\left(\frac{\alpha_{23}+\alpha_{12}}{2}\right)}{\sin\left(\frac{\alpha_{23}-\alpha_{12}}{2}\right)}. \tag{3.17}$$

Appendix B shows a derivation of the system of equations in (3.17), which is the same as the system of equations in (3.7). Chen et al. showed that equations in (3.16) and (3.17) describe the thick-panel version of the flat-foldable 4C (Chen et al. 2015b).

The four sector angles and four panel heights are known values, and the four dihedral angles are variables. The angle relations in (3.17) are the same as the angle relations in (3.7). Given input angle ϕ_1, the remaining dihedral angles are determined using the equations in (3.17), indicating the thick-panel flat-foldable 4C is rigidly foldable with only one DOF. The kinematic equations in (3.16) and (3.17) are those of the Bennett linkage (Chen et al., 2015b). Figure 3.10 shows the thick-panel flat-foldable 4C rigidly folding from its flat unfolded state to its flat folded state. Like the equations for the origami flat-foldable 4C, the equations in (3.17) state that $\phi_1 = \phi_3$ and $\phi_2 = \phi_4$, which are useful relations for the assembly of the thick-panel Double 4C.

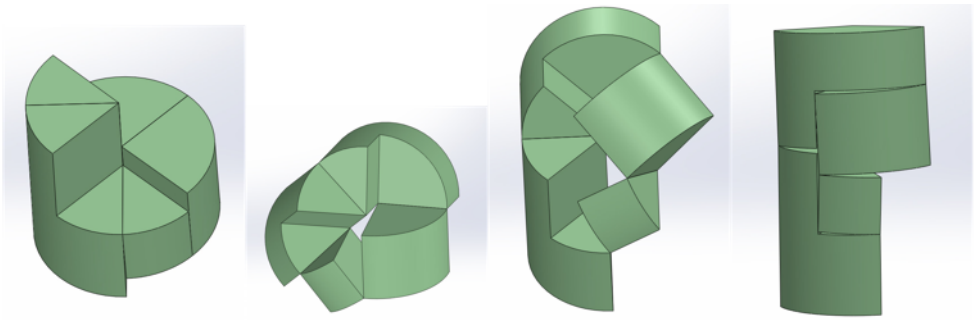


Figure 3.10: Folding sequence of the thick-panel flat-foldable 4C

3.3.2 Thick-Panel Double 4C

The system of equations in (3.17) describes the relations among the dihedral angles in the thick-panel flat-foldable 4C. These equations hold regardless of the partially folded state. The thick-panel Double 4C is the composite origami structure constructed from two copies of the thick-panel flat-foldable 4C. The assembly of the thick-panel Double 4C resembles that of its origami counterpart. While the construction of the origami Double 4C involves attaching creases, the construction of the thick-panel Double 4C involves attaching pairs of edges with revolute joints.

To construct the thick-panel Double 4C, a copy of the thick-panel flat-foldable 4C is made. All corresponding components on the copy are labeled with a prime after the name. Figure 3.11 shows the original 4C in green and the copy in yellow. To combine these two thick-panel flat-foldable 4Cs, edges O_1P_5 and O_1P_8 on the green copy are attached to edges $O_1'P_8'$ and $O_1'P_5'$, respectively, on the yellow copy. As a result, vertices O_1 and O_1' are the same vertex, points P_5 and P_8' are the same point, and points P_8 and P_5' are the same point, as shown in Figure 3.11. This construction also attaches edges O_6P_6 and $O_7'P_7'$ and attaches edges O_7P_7 and $O_6'P_6'$. As a result, the following pairs of points are the same point: O_6 and O_7', O_7 and O_6', P_6 and P_7', and P_7 and P_6'.

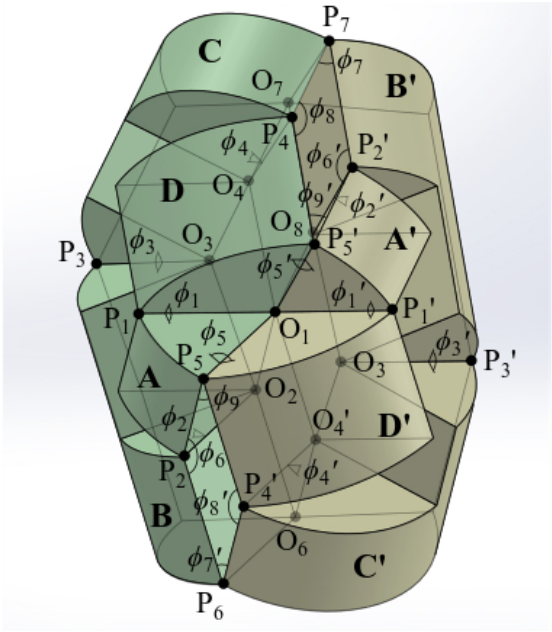


Figure 3.11: Thick-panel Double 4C in a partially folded state

Consider the thick-panel Double 4C in the partially folded state shown in Figure 3.11, which has 18 dihedral angles labeled. For i = 1, 2, 3, and 4, let ϕ_i be the dihedral angle at O_iP_i in the green thick-panel flat-foldable 4C, and ϕ_i' be the dihedral angle at $O_i'P_i'$ in the yellow thick-panel flat-foldable 4C, as shown in Figure 3.11. The dihedral angle between C and B' is ϕ_7, and the dihedral angle between B and C' is ϕ_7'. Each pair of adjacent panels in the thick-panel Double 4C forms a pair of supplementary dihedral angles. Panels A and B form ϕ_2 and ϕ_6, panels C and D form ϕ_4 and ϕ_8, and panels A and D' form ϕ_5 and ϕ_9. Similarly, panels A' and B' form ϕ_2' and ϕ_6', panels C' and D' form ϕ_4' and ϕ_8', and panels A' and D form ϕ_5' and ϕ_9'. The spherical 4-bar linkage composed of panels A, D, A', and D' in Figure 3.11 is the same as the corresponding spherical 4-bar linkage in the origami Double 4C. Therefore, the equations in (3.10) hold for the thick-panel Double 4C as well. These equations and the relations among supplementary dihedral

angles give the following set of equations describing all 18 dihedral angles in the thick-panel Double 4C:

$$\phi_1 = \phi_3 = \phi_1' = \phi_3', \ \phi_2 = \phi_4 = \phi_7 = \phi_9 = \phi_2' = \phi_4' = \phi_7' = \phi_9',$$

$$\phi_5 = \phi_6 = \phi_8 = \phi_5' = \phi_6' = \phi_8', \ \phi_2 = \pi - \phi_5, \ \frac{\tan\frac{\phi_1}{2}}{\tan\frac{\phi_2}{2}} = \frac{\sin\left(\frac{\alpha_{23}+\alpha_{12}}{2}\right)}{\sin\left(\frac{\alpha_{23}-\alpha_{12}}{2}\right)}. \tag{3.18}$$

Given input angle ϕ_1, the remaining 17 angles are determined using the system of equations in (3.18). Each dihedral angle ranges from 0 to π, so the thick-panel Double 4C is a flat-foldable and rigidly foldable structure with only one DOF. Figure 3.12 shows the thick-panel Double 4C rigidly folding from its flat unfolded state to its flat folded state without self-intersection. Figure 3.12 also shows a 3D-printed thick-panel Double 4C. The system of equations in (3.18) states that $\phi_i = \phi_i'$ for i = 1, 2, 3, and 4. This implies that both thick-panel flat-foldable 4Cs are always in identical partially folded states as the thick-panel Double 4C deploys.

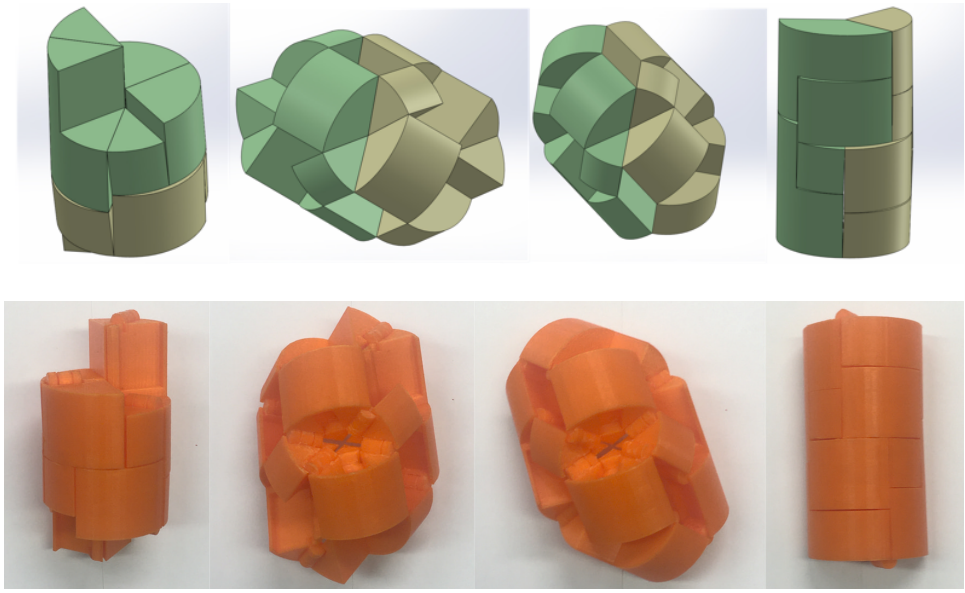


Figure 3.12: Folding sequence of the thick-panel Double 4C

The assembly of the thick-panel Double 4C reveals it to be an assembly of six 4-bar linkages, each consisting of four panels connected in a loop. Figure 3.13(a) shows the schematic diagram of the thick-panel Double 4C that preserves the shapes of the panels. A line between adjacent panels represents a revolute joint. Panels A, B, C, and D and panels A', B', C', and D' each form a Bennett linkage because they each form a thick-panel flat-foldable 4C. Panels A, B, C', and D' and panels A', B', C, and D each form a parallelogram linkage because the voids within the loops of panels are always right parallelogram prisms. Panels A, D, A', and D' form a spherical linkage because they all share vertex O_1. Panels B, C, B', and C' form a Bennett linkage because the revolute joints' axes do not all intersect at a common point. The thick-panel Double 4C has only one DOF, and each of these mechanisms also has only one DOF. Figure 3.13(b) shows a simplified schematics diagram in which panels are represented as dots, and a line between adjacent dots represents a revolute joint. The connections diagram in Figure 3.13(b) is a planar graph of a cube. The six faces of the planar graph in Figure 3.13(b) represent the six 4-bar linkages in the thick-panel Double 4C.

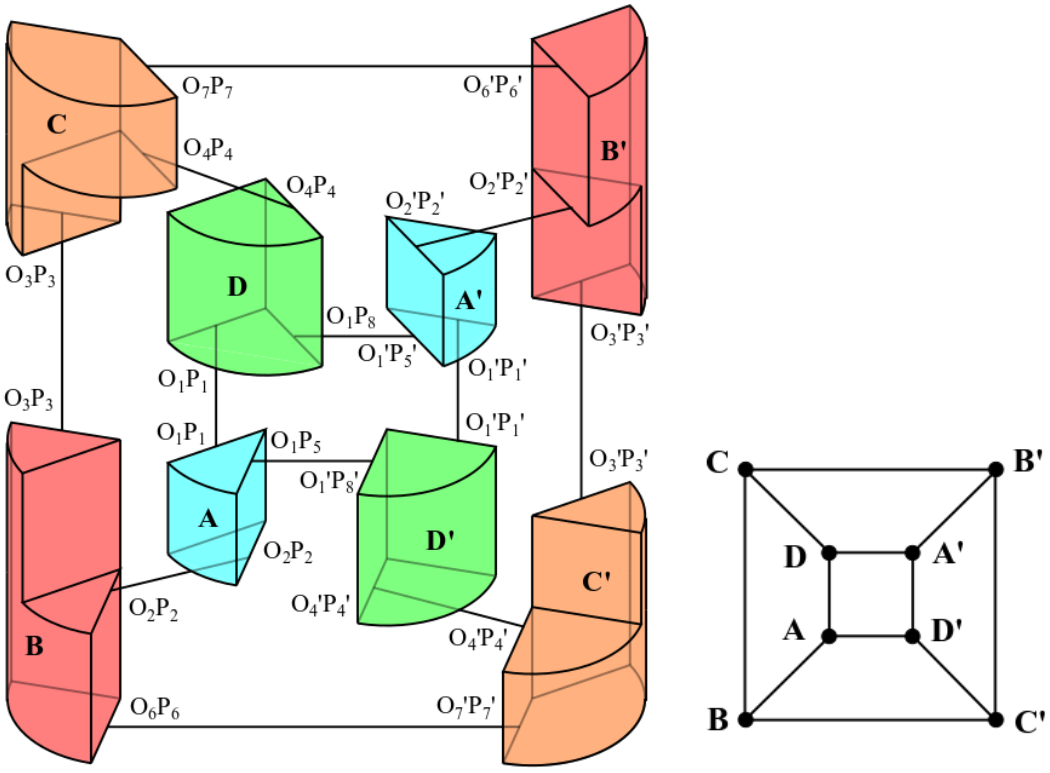


Figure 3.13: Schematic diagrams of thick-panel Double 4C:

(a) preserving the panel shapes and (b) simplifying the connections diagram

When converting the origami Double 4C to the thick-panel Double 4C, all but one of the component mechanisms are transformed. Table 3.1 details the mechanisms in both the origami and thick-panel Double 4C. The mechanism composed of panels A, B, C, and D and the one composed of A', B', C', and D' each transform from a spherical 4-bar linkage to a Bennett linkage. For both mechanisms the sum of their sector angles is 2π. The mechanism composed of panels A, B, C', and D' and the one composed of panels A', B', C, and D each transform from a scissor mechanism to a parallelogram linkage. Both mechanisms have the property in which opposite panels are parallel or coplanar. The mechanism composed of panels A, D, A', and D' remains a spherical 4-bar linkage as all 4

panels still share a common vertex. The mechanism composed of panels B, C, B', and C' transforms from a spherical 4-bar linkage to a Bennett linkage. Both mechanisms have the property in which opposite panels are congruent. Therefore, converting the Double 4C to its thick-panel counterpart transforms its component mechanisms, but some of their kinematic properties remain constant. The kinematic equations describing the spherical 4-bar and Bennett linkages are identical. Similarly, the kinematic equations describing the scissor mechanism and parallelogram linkage are identical. Furthermore, each of these mechanisms has only one DOF of mobility.

Table 3.1: Mechanisms in the Double 4C and Thick-Panel Double 4C

<table>
<tr><th colspan="2">Double 4C</th><th colspan="2">Thick-Panel Double 4C</th></tr>
<tr><td>Panels</td><td>Mechanisms</td><td>Panels</td><td>Mechanisms</td></tr>
<tr><td>A, B, C, D</td><td rowspan="4">Spherical 4-bar Linkage</td><td>A, B, C, D</td><td rowspan="3">Bennett Linkage</td></tr>
<tr><td>A', B', C', D'</td><td>A', B', C', D'</td></tr>
<tr><td>B, C, B', C'</td><td>B, C, B', C'</td></tr>
<tr><td>A, D, A', D'</td><td>A, D, A', D'</td><td>Spherical 4-bar Linkage</td></tr>
<tr><td>A, B, C', D'</td><td rowspan="2">Scissor Mechanism</td><td>A, B, C', D'</td><td rowspan="2">Parallelogram Linkage</td></tr>
<tr><td>A', B', C, D</td><td>A', B', C, D</td></tr>
</table>

The construction of the thick-panel Double 4C reveals similarities to the origami version. The assembly of the origami Double 4C illustrates the potential to construct mobile assemblies of mechanisms by attaching origami models along their creases. Stacking crease-stackable 4C origami tessellations forms a lattice of Double 4Cs. Meanwhile, the assembly of the thick-panel Double 4C shows how to add thickness to the panels of origami models while maintaining the kinematic relations among their dihedral angles. This suggests there is a method to construct thick-panel versions of 4C origami tessellations that can stack to form a lattice of thick-panel Double 4Cs.

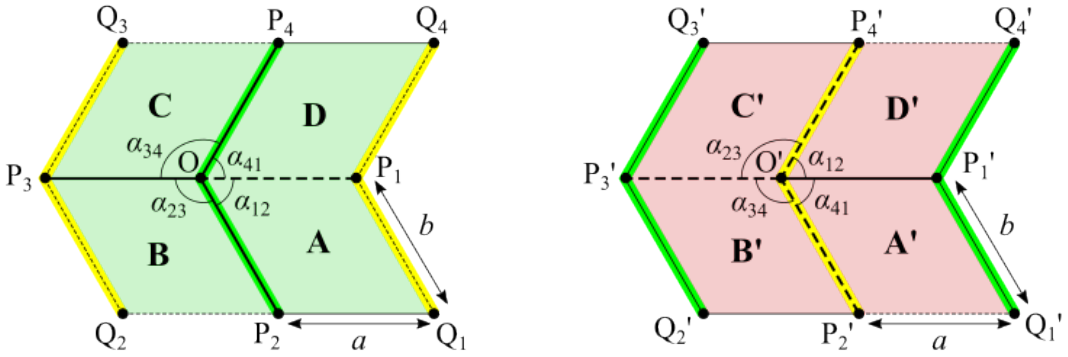
3.4 Crease-Stackable 4C Origami Tessellation

3.4.1 Crease-Stackable Classical Miura-ori Pattern

The classical Miura-ori pattern is a 4C origami tessellation in which every vertex is an identical flat-foldable 4C (Schenk and Guest 2013a). Since the crease patterns of origami tessellations have repetitive geometry, the entire crease pattern can be generated from a single unit, which is a collection of panels. Figure 3.14(a) shows an example of a type-M 4-panel Miura-ori unit used to assemble the classical Miura-ori pattern. Figure 3.14(b) is the type-V version, in which the parity of each crease is flipped. Each unit is a symmetric flat-foldable 4C in which the panels are congruent parallelograms with a and b as the side lengths, as shown in Figure 3.14. The sector angles and dihedral angles in the Miura-ori unit correspond to those in the flat-foldable 4C in Figure 3.2, so equation (3.3) holds. For i = 1, 2, 3, and 4, the sector angle between OP_i and $OP_{(i+1)}$ is $\alpha_{i(i+1)}$, and the dihedral angle at OP_i is ϕ_i. When i = 4, every instance of $(i + 1)$ is replaced with 1. Since the 4C is symmetric, the following equations hold: $\alpha_{12} = \alpha_{41}$, $\alpha_{23} = \alpha_{34}$, and $\alpha_{12} = \pi - \alpha_{23}$. Substituting these values in (3.7) gives

$$\phi_1 = \phi_3,\ \ \phi_2 = \phi_4,\ \ \cos\alpha_{12} \tan\frac{\phi_1}{2} = \tan\frac{\phi_2}{2}. \tag{3.19}$$

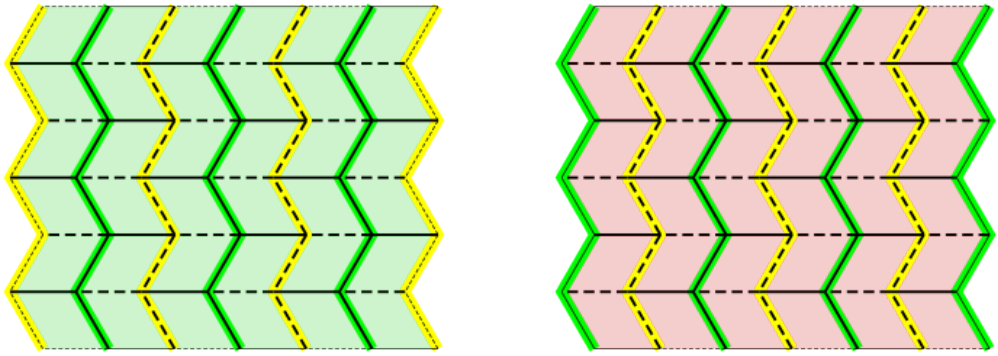
Appendix A shows the derivation of the system of equations in (3.19) for the symmetric flat-foldable 4C. The equations in (3.19) state that the Miura-ori units in Figure 3.14 are flat-foldable and rigidly foldable with only one DOF. The type-M Miura-ori unit is crease-stackable with the type-V Miura-ori unit because a set of creases on one unit can be attached to a set of creases on the other unit to form a rigidly foldable structure. For both units in Figure 3.14, the green and yellow creases indicate the upper and lower creases, respectively, that are used when stacking one unit on another.



(a) (b)

Figure 3.14: Two Miura-ori units: (a) type-M and (b) type-V

Arranging the Miura-ori units in a lattice forms the classical Miura-ori pattern. For any positive integers M and N, the $M \times N$ Miura-ori pattern is M units long and N units wide. Figure 3.15(a) and (b) are examples of 3×3 Miura-ori patterns generated from copies of the type-M unit in Figure 3.14(a) and the type-V unit in Figure 3.14(b), respectively. In both origami tessellations, the green and yellow creases form zigzags. These creases indicate the upper and lower creases that are used when stacking one sheet on another.



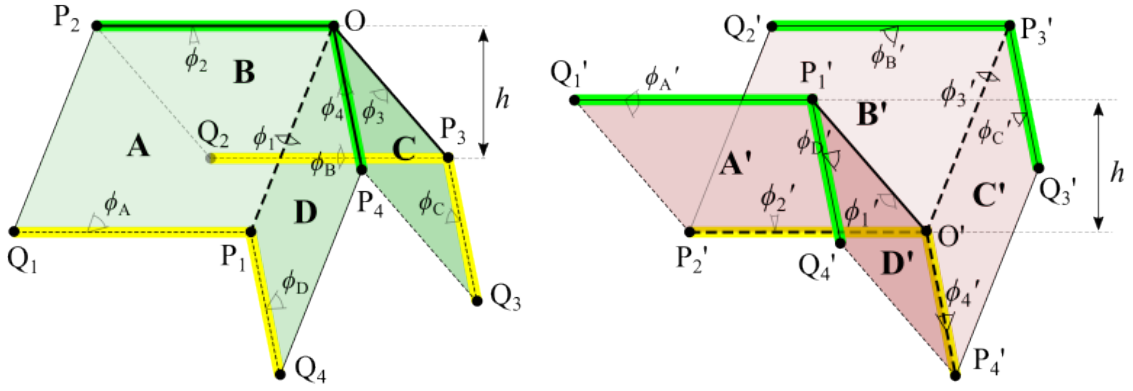
(a) (b)

Figure 3.15: Two 3×3 classical Miura-ori patterns generated from

(a) type-M units and (b) type-V units

The classical Miura-ori pattern is flat-foldable because every vertex in the crease pattern is a flat-foldable 4C. Also, the origami tessellation does not collide with itself as it folds. To show that the classical Miura-ori crease pattern is rigidly foldable, the system of equations in (3.19) is applied to each vertex in the crease pattern. The result is a combined system of equations describing all dihedral angles in the crease pattern. The dihedral angle of every crease that lies on the horizontal parallel lines in Figure 3.15 equals ϕ_1. The dihedral angle of every crease that lies on the vertical zigzag lines in Figure 3.15 equals ϕ_2. Given input angle ϕ_1, all remaining dihedral angles are computed using the equations in (3.19). Therefore, the $M \times N$ classical Miura-ori pattern is flat-foldable and rigidly foldable with only one DOF.

Figure 3.16(a) and (b) show a type-M and type-V Miura-ori unit, respectively, in a partially folded state. Both Miura-ori units are mirror images of each other. For the partially folded type-M unit in Figure 3.16(a), the green creases lie on a plane, and the yellow creases lie on a parallel plane. Showing this geometric property holds regardless of the partially folded state proves the type-M Miura-ori unit is crease-stackable with the type-V Miura-ori unit.



(a) (b)

Figure 3.16: Two Miura-ori units in partially folded states: (a) type-M and (b) type-V

The two green creases in Figure 3.16(a) lie on a unique plane. The yellow creases on panels A and D also lie on a unique plane. Let ϕ_A and ϕ_D be the angles between this plane and panels A and D, respectively, as shown in Figure 3.16(a). By symmetry of the sector angles in panels A and D, it follows that $\phi_A = \phi_D$. By spherical law of cosines, the following equation holds:

$$\tan\phi_A = \left(\cos\alpha_{12} \tan\frac{\phi_1}{2} \right)^{-1}. \tag{3.20}$$

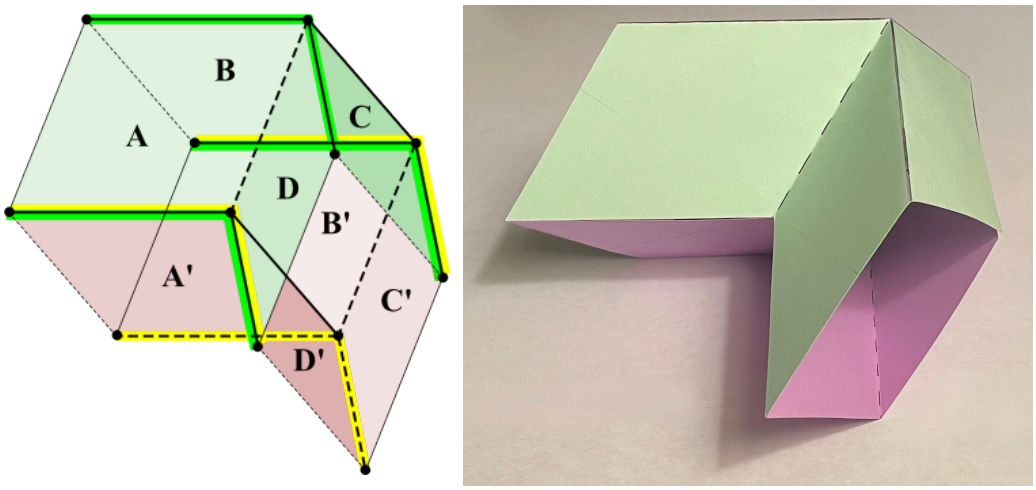
The yellow creases on panels B and C lie on a unique plane. Let ϕ_B and ϕ_C be the angles between this plane and panels B and C, respectively, as shown in Figure 3.16(a). By symmetry of the sector angles in panels B and C, it follows that $\phi_B = \phi_C$. By spherical law of cosines, the following equation holds:

$$\tan\phi_B = \left(\cos\alpha_{12} \tan\frac{\phi_3}{2} \right)^{-1}. \tag{3.21}$$

Since $\phi_1 = \phi_3$, the equations in (3.20) and (3.21) imply that $\phi_A = \phi_B = \phi_C = \phi_D$. The green and yellow creases in panel A are parallel, and the distance between them is $a(\sin\alpha_{12})$. Similarly, the green and yellow creases in panel B are parallel, and the distance between them is also $a(\sin\alpha_{12})$. Therefore, the two green creases lie on a plane, and the four yellow creases lie on a parallel plane, as shown in Figure 3.16(a). Let the height, h, of the Miura-ori unit be the distance between these two planes, which is expressed as:

$$h = \frac{a\sin\alpha_{12}}{\sqrt{1+\left(\cos\alpha_{12} \tan\frac{\phi_1}{2} \right)^2}}. \tag{3.22}$$

The reflection of the type-M Miura-ori unit about the plane containing its yellow creases is the type-V Miura-ori unit. This reflection stacks the type-M unit on the type-V unit, producing the Miura-ori tube unit. The yellow creases on the type-M unit in Figure 3.16(a) are attached to the green creases on the type-V unit in Figure 3.16(b). The Miura-ori tube unit in Figure 3.17 is a flat-foldable and rigidly foldable stacked origami structure with only one DOF. The Miura-ori tube unit is also the simplest unit of the Miura-ori tube. Alternatively, stacking the type-V unit on a type-M unit produces the Double 4C described earlier.



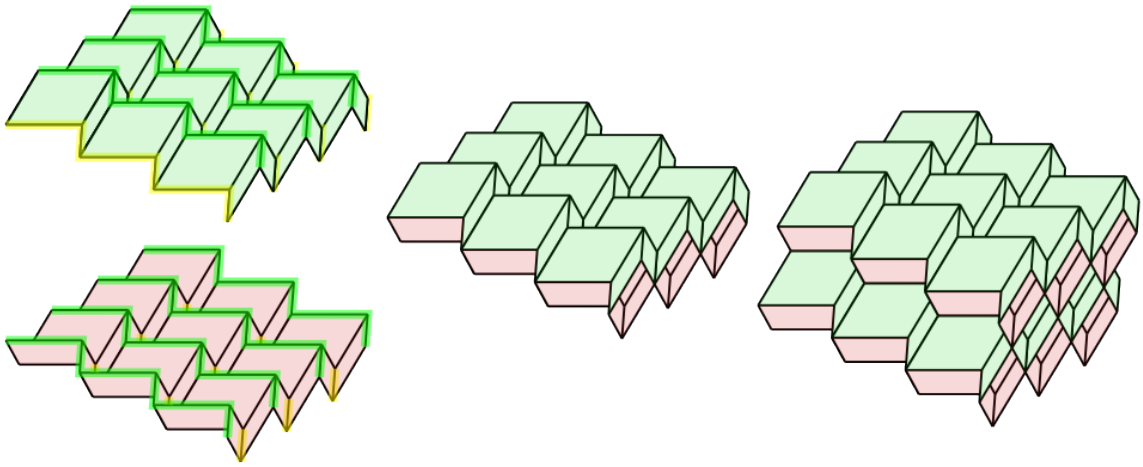
(a) (b)

Figure 3.17: Miura-ori tube unit:

(a) stacking a type-M on a type-V unit and (b) a physical model

Since the Miura-ori unit is crease-stackable, the classical Miura-ori pattern is also crease-stackable. In Figure 3.18(a), the type-M 3 × 3 classical Miura-ori pattern is stacked on the type-V 3 × 3 classical Miura-ori pattern. The yellow creases in the type-M sheet are attached to the corresponding green creases in the type-V sheet. The result is the 2-layer

stacked 3 × 3 classical Miura-ori pattern in Figure 3.18(b). Similarly, stacking two of these structures results in the 4-layer stacked 3 × 3 classical Miura-ori pattern in Figure 3.18(c). For any positive integers L, M, and N, stacking L sheets of the $M \times N$ Miura-ori pattern, which alternate between type-M and type-V sheets, results in the L-layer stacked $M \times N$ classical Miura-ori pattern. This stacked structure also consists of a lattice of Double 4Cs and Miura-ori tube units. Therefore, the stacked Miura-ori pattern is a flat-foldable and rigidly foldable structure with only one DOF.



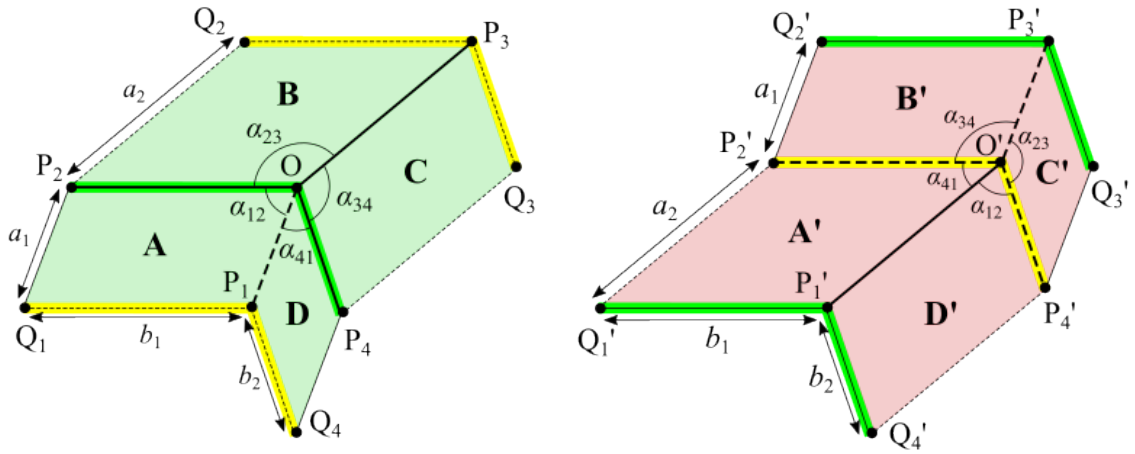
(a) (b) (c)

Figure 3.18: Stacking sheets of the 3 × 3 classical Miura-ori pattern:
(a) type-M and type-V sheets, (b) 2-layer structure, and (c) 4-layer structure

3.4.2 Crease-Stackable Generalized Miura-ori Pattern

The classical Miura-ori pattern is a flat-foldable, rigidly foldable, and crease-stackable origami tessellation. These properties also apply to the generalized Miura-ori pattern in which the 4Cs are identical and flat-foldable but not necessarily symmetric. The four creases in the 4C can be any length. The crease pattern of the generalized Miura-ori is a parallelogram tessellation with up to four distinct panels. Figure 3.19(a) shows a type-M

4-panel generalized Miura-ori unit used to assemble the generalized Miura-ori pattern. Figure 3.19(b) is the type-V version, in which the four panels in Figure 3.19(a) are rearranged, and the parity of each crease is flipped. Unlike the Miura-ori units for the classical Miura-ori pattern, the type-M and type-V generalized Miura-ori units are not mirror images of each other. Each unit is a flat-foldable 4C in which the panels are parallelograms, as shown in Figure 3.19. The crease lengths in the generalized 4C are a_1, b_1, a_2, and b_2. The sector angles and dihedral angles in the generalized Miura-ori unit correspond to those in the flat-foldable 4C in Figure 3.2, so equation (3.3) holds. For i = 1, 2, 3, and 4, the sector angle between OP_i and $OP_{(i+1)}$ is $\alpha_{i(i+1)}$, and the dihedral angle at OP_i is ϕ_i. When $i = 4$, every instance of $(i + 1)$ is replaced with 1. Therefore, the set of equations in (3.7) also describes the relations among the dihedral angles in the generalized Miura-ori unit.



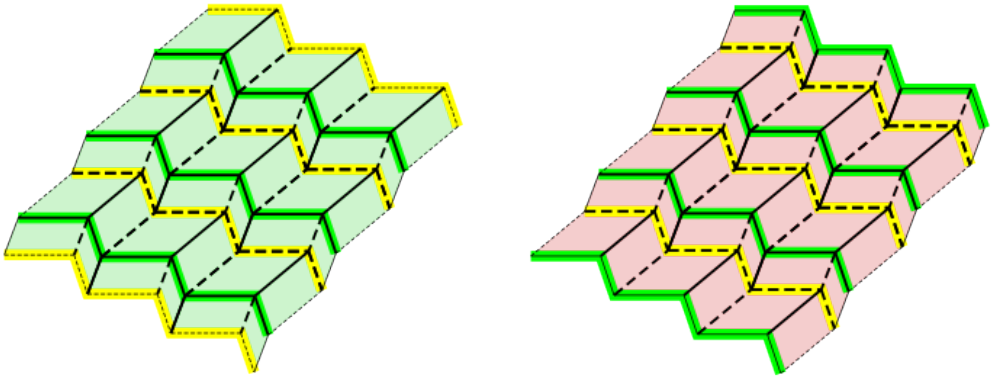
(a) (b)

Figure 3.19: Two generalized Miura-ori units: (a) type-M and (b) type-V

The generalized Miura-ori units in Figure 3.19 are flat-foldable and rigidly foldable with only one DOF. The type-M generalized Miura-ori unit is crease-stackable with the

type-V generalized Miura-ori unit because a set of creases on one unit can be attached to a set of creases on the other unit to form a rigidly foldable structure. For both units in Figure 3.19, the green and yellow creases indicate the upper and lower creases, respectively, that are used when stacking one unit on another.

Arranging the generalized Miura-ori units in a lattice forms the generalized Miura-ori pattern. For positive integers M and N, the $M \times N$ generalized Miura-ori pattern is a grid of generalized Miura-ori units that is M units long and N units wide. Figure 3.20(a) and Figure 3.20(b) are examples of 3×3 generalized Miura-ori patterns generated from copies of the type-M unit in Figure 3.19(a) and type-V unit in Figure 3.19(b), respectively. In both origami tessellations, the green and yellow creases form zigzags. These creases indicate the upper and lower creases used when stacking one sheet on another.



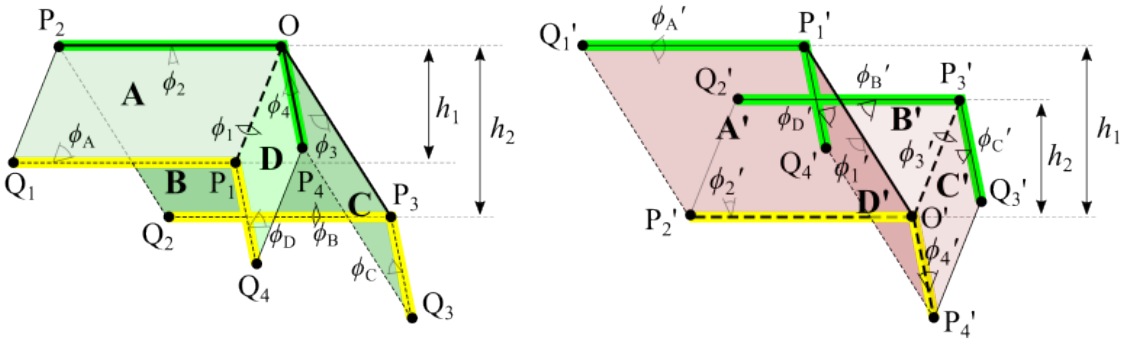
(a) (b)

Figure 3.20: Two 3×3 generalized Miura-ori crease patterns generated from (a) type-M units and (b) type-V units

The generalized Miura-ori tessellation is flat-foldable because every vertex in the crease pattern is a flat-foldable 4C. Also, as the origami tessellation folds, it does not collide with itself. To show that the generalized Miura-ori crease pattern is rigidly foldable, the

system of equations in (3.7) is applied to each vertex in the crease pattern. The result is a combined system of equations describing all dihedral angles in the crease pattern. The dihedral angle of every crease that lies on the horizontal zigzag lines in Figure 3.20 equals ϕ_1. The dihedral angle of every crease that lies on the vertical zigzag lines in Figure 3.20 equals ϕ_2. Given input angle ϕ_1, all remaining dihedral angles in the crease pattern are computed using the equations in (3.7). Therefore, the $M \times N$ generalized Miura-ori pattern is a flat-foldable and rigidly foldable origami tessellation with only one DOF.

Figure 3.21(a) and (b) show a type-M and type-V generalized Miura-ori unit, respectively, in a partially folded state. For the partially folded type-M unit in Figure 3.21(a), the green creases lie on a plane, the yellow creases on panels A and D lie on a parallel plane, and the yellow creases on panels B and C lie on another parallel plane. If this geometric property holds regardless of the partially folded state, then the type-M unit is crease-stackable with the type-V unit.



(a) (b)

Figure 3.21: Two generalized Miura-ori units in partially folded states:

(a) type-M and (b) type-V

The yellow creases on panels A and D lie on a unique plane. Let ϕ_A and ϕ_D be the angles between this plane and panels A and D, respectively, as shown in Figure 3.21(a). The yellow creases on panels B and C also lie on a unique plane. Let ϕ_B and ϕ_C be the angles between this plane and panels B and C, respectively, as shown in Figure 3.21(a). The proof showing that $\phi_A = \phi_B = \phi_C = \phi_D$ in the symmetric Miura-ori unit applies to the generalized Miura-ori unit as well. Therefore, the green creases lie on a plane, the yellow creases on panels A and D lie on a parallel plane, and the yellow creases on panels B and C lie on another parallel plane.

In Figure 3.21(a), the green and yellow creases in panel A are parallel, and the distance between them is $a_1(\sin\alpha_{12})$. Also, the green and yellow creases in panel B are parallel, and the distance between them is $a_2(\sin\alpha_{23})$. Let h_1 be the distance between the plane containing the two green creases and the plane containing the two yellow creases on panels A and D. Similarly, let h_2 be the distance between the plane containing the two green creases and the plane containing the two yellow creases on panels B and C. These two heights are expressed as:

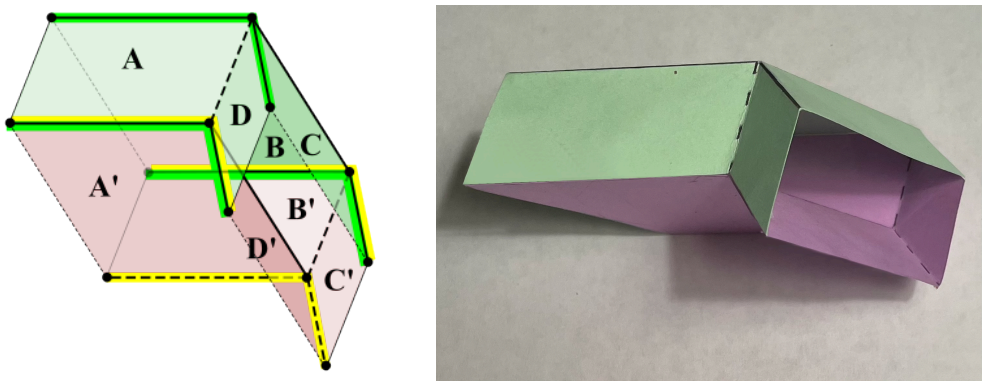
$$h_1 = \frac{a_1 \sin\alpha_{12}}{\sqrt{1+\left(\cos\alpha_{12}\tan\frac{\phi_1}{2}\right)^2}}, \quad h_2 = \frac{a_2 \sin\alpha_{23}}{\sqrt{1+\left(\cos\alpha_{23}\tan\frac{\phi_1}{2}\right)^2}}. \tag{3.23}$$

The height of the generalized Miura-ori unit in Figure 3.21(a) is the maximum height between h_1 and h_2. For the type-V unit in Figure 3.21(b), the values of h_1 and h_2 are swapped.

The following proof shows the type-M and type-V generalized Miura-ori units are crease-stackable with each other. The yellow creases on panels A and D on the type-M unit

are attached to the green creases on panels A' and D' on the type-V unit, respectively, as shown in Figure 3.21. Panels A, D, A', and D' form a 4C cone whose sector angles are α_{23}, α_{34}, α_{23}, and α_{34}. Since opposite sector angles are congruent, opposite dihedral angles are equal, so $\phi_1 = \phi_1'$. Since the type-M and type-V units are flat-foldable 4Cs, the equations in (3.7) imply that $\phi_2 = \phi_2'$ and $\phi_4 = \phi_4'$. Since panels A and B' are congruent, panels B and A' are congruent, and $\phi_2 = \phi_2'$, panels A, B, B', and A' form a parallelogram linkage. Since panels C and D' are congruent, panels C and D' are congruent, and $\phi_4 = \phi_4'$, panels C, D, D', and C' form a parallelogram linkage. Therefore, the yellow creases on panels B and C on the type-M unit are attached to the green creases on panels B' and C' on the type-V unit, respectively, showing that the type-M unit and type-V unit are crease-stackable with each other.

Stacking a type-M on a type-V generalized Miura-ori unit produces the generalized Miura-ori tube unit. The yellow creases in the type-M generalized Miura-ori unit in Figure 3.21(a) are attached to the green creases in the type-V generalized Miura-ori unit in Figure 3.21(b). The generalized Miura-ori tube unit in Figure 3.22 is a flat-foldable and rigidly foldable origami structure with only one DOF. The generalized Miura-ori tube unit is also the simplest unit of the generalized Miura-ori tube. Stacking the type-V unit on a type-M unit produces the Double 4C described earlier.



(a) (b)

Figure 3.22: Generalized Miura-ori tube unit:

(a) stacking a type-M on a type-V unit and (b) a physical model

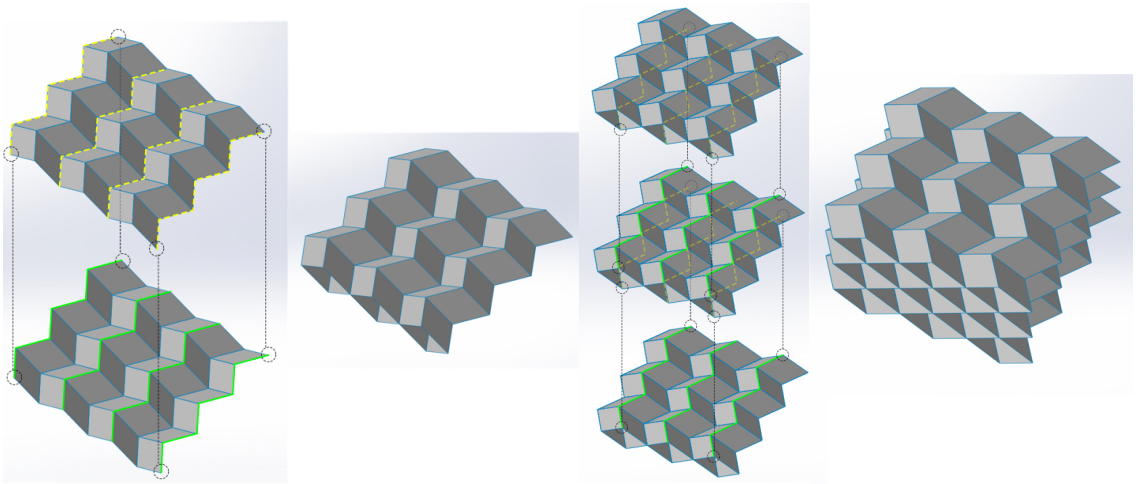
Since the generalized Miura-ori unit is crease-stackable, the generalized Miura-ori pattern is also crease-stackable. The same stacking method used in Figure 3.18 applies to the generalized Miura-ori pattern. For any positive integers L, M, and N, stacking L sheets of the $M \times N$ generalized Miura-ori pattern, which alternate between type-M and type-V sheets, results in the L-layer stacked $M \times N$ generalized Miura-ori pattern. This stacked structure also consists of a lattice of Double 4Cs and generalized Miura-ori tube units. Therefore, the stacked generalized Miura-ori pattern is a flat-foldable and rigidly foldable structure with only one DOF.

3.5 Stacking Miura-ori Patterns

3.5.1 Crease Stacking Miura-ori Patterns

There are a variety of methods to stack sheets of the Miura-ori pattern, resulting in a variety of stacked structures. The method used in Figure 3.18 is a form of crease stacking. Figure 3.23(a) and Figure 3.23(b) show the construction of the 2-layer stacked 3 × 3 Miura-

ori pattern and the 6-layer stacked 3 × 3 Miura-ori pattern, respectively. Each of these stacked structures alternate between type-M and type-V sheets. To construct the entire structure, each Miura-ori sheet is folded and then stacked along the highlighted creases in Figure 3.23. Regardless of the number of sheets used, the stacked Miura-ori pattern is bidirectionally flat-foldable and rigidly foldable with only one DOF.

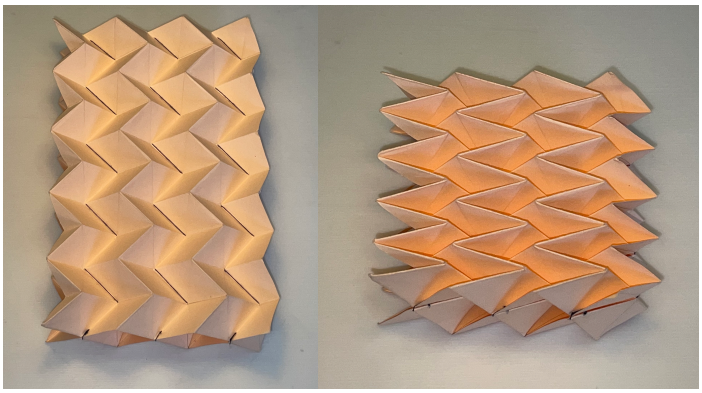


(a) (b)

Figure 3.23: Stacking pairs of type-M and type-V 3 × 3 Miura-ori sheets along their creases: (a) one pair and (b) three pairs

When constructing physical models, one method to attach sheets of the Miura-ori pattern is to sew them along the green and yellow highlighted creases in Figure 3.23. Figure 3.24 shows an example of two sheets of the Miura-ori pattern sewn together along the zigzag crease lines. Holes are made at the vertices, and the stitches trace the zigzag crease lines. Figure 3.24 shows this stacked Miura-ori pattern is flat-foldable and rigidly foldable. While it is a convenient method to construct stacked Miura-ori patterns, crease stacking comes with its limitations. The area of contact between sheets is relatively small as the

width of a crease is infinitesimal. A larger area of contact between sheets would make the connection between sheets stronger and more durable. Also, for the zigzag edges in Figure 3.23(a) that are on the boundaries of the sheets, overhanging flaps are needed so that the creases can be attached. For origami prototypes, crease stacking is a convenient method to construct stacked Miura-ori patterns and Miura-ori tubes.



(a) (b)

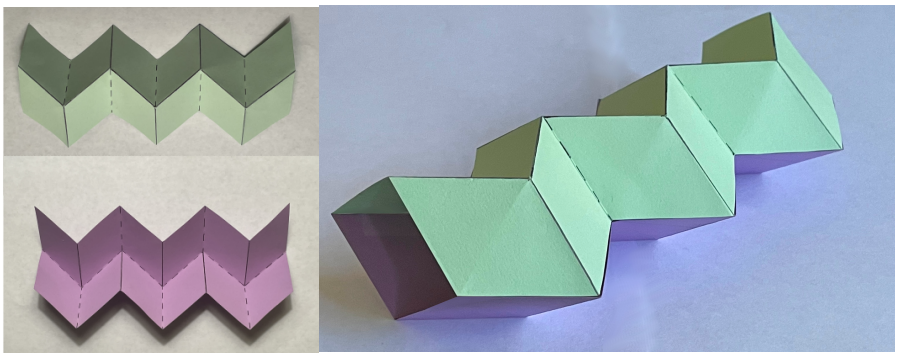
Figure 3.24: A 2-layer stacked Miura-ori pattern:

(a) partially folded state and (b) mostly folded state

3.5.2 Panel Stacking Miura-ori Tubes

The second method to stack sheets of the Miura-ori pattern is panel stacking. While crease stacking attaches two models along a set of creases, panel stacking attaches two models along a set of panels. Geometrically speaking, panel stacking two origami models means attaching a set of panels on one model to a set of panels on the other model such that corresponding boundary creases match. Crease stacking is used to construct Miura-ori tubes, but panel stacking is used to stack copies of Miura-ori tubes. Figure 3.25 shows the construction of the Miura-ori tube in which the ratio of each parallelogram's adjacent sides is 1. In Figure 3.25(a) the boundary zigzag edges in the type-M 1 × 3 Miura-ori sheet are

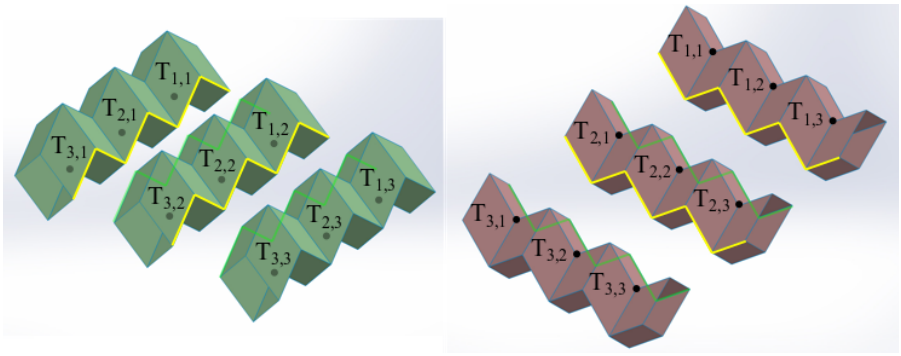
stacked on the boundary zigzag edges in the type-V 1 × 3 Miura-ori sheet. Copies of the Miura-ori tube in Figure 3.25(b) are arranged in layers as shown in Figure 3.26(a) and Figure 3.26(b). These two layers are arranged in perpendicular directions.



(a) (b)

Figure 3.25: Construction of Miura-ori tube:

(a) type-M and type-V 1 × 3 Miura-ori sheets and (b) 1 × 3 Miura-ori tube



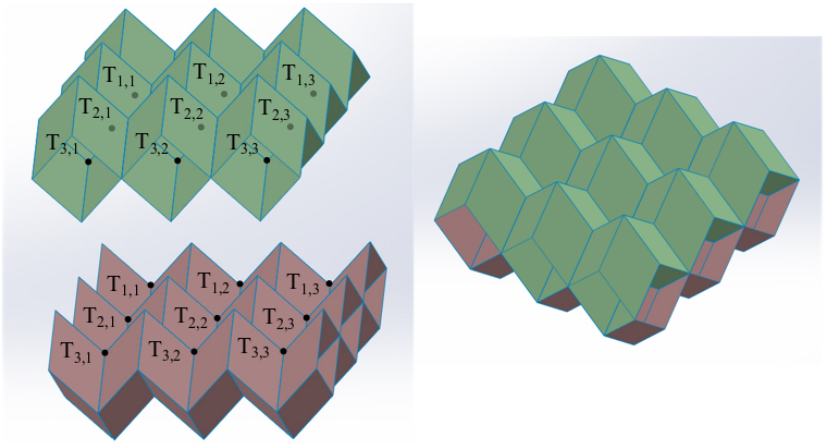
(a) (b)

Figure 3.26: Arranging Miura-ori tubes in two layers in perpendicular directions:

(a) three green tubes and (b) three red tubes

The Miura-ori tubes in Figure 3.26 are attached along their creases to form the layers in Figure 3.27(a). The upper and lower surfaces of these two layers are the non-developable egg box pattern (Schenk and Guest, 2011), which are the surfaces used for

panel stacking. These two layers are stacked to match each pair of corresponding panels. As shown in Figure 3.27(a), each labeled point on the green layer is attached to the corresponding labeled point on the red layer. Stacking the two layers in this manner results in the stacked egg box pattern in Figure 3.27(b), which is bidirectionally flat-foldable and rigidly foldable.



(a) (b)

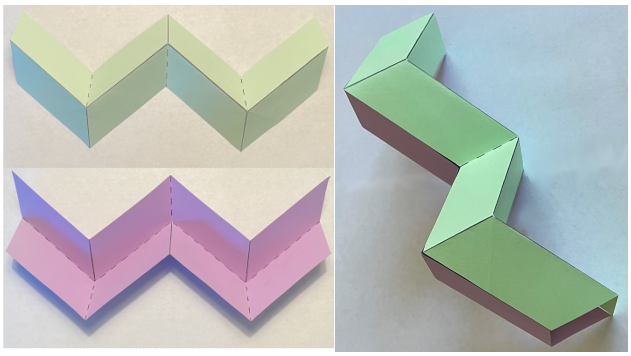
Figure 3.27: Stacking Miura-ori tubes along their panels:

(a) two Miura-ori tube layers and (b) stacked egg box pattern

Unlike crease stacking, panel stacking uses a larger area of contact, so the connection between layers is stronger. On the other hand, panel stacking assumes the thickness of the panels is negligible. When thickness of the sheet is considered, the areas of contact are misaligned. Also, not all crease-stackable origami tessellations can be stacked along their panels to form a different stacked structure. For instance, stacking identical Miura-ori sheets along their panels would result in the same pattern. Combining crease stacking with panel stacking results in more intricate stacked Miura-ori structures.

3.5.3 Weaving Miura-ori Tubes

The third method to stack sheets of the Miura-ori pattern is weaving, which combines crease stacking and panel stacking. Crease stacking aligns sets of creases while panel stacking aligns sets of panels. Weaving is a method that offsets the creases so that they remain collinear and offsets the panels so that they remain coplanar. This new stacking method is demonstrated using Miura-ori tubes. Figure 3.28 shows the construction of the Miura-ori tube in which the ratio of the parallelogram's sides is 2. In Figure 3.28(a) the boundary zigzag edges in the type-M 1 × 2 Miura-ori sheet are stacked on the boundary zigzag edges in the type-V 1 × 2 Miura-ori sheet. Each of the panels in the Miura-ori tube in Figure 3.28(b) can be split into two rhombi. Weaving the Miura-ori tubes involves aligning these rhombi.



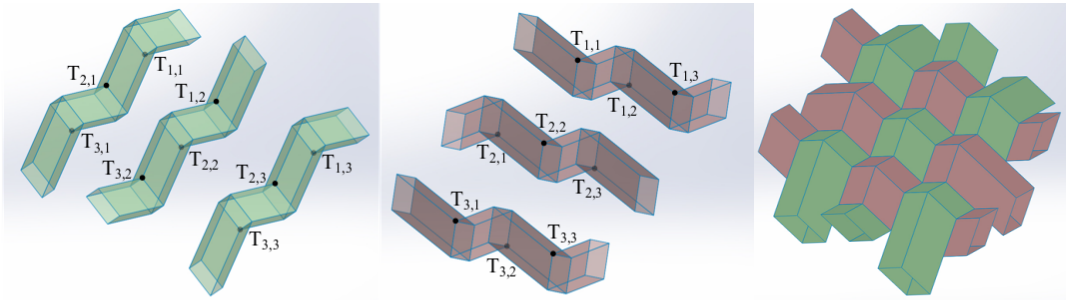
(a) (b)

Figure 3.28: Construction of Miura-ori tube:

(a) type-M and type-V 1 × 2 Miura-ori sheets and (b) 1 × 2 Miura-ori tube

Two layers of three Miura-ori tubes in parallel are arranged in perpendicular directions, as shown in Figure 3.29(a) and Figure 3.29(b). The green tubes are held in place while the red tubes are threaded over and under the green tubes. As shown in Figure 3.29(a)

and Figure 3.29(b), each labeled point on the green tubes is attached to the corresponding labeled point on the red tubes. These tubes are woven in a plain weave to obtain the 3 × 3 woven Miura-ori pattern in Figure 3.29(c). The intersection between a green tube and a perpendicular red tube is a 4C cone consisting of four congruent rhombi, and each panel of the Miura-ori tube is comprised of two of these rhombi. The labeled points in Figure 3.29(a) and Figure 3.29(b) are the vertices of these 4C cones, and each layer of tubes has the same arrangement of these 4C cones. Since each layer of tubes is flat-foldable and rigidly foldable, the woven Miura-ori pattern is as well.



(a) (b) (c)

Figure 3.29: Weaving Miura-ori tubes: (a) three green tubes, (b) three red tubes, and (c) the 3 × 3 woven Miura-ori pattern

The physical model of the 3 × 3 woven Miura-ori pattern in Figure 3.30 demonstrates bidirectionally flat-foldability and rigidly foldability. Weaving uses surfaces of panels as areas of contact, and the thickness of the panels is assumed to be negligible. When weaving the Miura-ori tubes, the panels are required to deform even though the woven structure is rigidly foldable. One advantage of weaving the Miura-ori tubes is that adhesives are not required to hold the Miura-ori tubes together. For origami prototypes, weaving is a convenient method to construct more intricate stacked Miura-ori structures.

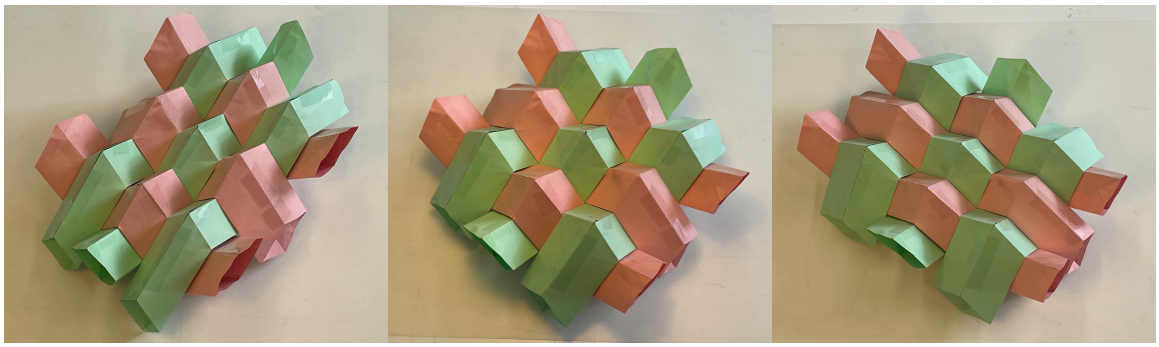


Figure 3.30: Physical model of a 3 × 3 woven Miura-ori pattern in partially folded states

3.6 Conclusion

This chapter analyzes the geometry and kinematics of flat-foldable and rigidly foldable 4C origami tessellations, each of which is either the classical Miura-ori pattern or a generalized version of the Miura-ori pattern. The focus is on origami tessellations that are flat-foldable because this property simplifies the equations describing the geometry of 4Cs. These equations help show that certain 4C origami tessellations are rigidly foldable and crease-stackable, which is a geometric property defined in this chapter. Origami researchers have stacked sheets of the Miura-ori pattern to form stacked origami structures, but there was no standard convention to stack sheets of origami tessellations until now (Ma et al., 2018; Cheung et al., 2014). Examining the generalized flat-foldable 4C reveals the geometric properties that make 4C origami tessellations crease-stackable. This approach is not exhaustive as not all crease-stackable origami tessellations are flat-foldable. Nonetheless, the 4C origami tessellations shown in this chapter demonstrate how the Miura-ori pattern can be generalized while remaining crease-stackable.

Each vertex in the crease pattern of a generalized Miura-ori pattern is a flat-foldable 4C whose kinematic equations are determined using the matrix method. When the four

dihedral angles are numbered in clockwise order, the derived equations state that $\phi_1 = \phi_3$ and $\phi_2 = \phi_4$ for any flat-foldable 4C. These angle relations are demonstrated in the construction of the Double 4C, which attaches two identical flat-foldable 4Cs by crease stacking. An examination of the 4-bar mechanisms in the Double 4C reveals it is composed of scissor mechanisms. In each scissor mechanism, opposite pairs of panels are coplanar. In addition, a geometric proof on the circular flat-foldable 4C shows that there exist four vertices on the circular boundary that are always coplanar. This coplanarity property is what makes the generalized Miura-ori pattern crease-stackable.

Given the origami flat-foldable 4C, the thick-panel version is constructed. Each panel in the origami model is given thickness to form the thick-panel flat-foldable 4C. The kinematic equations for the thick-panel flat-foldable 4C match those of the Bennett linkage. Two copies of the thick-panel flat-foldable 4C are combined to form the thick-panel Double 4C. The kinematic equations describing the dihedral angles in the thick-panel Double 4C match those of its origami counterpart. An examination of the 4-bar mechanisms in the thick-panel Double 4C reveals it is composed of parallelogram linkages. In each parallelogram linkage, opposite dihedral angles are equal. The construction of these thick-panel structures could inspire the design of thick-panel versions of generalized Miura-ori patterns.

Geometric proofs show the classical Miura-ori pattern is flat-foldable and rigidly foldable with only one DOF. The generalized Miura-ori pattern also possesses these properties. Another geometric proof shows that the classical Miura-ori crease pattern contains two sets of coplanar creases on zigzag lines that lie on two parallel planes. This geometric property holds regardless of the partially folded state, which proves the classical

Miura-ori pattern is crease-stackable. A similar geometric proof shows that the generalized Miura-ori pattern is crease-stackable as well. Crease stacking is used to assemble the L-layer stacked $M \times N$ Miura-ori pattern from identical sheets of the Miura-ori pattern. This stacked structure is a mechanical metamaterial whose mechanical properties can be further studied. The coplanarity property found in these origami tessellations is sufficient but not necessary to show they are crease-stackable. This approach does not consider crease-stackable origami tessellations that stack along sets of creases that are not coplanar. Future research may show certain arc-shaped Miura-ori patterns are crease-stackable (Gattas et al., 2013).

Finally, three methods to stack the Miura-ori pattern are demonstrated. Crease stacking attaches sheets of the Miura-ori pattern along their creases while panel stacking attaches sheets of the Miura-ori pattern along their panels. Crease stacking is the more convenient stacking method while panel stacking uses a larger area of contact between Miura-ori sheets. Weaving Miura-ori tubes uses both crease stacking and panel stacking. The woven Miura-ori pattern weaves Miura-ori tubes in a plain weave, which is a structure that cannot be achieved through crease stacking alone. These three methods of stacking demonstrate the variety of stacked origami structures that can be constructed from sheets of the Miura-ori pattern. Since identical copies of the Miura-ori pattern are used, the stacked structures in this chapter are bidirectionally flat-foldable. Past research has shown distinct layers of the Miura-ori pattern can stack to form self-locking stacked structures (Schenk and Guest, 2013a). Further research is needed to determine whether the stacked egg box pattern and woven Miura-ori pattern are achievable using distinct sheets of the Miura-ori pattern.

4

Origami Claw Tessellation (OCT)

4.1 Introduction

Many classical origami tessellations that are flat-foldable and rigidly foldable are 4C origami tessellations, which are derivatives of the Miura-ori pattern (Yellowhorse et al., 2018; Evans et al., 2015). Their crease patterns are topologically equivalent to that of the Miura-ori pattern, restricting each of them to one DOF (Gattas et al., 2013; Sareh and Guest, 2015a). On the other hand, there are other origami tessellations that are comprised of higher-degree vertices, some of which are flat-foldable and rigidly foldable with multiple DOFs (Tachi, 2009; Schenk and Guest, 2011). The natural question that arises is whether there exists an origami tessellation that is not only flat-foldable and rigidly foldable with multiple DOFs but also crease-stackable. This chapter presents an origami tessellation called the origami claw tessellation, OCT, that satisfies these criteria. The OCT is an origami tessellation that combines both 4Cs and 6Cs in its crease pattern (Xing and You, 2022). This hybrid design gives the OCT multiple DOFs while preserving important geometric properties found in the Miura-ori pattern. Stacking copies of the OCT along sets of creases forms the stacked OCT. Since the OCT has multiple DOFs, the creases can be attached a few at a time when stacking the layers, which is an advantage over crease-stackable 4C origami tessellations. Even though the OCT has multiple DOFs, the stacked OCT has only one DOF.

This chapter has the following layout. Section 4.2 examines the geometry and kinematics of the OCT's crease pattern. Kinematic analysis on the claw unit, the basic unit

of the OCT, shows it is crease-stackable. Each OCT is an $M \times N$ grid of claw units for some positive integers M and N. Section 4.3 uses a numerical method alongside the matrix method to compute the number of DOFs in the OCT. For any positive integers M and N greater than or equal to 2, the $M \times N$ OCT has five DOFs. Each of these five DOFs are described geometrically. Section 4.4 shows that two claw units can stack to form the stacked claw unit. Interestingly, while the claw unit has three DOFs, the stacked claw unit has only one DOF. The $M \times N$ OCT is also crease-stackable, and multiple copies of OCTs can stack to obtain the stacked OCT, reducing the number of DOFs from five to one. Section 4.5 discusses distinct claw units that are crease stackable with each other. The term family is used to describe a set of such claw units. Stacking OCTs in the same family results in a self-locking structure. Section 4.6 is a discussion of the origami models constructed.

4.2 Origami Claw Tessellation (OCT)

The crease pattern of OCT consists of both 4Cs and 6Cs. Each 4C is identical, and so is each 6C. The OCT is composed of copies of a flat-foldable 6C called the claw unit. The claw unit contains six panels, and their geometry depends on angles, α and β, and side lengths, a_1, a_2, a_3, and a_4, as shown in Figure 4.1. The following restriction is imposed:

$$0 < \alpha < \beta < \frac{\pi}{2}. \tag{4.1}$$

As shown in Figure 4.1, the sector angles of the claw unit are expressed in terms of α and β: $\alpha_{12} = (\beta - \alpha)$, $\alpha_{23} = (\pi - \beta - \alpha)$, $\alpha_{34} = (\pi - \beta)$, $\alpha_{45} = \alpha$, $\alpha_{56} = \alpha$, and $\alpha_{61} = \beta$. The law of sines imposes the following restriction on the side lengths:

$$\frac{a_1}{\sin(\beta-\alpha)} = \frac{a_2}{\sin(\beta+\alpha)} = \frac{a_3}{\sin(\alpha)} = \frac{a_4}{\sin(\beta)}. \tag{4.2}$$

The relations in (4.2) imply that given angles α and β and side length a_1, the geometry of the claw unit is uniquely determined. In Figure 4.1, the angles are $\alpha = \pi / 6$ and $\beta = \pi / 3$, and the side lengths are $a_1 = 1$, $a_2 = 2$, $a_3 = 1$, and $a_4 = 1.7321$. Panels A and D are congruent triangles, panels B and E are congruent triangles, and panels C and F are equiangular parallelograms. The claw unit in Figure 4.1 is a type-M claw unit because it contains four mountain creases and two valley creases. In a type-V claw unit, the parities of the creases in Figure 4.1 are flipped.

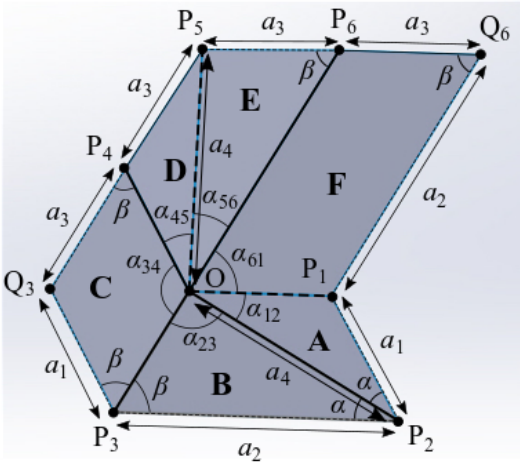


Figure 4.1: Claw unit with $\alpha = \pi / 6$ and $\beta = \pi / 3$

Unlike the classical Miura-ori unit, the claw unit is not symmetric, so the type-M claw unit and the type-V claw unit each have two different orientations. This results in four different types of claw units: type-M1, type-M2, type-V1, and type-V2, which are shown in Figure 4.2(a – d), respectively. In each of these claw units, creases highlighted in green or yellow indicate creases that lie in one of two parallel planes. The green creases lie in the upper plane, and the yellow creases lie in the lower plane. This geometric property makes

the type-M1 and type-M2 claw units crease-stackable with the type-V1 and type-V2 claw units, respectively, which will be shown in a geometric proof later in this section.

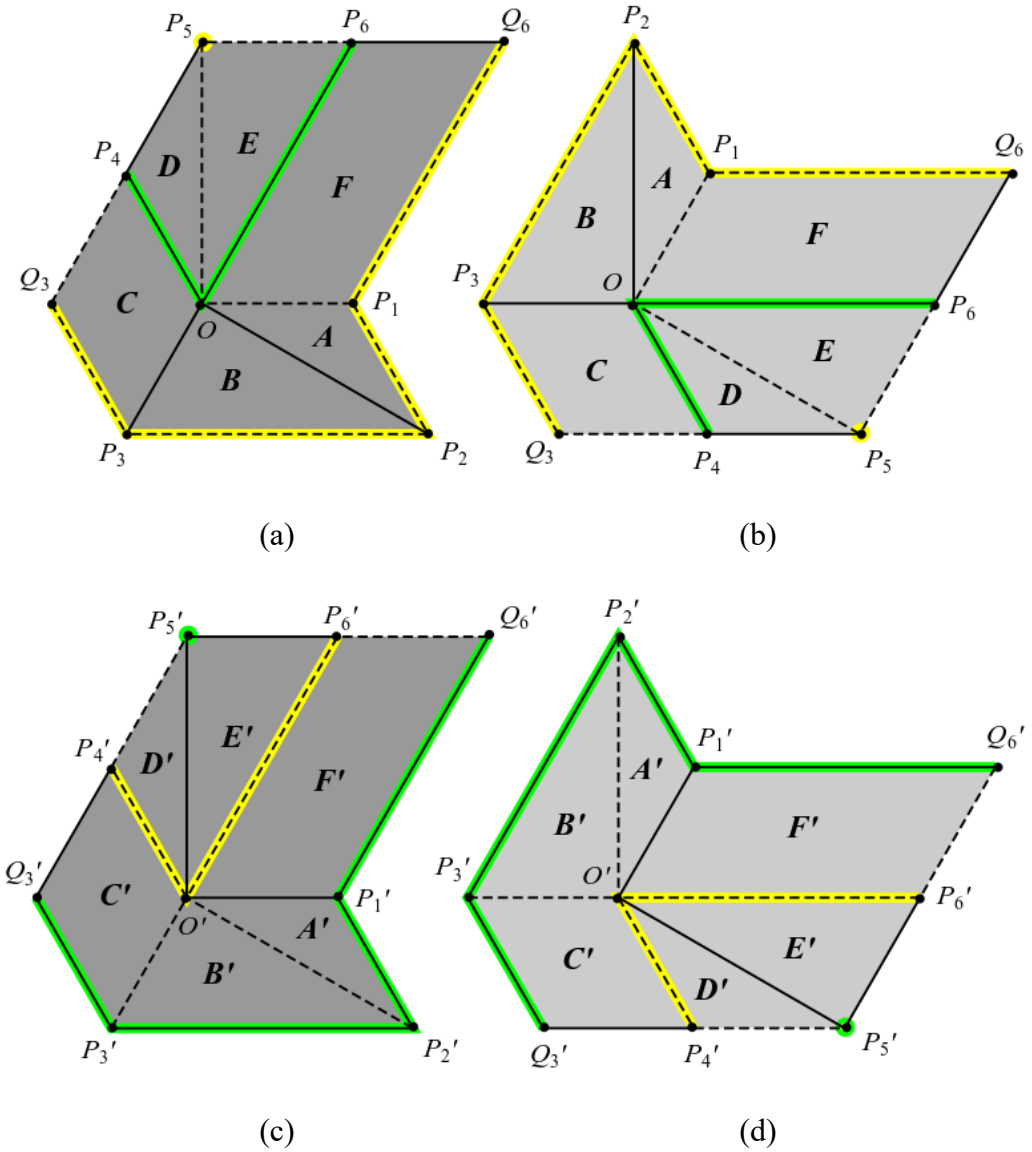


Figure 4.2: Four types of claw units:

(a) type-M1, (b) type-M2, (c) type-V1, and (d) type-V2

The type-M OCT consists of type-M1 and type-M2 claw units while the type-V OCT consists of type-V1 and type-V2 claw units. The type-M OCT in Figure 4.3 shows

the type-M1 and type-M2 claw units arranged in a grid. No two type-M1 claw units share a crease, and neither do any two type-M2 claw units. For any positive integers M and N, the $M \times N$ OCT is M claw units long and N claw units wide. Figure 4.3 shows a 4 × 4 OCT with type-M1 and type-M2 claw units shaded in a checkerboard pattern with one of the type-M1 claw units labeled.

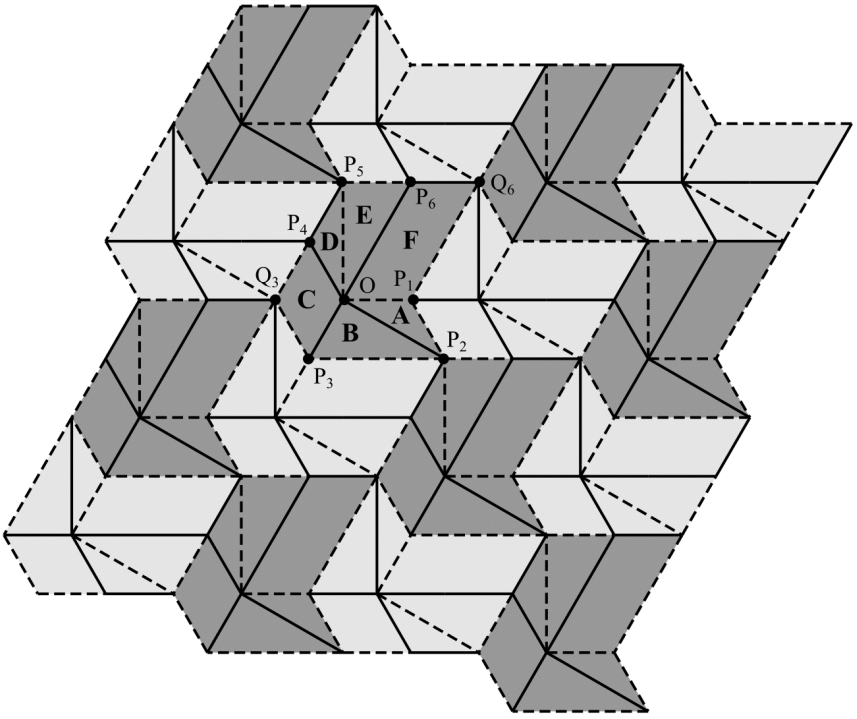


Figure 4.3: A 4 × 4 OCT

For each 4C and 6C in the OCT, the absolute difference between the number of mountain creases and valley creases incident to the vertex is always 2, so Maekawa's theorem is satisfied. The sector angles in each 4C are β, $(\pi - \beta)$, $(\pi - \beta)$, and β, and the sector angles in each 6C are $(\beta - \alpha)$, $(\pi - \beta - \alpha)$, $(\pi - \beta)$, α, α, and β, so Kawasaki's theorem is satisfied. Therefore, each 4C and 6C is flat-foldable. Figure 4.4 shows a 2 × 2 OCT folding from its flat unfolded state, I, to its flat folded state, V, showing the OCT does not

collide with itself as it folds. Figure 4.4 also demonstrates the OCT is rigidly foldable, which is proven by examining the relations among the dihedral angles of the creases.

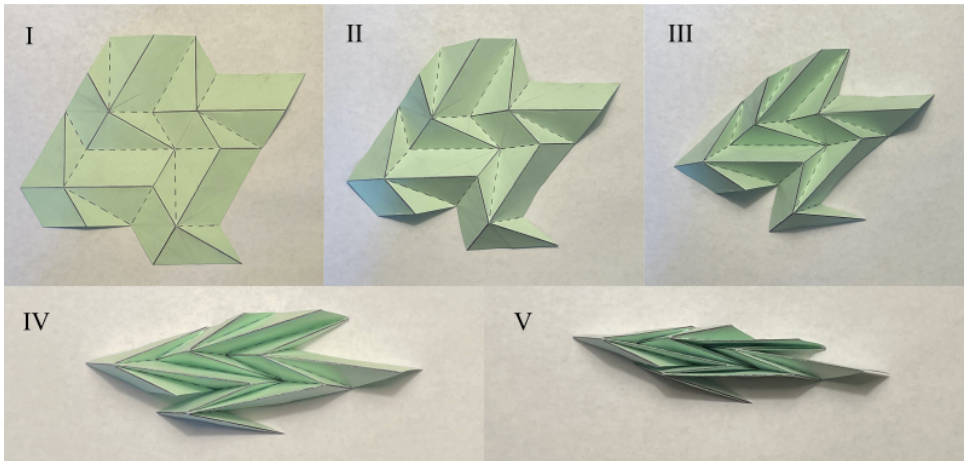


Figure 4.4: A 2 × 2 OCT rigidly folding

A 4C lies between any two adjacent claw units in an OCT, as shown in Figure 4.3. The OCT's 4C is composed of four panels found in the claw unit in Figure 4.1. Using the parameters for the claw unit, the sector angles in the 4C are β, $(\pi - \beta)$, $(\pi - \beta)$, and β, which are also the sector angles of the classical Miura-ori unit. Figure 4.5 shows a 4C in a partially folded state with its dihedral angles labeled. The closure equations for the 4C gives the following system of equations:

$$\phi_1 = \phi_3, \;\; \phi_2 = \phi_4, \;\; \cos\beta \tan\frac{\phi_1}{2} = \tan\frac{\phi_2}{2}. \tag{4.3}$$

Appendix A shows the derivation of the equations in (4.3). Given input angle ϕ_1, the three remaining dihedral angles in the 4C are computed using the equations in (4.3). Figure 4.6 shows a graph of the angle relations in the 4C with $\alpha = \pi / 6$ and $\beta = \pi / 3$ according to (4.3) with ϕ_1 as the input angle.

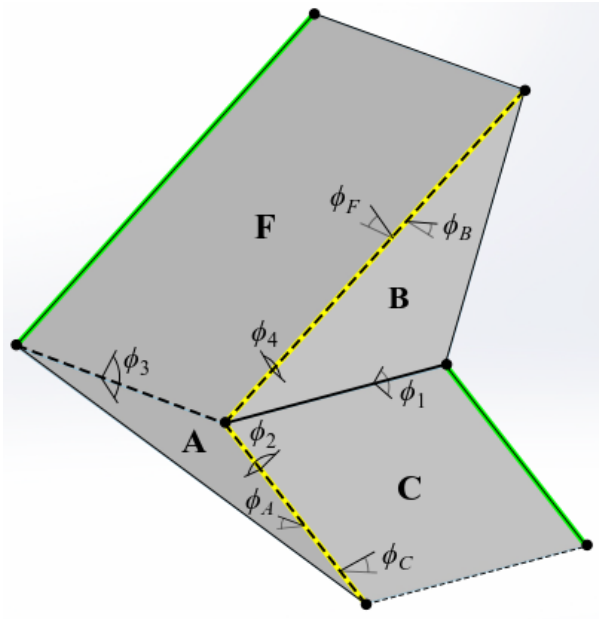


Figure 4.5: The OCT's 4C in a partially folded state

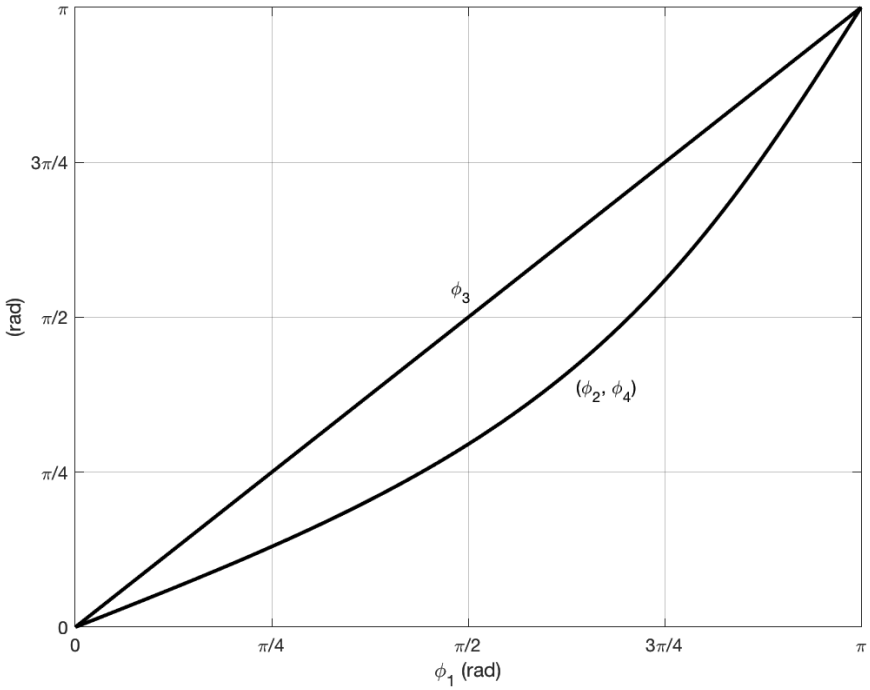


Figure 4.6: Dihedral angle relations in the OCT's 4C with $\alpha = \pi / 6$ and $\beta = \pi / 3$

The following proof shows that for the 4C in Figure 4.5, the green creases lie on a plane, and the yellow creases also lie on a parallel plane. The following are the dihedral

angles in the 4C and their respective pair of adjacent panels: ϕ_1 lies between B and C, ϕ_2 lies between A and C, ϕ_3 lies between A and F, and ϕ_4 lies between B and F. The two yellow creases lie on a unique plane. Let ϕ_A, ϕ_B, ϕ_C, and ϕ_F be the angles between this plane and panels A, B, C, and F, respectively, as shown in Figure 4.5. By symmetry of the sector angles, the following dihedral angle equalities hold: $\phi_A = \phi_F$ and $\phi_B = \phi_C$. By spherical law of cosines, the following equations hold:

$$\tan\phi_A = \left(\cos\beta\tan\frac{\phi_3}{2}\right)^{-1},\ \tan\phi_B = \left(\cos\beta\tan\frac{\phi_1}{2}\right)^{-1}. \tag{4.4}$$

Since $\phi_1 = \phi_3$, the equations in (4.4) imply that $\phi_A = \phi_B = \phi_C = \phi_F$. The green and yellow creases in panel C are parallel, and the distance between them is $a_3(\sin\beta)$. Similarly, the green and yellow creases in panel F are parallel, and the distance between them is also $a_3(\sin\beta)$. Therefore, the two green creases lie on a plane, and the two yellow creases lie on a parallel plane. Since this geometric property always holds, the type-M 4C is crease-stackable with the type-V 4C.

Each claw unit is a 6C whose sector angles are $(\beta - \alpha)$, $(\pi - \beta - \alpha)$, $(\pi - \beta)$, α, α, and β. Figure 4.7 shows an example of a claw unit in a partially folded state with its dihedral angles labeled. The closure equations for the 6C gives a 3-DOF system of equations, which are equations (C.4), (C.5), and (C.6) derived in Appendix C. Suppose the following dihedral angle equalities hold: $\phi_1 = \phi_3$ and $\phi_2 = \phi_5$. Equations (C.4), (C.5), and (C.6) in Appendix C can be simplified to the following 1-DOF system of equations:

$$\phi_1 = \phi_3,\ \phi_2 = \phi_5, \phi_4 = \phi_6,\ \cos\beta\tan\frac{\phi_1}{2} = \cos\alpha\tan\frac{\phi_2}{2} = \tan\frac{\phi_4}{2}. \tag{4.5}$$

Given input angle ϕ_1, the five remaining dihedral angles in the claw unit are computed using the equations in (4.5). Figure 4.8 shows a graph of the angle relations in the claw unit with $\alpha = \pi / 6$ and $\beta = \pi / 3$ according to (4.5) with ϕ_1 as the input angle.

The kinematic motions of the claw unit resemble those of the flat-foldable 4C because of shared geometric properties. If panels C and D were a single flat panel, and panels E and F were a single flat panel, then the model in Figure 4.7 would become a flat-foldable 4C with dihedral angles, ϕ_1, ϕ_2, ϕ_3, and ϕ_5. Here, the crease with dihedral angle ϕ_5 would be a mountain instead of a valley. The claw unit in Figure 4.7 would become a flat-foldable type-M 4C whose sector angles are $(\beta - \alpha)$, $(\pi - \beta - \alpha)$, $(\pi - \beta + \alpha)$, and $(\beta - \alpha)$. Equations $\phi_1 = \phi_3$ and $\phi_2 = \phi_5$ would hold, which are the angle equalities used to obtain the system of equations in (4.5). In short, the claw unit in Figure 4.7 can be converted to a flat-foldable 4C by inverting the parity of the crease between panels D and E while panels A, B, C, and F remain fixed. If the yellow and green creases lie on parallel planes for the flat-foldable 4C, then the same geometric property holds for the claw unit.

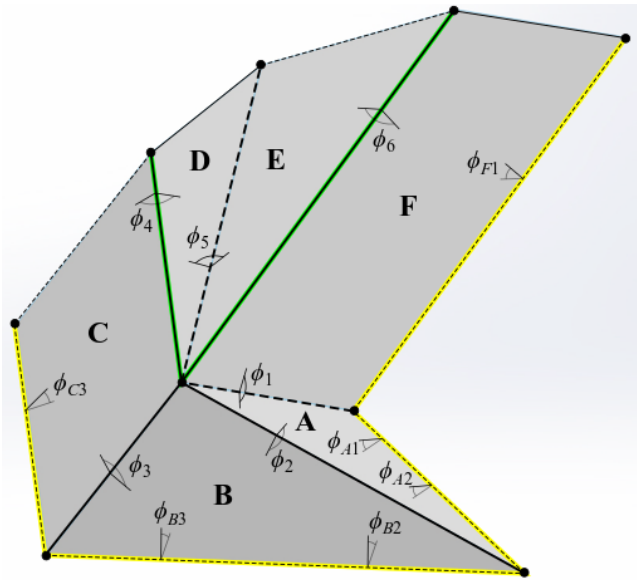


Figure 4.7: Claw unit in a partially folded state

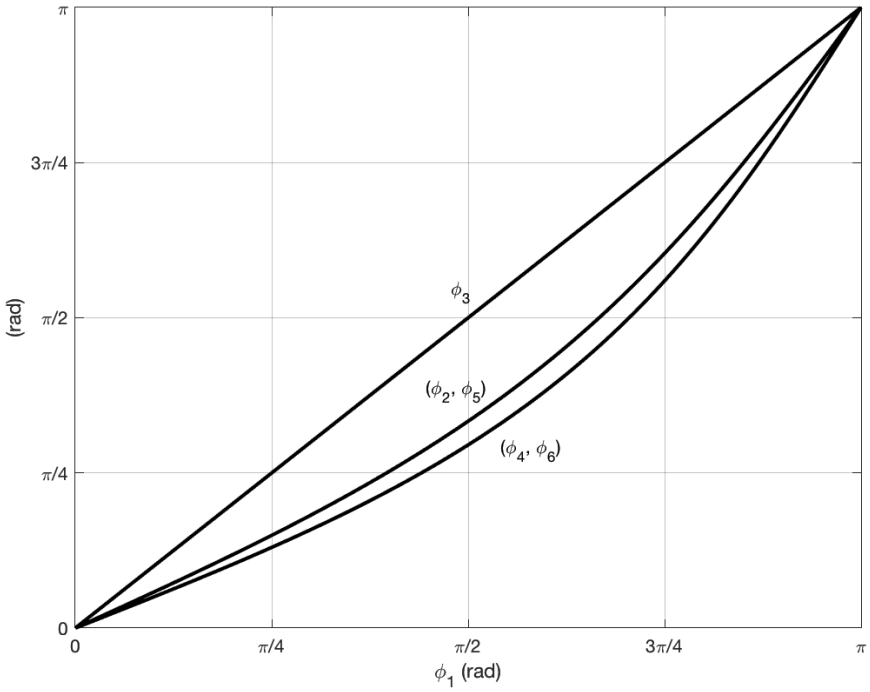


Figure 4.8: Dihedral angle relations in the claw unit with $\alpha = \pi / 6$ and $\beta = \pi / 3$ according to the equations in (4.5)

The following proof shows that when the claw unit in Figure 4.7 folds according to the equations in (4.5), the green creases lie on a plane, and the yellow creases also lie on a parallel plane. The following are the dihedral angles in the 4C and their respective pairs of adjacent panels: ϕ_1 lies between A and F, ϕ_2 lies between A and B, ϕ_3 lies between B and C, ϕ_4 lies between C and D, ϕ_5 lies between D and E, and ϕ_6 lies between E and F. The yellow creases on panels A and F lie on a unique plane. Let ϕ_{A1} and ϕ_{F1} be the angles between this plane and panels A and F, respectively, as shown in Figure 4.7. When the claw unit in Figure 4.7 is folded according to the equations in (4.5), by symmetry of the sector angles, the dihedral angle equality, $\phi_{A1} = \phi_{F1}$, holds. By spherical law of cosines, the following equation holds:

$$\tan\phi_{A1} = \left(\cos\beta \tan\frac{\phi_1}{2} \right)^{-1}. \tag{4.6}$$

The yellow creases on panels A and B lie on a second unique plane. Let ϕ_{A2} and ϕ_{B2} be the angles between this plane and panels A and B, respectively, as shown in Figure 4.7. By symmetry of the sector angles, the dihedral angle equality, $\phi_{A2} = \phi_{B2}$, holds. By spherical law of cosines, the following equation holds:

$$\tan\phi_{A2} = \left(\cos\alpha \tan\frac{\phi_2}{2} \right)^{-1}. \tag{4.7}$$

The yellow creases on panels B and C lie on a third unique plane. Let ϕ_{B3} and ϕ_{C3} be the angles between this plane and panels B and C, respectively, as shown in Figure 4.7. By symmetry of the sector angles, the dihedral angle equality, $\phi_{B3} = \phi_{C3}$, holds. By spherical law of cosines, the following equation holds:

$$\tan\phi_{B3} = \left(\cos\beta \tan\frac{\phi_3}{2} \right)^{-1}. \tag{4.8}$$

Equations (4.5), (4.6), (4.7), and (4.8) imply that $\phi_{A1} = \phi_{A2} = \phi_{B2} = \phi_{B3} = \phi_{C3} = \phi_{F1}$. The green and yellow creases in panel C are parallel, and the distance between them is $a_3(\sin\beta)$. Similarly, the green and yellow creases in panel F are parallel, and the distance between them is also $a_3(\sin\beta)$. Therefore, the two green creases lie on a plane, and the four yellow creases lie on a parallel plane. The reflection of the type-M1 claw unit in Figure 4.7 about the plane containing its yellow creases is the type-V1 claw unit. This reflection stacks the type-M1 unit on the type-V1 unit. Since this geometric property always holds, the type-M1 claw unit is crease-stackable with the type-V1 claw unit. Similarly, the type-M2 claw unit is crease-stackable with the type-V2 claw unit. Furthermore, since the OCT's 4C and claw unit are crease-stackable, the OCT is crease-stackable as well.

The following proof shows that the OCT has at least one rigidly foldable mode. The OCT in Figure 4.3 will be used as an example. The system of equations in (4.3) and (4.5) are applied to each 4C and 6C, respectively, in the OCT. Both (4.3) and (4.5) are 1-DOF systems of equations. Let ϕ_1, the dihedral angle in the claw unit shown in Figure 4.7, be the input for the labeled claw unit in the OCT in Figure 4.3. Dihedral angles ϕ_1 is the input for the 6C at vertex O, and the remaining dihedral angles, ϕ_2, ϕ_3, ϕ_4, ϕ_5, and ϕ_6, are determined using (4.5). These dihedral angles serve as inputs for adjacent vertices.

Dihedral angles ϕ_1, ϕ_3, ϕ_4, and ϕ_6 are the inputs for the 4Cs at vertices P_1, P_3, P_4, and P_6, respectively. Their remaining dihedral angles are determined using (4.3). Dihedral angles ϕ_2 and ϕ_5 are the inputs for the 6Cs at vertices P_2 and P_5, respectively, and these inputs are compatible with the known dihedral angles. Their remaining dihedral angles are determined using (4.5). Vertices P_3 and P_4 each share one dihedral angle with vertex Q_3, and these dihedral angles are compatible inputs. The remaining dihedral angles of the 6C at Q_3 are determined using the system of equations in (4.5). Vertices P_6 and P_1 each share one dihedral angle with vertex Q_6, and these dihedral angles are compatible inputs. The remaining dihedral angles of the 6C at Q_6 are determined using the system of equations in (4.5). To determine the remaining dihedral angles in the OCT, the previous operations can be performed on adjacent vertices using the system of equations in (4.3) and (4.5) because all input dihedral angles used are compatible. Therefore, input dihedral angle ϕ_1 determines all remaining dihedral angles in the OCT, so the OCT has at least one DOF.

The above proof applies to OCTs of any size. Input dihedral angle ϕ_1 ranges from 0 to π, and when ϕ_1 equals 0 and π, all remaining dihedral angles equal 0 and π, respectively. Therefore, for any positive integers M and N, the $M \times N$ OCT is a flat-foldable and rigidly

foldable origami tessellation with at least one DOF. The one DOF corresponding to the system of equations in (4.3) and (4.5) is the planar folding mode. When the OCT folds according to the planar folding mode, the green and yellow creases in each claw unit, as shown in Figure 4.2, lie on two coplanar planes. When two sheets of the OCT are stacked along their creases, they form the stacked OCT. The stacked OCT folds with only one DOF, the planar folding mode, which will be demonstrated later.

4.3 Computing DOFs of OCT

Even though the $M \times N$ OCT is rigidly foldable with at least one DOF, the exact number of DOFs needs to be computed. Gan and Pellegrino implemented a numerical method to calculate the DOFs in mechanical linkages (Gan and Pellegrino, 2006). A modified numerical method is used to calculate the number of DOFs in the OCT. The numerical method not only computes the number of DOFs in the OCT but also describes each degree of mobility geometrically.

For any positive integers M and N, the $M \times N$ OCT is comprised of v vertices and c creases, in which $v = (4MN - 2M - 2N + 1)$ and $c = (10MN - 2M - 2N)$. Appendix D details the types of vertices and creases in the OCT. Figure 4.9 shows a 2×2 OCT with $\alpha = \pi / 6$ and $\beta = \pi / 3$ and its vertices and creases numbered. The vector of c dihedral angles, ϕ, in which $\phi = (\phi_1, \phi_2, \ldots, \phi_c)^T$ and ϕ_i is the dihedral angle of crease i for $1 \leq i \leq c$, uniquely determines the partially folded state of the OCT. The fold angle, θ_i, of each crease depends on the crease's parity. Let $\theta_i = \phi_i - \pi$ if crease i is a mountain, and $\theta_i = \pi - \phi_i$ if crease i is a valley. The vector of fold angles, $\theta = (\theta_1, \theta_2, \ldots, \theta_c)^T$, also uniquely determines the partially folded state of the OCT. The numerical method starts with an initial partially folded state

in which $0 < \theta_i < \pi$ for $1 \le i \le c$. For the initial state of the $M \times N$ OCT, let $\phi_4 = \pi / 2$. The remaining dihedral angles are computed using the equations in (4.3) and (4.5). Each fold angle is obtained as described earlier, so the initial state is represented by θ.

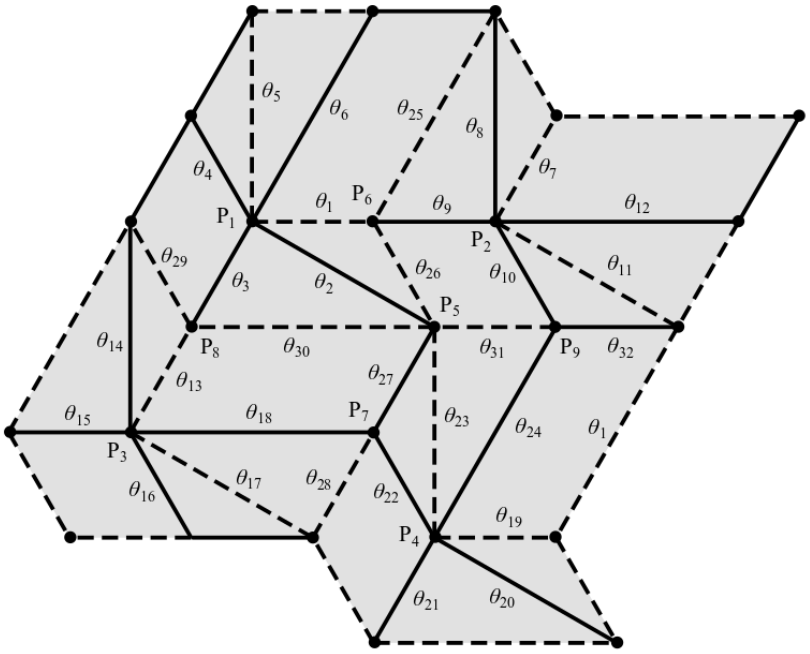


Figure 4.9: Numbering of creases and vertices in the 2 × 2 OCT

The numerical method uses the matrix method on each vertex in the crease pattern. Consider a single vertex, P_1, which is a 6C. For $i = 1, 2, 3, 4, 5$, and 6 the sector angles are $\alpha_{i(i+1)}$, and the fold angles are θ_i. When $i = 6$, every instance of $(i + 1)$ is replaced with 1. The matrix method uses the following transformation matrices:

$$Q\left(\alpha_{i(i+1)},\theta_i\right)=\begin{pmatrix} \cos\theta_i & \cos\alpha_{i(i+1)}\sin\theta_i & \sin\alpha_{i(i+1)}\sin\theta_i \\ -\sin\theta_i & \cos\alpha_{i(i+1)}\cos\theta_i & \sin\alpha_{i(i+1)}\cos\theta_i \\ 0 & -\sin\alpha_{i(i+1)} & \cos\alpha_{i(i+1)} \end{pmatrix}. \tag{4.9}$$

The following closure equation holds for vertex P_1:

$$\prod_{i=1}^{6} Q\left(\alpha_{i(i+1)}, \theta_i\right) = I_{3\times3}. \tag{4.10}$$

Here, $I_{3\times3}$ is the 3 × 3 identity matrix. Each vertex in the OCT generates a closure equation in the same form as (4.10).

Each DOF in the OCT corresponds to an infinitesimal change in θ represented by $\Delta\theta = (\Delta\theta_1, \Delta\theta_2, \ldots, \Delta\theta_c)^{\mathrm{T}}$. For $1 \le i \le c$, each $\Delta\theta_i$ corresponds to a small change in the fold angle at crease i. When this change is applied to the initial state, the new state also satisfies each of the vertices' closure equations. Applying these changes to the initial state of vertex 1 gives the following closure equation:

$$\prod_{i=1}^{6} Q\left(\alpha_{i(i+1)}, \theta_i + \Delta\theta_i\right) = I_{3\times3}. \tag{4.11}$$

The LHS of (4.12) is a product of 3 × 3 matrices, and each of them can be simplified with first order approximations of trigonometric functions. Using the derivatives of each transformation matrix with respect to θ_i,

$$Q'\left(\alpha_{i(i+1)}, \theta_i\right) = \begin{pmatrix} -\sin\theta_i & \cos\alpha_{i(i+1)}\cos\theta_i & \sin\alpha_{i(i+1)}\cos\theta_i \\ -\cos\theta_i & -\cos\alpha_{i(i+1)}\sin\theta_i & -\sin\alpha_{i(i+1)}\sin\theta_i \\ 0 & 0 & 0 \end{pmatrix}, \tag{4.12}$$

equation (4.11) can be simplified to (4.13),

$$\prod_{i=1}^{6} \left(Q\left(\alpha_{i(i+1)}, \theta_i\right) + Q'\left(\alpha_{i(i+1)}, \theta_i\right)\Delta\theta_i\right) = I_{3\times3}. \tag{4.13}$$

Taking the first-order terms in (4.13) gives

$$\sum_{i=1}^{6} M_i \Delta\theta_i = 0_{3\times3}, \tag{4.14}$$

in which $0_{3\times3}$ is the 3 × 3 zero matrix, and for $1 \le i \le 6$, matrix M_i is the equal to

$$M_i = Q(\alpha_{12}, \theta_1)...Q'(\alpha_{i(i+1)}, \theta_i)...Q(\alpha_{n1}, \theta_n). \tag{4.15}$$

Matrix M_i is the product of six transformation matrices in which the i^{th} matrix is replaced by its derivative with respect to θ_i. For $1 \le i \le 6$, matrix M_i is in the following form:

$$M_i = \begin{pmatrix} m_{1i} & m_{2i} & m_{3i} \\ m_{4i} & m_{5i} & m_{6i} \\ m_{7i} & m_{8i} & m_{9i} \end{pmatrix}. \tag{4.16}$$

The entries in M_i are rearranged to form matrix J,

$$J = (m_{ji}). \tag{4.17}$$

According to (4.17), the entry in the j^{th} row and i^{th} column of J is m_{ji}. Matrix J is called the Jacobian matrix, which satisfies

$$J \begin{pmatrix} \Delta\theta_1 \\ \Delta\theta_2 \\ \Delta\theta_3 \\ \Delta\theta_4 \\ \Delta\theta_5 \\ \Delta\theta_6 \end{pmatrix} = 0_{9\times1}. \tag{4.18}$$

In (4.18), J is a 9×6 matrix and $0_{9\times1}$ is the 9×1 zero vector. All 9 entries in M_i are in the i^{th} column of J because it corresponds to the i^{th} crease angle. The equation in (4.18) is a homogeneous system of linear equations. The number of linearly independent solutions to (4.18) equals the number of DOFs in P_1 because each DOF represents a solution for $\Delta\theta$ that is not a linear combination of the remaining DOFs (Gan and Pellegrino, 2006). In other words, the dimension of the null space of J equals the number of DOFs in P_1.

Since the OCT has multiple vertices, the i^{th} vertex in the OCT generates Jacobian matrix J_i where $1 \leq i \leq v$. The entries in $J_1, J_2, \ldots, J_v$ can be rearranged to form a combined Jacobian matrix J_{comb}, which satisfies

$$J_{comb}\Delta\theta = 0_{9v\times 1}. \tag{4.19}$$

In equation (4.19), J_{comb} is a $(9v) \times c$ matrix, $\Delta\theta$ is a $c \times 1$ vector, and $0_{9v\times 1}$ is the $(9v) \times 1$ zero vector. Each 9×1 column in Jacobian matrix J_i for $1 \leq i \leq v$ corresponds to one of the c creases. Suppose the j^{th} column in J_i corresponds to crease k, for $1 \leq k \leq c$. The 9×1 j^{th} column in J_i is the 9×1 column vector in J_{comb} in rows $(9i - 8)$ through $(9i)$, inclusive, and column k. All remaining entries in J_{comb} not occupied by a column in one of the vertices' Jacobian matrices are zeroes. The dimension of the null space of J_{comb} equals the DOF of the OCT.

A MATLAB program was used to compute the Jacobian matrices of $M \times N$ OCTs using the parameters described in Appendix D. This program computes the singular value decomposition, SVD, of the Jacobian matrix and obtains a set of linearly independent vectors that span its null space. The dimension of the null space equals the number of DOFs in the OCT. Figure D.2 in Appendix D is an example of a null space of a 2×2 OCT's Jacobian matrix. The numbers of DOFs in each $M \times N$ OCT, in which M and N are positive integers no greater than 20, are computed in a Table 4.1. Modulating the input angle parameters in the program does not change the number of DOFs, so Table 4.1 is independent of the values of the OCT's angle parameters. When $M, N \geq 2$, the $M \times N$ OCT has five DOFs, and there is no observed change in the number of DOFs as M and N increase. Therefore, the number of DOFs in the $M \times N$ OCT stabilizes at five. Intuitively,

as the $M \times N$ OCT grows, the mobility added by the 6Cs are balanced out by the mobility restricted by the 4Cs.

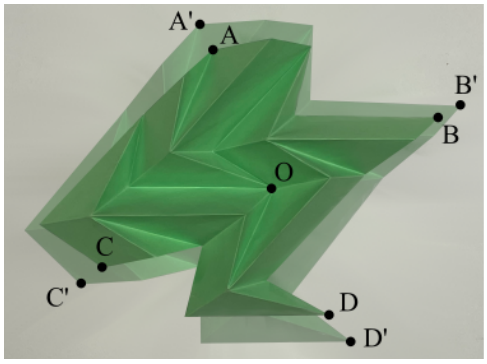
Table 4.1: Number of DOFs in the $M \times N$ OCT

M \ N	1	≥ 2
1	3	$2N + 1$
≥ 2	$2M + 1$	5

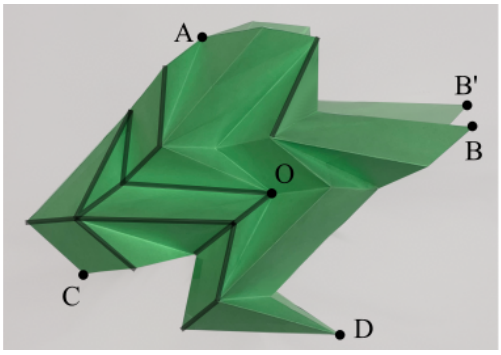
For the 2 × 2 OCT, the five DOFs correspond to five linearly independent vectors that are solutions to the equation in (4.19). To simplify these DOFs, linear transformations are performed to obtain a new set of five linearly independent vectors that maximizes the number of zeroes as entries, which correspond to creases that remain fixed. These linear transformations are comparable to the operations in Gaussian elimination. Figure D.2 in Appendix D represents each of these five DOFs as columns. The first column contains no entries equal to zero while the remaining four columns contain multiple entries equal to zero.

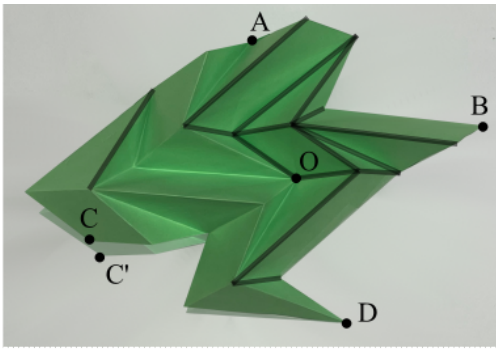
The five DOFs in the 2 × 2 OCT are the following folding modes, as shown in Figure 4.10(a – e): planar folding, upper-right half folding, lower-left half folding, upper-right corner folding, and lower-left corner folding. Before and after images of the 2 × 2 OCT indicate movement of specific vertices. Figure 4.10(a) shows the planar folding mode, in which no creases are fixed. The 2 × 2 OCT in Figure 4.4 shows the coordinated folding according to the planar folding mode. Each claw unit and 4C in the OCT fold according to the system of equations in (4.3) and (4.5), respectively, which is consistent with the results from the analytical model. Figures 4.10(b – e) show the four remaining DOFs, in which

certain creases remain fixed. These fixed creases are highlighted in Figures 4.10(b – e). The five folding modes in Figure 4.10 show that the 2 × 2 OCT has five DOFs.

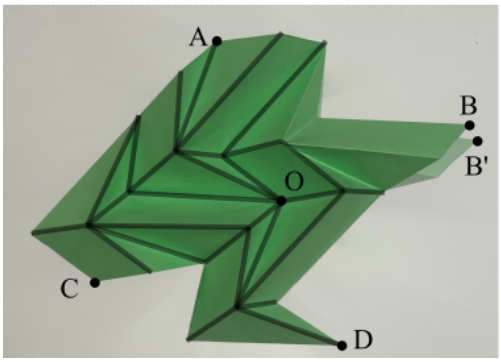


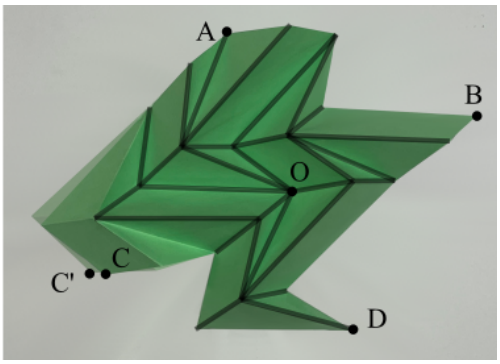
(a)





(b) (c)





(d) (e)

Figure 4.10: Five DOFs of the 2 × 2 OCT with highlighted lines indicating fixed creases: (a) planar folding, (b) upper-right half folding, (c) lower-left half folding, (d) upper-right corner folding, and (e) lower-left corner folding

For larger OCTs, such as the 3 × 3 OCT in Figure 4.11, planar folding folds all creases in the OCT while the remaining four folding modes only fold localized collections of creases. Upper-right half folding only folds creases in three claw units in the upper-right corner, and lower-left half folding only folds creases in three claw units in the lower-left corner. These creases are highlighted in blue in Figure 4.11. Upper-right corner folding only folds four creases in the claw unit in the upper-right corner, and lower-left corner folding only folds four creases in the claw unit in the lower-left corner. These creases are highlighted in red in Figure 4.11.

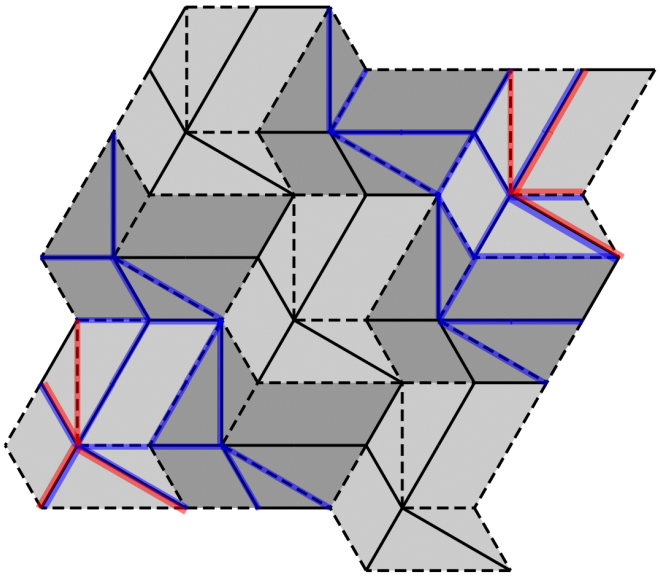
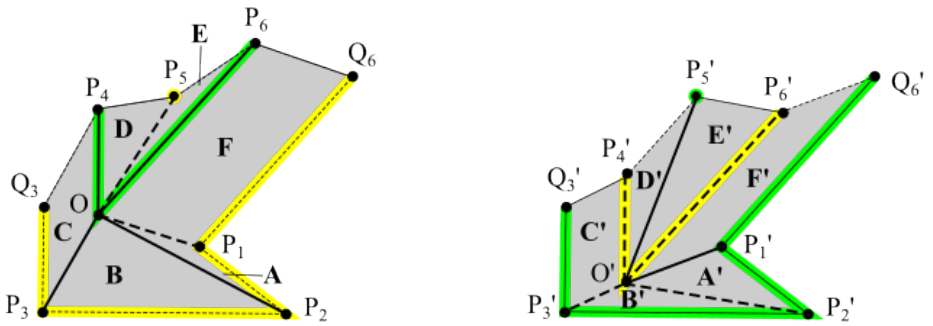


Figure 4.11: Creases in the 3 × 3 OCT that fold according to the five DOFs

4.4 Stacked OCT

The geometric proofs in section 4.2 show that when a claw unit folds according to (4.5), there are creases and boundary edges that lie on two parallel planes. Figure 4.12(a) and Figure 4.12(b) show type-M1 and type-V1 claw units, respectively, in partially folded

states. The green creases lie on an upper plane, and the yellow creases lie on a parallel lower plane, making the type-M1 claw unit crease-stackable with the type-V1 claw unit.



(a) (b)

Figure 4.12: Claw units in partially folded states: (a) type-M1 and (b) type-V1

The crease patterns of the type-M1 and type-V1 claw units are provided in Figure 4.2(a) and Figure 4.2(c), respectively. To form the stacked claw unit, the yellow boundary edges on the type-M1 claw unit are attached to the green boundary edges on the type-V1 claw unit. These boundary edges become creases in the stacked claw unit. A diagram of the stacked claw unit with its dihedral angles labeled is shown in Figure 4.13. The dihedral angles for each claw unit are labeled in the same convention as those in Figure 4.7. The dihedral angles in the type-M1 claw unit are ϕ_1, ϕ_2, ϕ_3, ϕ_4, ϕ_5, and ϕ_6, and the dihedral angles in the type-V1 claw unit are ϕ_1', ϕ_2', ϕ_3', ϕ_4', ϕ_5', and ϕ_6'. Let the dihedral angles between panels F and F', A and A', B and B', and C and C' be ϕ_7, ϕ_8, ϕ_9 and ϕ_{10}, respectively.

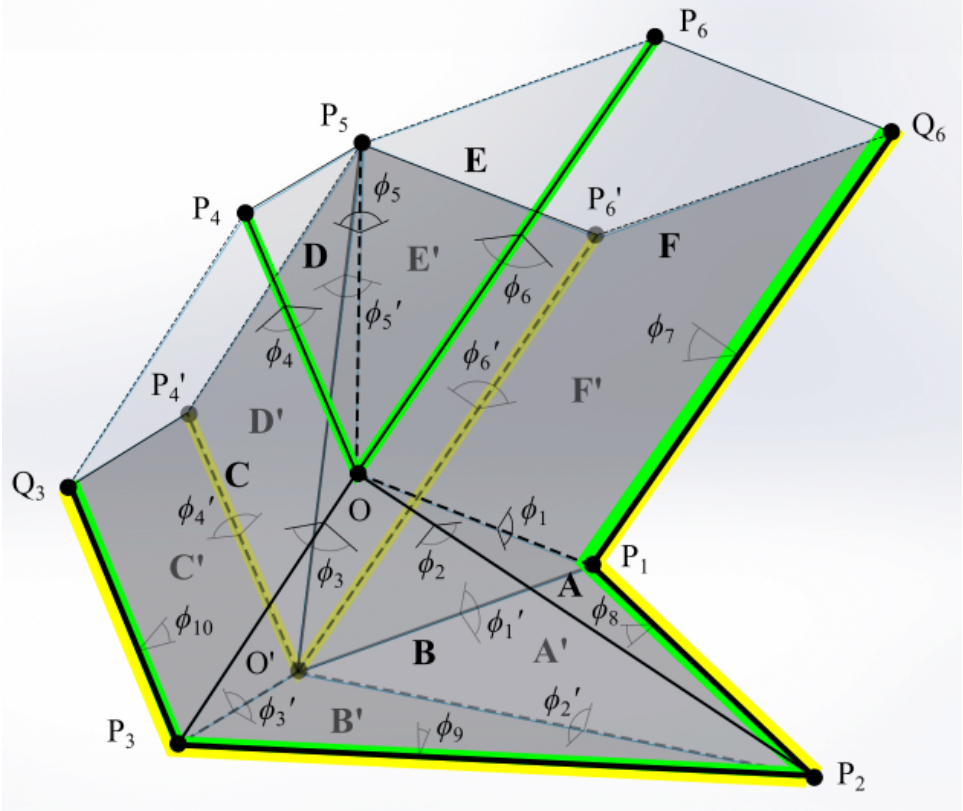
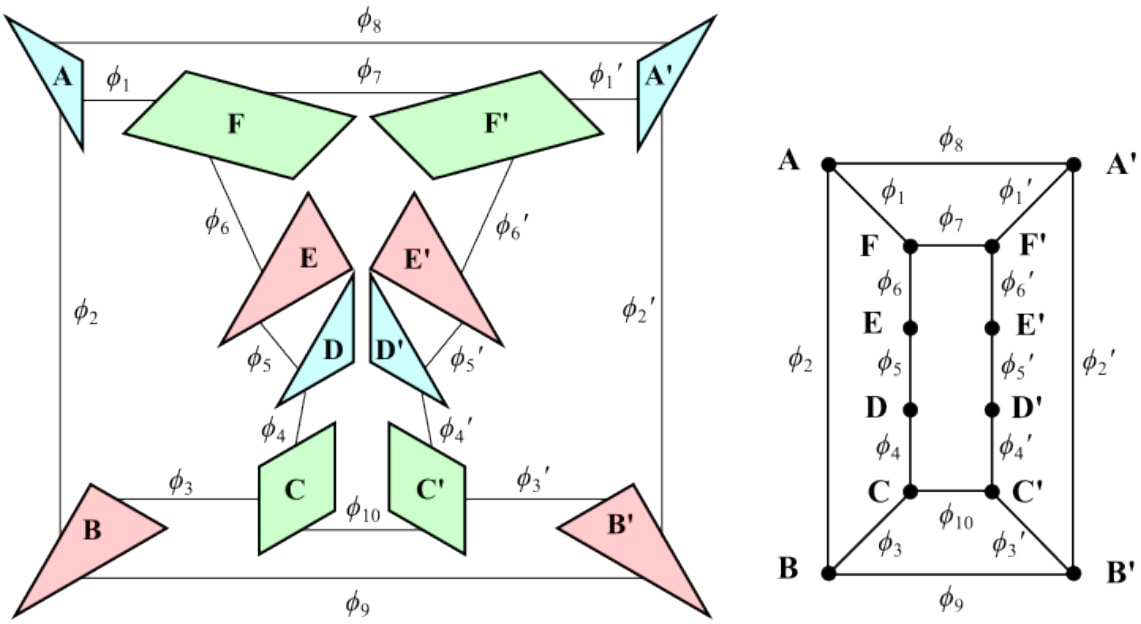


Figure 4.13: Stacked claw unit in a partially folded state.

Examination of the stacked claw unit reveals it contains three 4Cs at points P_1, P_2 and P_3 and two 6Cs at vertices O and O'. The 4C at P_1 consists of panels A, F, A', and F', the 4C at P_2 consists of panels A, B, A', and B', and the 4C at P_3 consists of panels B, C, C', and B'. Each of these 4Cs is a 4C cone in which the four sector angles are congruent. The two 6Cs at vertices O and O' are claw units, which have been discussed. Figure 4.14(a) shows a schematic diagram of the stacked claw unit that preserves the shapes of the panels. A line between adjacent panels represents a crease whose corresponding dihedral angle is labeled. Figure 4.14(b) is a simplified schematic diagram in which panels are represented as dots, and a line between adjacent dots represents a crease.



(a) (b)

Figure 4.14: Schematic diagrams of the stacked claw unit:

(a) preserving the panel shapes and (b) simplifying the connections diagram

To show all 16 dihedral angles can be determined by one input, let ϕ_1 be the input dihedral angle. The 4C linking panels A, F, A', and F' in a trapezoid in Figure 4.14(b) is a 1-DOF spherical 4-bar linkage, so dihedral angles, ϕ_7, ϕ_8 and ϕ_1', are uniquely determined. The 4C linking panels A, B, B', and A' in a rectangle in Figure 4.14(b) is a 1-DOF spherical 4-bar linkage. Since ϕ_8 is known, dihedral angles, ϕ_2, ϕ_9 and ϕ_2', are uniquely determined. The 4C linking panels B, C, C', and B' in a trapezoid in Figure 4.14(b) is a 1-DOF spherical 4-bar linkage. Since ϕ_9 is known, dihedral angles, ϕ_3, ϕ_{10} and ϕ_3', are uniquely determined. Appendix C shows that the dihedral angle relations among ϕ_1, ϕ_2, ϕ_3, ϕ_1', ϕ_2', and ϕ_3' obtained from the three 4Cs reduce each 3-DOF system of equations describing the claw units to a 1-DOF system of equations. The 6C linking panels A, B, C, D, E and F in a

trapezoid in Figure 4.14(b) is a spherical 6-bar linkage. Since ϕ_1, ϕ_2, and ϕ_3 are known, and their relations are compatible with the 6C, dihedral angels, ϕ_4, ϕ_5, and ϕ_6, are uniquely determined using the closure equations of the 6C. Similarly, the 6C linking panels A', B', C', D', E' and F' in a trapezoid in Figure 4.14(b) is a spherical 6-bar linkage. Since ϕ_1', ϕ_2', and ϕ_3' are known, and their relations are compatible with the 6C, dihedral angles, ϕ_4', ϕ_5', and ϕ_6', are uniquely determined using the closure equations of the 6C. All 16 dihedral angles are determined, and their relations are compatible with each other, so the stacked claw unit has only one DOF. Stacking two claw units, which are 3-DOF 6Cs, creates three 4Cs, which reduce the number of DOFs to one. This reduction is comparable to the limitation of the number of DOFs in the $M \times N$ OCT due to the prevalence of 4Cs. Combining the closure equations for the 4Cs and 6Cs yields the following system of equations for the stacked claw unit in Figure 4.14:

$$\begin{gathered}\phi_1 = \phi_3 = \phi_1' = \phi_3', \ \phi_2 = \phi_5 = \phi_2' = \phi_5', \phi_4 = \phi_6 = \phi_4' = \phi_6', \\ \phi_7 = \phi_8 = \phi_9 = \phi_{10}, \cos\beta \tan\frac{\phi_1}{2} = \cos\alpha \tan\frac{\phi_2}{2} = \tan\frac{\phi_4}{2} = \left(\tan\frac{\phi_7}{2}\right)^{-1}.\end{gathered} \tag{4.20}$$

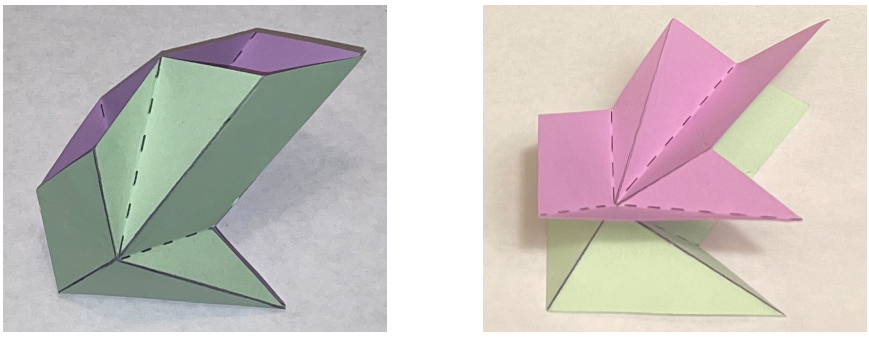
Given input angle ϕ_1, the remaining 15 angles are determined using the system of equations in (4.20). Each dihedral angle ranges from 0 to π, so the stacked claw unit is a flat-foldable and rigidly foldable structure with only one DOF. The equations in (4.20) state that $\phi_i = \phi_i'$ for i = 1, 2, 3, 4, 5, and 6, so both claw units are always in matching partially folded states as the stacked claw unit folds. The equations in (4.20) also imply that panels D and D' meet at point P_5, as do panels E and E'. This reveals two additional 4-bar linkages. Panels C, D, D', and C', and panels E, F, E', and F' each form a parallelogram linkage, in which opposite dihedral angles are equal. Table 4.2 details all discussed

mechanisms in the stacked claw unit.

Table 4.2: Mechanisms in the stacked claw unit

Panels	Mechanism
A, B, C, D, E, and F	Spherical 6-bar Linkage
A', B', C', D', E', and F'	
A, F, F', and A'	Spherical 4-bar Linkage
A, B, B', and A'	
B, C, C', and B'	
C, D, D', and C'	Parallelogram 4-bar Linkage
E, F, F', and E'	

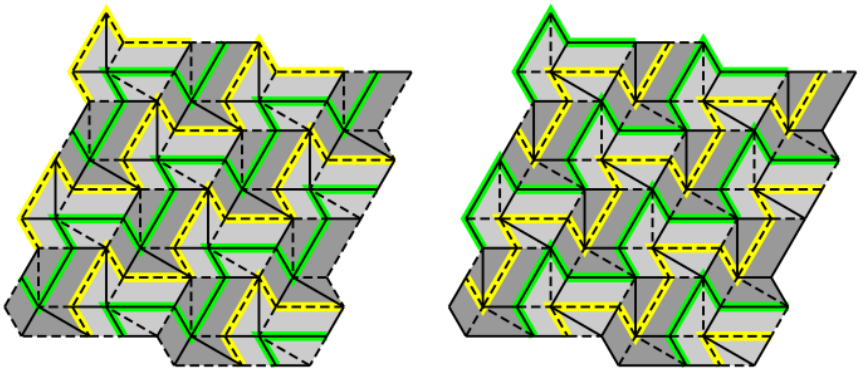
There are two ways to stack the type-M1 and type-V1 claw units. Attaching boundary edges, P_1Q_6, P_1P_2, P_2P_3, and P_3Q_3, in the type-M1 claw unit to boundary edges, $P_1'Q_6'$, $P_1'P_2'$, $P_2'P_3'$, and $P_3'Q_3'$, respectively, in the type-V1 claw unit forms the stacked claw unit in Figure 4.15(a). Here, the type-M1 unit is stacked on the type-V1 unit. Attaching creases, OP_4 and OP_6, in the type-V1 claw unit to creases, $O'P_4'$ and $O'P_6'$, respectively, in the type-M1 claw unit forms the stacked structure in Figure 4.15(b). Here, the type-V1 unit is stacked on the type-M1 unit. These two constructions also apply to type-M2 and type-V2 claw units. For the stacked structure in Figure 4.15(b), vertices O and O' are merged, and panels D, E, E', and D' form a 1-DOF 4C at vertex O. When two stacked claw units are attached, this stacked structure forms. Therefore, if multiple stacked claw units are stacked, then a dihedral angle of one stacked claw unit can be used as an input to uniquely determine all dihedral angles in the other stacked claw unit.



(a) (b)

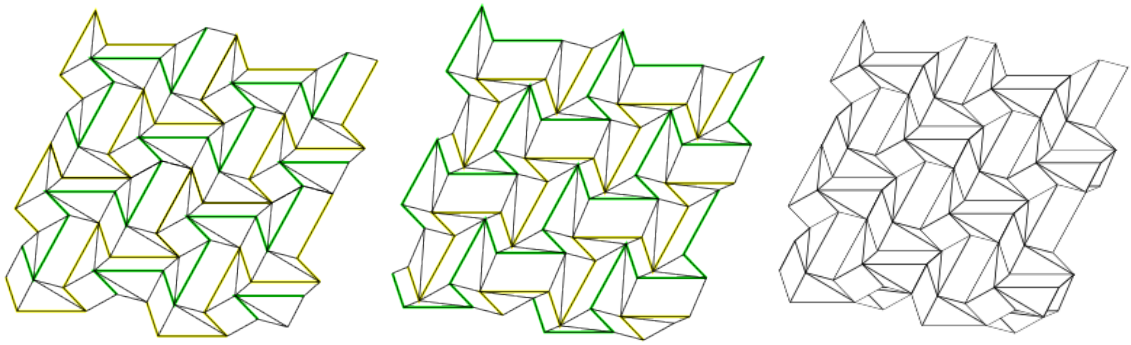
Figure 4.15: Stacking claw units: (a) type-M1 on type-V1 and (b) type-V1 on type-M1

Since two claw units can be stacked along their creases, the $M \times N$ OCT is also crease-stackable. Figure 4.16(a) and Figure 4.16(b) show a type-M and type-V 4 × 4 OCT, respectively. The green and yellow creases form zigzags in the OCT. Figure 4.17(a) and Figure 4.17(b) show the type-M and type-V 4 × 4 OCT, respectively, in partially folded states. In both OCTs, the green creases lie in an upper plane, and the yellow creases lie in a lower parallel plane. To form the stacked 4 × 4 OCT in Figure 4.17(c), the yellow creases in the type-M sheet are attached to the corresponding green creases in the type-V sheet. This stacked OCT is a lattice of stacked claw units.



(a) (b)

Figure 4.16: Two 4 × 4 OCTs: (a) type-M and (b) type-V

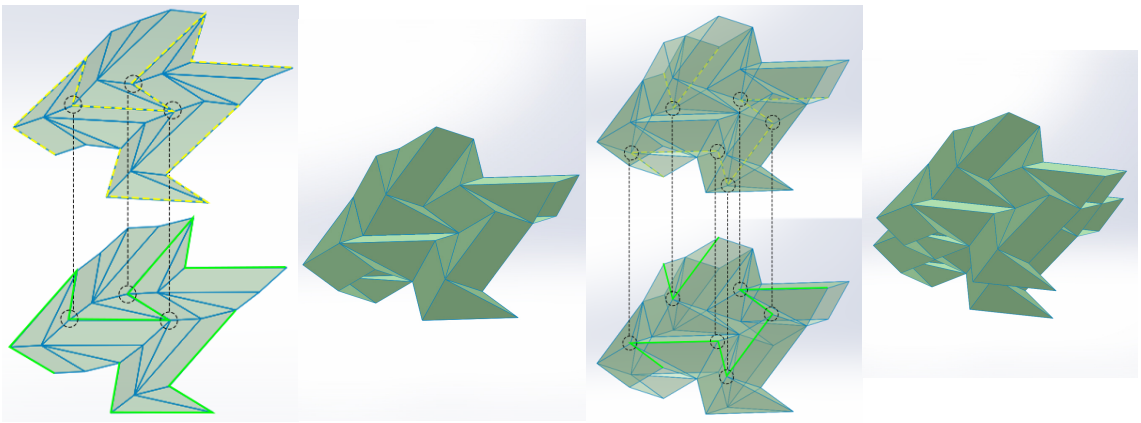


(a) (b) (c)

Figure 4.17: Stacking sheets of the 4 × 4 OCT:

(a) type-M, (b) type-V, and (c) 2-layer stacked 4 × 4 OCT

For any positive integers M and N and positive even integer L, stacking L sheets of the $M \times N$ OCT, results in the L-layer stacked $M \times N$ OCT. These OCTs alternate between type-M and type-V OCTs. Figures 4.18(a) and Figure 4.18(b) show the construction of the 2-layer 2 × 2 OCT from a type-M and type-V 2 × 2 OCT. Figure 4.18(c) and Figure 4.18(d) show the construction of the 4-layer 2 × 2 OCT from two identical 2-layer 2 × 2 OCTs. Figure 4.19 shows a physical model of the 2-layer stacked 2 × 2 OCT. The L-layer stacked $M \times N$ OCT is a flat-foldable and rigidly foldable structure with only one DOF.



(a) (b) (c) (d)

Figure 4.18: Stacking 2 × 2 OCTs: (a) two 2 × 2 OCTs, (b) 2-layer stacked 2 × 2 OCT, (c) two 2-layer stacked 2 × 2 OCTs, and (d) 4-layer stacked 2 × 2 OCT

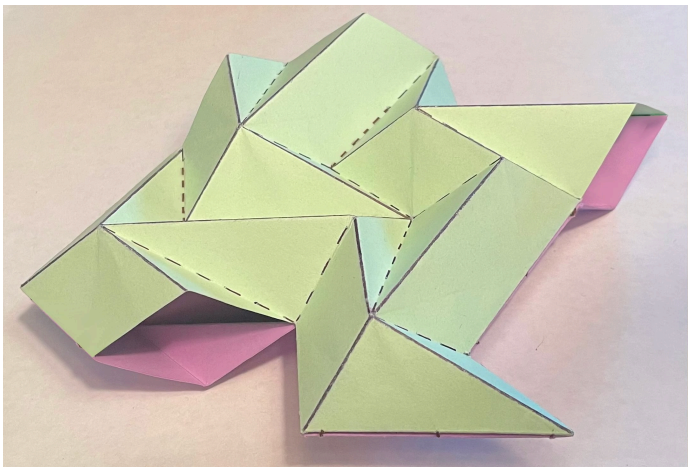
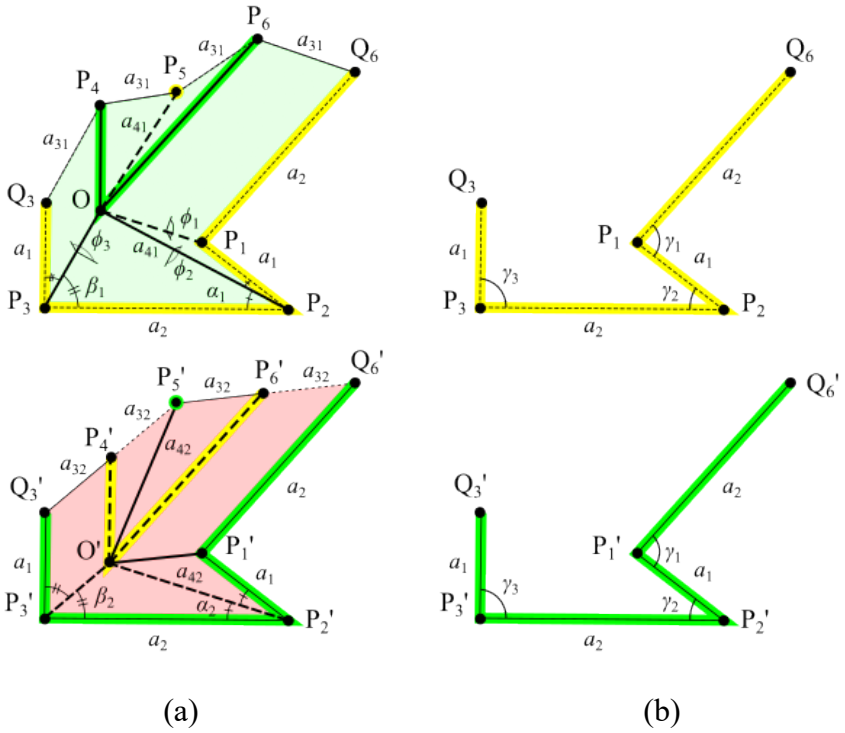


Figure 4.19: 2-layer stacked 2 × 2 OCT

4.5 Self-Locking Stacked OCT

While identical OCTs are crease-stackable with each other, crease-stackable OCTs need not be identical. Stacking OCTs that are not identical results in a self-locking stacked structure. In this structure, one layer can fold from its flat unfolded state to its flat folded state while another layer can only fold from a partially folded state to its flat folded state.

When the claw unit is folded using the planar folding mode, there are two sets of creases that lie on two parallel planes. The green claw unit in Figure 4.20(a) shows these two sets of creases in green and yellow. The set of yellow boundary edges forms a planar zigzag shown in Figure 4.20(b). When the six creases in the claw unit are projected onto this plane, a new 6C, shown in red, fulfilling all requirements for a claw unit is made. Here, a family of claw units is defined. Two claw units are in the same family if the planar projection of one claw unit is the crease pattern of the other.



(a) (b)

Figure 4.20: Planar projection of one claw unit on another:

(a) claw units and (b) their respective planar zigzags

If two claw units have partially folded states such that their respective planar zigzags match, then the claw units can be stacked by attaching the corresponding creases on both zigzags. This geometric property makes the two claw units in Figure 4.20(a)

crease-stackable with each other, so they are in the same family. The following derivation reveals the conditions necessary for two claw units to have matching planar zigzags. Figure 4.20(a) shows the partially folded green claw unit projected onto a plane parallel to the plane containing its planar zigzag. This planar projection is the red claw unit. The green claw unit's angle parameters are α_1 and β_1, and the red claw unit's angle parameters are α_2 and β_2.

The following derivation determines the relationship between the angle parameters of two claw units in the same family. Crease-stackability implies that side lengths a_1 and a_2 are constants for both claw units. Rearranging the angle relations in (4.2) gives

$$\frac{a_2}{a_1} = \frac{\sin(\beta - \alpha)}{\sin(\beta + \alpha)}. \tag{4.21}$$

Using trigonometric identities, equation (4.21) can be rearranged to form

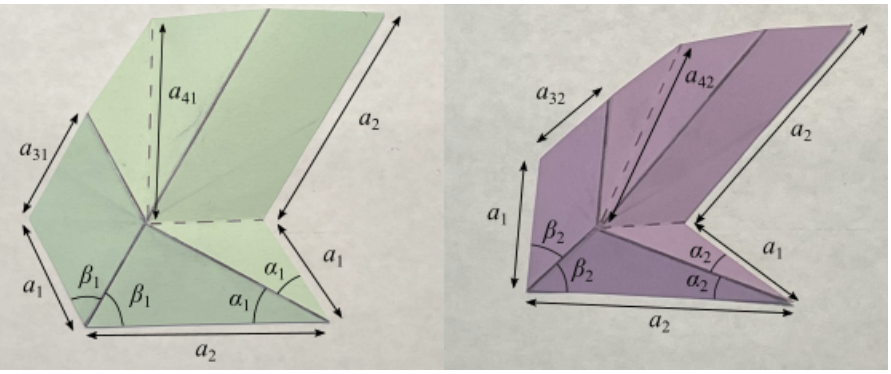
$$\frac{a_2 - a_1}{a_2 + a_1} = \frac{\tan\alpha}{\tan\beta}. \tag{4.22}$$

The LHS of (4.22) is a constant, so two claw units are in the same family if side lengths a_1 and a_2 are constants and (4.22) is satisfied. Rearranging the equations in (4.2) gives the following equations describing side lengths a_3 and a_4 in terms of a_1, α, and β:

$$a_3 = \frac{a_1 \sin\alpha}{\sin(\beta - \alpha)}, a_4 = \frac{a_1 \sin\beta}{\sin(\beta - \alpha)}. \tag{4.23}$$

When the restriction in (4.1) is imposed, equation (4.22) implies that $\alpha_1 > \alpha_2$ if and only if $\beta_1 > \beta_2$. Given any two distinct claw units in the same family, one is considered larger than the other based on the values of α and β. Figure 4.21(a) and (b) show two distinct claw units in the same family, in which the constant in the LHS of (4.22) is (1 / 3). For the green claw unit, the angle parameters are $\alpha_1 = \pi / 6$ and $\beta_1 = \pi / 3$ and the side lengths are

$a_1 = 1$, $a_2 = 2$, $a_{31} = 1$, and $a_{41} = 1.7321$. For the red claw unit, the angle parameters are $\alpha_2 = \tan^{-1}(1 / 3)$ and $\beta_2 = \pi / 4$ and the side lengths are $a_1 = 1$, $a_2 = 2$, $a_{32} = 0.7071$, and $a_{42} = 1.5811$. Since $\alpha_1 > \alpha_2$, the claw unit in Figure 4.21(a) is larger than the one in Figure 4.21(b)



(a) (b)

Figure 4.21: Claw units in the same family:

(a) $(\alpha_1, \beta_1) = (\pi / 6, \pi / 3)$ and (b) $(\alpha_2, \beta_2) = (\tan^{-1}(1 / 3), \pi / 4)$

The following derivation shows that given a claw unit with side lengths, a_1 and a_2, angles, α and β, satisfying (4.22), and one input dihedral angle, ϕ_1, the three angles in the planar zigzag can be determined. Each planar zigzag consists of three angles, γ_1, γ_2, and γ_3. The spherical law of cosines on points P_1, P_2, and P_3, yields the following equations:

$$\sin\left(\frac{\gamma_1}{2}\right) = \sin\beta \sin\left(\frac{\phi_1}{2}\right),$$

$$\sin\left(\frac{\gamma_2}{2}\right) = \sin\alpha \sin\left(\frac{\phi_2}{2}\right), \tag{4.24}$$

$$\sin\left(\frac{\gamma_3}{2}\right) = \sin\beta \sin\left(\frac{\phi_3}{2}\right).$$

The equations in (4.5) gives the following relations:

$$\phi_1 = \phi_3,\ \cos\beta \tan\left(\frac{\phi_1}{2}\right) = \cos\alpha \tan\left(\frac{\phi_2}{2}\right). \tag{4.25}$$

Using the relations in (4.25) and additional trigonometric identities, the equations in (4.24) can be simplified to the following equations:

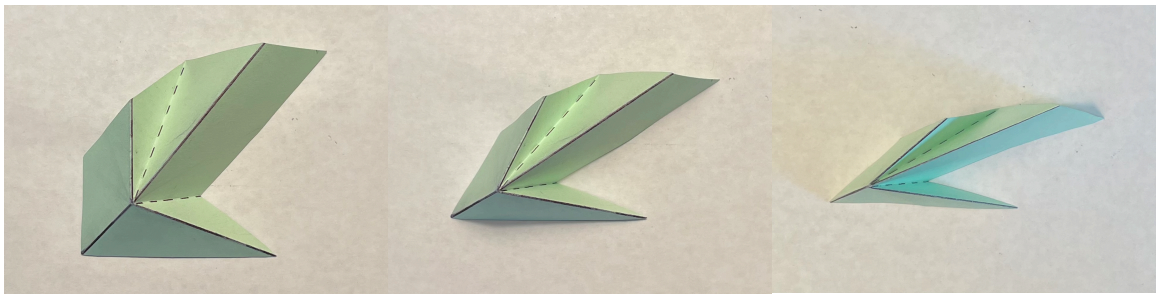
$$\sin\left(\frac{\gamma_1}{2}\right) = \sin\beta \sin\left(\frac{\phi_1}{2}\right),\ \gamma_1 = \gamma_3,\ \tan\left(\frac{\gamma_2}{2}\right) = \left(\frac{\tan\alpha}{\tan\beta}\right)\tan\left(\frac{\gamma_1}{2}\right). \tag{4.26}$$

Since the claw unit's angles satisfy (4.22), this relation can be substituted into the third equation in (4.26). The equations in (4.26) imply angles γ_1, γ_2, and γ_3 are each a function of ϕ_1. Also, the relations among γ_1, γ_2, and γ_3 are independent of the values of α and β.

Given two claw units in the same family with input dihedral angles ϕ_1 and ϕ_1', equation (4.24) gives the following equation:

$$\sin\beta_1 \sin\left(\frac{\phi_1}{2}\right) = \sin\beta_2 \sin\left(\frac{\phi_1'}{2}\right). \tag{4.27}$$

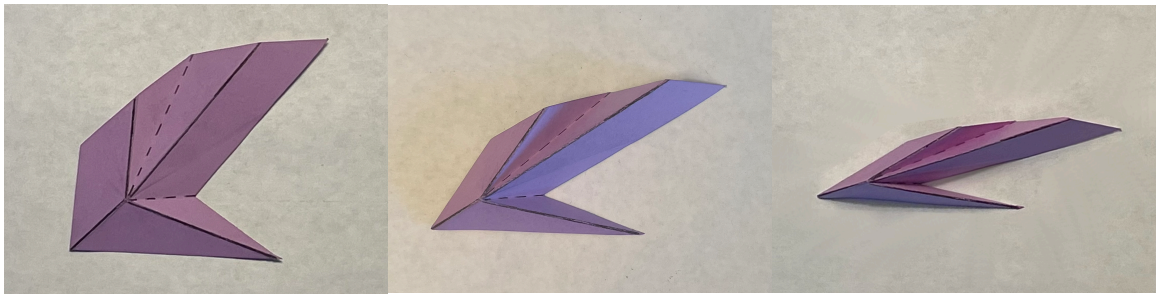
Using equation (4.27), input angle ϕ_1 determines dihedral angle ϕ_1'. Using the equations in (4.5), input angles ϕ_1 and ϕ_1' determine the remaining dihedral angles in both claw units. Figure 4.22 and Figure 4.23 show the folding sequences of the two claw units. Each partially folded state is determined by the values of ϕ_1 and ϕ_1' for the larger and smaller claw unit, respectively. In Figure 4.22(a – c) and Figure 4.23(a – c), the three partially folded states have planar zigzags with $\gamma_1 = \pi / 2$, $\gamma_1 = \pi / 3$, and $\gamma_1 = \pi / 4$, respectively. The three partially folded states in Figure 4.22(a – c) are crease-stackable with those in Figure 4.23(a – c), respectively. The method used to construct the stacked claw unit in Figure 4.13 is also used to construct the self-locking stacked claw unit.



(a) (b) (c)

Figure 4.22: Folding sequence of the claw unit with $(\alpha_1, \beta_1) = (\pi / 6, \pi / 3)$:

(a) $\phi_1 = 1.9106$, (b) $\phi_1 = 1.2310$, and (c) $\phi_1 = 0.9154$

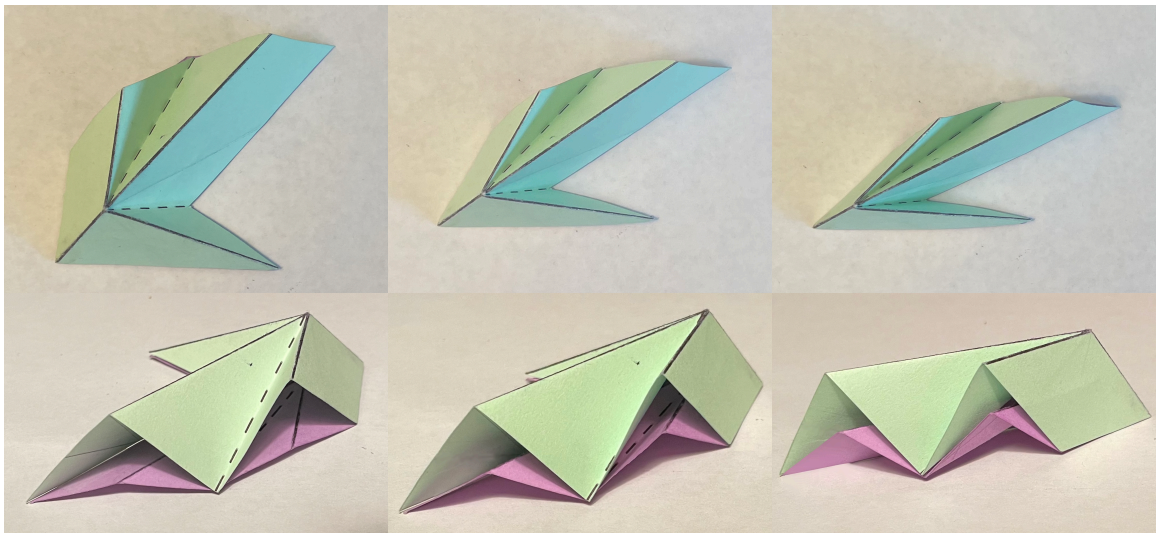


(a) (b) (c)

Figure 4.23: Folding sequence of the claw unit with $(\alpha_2, \beta_2) = (\tan^{-1}(1 / 3), \pi / 4)$:

(a) $\phi_1' = \pi$, (b) $\phi_1' = \pi / 2$, and (c) $\phi_1' = 1.1437$

Figures 4.24 shows the folding sequence of the self-locking stacked claw unit obtained from attaching the claw units in Figure 4.22 to those in Figure 4.23. Two perspectives are shown for each partially folded state. Figure 4.24(a) is the self-locking state. In this state, the larger claw unit is in a partially folded state while the smaller claw unit is fully unfolded.



(a) (b) (c)

Figure 4.24: Folding sequence of the self-locking stacked claw unit:

(a) (ϕ_1, ϕ_1') = (1.9106, π), (b) (ϕ_1, ϕ_1') = (1.2310, π / 2), and (c) (ϕ_1, ϕ_1') = (0.9154, 1.1437)

Equation (4.22) implies that the larger claw unit does not fold with its full range of motion, but the smaller one does. While dihedral angle ϕ_1' ranges from 0 to π, dihedral angle ϕ_1 ranges from 0 to ϕ_{1max}, which is computed using the following formula:

$$\phi_{1max} = 2\sin^{-1}\left(\frac{\sin\beta_2}{\sin\beta_1}\right). \tag{4.28}$$

The formula in (4.28) is derived from (4.27) when $\phi_1' = \pi$, which corresponds to the state in which the smaller claw unit is fully unfolded. The graph in Figure 4.25 shows the relations between ϕ_1 and the other dihedral angles in the two claw units. The green and purple plots correspond to the dihedral angles in the upper and lower claw units, respectively. The green plots are a truncated version of those shown in Figure 4.8 because ϕ_{1max} is an upper bound of ϕ_1. The partially folded states of the self-locking stacked claw

unit in Figure 4.24(a – c) are represented by the vertical dotted lines (a – c), respectively, in the graph.

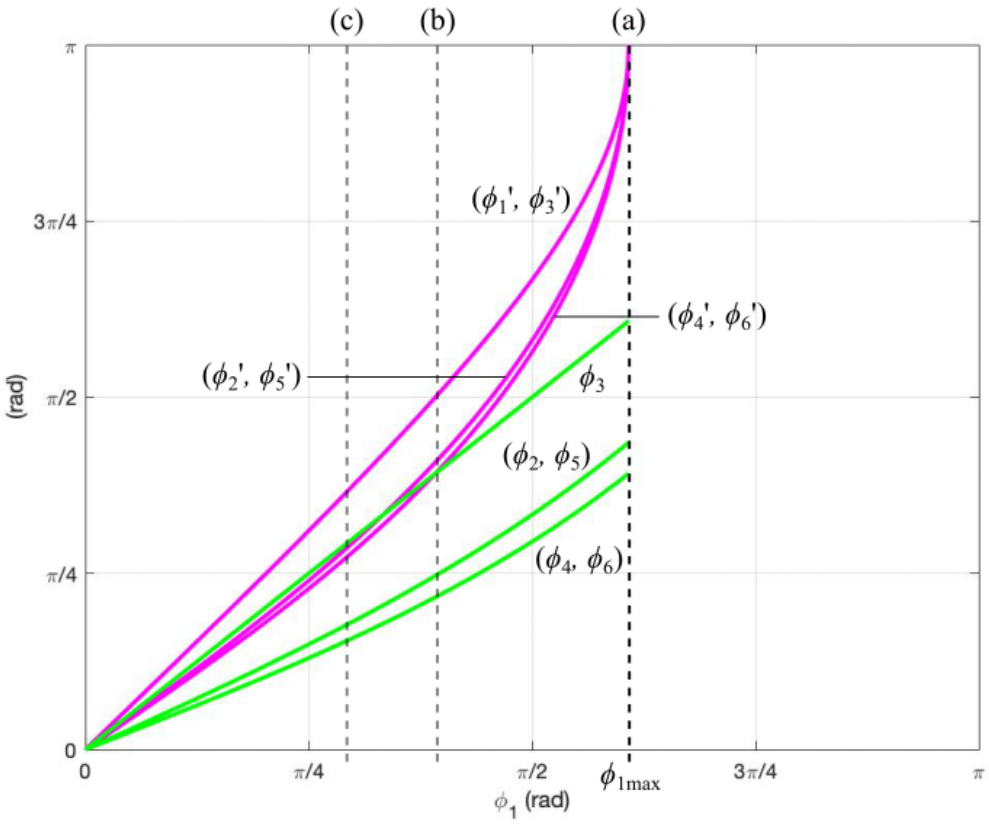
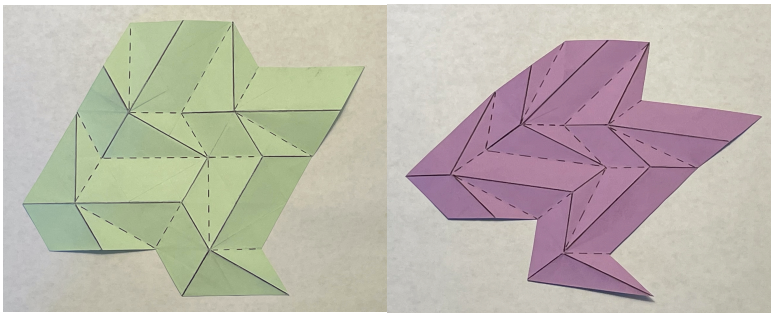


Figure 4.25: Dihedral angle relations in the self-locking stacked claw unit

The self-locking stacked claw unit in Figure 4.24 depicts one constructed from two type-M claw units, but one can also be constructed from a type-M and a type-V claw unit. The bottom layer of the self-locking stacked claw unit in Figure 4.24 can be inverted to a type-V claw unit. Inverting the bottom claw unit reflects it about the plane containing its planar zigzag, so the graph in Figure 4.25 would still describe the dihedral angles in this modified self-locking stacked claw unit. The self-locking state in Figure 4.24(a) allows the bottom claw unit to transition between a type-M claw unit and a type-V claw unit. In Figure 4.25, this transition would occur when $\phi_1 = \phi_{1max}$.

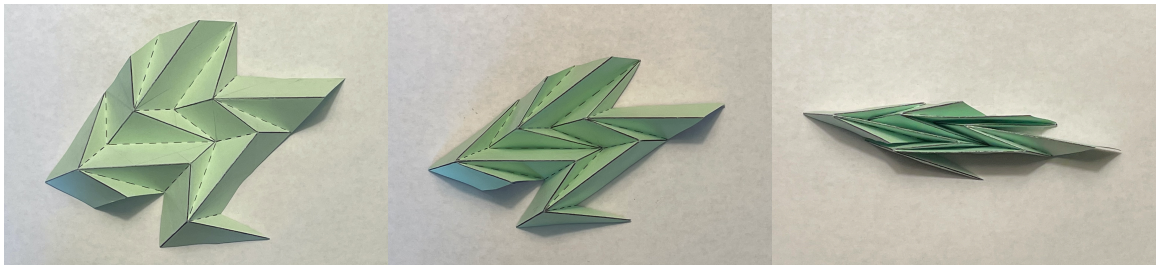
OCTs in the same family are composed of claw units in the same family, so OCTs in the same family crease-stackable with each other. The 2 × 2 OCTs in Figure 4.26(a) and Figure 4.26(b) are composed of claw units in Figure 4.21(a) and Figure 4.21(b), respectively. Stacking distinct OCTs in the same family forms the self-locking stacked OCT. The self-locking stacked OCT can only fold from its flat folded state to a partially folded state, which is its self-locking state. In this state, one OCT is in its flat unfolded state while the other OCT is in a partially folded state. The three partially folded states in Figure 4.27(a – c) are crease-stackable with those in Figure 4.28(a – c), respectively.



(a) (b)

Figure 4.26: 2 × 2 OCTs in the same family:

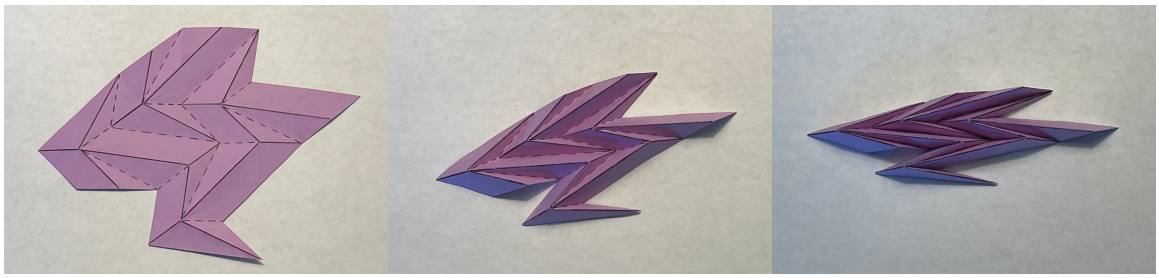
(a) $(\alpha_1, \beta_1) = (\pi / 6, \pi / 3)$ and (b) $(\alpha_2, \beta_2) = (\tan^{-1}(1 / 3), \pi / 4)$



(a) (b) (c)

Figure 4.27: Folding sequence of the 2 × 2 OCT with $(\alpha_1, \beta_1) = (\pi / 6, \pi / 3)$:

(a) $\phi_1 = 1.9106$, (b) $\phi_1 = 1.2310$, and (c) $\phi_1 = 0.9154$

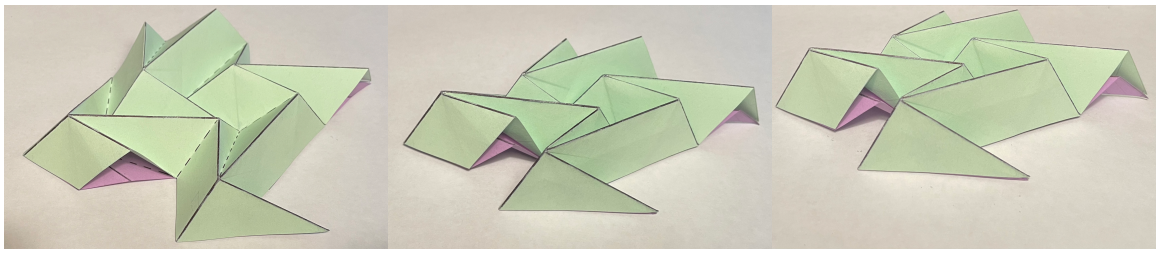


(a) (b) (c)

Figure 4.28: Folding sequence of the 2 × 2 OCT with $(\alpha_2, \beta_2) = (\tan^{-1}(1 / 3), \pi / 4)$:

(a) $\phi_1' = \pi$, (b) $\phi_1' = \pi / 2$, and (c) $\phi_1' = 1.1437$

Stacking two OCTs along their creases results in the self-locking stacked OCT. Figure 4.29 shows the folding sequence of the self-locking stacked 2 × 2 OCT obtained from attaching the OCTs in Figure 4.27 and Figure 4.28. This folding sequence corresponds to that of the self-locking stacked claw unit in Figure 4.24. Figure 4.29(a) is the self-locking state, in which the OCT generated from the claw unit in Figure 4.21(a) is in a partially folded state while the OCT generated from the claw unit in Figure 4.21(b) is fully unfolded. The construction method used to form the stacked OCT with multiple layers is used to construct the self-locking stacked OCT. More than two OCT sheets in the same family can be stacked to form a self-locking structure. Stacking two copies of the self-locking stacked OCT in Figure 4.29 forms the self-locking 4-layer stacked 2 × 2 OCT in Figure 4.30.



(a) (b) (c)

Figure 4.29: Folding sequence of the self-locking stacked 2 × 2 OCT:

(a) $(\phi_1, \phi_1') = (1.9106, \pi)$, (b) $(\phi_1, \phi_1') = (1.2310, \pi / 2)$, and (c) $(\phi_1, \phi_1') = (0.9154, 1.1437)$

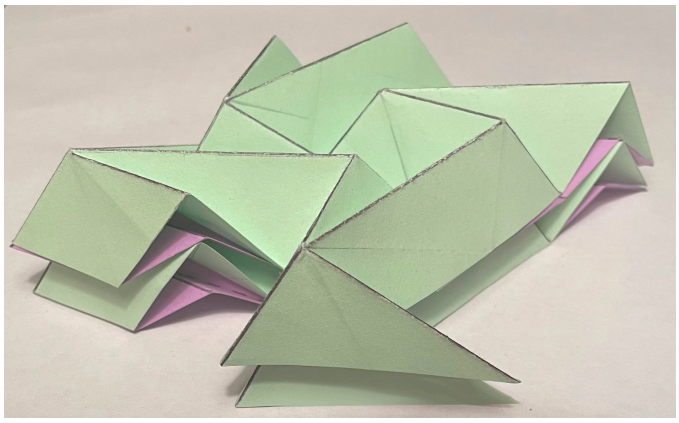


Figure 4.30: Self-locking 4-layer stacked 2 × 2 OCT

4.6 Conclusion

This chapter focuses on the geometry and kinematics of the OCT and its stacked structures. There have been attempts to design crease-stackable origami tessellations with multiple DOFs, but such origami tessellations are derivatives of the Miura-ori pattern. This chapter proposes a crease-stackable origami tessellation with multiple DOFs. The OCT is a novel flat-foldable and rigidly foldable origami tessellation comprised of both 4Cs and 6Cs. The $M \times N$ OCT is an $M \times N$ grid of claw units, each of which is a 3-DOF 6C. Kinematic analysis on the claw unit reveals that there exists a 1-DOF system of equations

satisfying the relations of the dihedral angles. This system of equations is the claw unit's planar folding mode. A geometric proof shows that the claw unit is crease-stackable when this system of equations is satisfied. This proof shows that there are two sets of creases in the claw unit that always lie in two parallel planes. The claw unit is crease-stackable because reflecting it about one of these planes stacks it with another claw unit. By extension, the $M \times N$ OCT is also crease-stackable.

A numerical method shows that the $M \times N$ OCT features five DOFs when M and N are both at least 2, unlike many other origami tessellations with only one DOF. Each of these five DOFs is described in relation to the geometry of the 2×2 OCT. One of these DOFs is the planar folding mode. This DOF makes two sets of creases in the OCT lie in two parallel planes, which makes the OCT crease-stackable. The planar folding mode is also the sole DOF that remains when copies of OCTs are stacked. For the planar folding mode, no creases are fixed, but for the remaining four folding modes, some of the creases are fixed.

Stacking two claw units along their creases forms the stacked claw unit. Even though the claw unit is a flat-foldable 6C with three DOFs, the stacked claw unit is a flat-foldable and rigidly foldable structure with only one DOF. Similarly, the stacked OCT is formed when sheets of the OCT are stacked along their creases. When M and N are both at least 2, the $M \times N$ OCT has five DOFs, but the stacked $M \times N$ OCT is a flat-foldable and rigidly foldable structure with only one DOF. Unlike stacking sheets of the Miura-ori pattern, stacking sheets of the OCT reduces the number of DOFs from five to one.

A family of claw units is defined as a set of claw units in which any two are crease-stackable with each other. Two claw units in the same family have matching planar zigzags.

This geometric property allows them to form the self-locking stacked claw unit, which folds from a flat folded state to a self-locking state. Similarly, two OCTs generated from claw units in the same family are crease-stackable with each other, and they stack to form the self-locking stacked OCT. The geometry of the self-locking stacked OCT determines its self-locking state, which is useful for the design of deployable structures and mechanical metamaterials.

5

Modular Origami Horn/Claw Chain (MOHC/MOCC)

5.1 Introduction

The previously discussed origami tessellations are repeated geometric patterns that cover a plane, but only a finite section of the plane is used for the models. When these origami tessellations fold, their partially folded states match the shapes of curves. This chapter presents two types of origami tessellations whose partially folded states approximate the shape of a planar curve. This curve is approximated by a piecewise-linear curve, which is then converted to two types of crease patterns. These are the modular origami horn chain, MOHC, and the modular origami claw chain, MOCC. The MOHC consists of truncated horn units, which are 4Cs. Similarly, the MOCC consists of truncated claw units, which are 6Cs. Geometric proofs show that both the MOHC and MOCC are flat-foldable, rigidly foldable, and crease stackable. Stacking two MOHCs forms the stacked MOHC while stacking any even number of MOCC sheets forms the stacked MOCC. Additionally, families of MOHCs and MOCCs exist such that any two MOHCs or MOCCs in the same family are crease-stackable with each other. Stacking distinct MOHCs and MOCCs in the same family forms the self-locking stacked MOHC and self-locking stacked MOCC, respectively.

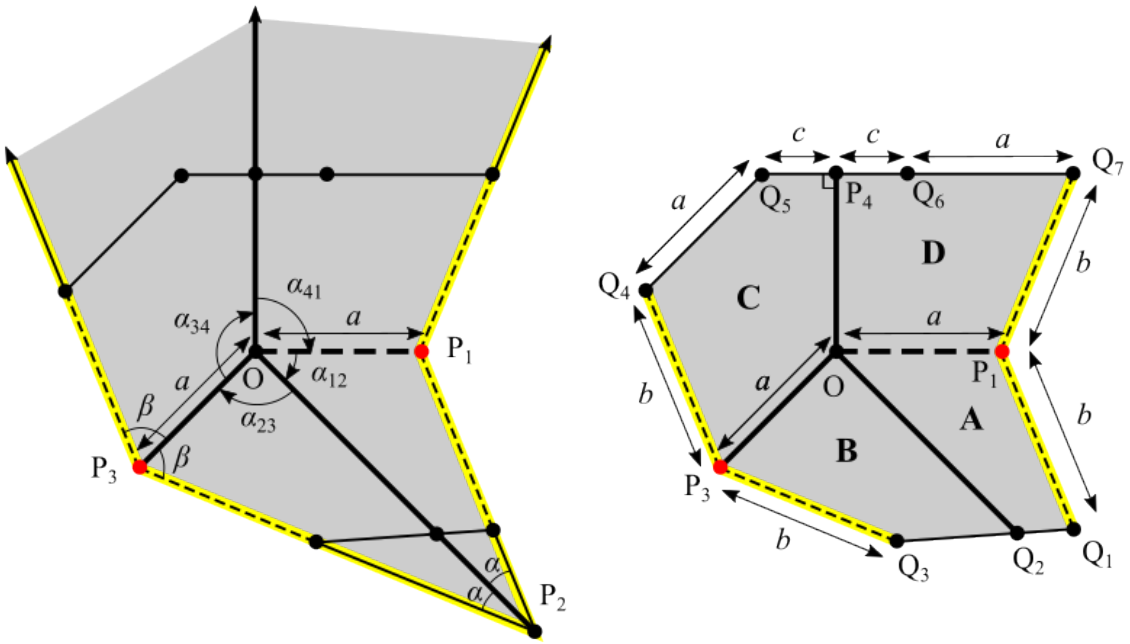
This chapter has the following layout. Section 5.2 examines the geometry and kinematics of the truncated horn units and claw units in the MOHC and MOCC, respectively. Examining these units reveals the geometry and kinematics of the MOHC and MOCC. Here, families of horn units and claw units are defined such that any two in the

same family are crease-stackable with each other. Section 5.3 presents an algorithm that transforms any non-intersecting planar curve into a MOHC and MOCC. The curve is converted to a piecewise-linear approximation, which is then converted to the crease patterns. Section 5.4 examines the construction of stacked MOHCs and stacked MOCCs from multiple MOHCs and MOCCs, respectively. Section 5.5 uses families of MOHCs and MOCCs to construct the self-locking stacked MOHC and self-locking stacked MOCC, respectively. Section 5.6 is a discussion of the origami models constructed.

5.2 Origami Horn and Claw Units

The horn unit is a flat-foldable 4C in which some of its boundary edges lie in a plane, making the horn unit crease-stackable. Let this 4C be a type-M vertex, so it has three mountains and one valley. Let the knuckle vertex be the center vertex of the 4C. Figure 5.1(a) shows a flat-foldable 4C with knuckle vertex O and sector angles, α_{12}, α_{23}, α_{34}, and α_{41}. Kawasaki's theorem states that these angles satisfy: $\alpha_{12} + \alpha_{34} = \alpha_{23} + \alpha_{41} = \pi$ (Hull, 2015). Given a crease length a, contour lines are drawn for the origami horn, which are boundaries of the horn unit shown in yellow. Let the bridge points, P_1 and P_3, be on the intersections of the horn unit's creases and the contour lines such that $OP_1 = OP_3 = a$, as shown in Figure 5.1(a). The following formulas describe angles α and β in terms of the horn unit's sector angles:

$$\alpha = \frac{\alpha_{41} - \alpha_{12}}{2}, \quad \beta = \frac{\alpha_{41} + \alpha_{12}}{2}. \tag{5.1}$$



(a) (b)

Figure 5.1: Horn unit (a) crease pattern and (b) truncated horn unit

As shown in Figure 5.1(a), the shaded region is an infinite region bounded by the contour lines. The four creases in the horn unit are the angle bisectors of the shaded region. The size of the horn unit is proportional to crease length a, which is independent of the values of α and β. Truncating the horn-shaped infinite region results in the truncated horn unit in Figure 5.1(b), which depends on side length b. This truncated horn unit has the following lengths: $P_1Q_1 = P_1Q_7 = P_3Q_3 = P_3Q_4 = b$ and $OP_1 = OP_3 = Q_4Q_5 = Q_6Q_7 = a$. Also, OP_1 and Q_6Q_7 are parallel, as are OP_3 and Q_4Q_5. The truncated horn unit consists of four panels: A, B, C, and D. Vertex Q_2 lies on Q_1Q_3, and panels A and B are the quadrilaterals obtained when line Q_1Q_3 truncates triangles OP_1P_2 and OP_2P_3, respectively, in Figure 5.1(b). Given $c = b(\sin\alpha)$, crease OP_4 is a perpendicular bisector of Q_5Q_6, such that $Q_5Q_6 = Q_5Q_6 = c$. Panels C and D are pentagons that are each a concatenation of a

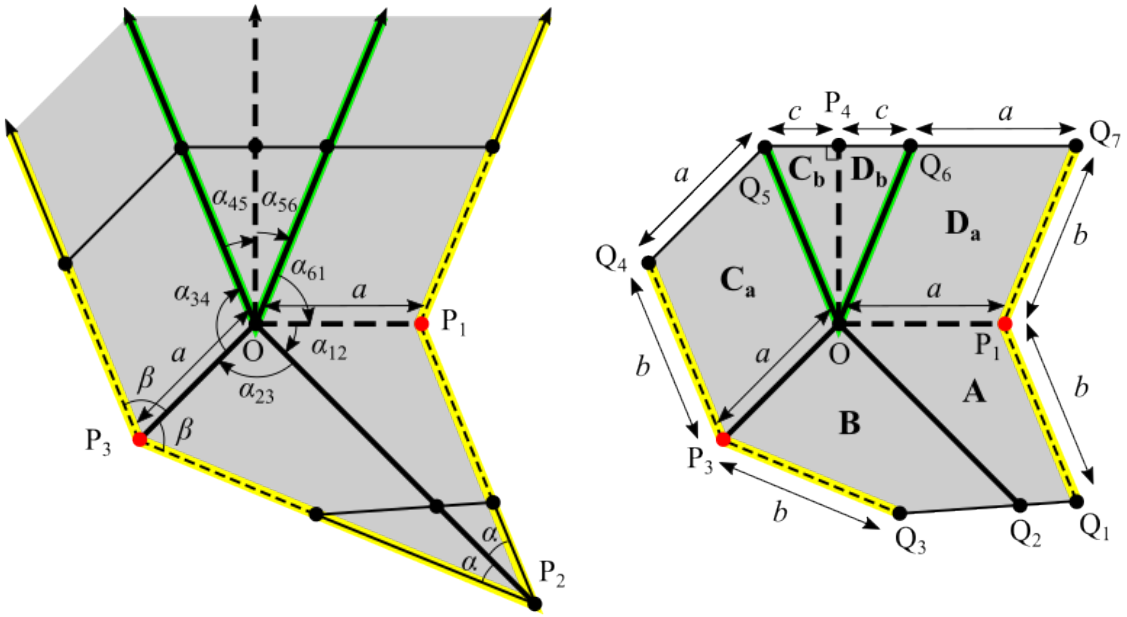
parallelogram and a right triangle. The geometry of the truncated horn unit in Figure 5.1(b) has parameters, α, β, a, and b, which have the following bounds:

$$0 < \alpha < \beta < \frac{\pi}{2}, \tag{5.2}$$

$$0 < b \leq \frac{a \sin(\beta - \alpha)}{\sin(\alpha)}. \tag{5.3}$$

The shape of the truncated horn unit in Figure 5.1(b) ensures the four yellow creases are coplanar regardless of the partially folded state, which will later be proven geometrically.

A similar procedure will construct the claw unit, a flat-foldable 6C in which some of its creases lie on two parallel planes, making the claw unit crease-stackable. Adding two creases incident to the knuckle vertex to the 4C in Figure 5.1(a) forms a 6C. These two added creases are mountains, and the parity of the crease between them is flipped, as shown in Figure 5.2(a). The 6C has four mountains and two valleys, making it a type-M vertex. Moreover, let the two added creases in green be parallel to the two closest contour lines in yellow, respectively. The sector angles are α_{12}, α_{23}, α_{34}, α_{45}, α_{56}, and α_{61}, and according to Kawasaki's theorem they satisfy $\alpha_{12} + \alpha_{34} + \alpha_{56} = \alpha_{23} + \alpha_{45} + \alpha_{61} = \pi$ (Hull, 2015). The angle equality, $\alpha_{45} = \alpha_{56}$, must be satisfied to make the 6C flat-foldable.



(a) (b)

Figure 5.2: Claw unit (a) crease pattern and (b) truncated claw unit

Angles α and β correspond to those in the origami horn unit in Figure 5.1(a). The following angle equations hold: $\alpha = \alpha_{45} = \alpha_{56}$ and $\beta = (\pi - \alpha_{34}) = \alpha_{61}$. Truncating the infinite region enclosed by the contour lines results in the truncated claw unit in Figure 5.2(b), which depends on crease length b. The truncated claw unit in Figure 5.2(b) is the same shape as the truncated horn unit in Figure 5.1(b) with two additional creases, OQ_5 and OQ_6. The truncated claw unit consists of six panels: A, B, C_a, C_b, D_a, and D_b. Panels A and B in Figure 5.2(b) are congruent to those in Figure 5.1(b). Panels C_a and D_a are congruent parallelograms, and panels C_b and D_b are congruent right triangles. The geometry of the truncated claw unit in Figure 5.2(b) has input parameters α, β, a, and b, which are restricted by equations (5.2) and (5.3). The shape of the truncated claw unit in Figure 5.2(b) ensures there is a folding mode in which the four yellow creases are coplanar regardless of the

partially folded state. Additionally, the plane containing the yellow creases is parallel to the plane containing the green creases, which will later be proven geometrically.

The kinematics of the horn and claw units in Figures 5.1(b) and 5.2(b), respectively, reveals the relations among their dihedral angles when these units are rigidly folded. Let the four dihedral angles of the horn unit in Figure 5.3(a) be ϕ_1, ϕ_2, ϕ_3, and ϕ_4 when it is in the partially folded state shown in Figure 5.3(b). The matrix method gives the following equations:

$$\phi_1 = \phi_3,\ \phi_2 = \phi_4,\ \cos\beta \tan\frac{\phi_1}{2} = \cos\alpha \tan\frac{\phi_2}{2}. \tag{5.4}$$

Let ϕ_1 be the input dihedral angle. The remaining dihedral angles are computed using the equations in (5.4), giving the horn unit only one DOF.

The following proof shows that all yellow creases in the horn unit lie in a plane. Each pair of yellow creases in Figure 5.3(b) lies on a plane, which forms two dihedral angles with two panels in the horn unit. These pairs of yellow creases overlap, so there are cases in which two dihedral angles are defined on a given crease. The plane and adjacent panel will be specified for each dihedral angle. The yellow creases in panels A and D in Figure 5.3(b) lie in a plane. Let ϕ_{A1} and ϕ_D be the angles between this plane and panels A and D, respectively, as shown in Figure 5.3(b). By symmetry of the sector angles in panels A and D, $\phi_{A1} = \phi_D$. By spherical law of cosines, the following equation holds:

$$\tan\phi_{A1} = \left(\cos\beta \tan\frac{\phi_1}{2} \right)^{-1}. \tag{5.5}$$

The yellow creases on panels A and B in Figure 5.3(b) lie in another plane. Let ϕ_{A2} and ϕ_{B1} be the angles between this plane and panels A and B, respectively, as shown in Figure

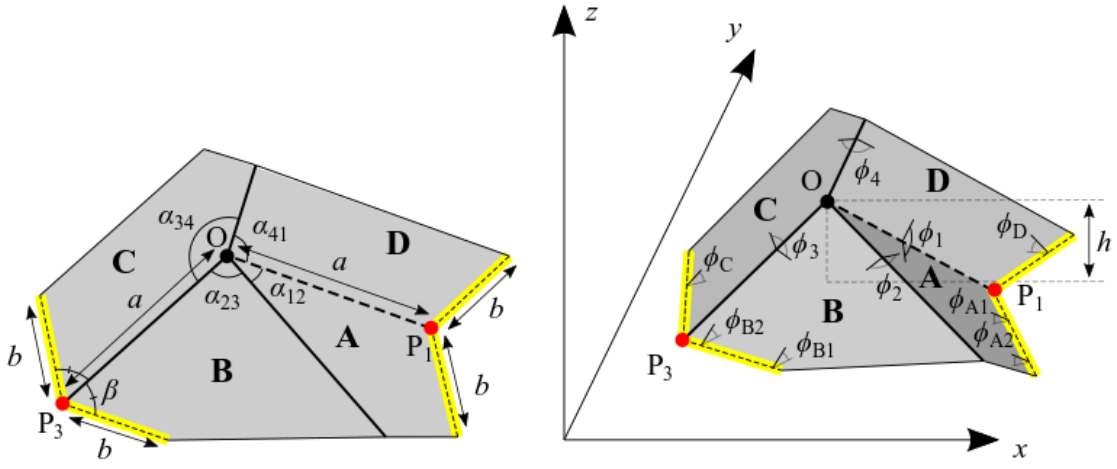
5.3(b). By symmetry of the sector angles in panels A and B, $\phi_{A2} = \phi_{B1}$. By spherical law of cosines, the following equation holds:

$$\tan\phi_{B1} = \left(\cos\alpha \tan\frac{\phi_2}{2}\right)^{-1}. \tag{5.6}$$

The yellow creases on panels B and C in Figure 5.3(b) lie in another plane. Let ϕ_{B2} and ϕ_C be the angles between this plane and panels B and C, respectively, as shown in Figure 5.3(b). By symmetry of the sector angles in panels B and C, $\phi_{B2} = \phi_C$. By spherical law of cosines, the following equation holds:

$$\tan\phi_{B2} = \left(\cos\beta \tan\frac{\phi_1}{2}\right)^{-1}. \tag{5.7}$$

The relations in (5.4), (5.5), (5.6), and (5.7) imply that $\phi_{A1} = \phi_D = \phi_{A2} = \phi_{B1} = \phi_{B2} = \phi_C$, so all three of the given planes are identical. Therefore, all four yellow creases in Figure 5.3(b) are coplanar regardless of the partially folded state, making the horn unit crease stackable.



(a) (b)

Figure 5.3: Truncated horn unit: (a) flat unfolded state and (b) partially folded state

Suppose the horn unit in Figure 5.3(b) is in 3D coordinate space, such that the yellow creases lie in the *xy*-plane, and the rest of the model lies in the space in which *z* is positive. Let the *z*-coordinate of the knuckle vertex be the knuckle height, *h*, of the horn unit in this partially folded state. Using the relations in (5.4), the following is the formula for *h*:

$$h = \frac{a \sin\beta}{\sqrt{1 + \left(\cos\beta \tan\frac{\phi_1}{2} \right)^2}}. \tag{5.8}$$

The formula for the *h* in (5.8) only depends on a, β, and ϕ_1, so it is independent of α. This equation will prove useful when stacking horn units.

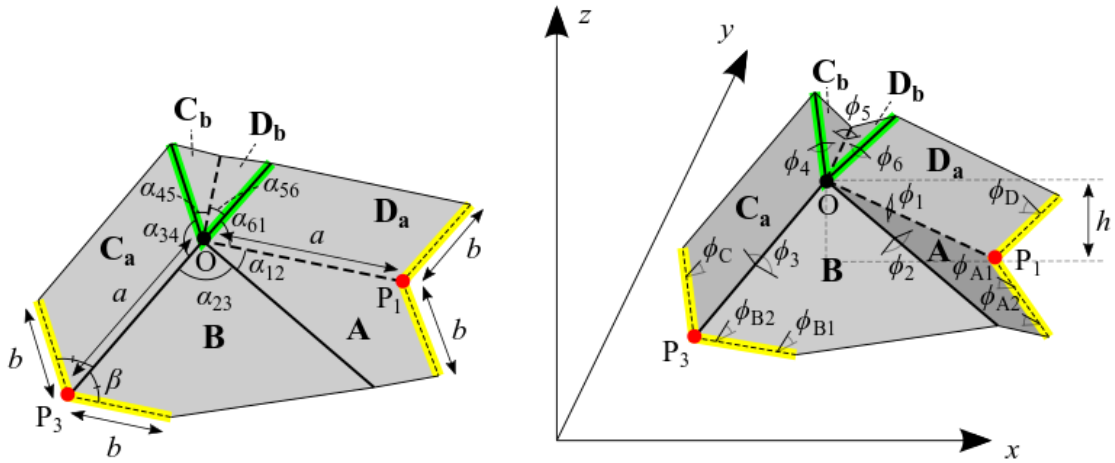
Now consider the claw unit. Let the six dihedral angles of the claw unit in Figure 5.4(a) be ϕ_1, ϕ_2, ϕ_3, ϕ_4, ϕ_5, and ϕ_6 when it is in the partially folded state shown in Figure 5.4(b). The matrix method gives equations (C.4), (C.5), and (C.6), which are derived in Appendix C. These three equations are a 3-DOF system of equations. Suppose the following dihedral angle equalities hold: $\phi_1 = \phi_3$ and $\phi_2 = \phi_5$. Equations (C.4), (C.5), and (C.6) in Appendix C can be simplified to the following 1-DOF system of equations:

$$\phi_1 = \phi_3,\ \phi_2 = \phi_5,\ \phi_4 = \phi_6,\ \cos\beta \tan\frac{\phi_1}{2} = \cos\alpha \tan\frac{\phi_2}{2} = \tan\frac{\phi_4}{2}. \tag{5.9}$$

Let ϕ_1 be the input dihedral angle. The remaining dihedral angles can be computed using the equations in (5.9), making the claw unit rigidly foldable. When the claw unit folds according to the relations in (5.9), the four yellow creases in Figure 5.4(b) are coplanar. The proof used to show the yellow creases in the horn unit lie in a plane can be used to show the yellow creases in the claw unit also lie in a plane.

The discovery of the equations in (5.9) came from the similarity between the geometry of the claw unit and the geometry of the horn unit. Panels C_a and C_b in Figure 5.4 combine to make panel C in Figure 5.3, and panels D_a and D_b in Figure 5.4 combine to make panel D in Figure 5.3. As a result, the claw unit in Figure 5.4(b) can be converted to the horn unit in Figure 5.3(b) by inverting the crease between panels C_b and D_b while the other panels remain fixed. The horn unit's dihedral angle relations imply that $\phi_1 = \phi_3$ and $\phi_2 = \phi_5$, which are the angle equalities used to obtain the system of equations in (5.9). When the claw unit folds according to (5.9), it is crease-stackable like the horn unit.

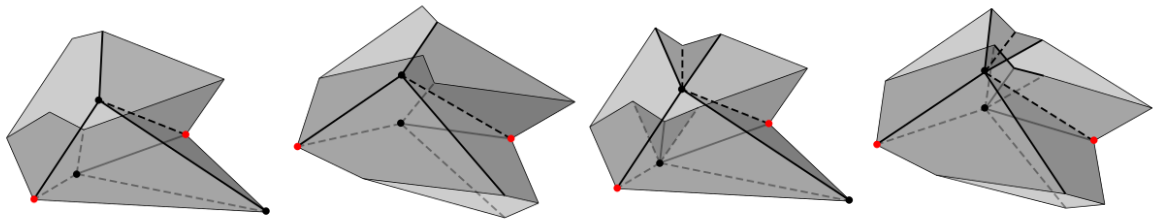
The green and yellow creases in panel C_a are parallel, and so are the green and yellow creases in panel D_a. Therefore, the plane containing the yellow creases is parallel to the plane containing the green creases in Figure 5.4(b). Also, the distance between these two planes is h, which is computed using equation (5.8). Therefore, both the horn units and claw units are flat-foldable, rigidly foldable, and crease stackable.



(a) (b)

Figure 5.4: Truncated claw unit: (a) flat unfolded state and (b) partially folded state

The horn unit in Figure 5.3 and claw unit in Figure 5.4 are type-M units. For each unit, the yellow creases are always coplanar. Reversing the crease parities in their crease patterns results in the type-V horn unit and type-V claw unit. Stacking the type-M horn unit on the type-V horn unit along their coplanar creases results in the stacked horn unit. Stacking the type-M claw unit on the type-V claw unit in a similar manner results in the stacked claw unit. Truncating these stacked origami models preserves their kinematics as long as the connections between adjacent panels are preserved. Since the stacked horn unit in Figure 5.5(a) is flat-foldable and rigidly foldable with one DOF, the truncated stacked horn unit in Figure 5.5(b) is as well. The same properties apply to the stacked claw unit in Figure 5.5(c) and the truncated stacked claw unit in Figure 5.5(d). The stacked units in Figure 5.5 show the horn units and claw units are crease-stackable with mirror images of themselves.



(a) (b) (c) (d)

Figure 5.5: Stacked units: (a) stacked horn unit, (b) truncated stacked horn unit, (c) stacked claw unit, and (d) truncated stacked claw unit

The connections diagrams in Figure 5.6(a) and (b) indicate connections between the panels in the stacked horn unit and stacked claw unit, respectively. Panels are black dots, and lines connect adjacent panels. For the stacked horn unit in Figure 5.6(a), panels A_1, A_2, B_2, and B_1, panels A_1, A_2, D_2, and D_1, and panels B_1, B_2, C_2, and C_1, panels C_1, C_2,

D_2, and D_1, panels A_1, B_1, C_1, and D_1, and panels A_2, B_2, C_2, and D_2 each form a spherical 4-bar linkage. For the stacked claw unit in Figure 5.6(b), panels A_1, A_2, B_2, and B_1, panels A_1, A_2, D_{2a}, and D_{1a}, and panels B_1, B_2, C_{2a}, and C_{1a} each form a spherical 4-bar linkage. Also, panels A_1, B_1, C_{1a}, C_{1b}, D_{1b}, and D_{1a} and panels A_2, B_2, C_{2a}, C_{2b}, D_{2b}, and D_{2a} each form a spherical 6-bar linkage. The geometric proof for the stacked claw unit in Section 4.4 shows that the linkages are compatible for both the stacked horn unit in Figure 5.6(a) and stacked claw unit in Figure 5.6(b). This proof shows that only one input dihedral angle is needed to determine the remaining ones, so both the stacked horn unit and stacked claw unit have only one DOF.

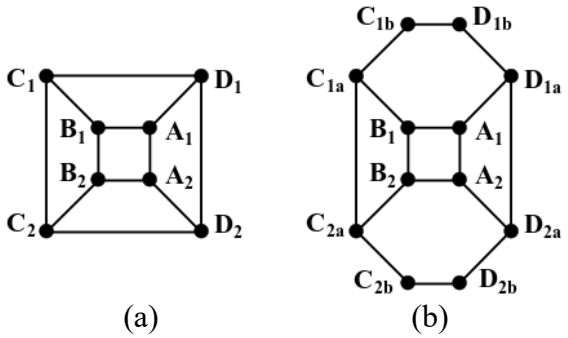


Figure 5.6: Connections diagrams: (a) the stacked horn unit and (b) stacked claw unit

While horn units are crease stackable with copies of each other, they are also crease stackable with other distinct horn units. A family of horn units is a set of horn units such that any two of them are crease-stackable with each other. The geometry of the horn unit is uniquely determined by parameters: α, β, a, and b. Given two horn units in the same family, crease length b is constant, and the following relations hold:

$$\frac{\tan\alpha_1}{\tan\beta_1} = \frac{\tan\alpha_2}{\tan\beta_2}, \tag{5.10}$$

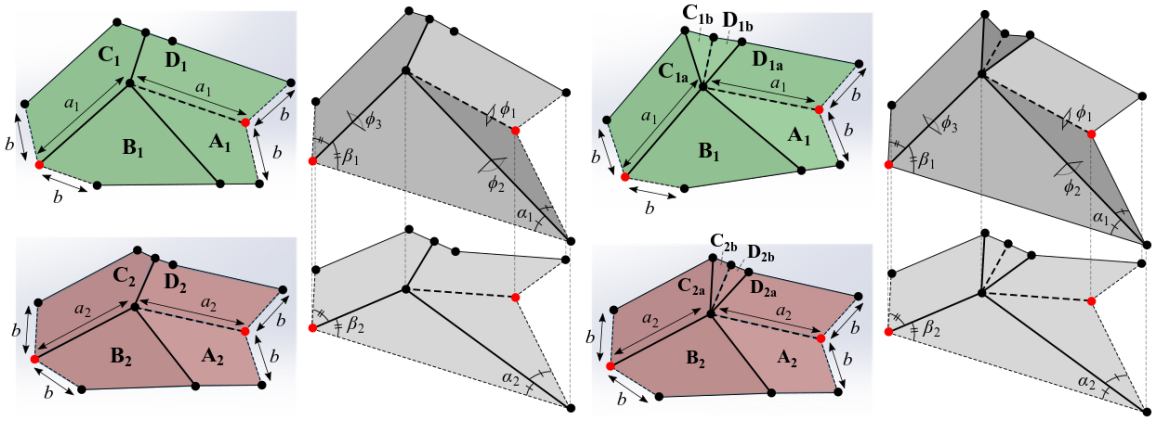
$$a_1 \cos\beta_1 = a_2 \cos\beta_2. \tag{5.11}$$

The relations in (5.10) and (5.11) are direct results from the law of sines. In Figure 5.7(a), the green and red horn units have $(\alpha_1, \beta_1) = (\pi / 6, \pi / 3)$ and $(\alpha_2, \beta_2) = (\tan^{-1}(1 / 3), \pi / 4)$, respectively.

The planar projection property demonstrates that the two distinct horn units in Figure 5.7(a) are in the same family. Previous proofs show that four boundary lines of the horn unit always lie on a common plane. The projection of the four creases incident to the knuckle vertex onto this plane is the crease pattern of a 4C, as shown in Figure 5.7(b). This 4C is flat-foldable, so another horn unit can be drawn from it. The two horn units in Figure 5.7(b) each have four boundary creases that form matching planar zigzags. The geometric proof in Section 4.5 describing the conditions for claw units to have matching planar zigzags applies to the horn units as well. These conditions, which are expressed in equation (4.22) in Section 4.5, are equivalent to equations (5.10) and (5.11). The two horn units in Figure 5.7(b) are crease-stackable with each other because when they are folded according to (5.9), their planar zigzags match. Therefore, the planar projection of any horn unit is another horn unit in the same family.

The claw units are also crease-stackable with other distinct claw units. A family of claw units is a set of claw units such that any two of them are crease-stackable with each other. The geometry of the claw unit is also uniquely defined by parameters α, β, a, and b. Given two claw units in the same family, crease length b is constant and equations (5.10) and (5.11) hold. In Figure 5.7(c), the green and red claw units have $(\alpha_1, \beta_1) = (\pi / 6, \pi / 3)$ and $(\alpha_2, \beta_2) = (\tan^{-1}(1 / 3), \pi / 4)$, respectively. The planar projection property also holds

for claw units, as shown in Figure 5.7(d). Stacking horn units and claw units from the same family forms self-locking stacked structures, which will be shown in a later section.



(a) (b) (c) (d)

Figure 5.7: Units in the same family:

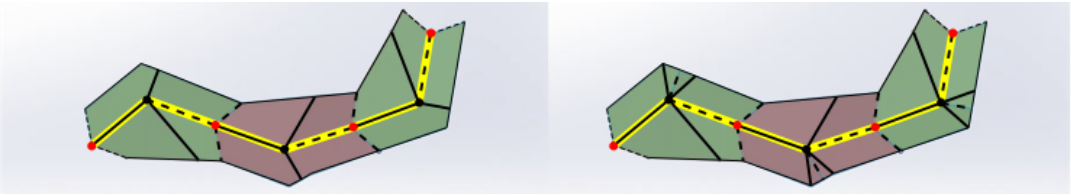
(a) two horn units, (b) projecting one horn unit on the other,

(c) two claw units, and (d) projecting one claw unit on the other.

So far, the horn unit and claw unit are shown to be flat-foldable, rigidly foldable, and crease-stackable. They are also crease stackable with units in the same family. The horn units and claw units are concatenated to form the MOHC and MOCC, respectively, which are flat-foldable, rigidly foldable, and crease-stackable as well. Families of MOHCs and MOCCs are defined similarly to the families of horn units and claw units. The geometry of the horn unit and claw unit can be adjusted, which allows the MOHC and MOCC to match the shapes of planar curves.

5.3 MOHC and MOCC Construction Algorithm

The modular origami horn chain, MOHC, is an origami tessellation composed of horn units, and the modular origami claw chain, MOCC, is an origami tessellation composed of claw units. For the MOHC and MOCC, the shape of the origami tessellation is the connected piecewise-linear curve of creases that passes through each unit. Figure 5.8(a) and Figure 5.8(b) show a MOHC and MOCC, respectively, whose shapes are the lines of creases highlighted. The vertices these lines pass through alternate between knuckle vertices in black and bridge vertices in red. Knuckle vertices are the vertices of the 4Cs and 6Cs for the horn units and claw units, respectively. Bridge vertices are the vertices on the boundaries between consecutive units. Both origami tessellations in Figure 5.8 are flat-foldable, and their fully unfolded states match the shape of a planar curve.



(a) (b)

Figure 5.8: Origami tessellations matching the shape of a planar curve:
(a) MOHC and (b) MOCC

The following design algorithm converts the non-intersecting planar curve to a MOHC and MOCC. First, the planar curve is converted to a piecewise-linear approximation. Crease length, a, is an input, and the smaller the crease length, the closer the approximation. Let the first knuckle vertex be one of the endpoints of the planar curve, as shown in Figure 5.9(a). A circular arc with radius $2a$ centered at the knuckle vertex is

drawn such that the arc intersects the planar curve, as shown in Figure 5.9(b). The intersection between the arc and the planar curve is the next knuckle vertex. This construction is repeated along the planar curve, as shown in Figure 5.9(c). Finally, the knuckle vertices are connected in sequential order. The midpoints between consecutive knuckle vertices are bridge vertices, as shown in Figure 5.9(d). In the piecewise-linear approximation in Figure 5.9(d), the distance between consecutive vertices is a, and the distance between consecutive knuckle vertices is $2a$. The shape of the piecewise-linear approximation is determined by the angles at each knuckle vertex, which are γ_1, γ_2, and γ_3 for the example in Figure 5.9(d). The number of angles in this list equals number of units in the MOHC and MOCC.

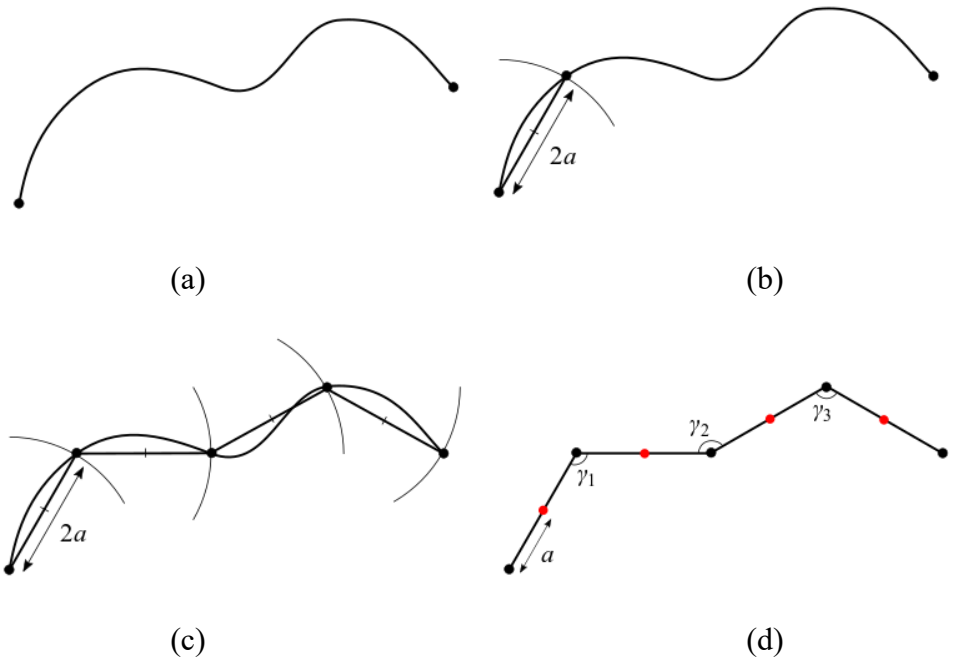
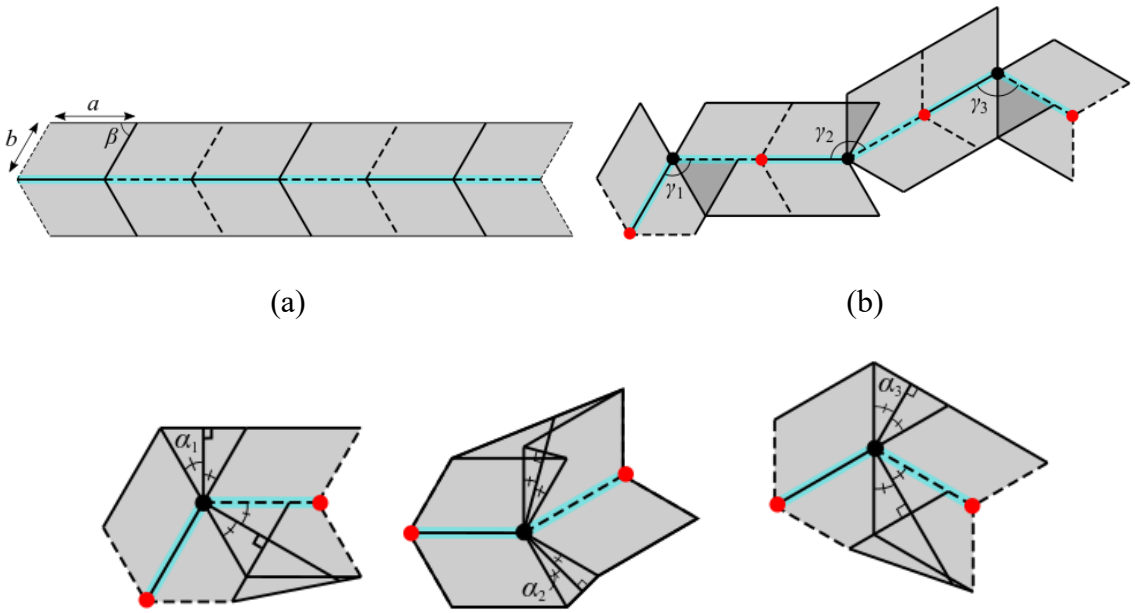


Figure 5.9: Converting a planar curve to a piecewise-linear approximation: (a) planar curve, (b) marking next vertex, (c) continuing to mark vertices, and (d) connecting the vertices and marking the midpoints of the segments

Next, the templates of the horn units and claw units are constructed using the piecewise-linear approximation in Figure 5.9(d). Given a pair of congruent parallelograms with lengths a and b and acute angle β, the Miura-ori crease pattern shown in Figure 5.10(a) is constructed. The highlighted line in this pattern is a straight line. The panels are rotated about the knuckle vertices, as shown in Figure 5.10(b), so that the highlighted line matches the shape of the piecewise-linear approximation in Figure 5.9(d). Four parallelogram panels are incident to each knuckle vertex, as shown in Figure 5.10(b), and the geometry of each template depends on the arrangement of the parallelograms. Angle β is provided, and for every angle γ at a knuckle vertex, angle α can be determined from $\alpha = (\pi - \gamma) / 2$. To prevent self-intersections, angle γ at any knuckle vertex has the following restrictions: $(\pi - \beta) \leq \gamma \leq \pi$. The templates for the horn units and claw units are shown in Figure 5.10(c). Each template contains all creases found in the horn units and claw units in their flat states.



(a) (b)

(c)

Figure 5.10: Constructing templates for horn units and claw units: (a) Miura-ori pattern, (b) rotating panels, and (c) templates for the horn units and claw units

The horn units and claw units can be constructed from the templates in Figure 5.10(c). The horn units in Figure 5.11(a) are concatenated to form the MOHC in Figure 5.11(b). Similarly, the claw units in Figure 5.11(c) are concatenated to form the MOCC in Figure 5.11(d). The horn unit and claw unit are flat-foldable and rigidly foldable. Each of the bridge vertices joining two adjacent horn units or two claw units is a symmetric flat-foldable 4C. Therefore, the MOHC and MOCC in Figure 5.11(b) and (d), respectively, are flat-foldable and rigidly foldable.

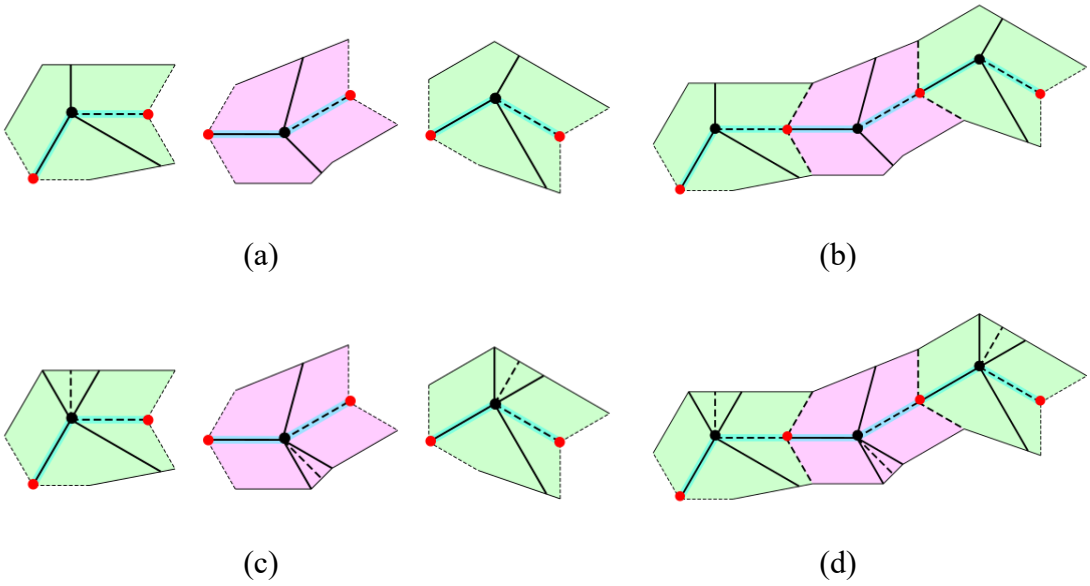


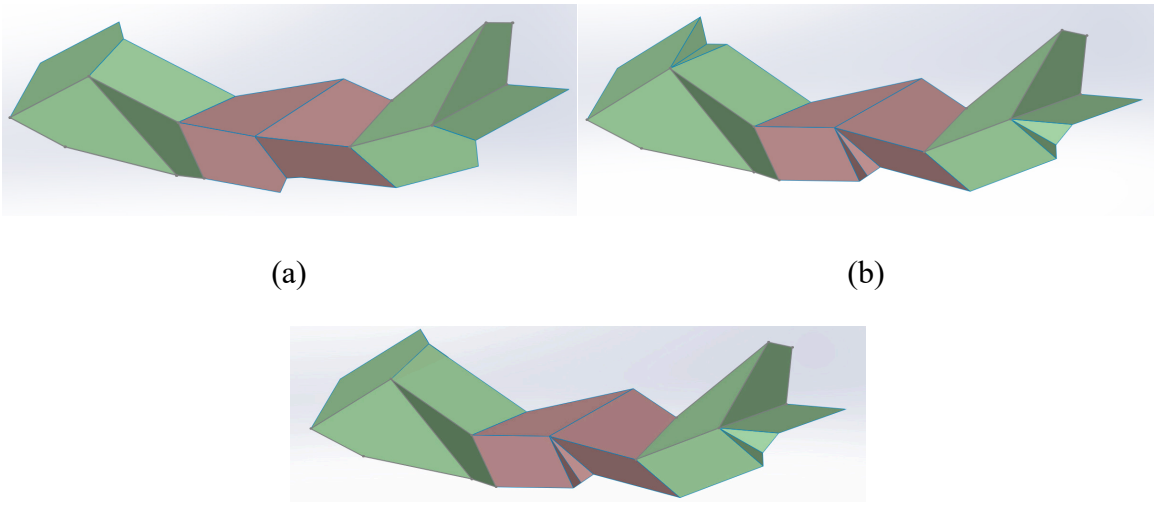
Figure 5.11: Concatenating horn units and claw units:

(a) horn units form (b) a MOHC and (c) claw units form (d) a MOCC

Each of the horn units in the MOHC can fold according to the equations in (5.4). Each bridge vertex joining two adjacent horn units is a symmetric 4C like the one found in the classical Miura-ori pattern. Equation (3.19) in Section 3.4 states that the dihedral angles of any two opposite creases in the bridge vertex are equal. Therefore, the dihedral angles of the creases along the highlighted line in Figure 5.11(b) are all equal. As the MOHC

folds, its horn units fold simultaneously. Each of the claw units in the MOCC can fold according to the equations in (5.9). At each bridge vertex joining two adjacent claw units, the dihedral angles of any two opposite creases are equal. Therefore, the dihedral angles of the creases along the highlighted line in Figure 5.11(d) are all equal. As the MOCC folds, its claw units fold simultaneously.

For both the MOHC and MOCC, angle β for each unit is constant, but angle α varies. The MOHC and MOCC in Figure 5.12(a) and Figure 5.12(b), respectively, have $\beta = \pi / 3$ and $(\alpha_1, \alpha_2, \alpha_3) = (\pi / 6, \pi / 9, \pi / 6)$ for the units from left to right. The horn units and claw units can even be combined into a hybrid chain, as shown in Figure 5.12(c). Let dihedral angle, ϕ_1, be the input angle, which determines the partially folded state of the MOHC and MOCC. The knuckle height, h, of the MOHC and MOCC can be calculated using equation (5.8) on any unit in the chain. The knuckle height of the MOHC and MOCC is a well-defined function of ϕ_1 because a and β are constant, and h is independent of α.



(a) (b)

(c)

Figure 5.12: Origami chains in partially folded states:

(a) MOHC, (b) MOCC, and (c) a chain combining horn units and claw units

The MOHC and MOCC have a plane containing all bridge vertices, and the distance between any knuckle vertex and this plane is the knuckle height. Also, both the MOHC and MOCC have a second plane containing all knuckle vertices. For both the MOHC and MOCC, let the plane containing the bridge vertices be the bridge plane, and let the plane containing the knuckle vertices be the knuckle plane. The knuckle plane and bridge plane are parallel. The MOHC contains a set of creases that always lie in the bridge plane. The MOCC contains a set of creases that always lie in the bridge plane and a set of creases that always lie in the knuckle plane. If the crease patterns of the MOHC and MOCC do not self-intersect, then the origami tessellations never experience self-collision as they fold. Each of the horn units and claw units possesses the planar projection property. Therefore, the planar projections of the MOHC and MOCC in a partially folded state are a MOHC and MOCC, respectively, in the same family.

Figure 5.13 shows a physical model of a MOHC composed of 8 identical horn units. The planar curve is a circle, which makes the piecewise-linear approximation an octagon. Each horn unit has the following parameters: $\alpha = \pi / 8$, $\beta = 3\pi / 8$, $a = 4$, and $b = 5$. As the MOHC folds from its fully unfolded state to its fully folded state, its corresponding piecewise-linear curve straightens into a line.

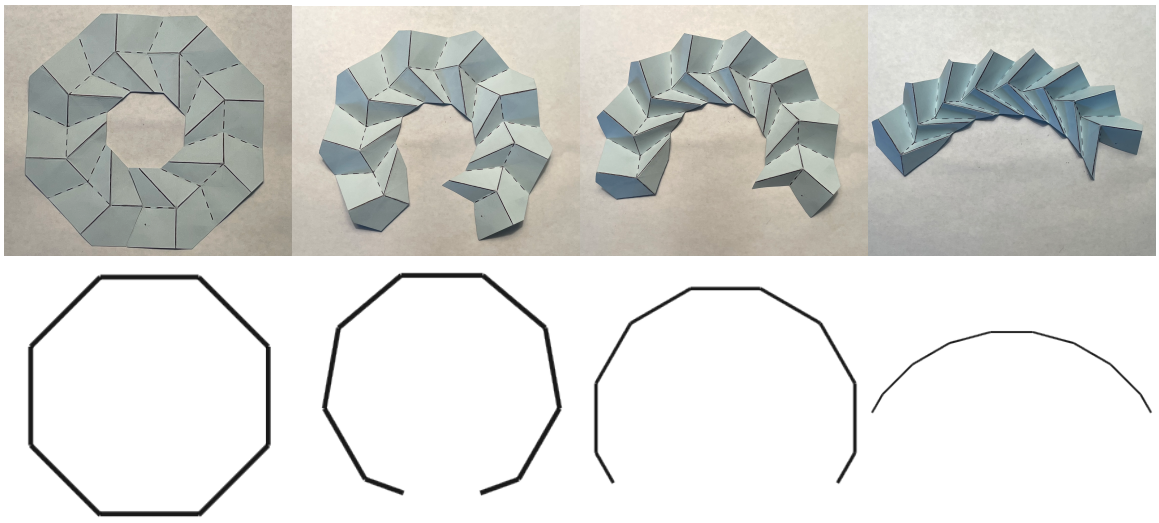


Figure 5.13: Deployment of a MOHC and its piecewise-linear curves

The transformation of the piecewise-linear curve in Figure 5.13 suggests a method to construct a MOHC and MOCC matching a planar curve in a specific partially folded state determined by input dihedral angle, ϕ_1. The piecewise-linear curve is converted to a new piecewise-linear curve based on the given values of α, β, and ϕ_1. Then, the previous algorithm is used to convert the new piecewise-linear curve to a MOHC and MOCC, which deploy to match the shape of the original planar curve at the given value of ϕ_1.

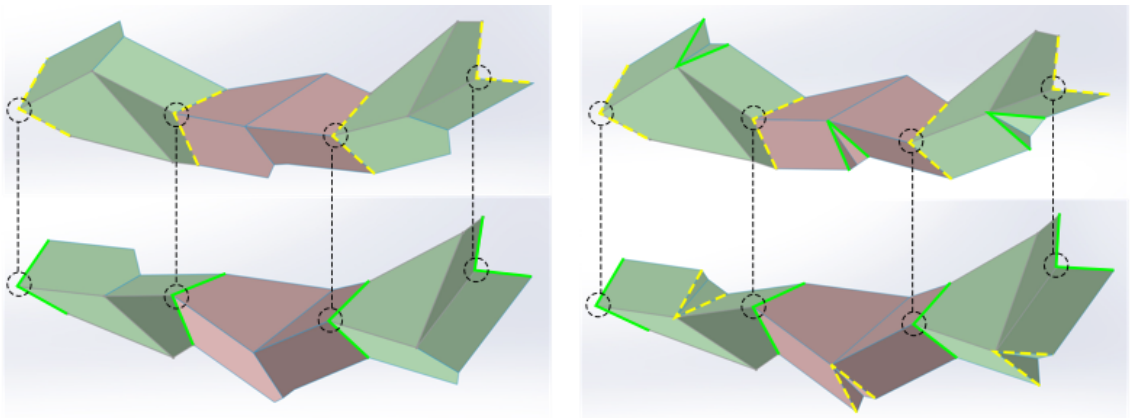
Given a MOHC and MOCC with angle parameters, α and β, and crease lengths, a and b, constructed from a piecewise-linear curve, a new MOHC and MOCC can be constructed. Each segment in the original piecewise-linear curve has length a, and the angle at each knuckle vertex in the curve is γ, in which $\gamma = \pi - 2\alpha$. To create a new piecewise-linear curve, each value of α, β, a, and b is replaced with α', β', a', and b', respectively. The value of b remains constant, so $b = b'$. Using the formulas describing families of horn and claw units, the following identity holds:

$$\sin\beta = \sin\beta' \sin\left(\frac{\phi_1}{2}\right). \tag{5.12}$$

Equations (5.10) and (5.11) are used to compute angle, α', and crease length, a'. Given the values of α', β', a', and b', the new piecewise-linear curve can be drawn. The previous algorithm is used to construct a MOHC and MOCC from this new piecewise-linear curve. The MOHC and MOCC match the shape of the original piecewise-linear curve at the partially folded state determined by input dihedral angle, ϕ_1.

5.4 Stacked MOHC and MOCC

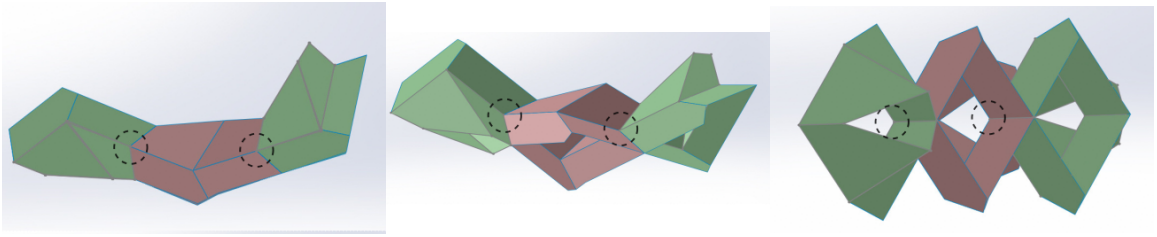
The MOHC and MOCC can deploy to match the shape of a non-intersecting planar curve, but as a single sheet, each of these origami tessellations lacks strength. Stacking MOHCs and MOCCs forms stacked structures that also deploy to match the shape of the planar curve. The stacked MOHC is composed of two MOHCs that have opposite crease parities. The type-M MOHC is composed of type-M horn units, and the type-V MOHC is composed of type-V horn units. Figure 5.14(a) shows a type-M MOHC stacked on a type-V MOHC to form the stacked MOHC. Similarly, the type-M MOCC is composed of type-M claw units, and the type-V MOCC is composed of type-V claw units. Figure 5.14(b) shows a type-M MOCC stacked on a type-V MOCC to form the stacked MOCC. Both the MOHC and MOCC have the following angle values for the units from left to right: $\beta = \pi / 3$ and $(\alpha_1, \alpha_2, \alpha_3) = (\pi / 6, \pi / 9, \pi / 6)$.



(a) (b)

Figure 5.14: Stacking two origami chains: (a) stacking MOHCs and (b) stacking MOCCs

The stacked MOHC can fold from its flat unfolded state in Figure 5.15(a) to a partially folded state in Figure 5.15(b) to its flat folded state in Figure 5.15(c). The stacked MOHC matches the shape of the planar curve in its flat unfolded state. This stacked structure folds with only one DOF because each of its stacked horn units has only one DOF. There is a Double 4C at each of the bridge vertices, which are circled in Figure 5.15. The graph in Figure 5.16 shows the relations between ϕ_1 and the other dihedral angles in the leftmost horn unit with angles $\alpha = \pi / 6$ and $\beta = \pi / 3$. The partially folded states of the MOHC in Figure 5.15(a – c) are represented by the vertical dotted lines (a – c), respectively, in the graph.



(a) (b) (c)

Figure 5.15: A stacked MOHC: (a) fully unfolded state,

(b) partially folded state, and (c) fully folded state

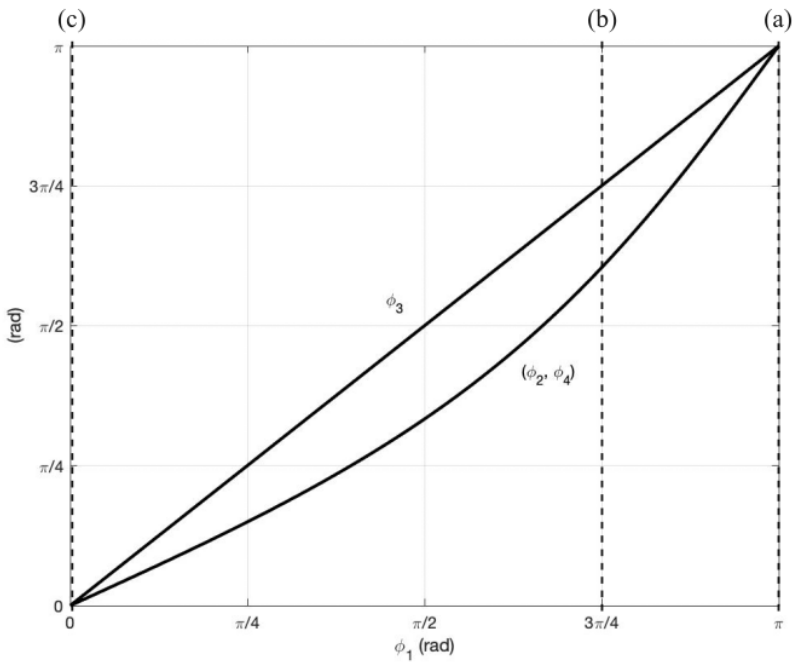
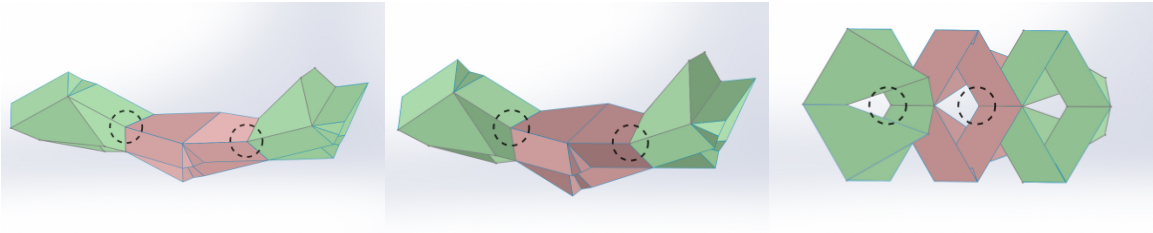


Figure 5.16: Dihedral angle relations in the MOHC with $\alpha = \pi / 6$ and $\beta = \pi / 3$

The stacked MOCC can fold from its flat unfolded state in Figure 5.17(a) to a partially folded state in Figure 5.17(b) to its flat folded state in Figure 5.17(c). The stacked MOCC matches the shape of the planar curve in its flat unfolded state. This stacked structure folds with only one DOF because each of its stacked claw units has only one DOF. There is a Double 4C at each of its bridge vertices, which are circled in Figure 5.17. The graph in Figure 5.18 shows the relations between ϕ_1 and the other dihedral angles in the leftmost claw unit with angles $\alpha = \pi / 6$ and $\beta = \pi / 3$. The partially folded states of the MOCC in Figure 5.17(a – c) are represented by the vertical dotted lines (a – c), respectively, in the graph.

While the stacked MOHC is composed of only two MOHCs, the stacked MOCC can be composed of any even number of MOCCs. The sheets in the stacked MOCC alternate between type-M and type-V MOCCs. Figure 5.17 shows a type-M MOCC stacked

on a type-V MOCC to form a 2-layer stacked MOCC. Figure 5.19 shows two 2-layer stacked MOCCs stacked to form a 4-layer stacked MOCC.



(a) (b) (c)

Figure 5.17: A 2-layer stacked MOCC: (a) fully unfolded state, (b) partially folded state, and (c) fully folded state

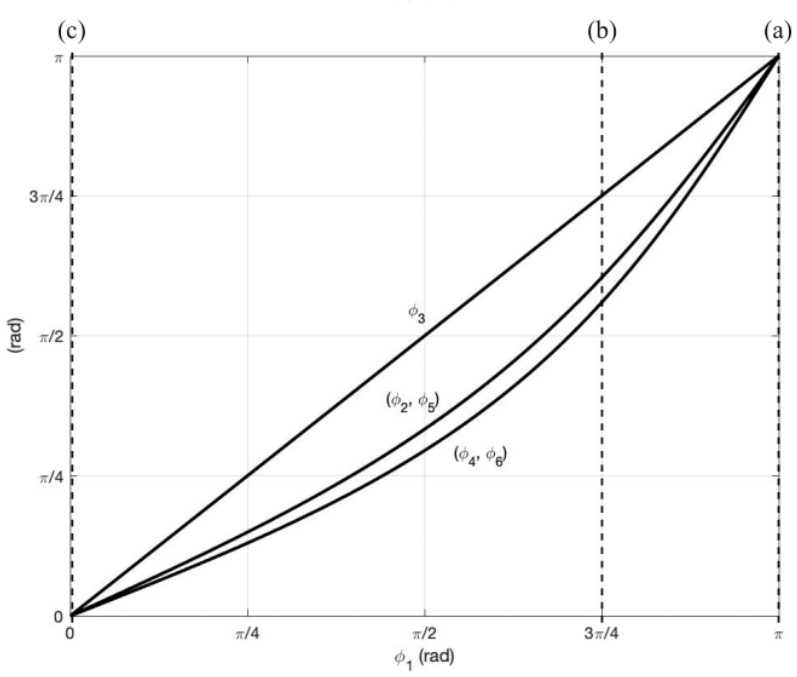


Figure 5.18: Dihedral angle relations in the MOCC with $\alpha = \pi / 6$ and $\beta = \pi / 3$

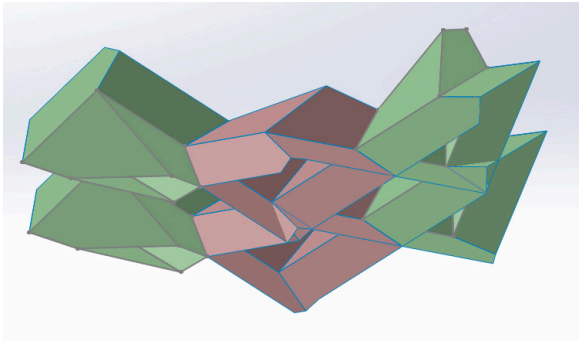
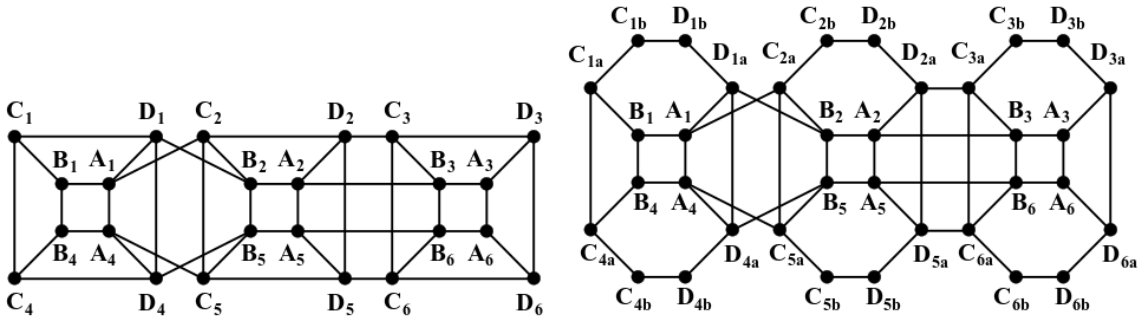


Figure 5.19: A 4-layer stacked MOCC

The connections diagrams in Figure 5.20(a) and (b) indicate connections between the panels in the stacked MOHC and the 2-layer stacked MOCC, respectively. These connections diagrams use the same conventions as the ones used in Figure 5.6. In Figure 5.20(a), the connection between adjacent stacked horn units depends on the direction they are turning in the planar curve. In Figure 5.20(a), the left and center units are turning in opposite directions while the center and right units are turning in the same direction. Similar connections between adjacent stacked claw units are found in the 2-layer stacked MOCC in Figure 5.20(b).



(a) (b)

Figure 5.20: Connections diagrams: (a) stacked MOHC and (b) 2-layer stacked MOCC

The stacked MOHC and 2-layer stacked MOCC are flat-foldable and rigidly foldable structures with only one DOF that deploy to match the shape of a non-intersecting planar curve. The MOHC in Figure 5.13 is stacked with a copy of itself to form the stacked MOHC in Figure 5.21. The deployment of the stacked MOHC demonstrates it is flat-foldable and rigidly foldable.

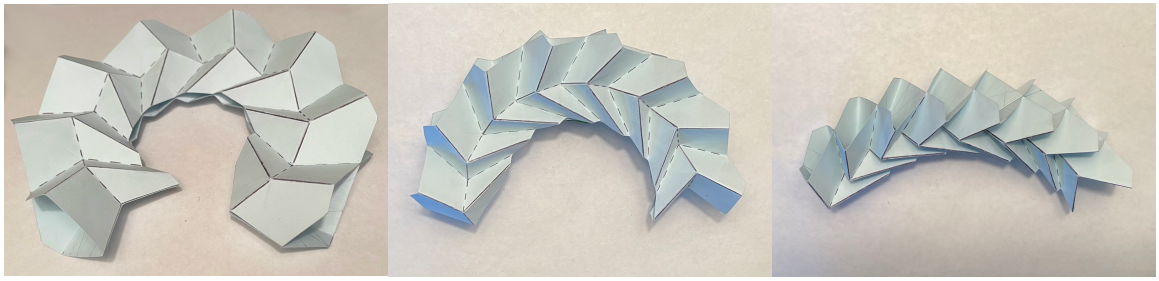


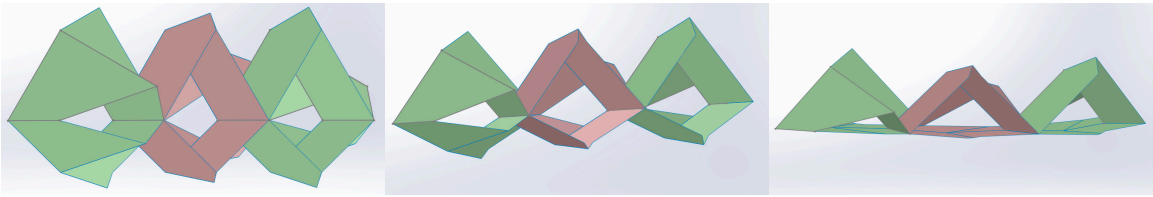
Figure 5.21: Deployment of a stacked MOHC

5.5 Self-Locking Stacked MOHC and MOCC

The stacked MOHC and stacked MOCC are stronger that their single-sheet counterparts, but their only locking states are their flat folded and flat unfolded states. If partially folded states of these stacked structures match the shape of the planar curve, then there needs to be a way to lock these stacked structures in a partially folded state. One solution is to construct self-locking stacked MOHCs and MOCCs. A self-locking model in this case can only deploy from its flat folded state to a partially folded state called the self-locking state. In this state, one sheet reaches its flat unfolded state while the other sheet remains in a partially folded state.

The geometry of the self-locking stacked MOHC and self-locking stacked MOCC depends on the values of β for each sheet and the values of α for the units on each sheet. The MOHC in Figure 5.22 has the following angle values: $(\alpha_1, \alpha_2, \alpha_3) = (\pi / 6, \pi / 9, \pi / 6)$

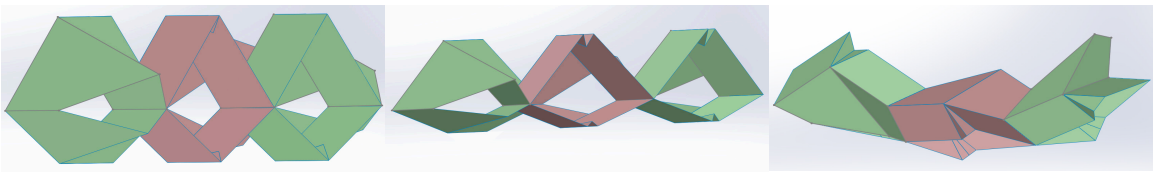
for the units from left to right and $(\beta_1, \beta_2) = (\pi / 3, \pi / 4)$ for the sheets from top to bottom. The self-locking stacked MOHC can fold from its flat folded state in Figure 5.22(a) to a partially folded state in Figure 5.22(b) to its self-locking state in Figure 5.22(c). This stacked structure is rigidly foldable with only one DOF, and it matches the shape of the planar curve in its self-locking state.



(a) (b) (c)

Figure 5.22: A self-locking stacked MOHC: (a) fully folded state, (b) partially folded state, and (c) self-locking state

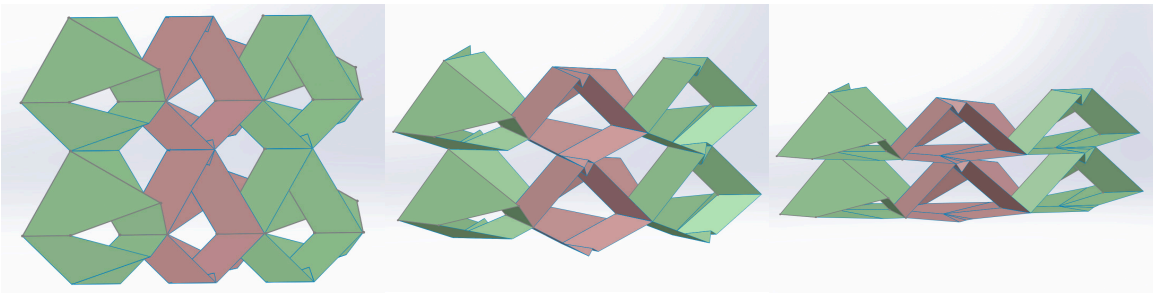
The construction of the self-locking stacked MOCC in Figure 5.23 uses the same parameters described previously. The self-locking stacked MOCC can fold from its flat folded state in Figure 5.23(a) to a partially folded state in Figure 5.23(b), to its self-locking state in Figure 5.23(c). This stacked structure is rigidly foldable with only one DOF, and it matches the shape of the planar curve in its self-locking state. While the self-locking stacked MOHC is composed of only two MOHCs, the self-locking stacked MOHC can be composed of any even number of MOCCs. Figure 5.23 shows a self-locking 2-layer stacked MOCC while Figure 5.24 shows a self-locking 4-layer stacked MOCC.



(a) (b) (c)

Figure 5.23: A self-locking 2-layer stacked MOCC:

(a) fully folded state, (b) partially folded state, and (c) self-locking state

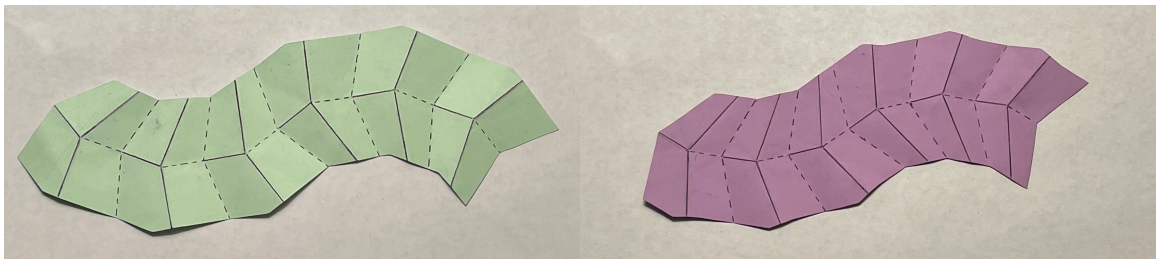


(a) (b) (c)

Figure 5.24: A self-locking 4-layer stacked MOCC:

(a) fully folded state, (b) partially folded state, and (c) self-locking state

The self-locking stacked MOHC and self-locking 2-layer stacked MOCC are rigidly foldable structures with one DOF. These self-locking stacked structures match the shape of the planar curve in their self-locking states. Figure 5.25 shows two MOHCs in the same family. Each MOHC is composed of identical horn units. The MOHC in Figure 5.25(a) has $\alpha_1 = \pi / 12$ and $\beta_1 = 5\pi / 12$, and its input dihedral angle is ϕ_{1g}. The MOHC in Figure 5.25(b) has $\alpha_2 = 0.1948$ and $\beta_2 = 7\pi / 18$, and its input dihedral angle is ϕ_{1p}. Dihedral angle ϕ_{1p} ranges from 0 to π, but dihedral angle ϕ_{1g} ranges from 0 to ϕ_{1max}, which is computed using (5.12), which is the identity for horn units in the same family. The maximum value of ϕ_{1g} for the MOHC in Figure 5.25(a) is $\phi_{1max} = 2.6744$.

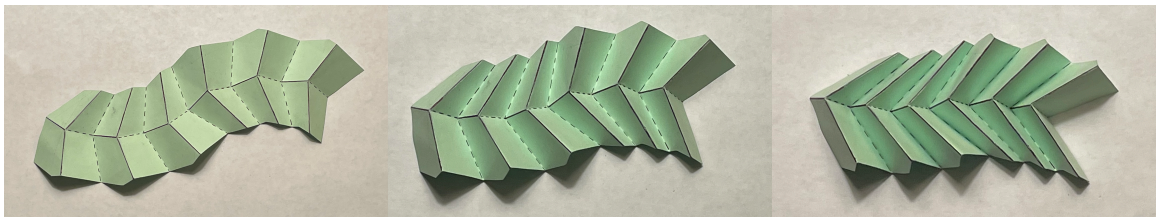


(a) (b)

Figure 5.25: MOHCs in the same family:

(a) $\alpha_1 = \pi / 12$, $\beta_1 = 5\pi / 12$ and (a) $\alpha_2 = 0.1948$, $\beta_2 = 7\pi / 18$

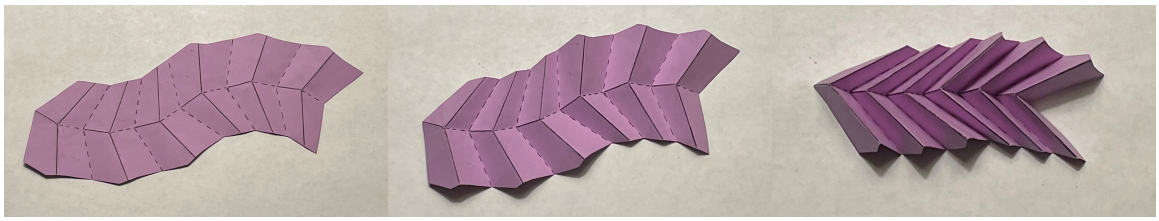
Figure 5.26 and Figure 5.27 show partially folded states of two MOHCs in the same family. The three partially folded states in Figure 5.26(a – c) are crease-stackable with those in Figure 5.27(a – c), respectively. Figure 5.28 shows the folding sequence of the self-locking stacked MOHC obtained from attaching the MOHCs in Figure 5.26 to those in Figure 5.27. The self-locking state is shown in Figure 5.28(a). In this state, the purple MOHC is fully unfolded while the green MOHC is in a partially folded state determined by the input dihedral angle, $\phi_{1g} = \phi_{1max}$.



(a) (b) (c)

Figure 5.26: Deployment of a MOHC:

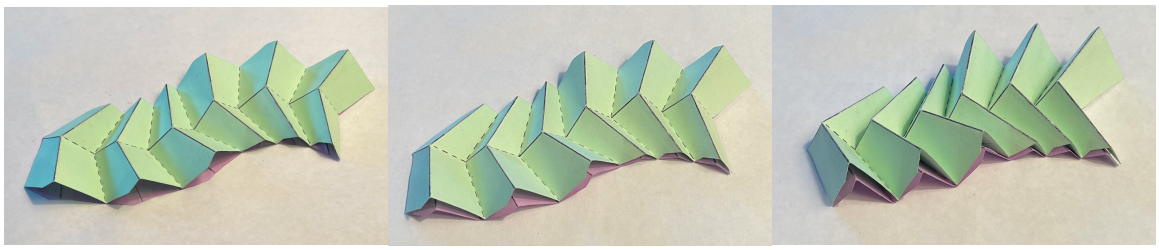
(a) $\phi_{1g} = \phi_{1max}$, (b) $\phi_{1g} = 3\pi / 4$, and (c) $\phi_{1g} = \pi / 2$



(a) (b) (c)

Figure 5.27: Deployment of a MOHC:

(a) $\phi_{1p} = \pi$, (b) $\phi_{1p} = 2.5044$, and (c) $\phi_{1p} = 1.6274$



(a) (b) (c)

Figure 5.28: Deployment of a self-locking stacked MOHC:

(a) $\phi_{1g} = \phi_{1max}$, $\phi_{1p} = \pi$, (b) $\phi_{1g} = 3\pi / 4$, $\phi_{1p} = 2.5044$, and (c) $\phi_{1g} = \pi / 2$, $\phi_{1p} = 1.6274$

The graph in Figure 5.29 shows the relations between ϕ_{1g} and the remaining dihedral angles in the two MOHCs. The green and purple plots correspond to the dihedral angles in the green and purple MOHCs, respectively. The green plots are a truncated version of those shown in Figure 5.16 because ϕ_{1max} is an upper bound of ϕ_{1g}. The partially folded states of the self-locking stacked MOHC in Figure 5.28(a – c) are represented by the vertical dotted lines (a – c), respectively, in the graph.

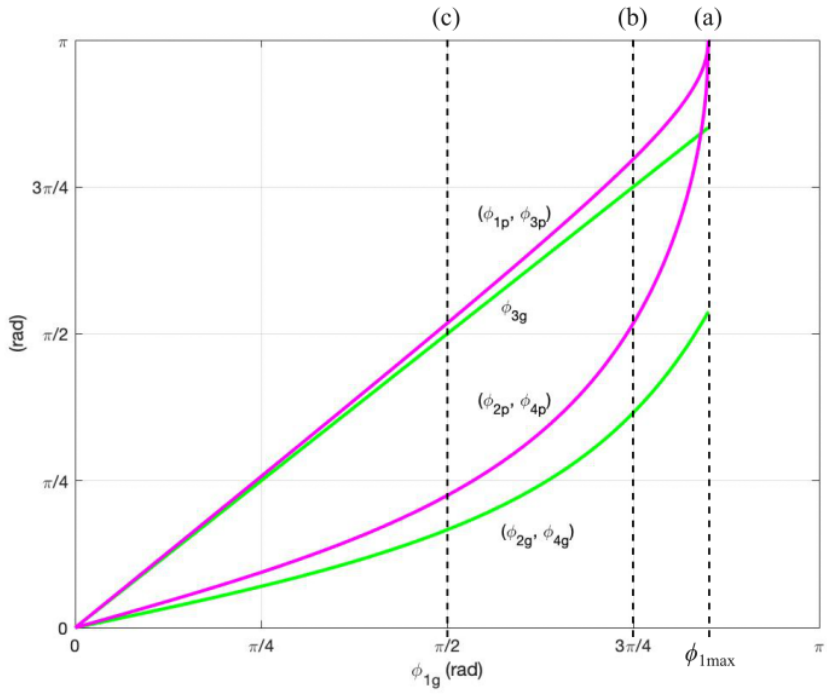


Figure 5.29: Dihedral angle relations in the self-locking stacked MOHC

5.6 Conclusion

This chapter focuses on the construction of the modular origami horn chain, MOHC, and modular origami claw chain, MOCC, which are composed of horn units and claw units, respectively. These origami tessellations are designed to fix the issues found in the rigidly foldable origami horns (Tachi, 2016). One issue with the rigidly foldable origami horn is that it may experience self-collision as it folds (Tachi, 2009). There is also no proposed method to self-lock the origami horn in a specific partially folded state. Conversely, the MOHC and MOCC do not experience self-collision as they fold, and they can stack to from self-locking stacked structures.

The design of the MOHC and MOCC starts with an examination of the geometry of the horn units and claw units, which are the units of the MOHC and MOCC, respectively.

Geometric proofs show that the horn unit and claw unit are flat-foldable, rigidly foldable, and crease-stackable. When the horn unit is in a partially folded state, a set of boundary edges lie in a plane. When the claw unit is in a partially folded state according to the planar folding mode, a set of creases lie in a plane, and a set of boundary edges lie in a parallel plane. For the horn unit and claw unit in partially folded states, the height only depends on angles, ϕ_1 and β, and side length, a.

An algorithm is presented to convert any non-intersecting planar curve to a MOHC and MOCC. The planar curve is converted to a piecewise-linear approximation, which is then converted to templates for the horn units and claw units. The MOHC and MOCC are concatenations of horn units and claw units, respectively. Both the MOHC and MOCC match the shape of the planar curve in their flat unfolded states. By converting the piecewise-linear curve into a new curve, a new MOHC and MOCC is constructed such that they match the shape of the planar curve in a specific partially folded state.

Copies of the MOHC and MOCC stack to form stacked MOHCs and stacked MOCCs, respectively. A Double 4C appears between any two consecutive stacked horn units and stacked claw units in the stacked MOHC and stacked MOCC, respectively, so the stacked units fold simultaneously in the stacked origami chain. The stacked MOHC and stacked MOCC are flat-foldable and rigidly foldable structures with one DOF. They also deploy to match the shape of the planar curve in their flat unfolded states. While the stacked MOHC is composed of two MOHCs, the stacked MOCC can be composed of any even number of MOCCs.

Finally, self-locking stacked MOHCs and MOCCs are assembled from distinct MOHCs and distinct MOCCs, respectively. The self-locking stacked MOHC and self-

locking stacked MOCC are rigidly foldable structures with one DOF. They also both deploy to match the shape of the planar curve in their self-locking states. Also, while the self-locking stacked MOHC is composed of two MOHCs in the same family, the self-locking stacked MOCC can be composed of any even number of MOCCs in the same family. The MOHC and MOCC along with their stacked structures can be constructed to match the shape of a desired non-intersecting planar curve, which is useful in the design of soft robotic limbs, folded plate shelters, and surgical devices.

6

Conclusion

6.1 Main Achievements

The research in this dissertation is focused on the geometry and kinematics of novel flat-foldable and rigidly foldable origami tessellations that are crease-stackable. Crease-stackability allows origami tessellations to stack along a designated set of creases to form rigidly foldable stacked structures. This research designed novel origami tessellations and their stacked structures, showing that crease-stackability is not restricted to the Miura-ori pattern and its derivatives. The following are the main achievements.

The Double 4C is a composite structure constructed from two identical flat-foldable 4Cs attached along two pairs of creases. This stacked origami structure demonstrates that the opposite dihedral angles in any flat-foldable 4C are always equal. This property is reflected in the fact that the Double 4C consists of two scissor mechanisms, and in each scissor mechanism, opposite panels are coplanar. A 1-DOF system of equations describes the dihedral angles in the Double 4C, which shows that it is a flat-foldable and rigidly foldable origami structure with only one DOF. Furthermore, an examination of the stacked Miura-ori pattern reveals a lattice of Double 4Cs. The discovery of the Double 4C reveals the geometric properties that make the Miura-ori pattern crease-stackable.

The thick-panel Double 4C adds thickness to each of the panels in the origami Double 4C. The kinematic equations for the thick-panel flat-foldable 4C match those of the Bennett linkage, which is a rigidly foldable mechanism with only one DOF. Two

copies of the thick-panel flat-foldable 4C are combined to form the thick-panel Double 4C. The kinematic equations describing the dihedral angles in the thick-panel Double 4C match those of its origami counterpart. An examination of the mechanical linkages in the thick-panel Double 4C reveals it is composed of two parallelogram linkages. In each parallelogram linkage, the opposite dihedral angles are equal. The construction of the thick-panel Double 4C can inspire the designs of thick-panel versions of crease-stackable Miura-ori patterns.

Three methods to stack sheets of the Miura-ori pattern are presented: crease stacking, panel stacking, and weaving. Crease stacking attaches sheets of the Miura-ori pattern along their creases while panel stacking attaches sheets of the Miura-ori pattern along their panels. Crease stacking and panel stacking are the methods used to assemble the stacked Miura-ori pattern and the stacked egg box pattern, respectively. Crease stacking is the more convenient stacking method while panel stacking uses a larger area of contact between Miura-ori sheets. Weaving Miura-ori tubes involves both crease stacking and panel stacking. The woven Miura-ori pattern weaves Miura-ori tubes in a plain weave, which is a structure that cannot be achieved through crease stacking alone. These methods of stacking demonstrate the variety of stacked origami structures that can be constructed from sheets of the Miura-ori pattern.

The OCT is a novel flat-foldable and rigidly foldable origami tessellation that is also crease-stackable. Unlike the Miura-ori pattern, the OCT has multiple DOFs because it is comprised of both 4Cs and 6Cs. The $M \times N$ OCT consists of an $M \times N$ grid of claw units, each of which is a 3-DOF 6C. A geometric proof shows that the claw unit is crease-stackable when a 1-DOF system of equations is satisfied. By extension, the $M \times N$ OCT

is also crease-stackable. A numerical method shows that the $M \times N$ OCT features five DOFs when M and N are both at least 2. When copies of OCTs are stacked to form the stacked OCT, the number of DOFs reduces from five to one. This feature is not found in crease-stackable origami tessellations based on the Miura-ori pattern. The one DOF that remains is the planar folding mode, which is due to the coupling between adjacent sheets in the stacked OCT. Furthermore, distinct OCTs are shown to be crease-stackable with each other, and they stack to form the self-locking stacked OCT. The self-locking state of the self-locking stacked OCT depends on its geometry, which is useful for the design of deployable structures and mechanical metamaterials.

The MOHC and MOCC are two types of flat-foldable, rigidly foldable, and crease-stackable origami tessellations that can deploy to match the shape of an arbitrary non-intersecting planar curve. An algorithm converts the planar curve to a MOHC and MOCC. The MOHC is a concatenation of horn units while the MOCC is a concatenation of claw units. Copies of the MOHC and MOCC are stacked to form the stacked MOHC and stacked MOCC, respectively, which are both flat-foldable and rigidly foldable stacked structures with only one DOF. They also deploy to match the shape of the planar curve in their flat unfolded states. Additionally, the construction of stacked MOHCs and stacked MOCCs is extended to self-locking stacked structures. The self-locking stacked MOHC and self-locking stacked MOCC are assembled from distinct sheets of MOHCs and distinct sheets of MOCCs, respectively, in the same family. Both the self-locking stacked MOHC and self-locking stacked MOCC are rigidly foldable stacked structures with only one DOF. They also deploy to match the shape of the planar curve in their self-locking states. The MOHC and MOCC are improvements on the rigidly foldable origami

horn proposed by Tachi, which cannot self-lock and may experience self-collisions (Tachi, 2016). These chain-like origami tessellations are applicable in origami robots designed to articulate along a specific path.

6.2 Future Works

The research in this dissertation presented original origami tessellations and stacked structures assembled from sheets of origami tessellations. Many more of these origami structures exist, which can inspire numerous origami-based applications in engineering. These origami tessellations and their stacked structures can be further analyzed in future works. The following are potential research directions.

Firstly, research on the thick-panel Double 4C suggests that thick-panel Miura-ori patterns can be constructed. Kinematic analysis on the thick-panel flat-foldable 4C reveals the relations among the thicknesses of the panels. To transform the origami Miura-ori pattern into a thick-panel Miura-ori pattern, each vertex in the Miura-ori pattern is converted into a thick-panel flat-foldable 4C. Each panel in the Miura-ori pattern is assigned a thickness such that the entire thick-panel structure remains rigidly foldable. Furthermore, copies of this thick-panel Miura-ori pattern can combine to form stacked structures that are rigidly foldable. Thick-panel origami tessellations are more suitable for engineering applications in which the thickness of materials needs to be accommodated. Converting origami tessellations to their thick-panel versions is useful for constructing deployable structures and mechanical metamaterials.

Secondly, the folding and stacking of 4C origami tessellations in Chapter 3 focused on stacked structures composed of identical flat-foldable origami tessellations.

Flat-foldable origami tessellations were chosen because this property simplifies the equations describing the geometry of 4Cs. Examining origami tessellations that are not necessarily flat-foldable would reveal more crease-stackable origami tessellations. Coplanarity of creases is another property that was used to show crease-stackability, but crease-stackability does not require creases to be coplanar. There may be crease-stackable origami tessellations that do not possess coplanar creases. It is also possible to construct stacked origami structures from distinct sheets of origami tessellations. Self-locking stacked structures are assembled using distinct origami tessellations that are crease-stackable with each other. The classical Miura-ori is generated from a 4-panel origami unit, but variations of this crease pattern are generated from multiple different origami units. Research on crease-stackable origami tessellations can be expanded to include those that are composed of multiple different units. Origami-inspired materials with graded stiffness can be constructed from non-uniform layers of the Miura-ori pattern.

Thirdly, the numerical method used in Chapter 4 serves as a predictor step in determining the DOFs of the OCT. Appendix D shows the result of a MATLAB program designed to calculate the changes in the fold angles relative to an OCT's initial partially folded configuration. These changes to the fold angles need to be corrected for error, so this MATLAB program needs a corrector step to obtain an actual folded configuration. Once both the predictor steps and corrector steps are incorporated, the numerical method can graph the movement of the OCT using each of its five DOFs. This numerical method has been implemented by Tachi in his rigid origami simulator, which simulates single-sheet origami models (Tachi, 2009). A modified version of this method can be used to compute the DOFs and track the movement of stacked origami tessellations. The OCT is

a crease-stackable origami tessellations with multiple DOFs, so these DOFs can be used to stack sheets by manipulating a few creases at a time. Conversely, stacking sheets of the Miura-ori pattern, which has only one DOF, requires manipulating all creases at once. A modified version of the numerical method can be used to determine an efficient deployment path to stack sheets of OCTs without collisions.

Finally, the MOHC and MOCC are origami tessellations that deploy to match the shape of an arbitrary non-intersecting planar curve, which can inspire designs for soft robotics, surgical devices, and space structures. Origami-inspired soft robots, such as robotic grippers and crawlers, fold sheet-like material into desired configurations. The stacked MOHC and stacked MOCC are both 1-DOF stacked origami structures, so using them in origami-inspired soft robots would simplify their actuation. Even though the self-locking state of the MOHC and MOCC is known, the deployment sequence of these models is not fully understood. More research on the kinematics of the MOHC and MOCC is needed to determine how the shapes of these origami tessellations transform as they unfold.

Appendices

Appendix A: Generalized Kinematics of 4C

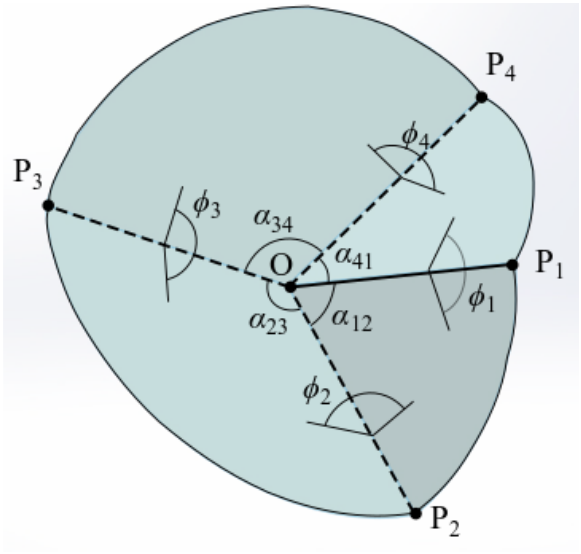


Figure A.1: Flat-foldable 4C in a partially folded state

The 4C shown in Figure A.1 has the following parameters:

Sector angles: $[\alpha_{12}, \alpha_{23}, \alpha_{34}, \alpha_{41}]$

Dihedral angles: $[\phi_1, \phi_2, \phi_3, \phi_4]$

Crease angles: $[\theta_1, \theta_2, \theta_3, \theta_4]$

Mountain/valley assignment (crease parities): $[p_1, p_2, p_3, p_4]$

If mountain (convexity), $p_i = -1$, and if valley (concavity), $p_i = 1$.

For $i = 1, 2, 3, 4$, let $\theta_i = p_i\,(\pi - \phi_i)$.

The following abbreviations and identities are used:

$$c(x) = \cos(x),\ s(x) = \sin(x),\ T(x) = \tan(x/2),$$

$$c(x) = \frac{1-T(x)^2}{1+T(x)^2},\ \ s(x) = \frac{2T(x)}{1+T(x)^2}.$$

For specific angle values, the following abbreviations are used, in which $(i + 1)$ is replaced with 1 when $i = 4$:

$$c_i = \cos(\theta_i),\ s_i = \sin(\theta_i),\ c_{i(i+1)} = \cos(\alpha_{i(i+1)}),\ s_{i(i+1)} = \sin(\alpha_{i(i+1)}),\ T_i = \tan(\theta_i /2).$$

The following is the transformation matrix from crease i to crease $(i + 1)$, in which $(i + 1)$ is replaced with 1 when $i = 4$:

$$Q(\alpha_{i(i+1)},\theta_i) = \begin{pmatrix} \cos\theta_i & \cos\alpha_{i(i+1)}\sin\theta_i & \sin\alpha_{i(i+1)}\sin\theta_i \\ -\sin\theta_i & \cos\alpha_{i(i+1)}\cos\theta_i & \sin\alpha_{i(i+1)}\cos\theta_i \\ 0 & -\sin\alpha_{i(i+1)} & \cos\alpha_{i(i+1)} \end{pmatrix}. \tag{A.1}$$

These transformation matrices satisfy the following closure equation:

$$\prod_{i=1}^{4} Q(\alpha_{i(i+1)},\theta_i) = I_{3\times3}. \tag{A.2}$$

The closure equation can be rearranged to form:

$$Q(\alpha_{12},\theta_1)Q(\alpha_{23},\theta_2) = Q(\alpha_{41},\theta_4)^{-1}Q(\alpha_{34},\theta_3)^{-1}. \tag{A.3}$$

Below are the LHS and RHS entries in (A.3):

<u>LHS:</u>

(1, 1): $c_1c_2 - c_{12}(s_1s_2)$

(1, 2): $c_{23}(c_1s_2) + c_{12}c_{23}(s_1c_2) - s_{12}s_{23}(s_1)$

(1, 3): $s_{23}(c_1s_2) + c_{12}s_{23}(s_1c_2) + s_{12}c_{23}(s_1)$

(2, 1): $-s_1c_2 - c_{12}(c_1s_2)$

(2, 2): $-c_{23}(s_1s_2) + c_{12}c_{23}(c_1c_2) - s_{12}s_{23}(c_1)$

(2, 3): $-s_{23}(s_1s_2) + c_{12}s_{23}(c_1c_2) + s_{12}c_{23}(c_1)$

(3, 1): $s_{12}(s_2)$

(3, 2): $-s_{12}c_{23}(c_2) - c_{12}s_{23}$

(3, 3): $-s_{12}s_{23}(c_2) + c_{12}c_{23}$

RHS:

(1, 1): $c_3c_4 - c_{34}(s_3s_4)$

(1, 2): $-s_3c_4 - c_{34}(c_3s_4)$

(1, 3): $s_{34}(s_4)$

(2, 1): $c_{41}(c_3s_4) + c_{34}c_{41}(s_3c_4) - s_{34}s_{41}(s_3)$

(2, 2): $-c_{41}(s_3s_4) + c_{34}c_{41}(c_3c_4) - s_{34}s_{41}(c_3)$

(2, 3): $-s_{34}c_{41}(c_4) - c_{34}s_{41}$

(3, 1): $s_{41}(c_3s_4) + c_{34}s_{41}(s_3c_4) + s_{34}c_{41}(s_3)$

(3, 2): $-s_{41}(s_3s_4) + c_{34}s_{41}(c_3c_4) + s_{34}c_{41}(c_3)$

(3, 3): $-s_{34}s_{41}(c_4) + c_{34}c_{41}$

A 1-DOF system of equations, in which ϕ_1 is the input, can be derived.

The entries in (3, 3) state:

$-s_{12}s_{23}(c_2) + c_{12}c_{23} = -s_{34}s_{41}(c_4) + c_{34}c_{41}$

This equation can be written as

$$T_2^2 = \frac{(N_1 + N_4)T_4^2 + (N_1 - N_3)}{(N_2 - N_4)T_4^2 + (N_2 + N_3)}. \tag{A.4}$$

Here, $N_1 = s_{12}s_{23} - c_{12}c_{23}$, $N_2 = s_{12}s_{23} + c_{12}c_{23}$,

$N_3 = s_{34}s_{41} - c_{34}c_{41}$, $N_4 = s_{34}s_{41} + c_{34}c_{41}$.

The entries in (3, 3), in which each index is shifted from i to $(i - 1)$, state:

$-s_{41}s_{12}(c_1) + c_{41}c_{12} = -s_{23}s_{34}(c_3) + c_{23}c_{34}$

This equation can be written as

$$T_1^2 = \frac{(M_1 + M_4)T_3^2 + (M_1 - M_3)}{(M_2 - M_4)T_3^2 + (M_2 + M_3)}, \tag{A.5}$$

Here, $M_1 = s_{41}s_{12} - c_{41}c_{12}$, $M_2 = s_{41}s_{12} + c_{41}c_{12}$,

$M_3 = s_{23}s_{34} - c_{23}c_{34}$, $M_4 = s_{23}s_{34} + c_{23}c_{34}$.

The entries in (1, 3) state:

$s_{23}(c_1s_2) + c_{12}s_{23}(s_1c_2) + s_{12}c_{23}(s_1) = s_{34}(s_4)$

This equation can be written as

$$T_1 = \frac{(P_1T_2^2 + P_2) \pm \sqrt{(P_1T_2^2 + P_2)^2 - 4(P_4(T_2^2 + 1))^2 + 4(s_{23}T_2)^2}}{2(P_4(T_2^2 + 1)) + 2(s_{23}T_2)}. \tag{A.6}$$

Here, $P_1 = s_{12}c_{23} - c_{12}s_{23}$, $P_2 = c_{12}s_{23} + s_{12}c_{23}$, $P_4 = s_{34}T_4/(1 + T_4^2)$.

For a developable flat-foldable 4C vertex, $\alpha_{12} + \alpha_{34} = \alpha_{23} + \alpha_{41} = \pi$.

For a non-developable flat-foldable 4C cone, $\alpha_{12} = \alpha_{34}$, $\alpha_{23} = \alpha_{41}$.

In both cases, (A.4) becomes

$$T_2^2 = T_4^2, \tag{A.7}$$

and (A.5) becomes

$$T_1^2 = T_3^2. \tag{A.8}$$

There are four cases to simplify (A.6):

a) $\theta_1 = \theta_3$, $\theta_2 = \theta_4$

b) $-\theta_1 = \theta_3$, $\theta_2 = \theta_4$

c) $\theta_1 = \theta_3$, $-\theta_2 = \theta_4$

d) $-\theta_1 = \theta_3$, $-\theta_2 = \theta_4$

In case (a), (A.6) becomes

$$T_1T_2 = \frac{\cos\left(\frac{\alpha_{23}+\alpha_{12}}{2}\right)}{\cos\left(\frac{\alpha_{23}-\alpha_{12}}{2}\right)},\ \tan\frac{\phi_1}{2}\tan\frac{\phi_2}{2} = \frac{\cos\left(\frac{\alpha_{23}-\alpha_{12}}{2}\right)}{\cos\left(\frac{\alpha_{23}+\alpha_{12}}{2}\right)}. \tag{A.9a}$$

In case (b), (A.6) becomes

$$\frac{T_1}{T_2} = -\frac{\sin\left(\frac{\alpha_{23}-\alpha_{12}}{2}\right)}{\sin\left(\frac{\alpha_{23}+\alpha_{12}}{2}\right)},\ \frac{\tan\frac{\phi_1}{2}}{\tan\frac{\phi_2}{2}} = \frac{\sin\left(\frac{\alpha_{23}+\alpha_{12}}{2}\right)}{\sin\left(\frac{\alpha_{23}-\alpha_{12}}{2}\right)}. \tag{A.9b}$$

In case (c), (A.6) becomes

$$\frac{T_1}{T_2} = -\frac{\cos\left(\frac{\alpha_{23}-\alpha_{12}}{2}\right)}{\cos\left(\frac{\alpha_{23}+\alpha_{12}}{2}\right)},\ \frac{\tan\frac{\phi_1}{2}}{\tan\frac{\phi_2}{2}} = \frac{\cos\left(\frac{\alpha_{23}+\alpha_{12}}{2}\right)}{\cos\left(\frac{\alpha_{23}-\alpha_{12}}{2}\right)}. \tag{A.9c}$$

In case (d), (A.6) becomes

$$T_1T_2 = \frac{\sin\left(\frac{\alpha_{23}+\alpha_{12}}{2}\right)}{\sin\left(\frac{\alpha_{23}-\alpha_{12}}{2}\right)},\ \tan\frac{\phi_1}{2}\tan\frac{\phi_2}{2} = \frac{\sin\left(\frac{\alpha_{23}-\alpha_{12}}{2}\right)}{\sin\left(\frac{\alpha_{23}+\alpha_{12}}{2}\right)}. \tag{A.9d}$$

For a flat-foldable 4C vertex in case (b), the following relations hold:

$$\phi_1 = \phi_3,\ \ \phi_2 = \phi_4,\ \ \frac{\tan\frac{\phi_1}{2}}{\tan\frac{\phi_2}{2}} = \frac{\sin\left(\frac{\alpha_{23}+\alpha_{12}}{2}\right)}{\sin\left(\frac{\alpha_{23}-\alpha_{12}}{2}\right)}. \tag{A.10}$$

For a symmetric flat-foldable 4C vertex in case (b) with $\alpha_{12} = (\pi - \alpha_{23}) = (\pi - \alpha_{34}) = \alpha_{41}$, the following relations hold:

$$\phi_1 = \phi_3,\ \ \phi_2 = \phi_4,\ \ \cos\alpha_{12} \tan\frac{\phi_1}{2} = \tan\frac{\phi_2}{2}. \tag{A.11}$$

For a flat-foldable 4C cone in case (a), the following relations hold:

$$\phi_1 = \phi_3,\ \ \phi_2 = \phi_4,\ \ \tan\frac{\phi_1}{2}\tan\frac{\phi_2}{2} = \frac{\cos\left(\frac{\alpha_{23} - \alpha_{12}}{2}\right)}{\cos\left(\frac{\alpha_{23} + \alpha_{12}}{2}\right)}. \tag{A.12}$$

Appendix B: Generalized Kinematics of Thick-Panel 4C

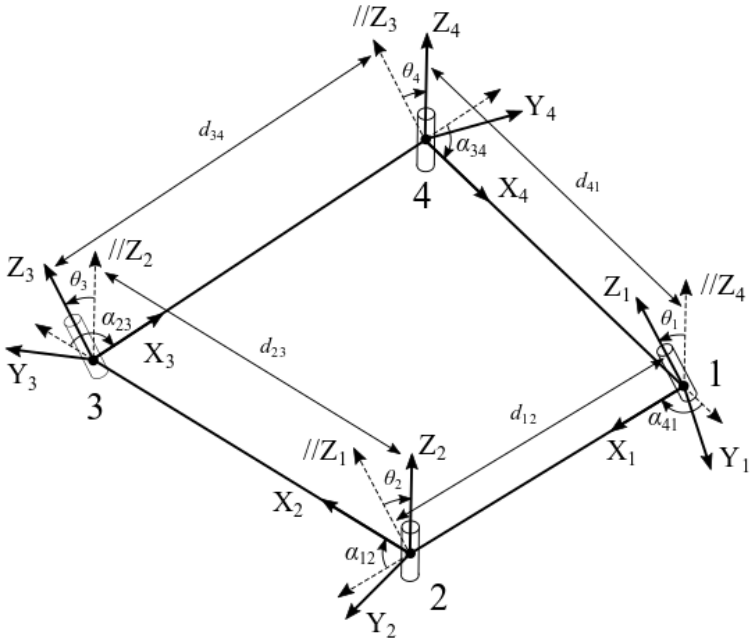


Figure B.1: Spatial 4-bar linkage with shifting coordinate systems

The thick-panel 4C shown in Figure B.1 has the following parameters:

Sector angles: [α_{12}, α_{23}, α_{34}, α_{41}]

Dihedral angles: [ϕ_1, ϕ_2, ϕ_3, ϕ_4]

Crease angles: [θ_1, θ_2, θ_3, θ_4]

Mountain/valley assignment (crease parities): [p_1, p_2, p_3, p_4]

If mountain (convexity), $p_i = -1$, and if valley (concavity), $p_i = 1$.

For $i = 1, 2, 3, 4$, let $\theta_i = p_i\,(\pi - \phi_i)$.

The following abbreviations and identities are used:

$$c(x) = \cos(x),\ s(x) = \sin(x),\ T(x) = \tan(x/2),$$

$$c(x) = \frac{1-T(x)^2}{1+T(x)^2},\ \ s(x) = \frac{2T(x)}{1+T(x)^2}.$$

For specific angle values, the following abbreviations are used, in which $(i + 1)$ is replaced with 1 when $i = 4$:

$$c_i = \cos(\theta_i),\ s_i = \sin(\theta_i),\ c_{i(i+1)} = \cos(\alpha_{i(i+1)}),\ s_{i(i+1)} = \sin(\alpha_{i(i+1)}),\ T_i = \tan(\theta_i /2).$$

The following is the transformation matrix from crease i to crease $(i + 1)$, in which $(i + 1)$ is replaced with 1 when $i = 4$:

$$Q(\alpha_{i(i+1)},\theta_i,d_{i(i+1)}) = \begin{pmatrix} \cos\theta_i & \cos\alpha_{i(i+1)}\sin\theta_i & \sin\alpha_{i(i+1)}\sin\theta_i & d_{i(i+1)}\cos\theta_i \\ -\sin\theta_i & \cos\alpha_{i(i+1)}\cos\theta_i & \sin\alpha_{i(i+1)}\cos\theta_i & -d_{i(i+1)}\sin\theta_i \\ 0 & -\sin\alpha_{i(i+1)} & \cos\alpha_{i(i+1)} & 0 \\ 0 & 0 & 0 & 1 \end{pmatrix}. \quad \text{(B.1)}$$

These transformation matrices satisfy the following closure equation:

$$\prod_{i=1}^{4} Q(\alpha_{i(i+1)},\theta_i,d_{i(i+1)}) = I_{4\times4}. \quad \text{(B.2)}$$

The closure equation can be rearranged to form:

$$Q(\alpha_{12},\theta_1,d_{12})Q(\alpha_{23},\theta_2,d_{23}) = Q(\alpha_{41},\theta_4,d_{41})^{-1}Q(\alpha_{34},\theta_3,d_{34})^{-1}. \quad \text{(B.3)}$$

Below are the LHS and RHS entries in (B.3):

<u>LHS:</u>

(1, 1): $c_1c_2 - c_{12}(s_1s_2)$

(1, 2): $c_{23}(c_1s_2) + c_{12}c_{23}(s_1c_2) - s_{12}s_{23}(s_1)$

(1, 3): $s_{23}(c_1s_2) + c_{12}s_{23}(s_1c_2) + s_{12}c_{23}(s_1)$

(1, 4): $d_{23}(c_1c_2) - d_{23}c_{12}(s_1s_2) + d_{12}(c_1)$

(2, 1): $-s_1c_2 - c_{12}(c_1s_2)$

(2, 2): $-c_{23}(s_1s_2) + c_{12}c_{23}(c_1c_2) - s_{12}s_{23}(c_1)$

(2, 3): $-s_{23}(s_1s_2) + c_{12}s_{23}(c_1c_2) + s_{12}c_{23}(c_1)$

(2, 4): $-d_{23}(s_1c_2) - d_{23}c_{12}(c_1s_2) - d_{12}(s_1)$

(3, 1): $s_{12}(s_2)$

(3, 2): $-s_{12}c_{23}(c_2) - c_{12}s_{23}$

(3, 3): $-s_{12}s_{23}(c_2) + c_{12}c_{23}$

(3, 4): $d_{23}s_{12}(s_2)$

(4, 1): 0

(4, 2): 0

(4, 3): 0

(4, 4): 1

RHS:

(1, 1): $c_3c_4 - c_{34}(s_3s_4)$

(1, 2): $-s_3c_4 - c_{34}(c_3s_4)$

(1, 3): $s_{34}(s_4)$

(1, 4): $-d_{34}(c_4)$

(2, 1): $c_{41}(c_3s_4) + c_{34}c_{41}(s_3c_4) - s_{34}s_{41}(s_3)$

(2, 2): $-c_{41}(s_3s_4) + c_{34}c_{41}(c_3c_4) - s_{34}s_{41}(c_3)$

(2, 3): $-s_{34}c_{41}(c_4) - c_{34}s_{41}$

(2, 4): $-d_{34}c_{41}(s_4)$

(3, 1): $s_{41}(c_3s_4) + c_{34}s_{41}(s_3c_4) + s_{34}c_{41}(s_3)$

(3, 2): $-s_{41}(s_3s_4) + c_{34}s_{41}(c_3c_4) + s_{34}c_{41}(c_3)$

(3, 3): $-s_{34}s_{41}(c_4) + c_{34}c_{41}$

(3, 4): $-d_{34}s_{41}(s_4)$

(4, 1): 0

(4, 2): 0

(4, 3): 0

(4, 4): 1

For a thick-panel flat-foldable 4C vertex, in which $\alpha_{12} + \alpha_{34} = \alpha_{23} + \alpha_{41} = \pi$ holds, the equations in (A.10) are used.

For a thick-panel flat-foldable 4C cone, in which $\alpha_{12} = \alpha_{34}$ and $\alpha_{23} = \alpha_{41}$ hold, the equations in (A.12) are used.

In both cases, the entries in (3, 4) produce the following relations:

$$\frac{d_{23}(s_2)}{s_{23}} = -\frac{d_{34}(s_4)}{s_{34}}, \quad \frac{d_{34}(s_3)}{s_{34}} = -\frac{d_{41}(s_1)}{s_{41}},$$
$$\frac{d_{41}(s_4)}{s_{41}} = -\frac{d_{12}(s_2)}{s_{12}}, \quad \frac{d_{12}(s_1)}{s_{12}} = -\frac{d_{23}(s_3)}{s_{23}}. \tag{B.4}$$

There are four cases to simplify (B.4):

a) $\theta_1 = \theta_3$, $\theta_2 = \theta_4$

b) $-\theta_1 = \theta_3$, $\theta_2 = \theta_4$

c) $\theta_1 = \theta_3$, $-\theta_2 = \theta_4$

d) $-\theta_1 = \theta_3$, $-\theta_2 = \theta_4$

In case (a), (B.4) becomes

$$\frac{d_{12}}{s_{12}} = -\frac{d_{23}}{s_{23}} = \frac{d_{34}}{s_{34}} = -\frac{d_{41}}{s_{41}}. \tag{B.5a}$$

In case (b), (B.4) becomes

$$\frac{d_{12}}{s_{12}} = \frac{d_{23}}{s_{23}} = -\frac{d_{34}}{s_{34}} = -\frac{d_{41}}{s_{41}}. \tag{B.5b}$$

In case (c), (B.4) becomes

$$\frac{d_{12}}{s_{12}} = -\frac{d_{23}}{s_{23}} = -\frac{d_{34}}{s_{34}} = \frac{d_{41}}{s_{41}}. \tag{B.5c}$$

In case (d), (B.4) becomes

$$\frac{d_{12}}{s_{12}} = \frac{d_{23}}{s_{23}} = \frac{d_{34}}{s_{34}} = \frac{d_{41}}{s_{41}}. \tag{B.5d}$$

For a thick-panel flat-foldable 4C vertex in case (b), the following relations hold:

$$\phi_1 = \phi_3,\ \ \phi_2 = \phi_4,\ \ \frac{\tan\frac{\phi_1}{2}}{\tan\frac{\phi_2}{2}} = \frac{\sin\left(\frac{\alpha_{23}+\alpha_{12}}{2}\right)}{\sin\left(\frac{\alpha_{23}-\alpha_{12}}{2}\right)},\ \frac{d_{12}}{s_{12}} = \frac{d_{23}}{s_{23}} = -\frac{d_{34}}{s_{34}} = -\frac{d_{41}}{s_{41}}. \tag{B.6}$$

For a thick-panel flat-foldable 4C cone in case (a), the following relations hold:

$$\phi_1 = \phi_3,\ \ \phi_2 = \phi_4,\ \ \tan\frac{\phi_1}{2}\tan\frac{\phi_2}{2} = \frac{\cos\left(\frac{\alpha_{23}-\alpha_{12}}{2}\right)}{\cos\left(\frac{\alpha_{23}+\alpha_{12}}{2}\right)},\ \frac{d_{12}}{s_{12}} = -\frac{d_{23}}{s_{23}} = \frac{d_{34}}{s_{34}} = -\frac{d_{41}}{s_{41}}. \tag{B.7}$$

Appendix C: Generalized Kinematics of 6C

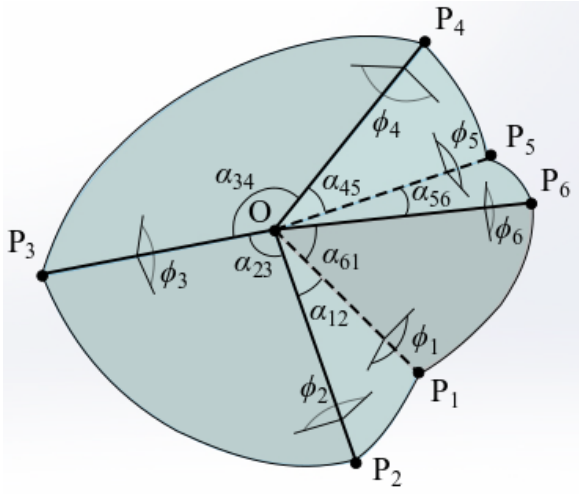


Figure C.1: Flat-foldable 6C in a partially folded state

The 6C shown in Figure C.1 has the following parameters:

Sector angles: [α_{12}, α_{23}, α_{34}, α_{45}, α_{56}, α_{61}]

Dihedral angles: [ϕ_1, ϕ_2, ϕ_3, ϕ_4, ϕ_5, ϕ_6]

Crease angles: [θ_1, θ_2, θ_3, θ_4, θ_5, θ_6]

Mountain/valley assignment (crease parities): [p_1, p_2, p_3, p_4, p_5, p_6]

If mountain (convexity), $p_i = -1$, and if valley (concavity), $p_i = 1$.

For $i = 1, 2, 3, 4, 5, 6$, let $\theta_i = p_i (\pi - \phi_i)$.

The following abbreviations and identities are used:

$$c(x) = \cos(x),\ s(x) = \sin(x),\ T(x) = \tan(x/2),$$

$$c(x) = \frac{1 - T(x)^2}{1 + T(x)^2},\ \ s(x) = \frac{2T(x)}{1 + T(x)^2}.$$

For specific angle values, the following abbreviations are used, in which $(i + 1)$ is replaced with 1 when $i = 6$:

$c_i = \cos(\theta_i)$, $s_i = \sin(\theta_i)$, $c_{i(i+1)} = \cos(\alpha_{i(i+1)})$, $s_{i(i+1)} = \sin(\alpha_{i(i+1)})$, $T_i = \tan(\theta_i/2)$.

The following is the transformation matrix from crease i to crease $(i + 1)$, in which $(i + 1)$ is replaced with 1 when $i = 6$:

$$Q(\alpha_{i(i+1)},\theta_i) = \begin{pmatrix} \cos\theta_i & \cos\alpha_{i(i+1)}\sin\theta_i & \sin\alpha_{i(i+1)}\sin\theta_i \\ -\sin\theta_i & \cos\alpha_{i(i+1)}\cos\theta_i & \sin\alpha_{i(i+1)}\cos\theta_i \\ 0 & -\sin\alpha_{i(i+1)} & \cos\alpha_{i(i+1)} \end{pmatrix}. \quad \text{(C.1)}$$

These transformation matrices satisfy the following closure equation:

$$\prod_{i=1}^{6} Q(\alpha_{i(i+1)},\theta_i) = I_{3\times3}. \quad \text{(C.2)}$$

The closure equation can be rearranged to form:

$$Q(\alpha_{12},\theta_1)Q(\alpha_{23},\theta_2)Q(\alpha_{34},\theta_3) = Q(\alpha_{61},\theta_6)^{-1}Q(\alpha_{56},\theta_5)^{-1}Q(\alpha_{45},\theta_4)^{-1}. \quad \text{(C.3)}$$

Below are the LHS and RHS entries in (C.3):

<u>LHS:</u>

(1, 1): $c_1c_2c_3 - c_{12}(s_1s_2c_3) - c_{23}(c_1s_2s_3) - c_{12}c_{23}(s_1c_2s_3) + s_{12}s_{23}(s_1s_3)$

(1, 2): $c_{34}(c_1c_2s_3) - c_{12}c_{34}(s_1s_2s_3) + c_{23}c_{34}(c_1s_2c_3) + c_{12}c_{23}c_{34}(s_1c_2c_3)$

$- s_{12}s_{23}c_{34}(s_1c_3) - s_{23}s_{34}(c_1s_2) - c_{12}s_{23}s_{34}(s_1c_2) - s_{12}c_{23}s_{34}(s_1)$

(1, 3): $s_{34}(c_1c_2s_3) - c_{12}s_{34}(s_1s_2s_3) + c_{23}s_{34}(c_1s_2c_3) + c_{12}c_{23}s_{34}(s_1c_2c_3)$

$- s_{12}s_{23}s_{34}(s_1c_3) + s_{23}c_{34}(c_1s_2) + c_{12}s_{23}c_{34}(s_1c_2) + s_{12}c_{23}c_{34}(s_1)$

(2, 1): $- s_1c_2c_3 - c_{12}(c_1s_2c_3) + c_{23}(s_1s_2s_3) - c_{12}c_{23}(c_1c_2s_3) + s_{12}s_{23}(c_1s_3)$

(2, 2): $- c_{34}(s_1c_2s_3) - c_{12}c_{34}(c_1s_2s_3) - c_{23}c_{34}(s_1s_2c_3) + c_{12}c_{23}c_{34}(c_1c_2c_3)$

$- s_{12}s_{23}c_{34}(c_1c_3) + s_{23}s_{34}(s_1s_2) - c_{12}s_{23}s_{34}(c_1c_2) - s_{12}c_{23}s_{34}(c_1)$

(2, 3): $- s_{34}(s_1c_2s_3) - c_{12}s_{34}(c_1s_2s_3) - c_{23}s_{34}(s_1s_2c_3) + c_{12}c_{23}s_{34}(c_1c_2c_3)$

$- s_{12}s_{23}s_{34}(c_1c_3) - s_{23}c_{34}(s_1s_2) + c_{12}s_{23}c_{34}(c_1c_2) + s_{12}c_{23}c_{34}(c_1)$

(3, 1): $s_{12}(s_2c_3) + s_{12}c_{23}(c_2s_3) + c_{12}s_{23}(s_3)$

(3, 2): $s_{12}c_{34}(s_2s_3) - s_{12}c_{23}c_{34}(c_2c_3) - c_{12}s_{23}c_{34}(c_3) + s_{12}s_{23}s_{34}(c_2) - c_{12}c_{23}s_{34}$

(3, 3): $s_{12}s_{34}(s_2s_3) - s_{12}c_{23}s_{34}(c_2c_3) - c_{12}s_{23}s_{34}(c_3) - s_{12}s_{23}c_{34}(c_2) + c_{12}c_{23}c_{34}$

RHS:

(1, 1): $c_4c_5c_6 - c_{45}(s_4s_5c_6) - c_{56}(c_4s_5s_6) - c_{45}c_{56}(s_4c_5s_6) + s_{45}s_{56}(s_4s_6)$

(1, 2): $-s_4c_5c_6 - c_{45}(c_4s_5c_6) + c_{56}(s_4s_5s_6) - c_{45}c_{56}(c_4c_5s_6) + s_{45}s_{56}(c_4s_6)$

(1, 3): $s_{45}(s_5c_6) + s_{45}c_{56}(c_5s_6) + c_{45}s_{56}(s_6)$

(2, 1): $c_{61}(c_4c_5s_6) - c_{45}c_{61}(s_4s_5s_6) + c_{56}c_{61}(c_4s_5c_6) + c_{45}c_{56}c_{61}(s_4c_5c_6)$

$- s_{45}s_{56}c_{61}(s_4c_6) - s_{56}s_{61}(c_4s_5) - c_{45}s_{56}s_{61}(s_4c_5) - s_{45}c_{56}s_{61}(s_4)$

(2, 2): $-c_{61}(s_4c_5s_6) - c_{45}c_{61}(c_4s_5s_6) - c_{56}c_{61}(s_4s_5c_6) + c_{45}c_{56}c_{61}(c_4c_5c_6)$

$- s_{45}s_{56}c_{61}(c_4c_6) + s_{56}s_{61}(s_4s_5) - c_{45}s_{56}s_{61}(c_4c_5) - s_{45}c_{56}s_{61}(c_4)$

(2, 3): $s_{45}c_{61}(s_5s_6) - s_{45}c_{56}c_{61}(c_5c_6) - c_{45}s_{56}c_{61}(c_6) + s_{45}s_{56}s_{61}(c_5) - c_{45}c_{56}s_{61}$

(3, 1): $s_{61}(c_4c_5s_6) - c_{45}s_{61}(s_4s_5s_6) + c_{56}s_{61}(c_4s_5c_6) + c_{45}c_{56}s_{61}(s_4c_5c_6)$

$- s_{45}s_{56}s_{61}(s_4c_6) + s_{56}c_{61}(c_4s_5) + c_{45}s_{56}c_{61}(s_4c_5) + s_{45}c_{56}c_{61}(s_4)$

(3, 2): $-s_{61}(s_4c_5s_6) - c_{45}s_{61}(c_4s_5s_6) - c_{56}s_{61}(s_4s_5c_6) + c_{45}c_{56}s_{61}(c_4c_5c_6)$

$- s_{45}s_{56}s_{61}(c_4c_6) - s_{56}c_{61}(s_4s_5) + c_{45}s_{56}c_{61}(c_4c_5) + s_{45}c_{56}c_{61}(c_4)$

(3, 3): $s_{45}s_{61}(s_5s_6) - s_{45}c_{56}s_{61}(c_5c_6) - c_{45}s_{56}s_{61}(c_6) - s_{45}s_{56}c_{61}(c_5) + c_{45}c_{56}c_{61}$

A 3-DOF system of equations, in which ϕ_4, ϕ_5, ϕ_6 are the inputs, can be derived.

The entries in (3, 1) state:

$s_{12}(s_2c_3) + s_{12}c_{23}(c_2s_3) + c_{12}s_{23}(s_3) =$

$s_{61}(c_4c_5s_6) - c_{45}s_{61}(s_4s_5s_6) + c_{56}s_{61}(c_4s_5c_6) + c_{45}c_{56}s_{61}(s_4c_5c_6)$

$- s_{45}s_{56}s_{61}(s_4c_6) + s_{56}c_{61}(c_4s_5) + c_{45}s_{56}c_{61}(s_4c_5) + s_{45}c_{56}c_{61}(s_4).$

This equation can be written as

$$T_1 = \frac{(P_1T_2^2 + P_2) \pm \sqrt{(P_1T_2^2 + P_2)^2 - 4(M_1(T_2^2 + 1))^2 + 4(s_{12}T_2)^2}}{2(M_1(T_2^2 + 1)) + 2(s_{12}T_2)}. \quad \text{(C.4)}$$

Here, $M_1 = [s_{61}(c_4c_5s_6) - c_{45}s_{61}(s_4s_5s_6) + c_{56}s_{61}(c_4s_5c_6) + c_{45}c_{56}s_{61}(s_4c_5c_6) - s_{45}s_{56}s_{61}(s_4c_6) +$

$s_{56}c_{61}(c_4s_5) + c_{45}s_{56}c_{61}(s_4c_5) + s_{45}c_{56}c_{61}(s_4)] / 2,$

$P_1 = c_{12}s_{23} - s_{12}c_{23}$, $P_2 = s_{12}c_{23} + c_{12}s_{23}.$

The entries in (3, 3) state:

$s_{12}s_{34}(s_2s_3) - s_{12}c_{23}s_{34}(c_2c_3) - c_{12}s_{23}s_{34}(c_3) - s_{12}s_{23}c_{34}(c_2) + c_{12}c_{23}c_{34} =$

$s_{45}s_{61}(s_5s_6) - s_{45}c_{56}s_{61}(c_5c_6) - c_{45}s_{56}s_{61}(c_6) - s_{45}s_{56}c_{61}(c_5) + c_{45}c_{56}c_{61}.$

This equation can be written as

$$T_3 = \frac{(Q_1T_2) \pm \sqrt{Q_1^2T_2^2 - 4(Q_2(T_2^2) + Q_3)^2 + (Q_4(T_2^2) + Q_5)^2}}{2(Q_2 - Q_4)(T_2^2) + 2(Q_3 - Q_5)}. \quad \text{(C.5)}$$

Here, $M_2 = s_{45}s_{61}(s_5s_6) - s_{45}c_{56}s_{61}(c_5c_6) - c_{45}s_{56}s_{61}(c_6) - s_{45}s_{56}c_{61}(c_5) + c_{45}c_{56}c_{61},$

$Q_1 = 4s_{12}s_{23}$, $Q_2 = M_2 - s_{12}s_{23}c_{34}$, $Q_3 = M_2 + s_{12}s_{23}c_{34},$

$Q_4 = c_{12}s_{23}s_{34} - s_{12}c_{23}s_{34}$, $Q_5 = c_{12}s_{23}s_{34} + s_{12}c_{23}s_{34}.$

The entries in (3, 3), in which each index is shifted from i to $(i - 1)$, state

$s_{61}s_{23}(s_1s_2) - s_{61}c_{12}s_{23}(c_1c_2) - c_{61}s_{12}s_{23}(c_2) - s_{61}s_{12}c_{23}(c_1) + c_{61}c_{12}c_{23} =$

$s_{34}s_{56}(s_4s_5) - s_{34}c_{45}s_{56}(c_4c_5) - c_{34}s_{45}s_{56}(c_5) - s_{34}s_{45}c_{56}(c_4) + c_{34}c_{45}c_{56}.$

This equation can be written as

$$T_2 = \frac{(R_1 T_1) \pm \sqrt{R_1^2 T_1^2 - 4(R_2(T_1^2) + R_3)^2 + (R_4(T_1^2) + R_5)^2}}{2(R_2 - R_4)(T_1^2) + 2(R_3 - R_5)}. \quad \text{(C.6)}$$

Here, $M_3 = s_{34}s_{56}(s_4s_5) - s_{34}c_{45}s_{56}(c_4c_5) - c_{34}s_{45}s_{56}(c_5) - s_{34}s_{45}c_{56}(c_4) + c_{34}c_{45}c_{56}$,

$R_1 = 4s_{61}s_{12}$, $R_2 = M_3 - s_{61}s_{12}c_{23}$, $R_3 = M_3 + s_{61}s_{12}c_{23}$,

$R_4 = c_{61}s_{12}s_{23} - s_{61}c_{12}s_{23}$, $R_5 = c_{61}s_{12}s_{23} + s_{61}c_{12}s_{23}$.

The fold angles, $\theta = [\theta_1, \theta_2, \theta_3, \theta_4, \theta_5, \theta_6]$, uniquely define a partially folded state of the 6C. To show equations (C.4), (C.5), and (C.6) form a 3-DOF system of equations, the following example is used. Suppose the values of the sector angles used are $\alpha_{12} = \pi / 6$, $\alpha_{23} = \pi / 2$, $\alpha_{34} = 2\pi / 3$, $\alpha_{45} = \pi / 6$, $\alpha_{56} = \pi / 6$, and $\alpha_{61} = \pi / 3$. Fold angles $\theta_4 = 1.5708$, $\theta_5 = -1.4274$, $\theta_6 = 1.5708$ are used as inputs. Equations (C.4), (C.5), and (C.6) produce the following values of the remaining fold angles: $\theta_1 = -0.9273$, $\theta_2 = 1.4274$, $\theta_3 = 0.9273$. Inputting the values of the fold angles in the LHS of (C.2) results in the 3×3 identity matrix, confirming these fold angles define a partially folded state for the 6C.

The flat-foldable 6C claw vertex has the following sector angles: $\alpha_{12} = (\beta - \alpha)$, $\alpha_{23} = (\pi - \beta - \alpha)$, $\alpha_{34} = (\pi - \beta)$, $\alpha_{45} = \alpha$, $\alpha_{56} = \alpha$, $\alpha_{61} = \beta$. When angle equalities, $\phi_1 = \phi_3$ and $\phi_2 = \phi_5$, are imposed, equations (C.4), (C.5), and (C.6) can be simplified to the following set of equations:

$$\phi_1 = \phi_3, \ \phi_2 = \phi_5, \ \phi_4 = \phi_6, \ \cos\beta \tan\frac{\phi_1}{2} = \cos\alpha \tan\frac{\phi_2}{2} = \tan\frac{\phi_4}{2}. \quad \text{(C.7)}$$

Appendix D: Numerical Method for OCT

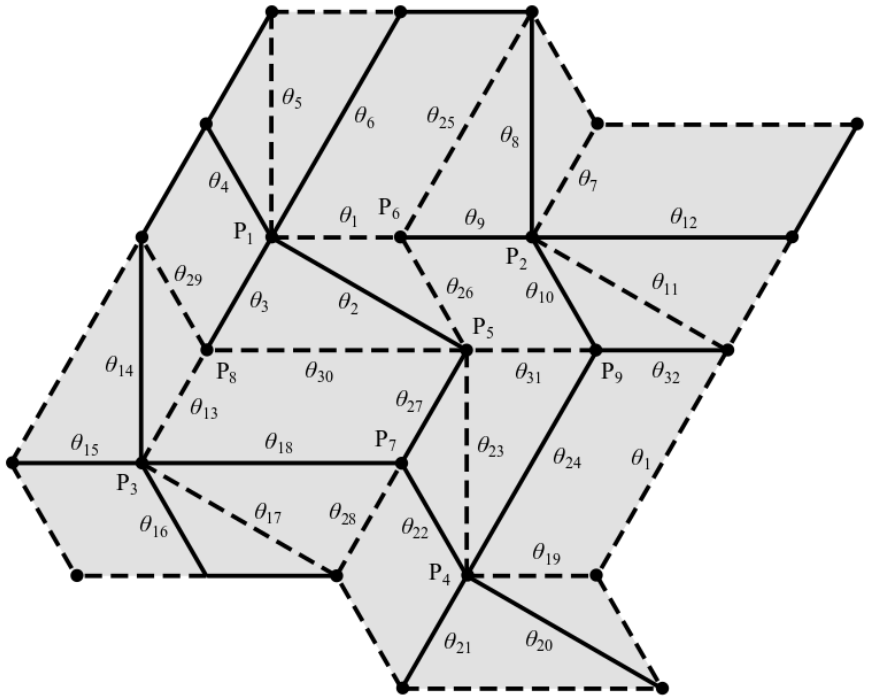


Figure D.1: Numbering of creases and vertices in the 2 × 2 OCT

The numerical method for the $M \times N$ OCT, in which M and N are positive integers, starts by numbering the creases and vertices strictly inside the crease pattern. A 2 × 2 OCT with its creases and vertices labeled is shown in Figure D.1. Without loss of generality, suppose the $M \times N$ OCT is composed of (MN) type-M claw units. The vertices and creases are numbered as follows.

The total number of vertices is $v = (4MN - 2M - 2N + 1)$. The (MN) type-M 6C vertices are numbered 1 to (MN). The ($MN - M - N + 1$) type-V 6C vertices are numbered ($MN + 1$) to ($2MN - M - N + 1$). The ($MN - M$) 4C vertices between two horizontally adjacent type-M claw units are numbered ($2MN - M - N + 2$) to

($3MN - 2M - N + 1$). The ($MN - N$) 4C vertices between two vertically adjacent type-M claw units are numbered ($3MN - 2M - N + 2$) to ($4MN - 2M - 2N + 1$).

The total number of creases is $c = (10MN - 2M - 2N)$. The ($6MN$) creases in a type-M claw unit are numbered 1 to ($6MN$). The ($2MN - 2M$) creases between two horizontally adjacent type-M claw units are numbered ($6MN + 1$) to ($8MN - 2M$). The ($2MN - 2N$) creases between two vertically adjacent type-M claw units are numbered ($8MN - 2M + 1$) to ($10MN - 2M - 2N$).

Angles α and β determine all sector angles in the OCT. Let $\alpha = \pi / 6$, $\beta = \pi / 3$. To determine the initial state, let $\phi_4 = \pi / 2$. The first six dihedral angles are determined by the following equations:

$$\phi_1 = \phi_3,\ \phi_2 = \phi_5,\ \phi_4 = \phi_6,\ \cos\beta \tan\frac{\phi_1}{2} = \cos\alpha \tan\frac{\phi_2}{2} = \tan\frac{\phi_4}{2}. \tag{D.1}$$

The remaining dihedral angles are determined as follows. For $1 \le i \le (MN)$ and $1 \le j \le 6$, let $\phi_{(6i+j-6)} = \phi_j$. For $(6MN + 1) \le i \le (10MN - 2M - 2N)$, let $\phi_i = \phi_4$. For $1 \le i \le c$, if crease i is a mountain, let $\theta_i = \phi_i - \pi$, and if crease i is a valley, let $\theta_i = \pi - \phi_i$.

Each vector of fold angles, $\theta = (\theta_1, \theta_2, \ldots, \theta_c)^T$, uniquely determines a partially folded state of the OCT. Each DOF in the OCT is represented by an infinitesimal change in θ represented by $\Delta\theta = (\Delta\theta_1, \Delta\theta_2, \ldots, \Delta\theta_c)^T$. A MATLAB program is written to implement the numerical method computing the DOFs of the $M \times N$ OCT. The numerical method computes the $(9v) \times c$ Jacobian matrix J_{comb}, which satisfies:

$$J_{comb}\Delta\theta = 0_{9v\times 1}. \tag{D.2}$$

Figure D.2 shows the null space of the Jacobian matrix, J_{comb}, for a 2×2 OCT, which is calculated by taking its singular value decomposition in MATLAB. Each column

represents a solution for $\Delta\theta$, which also represents one of the five DOFs in the 2 × 2 OCT.

	1	2	3	4	5
1	0.1078	-0.2726	0	0	0
2	-0.1334	0.2623	0.1911	0	0
3	-0.1078	0	0.0662	0	0
4	-0.1348	0	0.3971	0	0
5	0.1334	0.2098	-0.3057	0	0
6	-0.1348	-0.0909	0	0	0
7	0.1078	-0.0763	0	0.6167	0
8	-0.1334	0	0	-0.5934	0
9	-0.1078	0.2726	0	0	0
10	-0.1348	0.0710	0	0	0
11	0.1334	-0.3400	0	-0.4747	0
12	-0.1348	0.4960	0	0.2056	0
13	0.1078	0	-0.0662	0	0
14	-0.1334	0	0	0	0.3536
15	-0.1078	0	-0.1867	0	0.1225
16	-0.1348	0	-0.2559	0	0.7348
17	0.1334	0	0.4381	0	-0.5657
18	-0.1348	0	-0.3102	0	0
19	0.1078	0.2129	0	0	0
20	-0.1334	-0.2049	-0.1493	0	0
21	-0.1078	0	-0.0517	0	0
22	-0.1348	0	-0.3102	0	0
23	0.1334	-0.1639	0.2388	0	0
24	-0.1348	0.0710	0	0	0
25	0.1348	-0.3407	0	0	0
26	0.1348	-0.3407	0	0	0
27	-0.1078	0	-0.2482	0	0
28	0.1078	0	0.2482	0	0
29	0.1348	0	-0.0827	0	0
30	0.1348	0	-0.0827	0	0
31	0.1078	-0.0568	0	0	0
32	-0.1078	0.0568	0	0	0

Figure D.2: The null space of J_{comb} of the 2 × 2 OCT with $\alpha = \pi / 6$ and $\beta = \pi / 3$

References

Akitaya, H., Demaine, E. D., and Ku, J. S., (2017). "Simple Folding Is Really Hard." *Journal of Information Processing*, *25*, 580 – 589.

Akitaya, H., Demaine, E. D., Takashi, H., Hull T. C., Ku, J. S., and Tachi, T., (2018). "Rigid Foldability Is NP-Hard." *Journal of Computational Geometry*, *11*(*1*), 93 – 124.

Barreto, R. L. P., Morlin, F. V., de Souza, M. B., Carboni, A. P., and Martins, D., (2020). "Multiloop Origami Inspired Spherical Mechanisms." *Mechanism and Machine Theory*, *155*, 1 – 13.

Beggs, J. S., (1966). *Advanced Mechanism*. 132 – 136. New York: The Macmillan Company.

Callens, S. J. P., and Zadpoor, A. A., (2017). "From Flat Sheets to Curved Geometries: Origami and Kirigami Approaches." *Materials Today,* 1 – 24.

Chen, Y., Feng, H., Ma, J., Peng, R., You, Z., (2016). "Symmetric Waterbomb Origami." *Proceedings of the Royal Society A*, *472*, 1 – 20.

Chen, Y., Lv, W., Li, J., and You, Z., (2017). "An Extended Family of Rigidly Foldable Origami Tubes." *Journal of Mechanisms and Robotics*, *9*, 1 – 7.

Chen, Y., Lv, W., Peng, R., and Wei, G., (2019). "Mobile Assemblies of Four-Spherical-4R-Integrated Linkages and the Associated Four-Crease-Integrated Rigid Origami Patterns." *Mechanism and Machine Theory*, *142*, 1 – 25.

Chen, Y., Peng, R., and You, Z., (2015a). "Origami of Thick Panels." *Science*, *349*, 396 – 400.

Chen, Y., Peng, R., and You, Z., (2015b). "Supplementary Material for Origami of Thick Panels." *Science*, *349*, 396 – 400.

Chen, Y. and You, Z., (2005). "Mobile Assemblies Based on the Bennett Linkage." *Proceedings of the Royal Society A*, *461*, 1229 – 1245.

Cheung, K. C., Tachi, T., Calisch, S., Miura, K., (2014). "Origami Interleaved Tube Cellular Materials." *Smart Materials and Structures, 23,* 1 – 10.

Davis, E., Demaine, E. D., Demaine, M. L., and Ramseyer, J., (2013). "Reconstructing David Huffman's Origami Tessellations." *Journal of Mechanical Design, 135 (11)*, 1 – 8.

Eppstein, D., (2018). "Realization and Connectivity of the Graphs of Origami Flat Foldings." *Journal of Computational Geometry*, *10*(*1*), 257 – 280.

Escher, M. C., (2005). *M. C. Escher's Legacy: A Centennial Celebration,* 325. Rome: Springer Science & Business Media.

Evans, T.A. and Lang, R. J., (2015). "Rigidly Foldable Origami Twists." In Miura, K., Kawasaki, T., Tachi, T., Uehara, R., Lang, R. J., and Wang-Iverson, P. (Eds.), *Origami6*, 119 – 130. American Mathematical Society.

Evans, T. A., Lang, R. J., Magleby, S. P., and Howell, L. L., (2015). "Rigidly Foldable Origami Gadgets and Tessellations." *Royal Society Open Science*, *2*, 1 – 18.

Fang, H., Li, S., and Wang, K. W., (2016). "Self-Locking Degree-4 Vertex Origami Structures." *Proceedings of the Royal Society A, 472*, 1 – 22.

Fang, H., and Xia, Y., (2018). "Programmable Self-Locking Origami Mechanical Metamaterials." *Advanced Materials*, *30*, 2933 – 2945.

Filipov, E. T., Tachi, T., and Paulino, G. H., (2015). "Origami Tubes Assembled into Stiff, yet Reconfigurable Structures and Metamaterials." *PNAS*, *112(40),* 12321 – 12326.

Gan, W. W. and Pellegrino, S., (2006). "Numerical Approach to the Kinematic Analysis of Deployable Structures Forming a Closed Loop." *Proceedings of the Institution of Mechanical Engineers Part C: Journal of Mechanical Engineering Science*, *220*(*7*), 1045 – 1056.

Gattas, J. M., Wu, W., and You, Z., (2013). "Miura-Base Rigid Origami: Parameterizations of First-Level Derivative and Piecewise Geometries." *Journal of Mechanical Design, 135*, 1 – 11.

Gattas, J. M., and You, Z., (2015). "Geometric Assembly of Rigidly-Foldable Morphing Sandwich Structures." *Engineering Structure*, *94*, 149 – 159.

Grunbaum, B., and Shephard, G. C., (1977). "The Eighty-One Types of Isohedral Tilings in the Plane." *Mathematical Proceedings of the Cambridge Philosophical Society, 82*, 177 – 196.

Hu, Y., Liang, H., and Duan, H., (2019). "Design of Cylindrical and Axisymmetric Origami Structures Based on Generalized Miura-Ori Cell." *Journal of Mechanisms and Robotics*, *11*, 1 – 10.

Hull, T.C., (2013). "The Combinatorics of Flat Folds: a Survey." In Hull, T.C. (Ed.), *Origami3*, 29 – 38. Natick, Massachusetts: A K Peters.

Hull, T.C., (2015). "Counting Mountain-Valley Assignments for Flat-Folds." In Miura, K., Kawasaki, T., Tachi, T., Uehara, R., Lang, R. J., and Wang-Iverson, P. (Eds.), *Origami6*, 3 – 10. American Mathematical Society.

Hull, T. C., and Tachi, T., (2018). “Self-foldability of Monohedral Quadrilateral Origami Tessellations.” In Lang, R. J., Bolitho, M., and You, Z. (Eds.), *Origami7*, *2*, 521 – 532, United Kingdom: Tarquin Publications.

Ku, J. S. and Demaine, E. D., (2016). “Folding Flat Crease Patterns with Thick Materials.” *Journal of Mechanisms and Robotics*, *8*(*3*), 1 – 6.

Lang, R. J., (2018). *Twists, Tilings, and Tessellations: Mathematical Methods for Geometric Origami*. 29 – 34. Boca Raton: CRC Press.

Li, R., Yao, Y., and Kong, X., (2017). “Reconfigurable Deployable Polyhedral Mechanism Based on Extended Parallelogram Mechanism.” *Mechanism and Machine Theory, 116*, 467 – 480.

Liu, S., Lv, W. Chen, Y., and Lu, G., (2016). “Deployable Prismatic Structures with Rigid Origami Patterns.” *Journal of Mechanisms and Robotics*, *8,* 1 – 11.

Liu, X. J. and Wang, J., (2003). “Some New Parallel Mechanisms Containing the Planar Four-Bar Parallelogram.” *The International Journal of Robotics Research*, *22*(*9*), 717 – 732.

Lu, S., Zlatanov, D., and Ding, X., (2017). “Approximation of Cylindrical Surfaces with Deployable Bennett Networks.” *Journal of Mechanisms and Robotics, 9,* 1 – 6.

Ma, J., Song, J., and Chen, Y., (2018), “An Origami-Inspired Structure with Graded Stiffness.” *International Journal of Mechanical Sciences*, *136*, 134 – 142.

Meloni, M., Cai, J., Zhang, Q., Lee, D. S.-H., Li, M., Ma, R., Parashkevov, T. E., and Feng, J., (2021), “Engineering Origami: A Comprehensive Review of Recent Applications, Design Methods, and Tools.” *Advanced Science*, *8*, 1 – 31.

Miura, K., (1985). “Method of Packaging and Deployment of Large Membranes in Space.” *The Institute of Space and Astronautical Science Report*, *618*, 1 – 9.

Paris, J., Merz, J., Buffart, H., Hoffmann, S., Weigel, C., Husing, M., Trautz, M., and Corves, B., (2018). “Classification, Collection, and Simulation of Folding Mechanisms.” presented in International Conference on Reconfigurable Mechanisms and Robots (ReMAR), Delft, Netherlands, 20 to 22 June 2018.

Peng, R., Ma, J., and Chen, Y., (2018). “The Effect of Mountain-Valley Folds on the Rigid Foldability of Double Corrugated Pattern.” *Mechanism and Machine Theory*, *128*, 461 – 474.

Pennestri, E., Valentini, P.P., Figliolini, G., and Angeles, J., (2016). “Dual Cayley-Klein Parameters and Mobius Transform: Theory and Applications.” *Mechanism and Machine Theory, 106,* 50 – 67.

Saito, K., Tsukahara, A., and Okabe, Y., (2015). “Designing of Self-Deploying Origami Structures Using Geometrically Misaligned Crease Patterns.” *Proceedings of the Royal Society A*, *472*, 1 – 16.

Sareh, P., and Guest, S. D., (2013). “Minimal Isomorphic Symmetric Variations on the Miura Fold Pattern.” presented in Proceedings of the First Conference on Transformables 2013, Seville, Spain, 18 to 20 Sept. 2013.

Sareh, P., and Guest, S. D., (2015a). “Design of Isomorphic Symmetric Descendants of the Miura-ori.” *Smart Materials and Structures*, *24*, 1 – 12.

Sareh, P., and Guest, S. D., (2015b). “A Framework for the Symmetric Generalization of the Miura-ori.” *International Journal of Space Structures*, *30*(*2*), 141 – 152.

Schenk, M., and Guest, S. D., (2011). "Origami Folding: A Structural Engineering Approach." In Wang-Iverson, P., Lang, R. J., and Yim, M. (Eds.), *Origami*5, 291 – 303. A K Peters.

Schenk, M., and Guest, S. D., (2013a). "Geometry of Miura-Folded Metamaterials." *PNAS*, *110*(*9*), 3276 – 3281.

Schenk, M., and Guest, S. D., (2013b). "Geometry of Miura-Folded Metamaterials – Supplementary Information." *PNAS*, *110*(*9*), 3276 – 3281.

Suto, K., Adachi, A., Tachi, T., and Yamaguchi, Y., (2018). "An Edge-Extrusion Approach to Generate Extruded Miura-Ori and Its Double Tiling Origami Patterns." In Lang, R. J., Bolitho, M., and You, Z. (Eds.), *Origami7*, *2*, 435 – 450, United Kingdom: Tarquin Publications.

Tachi, T., (2009). "Generalization of Rigid Foldable Quadrilateral Mesh Origami." presented in Proceedings of the International Association for Shell and Spatial Structures Symposium 2009, Valencia, Spain, 28 Sept. to 2 Oct. 2009.

Tachi, T., (2010a). "Freeform Rigid-Foldable Structure Using Bidirectionally Flat-Foldable Planar Quadrilateral Mesh." In Ceccato, C., Hesselgren, L., Pauly, M., Pottmann, H., Wallner, J. (Eds.), *Advances in Architectural Geometry*, 87 – 102. Springer.

Tachi, T., (2010b). "Freeform Variations of Origami." *Journal for Geometry and Graphics*, *14*(*2*), 203 – 215.

Tachi, T., (2011). "Rigid-Foldable Thick Origami." In Wang-Iverson, P., Lang, R. J., and Yim, M. (Eds.), *Origami5*, 29 – 37. A K Peters.

Tachi, T., (2016). "Designing Rigidly Foldable Horns Using Bricard's Octahedron." *Journal of Mechanisms and Robotics*, *8,* 1 – 6.

Tachi, T., (2019). "Introduction to Structural Origami." *Journal of the International Association for Shell and Spatial Structures*, *60*(*1*), 7 – 18.

Tachi, T., and Hull, T. C., (2017). "Self-foldability of Rigid Origami." *Journal of Mechanisms and Robotics, 9,* 1 – 9.

Turner, N., Goodwine, B., and Sen, M., (2015). "A Review of Origami Applications in Mechanical Engineering." *Proceedings of the Institution of Mechanical Engineers, Part C: Journal of Mechanical Engineering Science*, *230*(*14*), 2345 – 2362.

Vlachaki, E. and Liapi, K. A., (2021). "Folded Surface Elements Coupled with Planar Scissor Linkages: A Novel Hybrid Type of Deployable Structures." *Curved and Layered Structures*, *8*, 137 – 146.

Xiang, X., Fu, Z., Zhang S., Lu, G., Ha, N. S., Liang, Y., and Zhang X., (2021). "The Mechanical Characteristics of Graded Miura-Ori Metamaterials." *Materials & Design*, *211*, 1 – 14.

Xing, D., and You, Z., (2019). "Constructing Scissor-like Structures and Parallelogram Linkages with 4-Crease Single-Vertex Flat-Foldable Rigid Origami and Their Thick-Panel Versions." presented in ASME 2019 International Design Engineering Technical Conferences, Anaheim, California, 18 to 21 Aug. 2019.

Xing, D., and You, Z., (2022). "Origami Claw Tessellation and Its Stacked Structure." presented in ASME 2022 International Design Engineering Technical Conferences, St. Louis, Missouri, 14 to 17 Aug. 2022.

Yang, F., Zhang, M., Ma, J., You, Z., Yu, Y., Chen, Y., and Paulino, G. H., (2022). "Design of Single Degree-of-Freedom Triangular Resch Patterns with Thick-panel Origami." Mechanism and Machine Theory, 169, 1 – 16.

Yellowhorse, A. D. and Howell, L. L., (2019). "Regular 2D and 3D Linkage-Based Origami Tessellations." presented in ASME 2019 International Design Engineering Technical Conferences, Anaheim, California, 18 to 21 Aug. 2019.

Yellowhorse, A. D., Lang, R. J., Tolman, K., and Howell, L. L., (2018). "Creating Linkage Permutations to Prevent Self-Intersection and Enable Deployable Networks of Thick-Origami." *Scientific Reports*, *8*, 1 – 9.

Yu, J., Dai, J. S., Zhao, T., Bi, S., and Zong, G., (2009). "Mobility Analysis of Complex Joints by Means of Screw Theory." *Robotica*, *27*, 915 – 927.

Yuan, L., Dai, H., Song, J., Ma, J., and Chen, Y., (2020). "The Behavior of a Functionally Graded Origami Structure Subjected to Quasi-static Compression." *Materials and Design*, *189*, 1 – 18.

Zhang, X. and Chen, Y, (2018). "Mobile Assemblies of Bennett Linkages from Four-Crease Origami Patterns." *Proceedings of the Royal Society A, 474*, 1 – 17.

Zhang, X. and Chen, Y., (2019). "Vertex-Splitting on a Diamond Origami Pattern." *Journal of Mechanisms and Robotics*, *11*, 1 – 12.

Zhuang, Y., Zhang, Y., and Duan X., (2015). "Complete Real Solution of the Five-Orientation Motion Generation Problem for a Spherical Four-Bar Linkage." *Chinese Journal of Mechanical Engineering*, *28*(*2*), 258 – 266.